



HAL
open science

Design of a virtual synchronous generator (VSG), a dynamic adaptive system, for Micro Grid stabilization with high penetration of renewable energies.

Audrey Moulichon

► **To cite this version:**

Audrey Moulichon. Design of a virtual synchronous generator (VSG), a dynamic adaptive system, for Micro Grid stabilization with high penetration of renewable energies.. Electric power. Université Grenoble Alpes, 2019. English. NNT : 2019GREAT064 . tel-02527619

HAL Id: tel-02527619

<https://theses.hal.science/tel-02527619>

Submitted on 1 Apr 2020

HAL is a multi-disciplinary open access archive for the deposit and dissemination of scientific research documents, whether they are published or not. The documents may come from teaching and research institutions in France or abroad, or from public or private research centers.

L'archive ouverte pluridisciplinaire **HAL**, est destinée au dépôt et à la diffusion de documents scientifiques de niveau recherche, publiés ou non, émanant des établissements d'enseignement et de recherche français ou étrangers, des laboratoires publics ou privés.

THÈSE

Pour obtenir le grade de

DOCTEUR DE LA COMMUNAUTE UNIVERSITE GRENOBLE ALPES

Spécialité : GENIE ELECTRIQUE

Arrêté ministériel : 25 mai 2016

Présentée par

Audrey MOULICHON

Thèse dirigée par **M. Nouredine HADJSAID**, Grenoble INP
et codirigée par **M. Mazen ALAMIR**, CNRS.

préparée au sein du **Laboratoire de Génie Electrique de
Grenoble (G2elab)** dans l'**École Doctorale Electronique,
Electrotechnique, Automatique, Traitement du Signal
(EEATS)**

Conception d'un système adaptatif dynamique de "Générateur Synchrone Virtuel" pour la stabilisation des micro-réseaux électriques à fort taux de pénétration d'énergie renouvelable.

Thèse soutenue publiquement le **11 décembre 2019**
devant le jury composé de :

Monsieur Johan DRIESEN

Professeur, KU Leuven, Président

Monsieur Marc PETIT

Professeur, CentraleSupélec, Rapporteur

Monsieur Malek GHANES

Professeur, Centrale Nantes, Rapporteur

Monsieur Nouredine HADJSAID

Professeur, Grenoble INP, Directeur de thèse

Monsieur Mazen ALAMIR

Directeur de recherche, CNRS, Co-directeur de thèse

Monsieur Vincent DEBUSSCHERE

Maître de conférences, Grenoble INP, Co-encadrant

Monsieur Lauric GARBUIO

Maître de conférences, Grenoble INP, Co-encadrant

Monsieur Mustapha RAHMANI

Dr Ingénieur R & D, Schneider Electric, Invité

Monsieur Miao-Xin WANG

Dr Power Conversion Manager, Schneider Electric, Invité



THÈSE

Pour obtenir le grade de

DOCTEUR DE LA COMMUNAUTE UNIVERSITE GRENOBLE ALPES

Spécialité : GENIE ELECTRIQUE

Arrêté ministériel : 25 mai 2016

Présentée par

Audrey MOULICHON

Thèse dirigée par **M. Nouredine HADJSAID**, Grenoble INP
et codirigée par **M. Mazen ALAMIR**, CNRS.

préparée au sein du **Laboratoire de Génie Electrique de
Grenoble (G2elab)** dans l'**École Doctorale Electronique,
Electrotechnique, Automatique, Traitement du Signal
(EEATS)**

**Design of an advanced virtual synchronous
generator (VSG), a dynamic adaptive system,
for microgrids stabilization with high
penetration of renewable energies.**

Thèse soutenue publiquement le **11 décembre 2019**
devant le jury composé de :

Monsieur Johan DRIESEN

Professeur, KU Leuven, Président

Monsieur Marc PETIT

Professeur, CentraleSupélec, Rapporteur

Monsieur Malek GHANES

Professeur, Centrale Nantes, Rapporteur

Monsieur Nouredine HADJSAID

Professeur, Grenoble INP, Directeur de thèse

Monsieur Mazen ALAMIR

Directeur de recherche, CNRS, Co-directeur de thèse

Monsieur Vincent DEBUSSCHERE

Maître de conférences, Grenoble INP, Co-encadrant

Monsieur Lauric GARBUIO

Maître de conférences, Grenoble INP, Co-encadrant

Monsieur Mustapha RAHMANI

Dr Ingénieur R & D, Schneider Electric, Invité

Monsieur Miao-Xin WANG

Dr Power Conversion Manager, Schneider Electric, Invité



Contents

Résumé	I
Abstract.....	I
Remerciements	III
Illustrations.....	VI
Tables	IX
Acronym.....	XI
Chapter 1. General Introduction.....	1
1.1 Context	1
1.2 Organisation of this thesis	3
1.3 Principal Contributions.....	4
1.4 List of publications during the thesis.....	5
Chapter 2. Synchronous Machine models for standardized and grid-friendly Virtual Synchronous Generators	7
2.1 Introduction	7
2.2 The dq-transformation.....	9
2.3 Synchronous machine models definition.....	11
2.4 Synchronous machine models comparison.....	20
2.5 Conclusion.....	35
2.6 Perspective.....	36
Chapter 3. Evolution of the current controllers for the VSG	39
3.1 Introduction	39
3.2 System's state-space model analytic description.....	40
3.3 Simple PI Controller as the current controller of VSG	46
3.4 The original solution to improve the closed loop system stability: integration of a state observer	53
3.5 Combined observer and PI controller for VSG current regulation.....	57
3.6 The proposed controller: LQR controller with an integrator and a state observer	62
3.7 Conclusion on the current controllers for VSG	75
3.8 Perspectives and extensions	76

Chapter 4. Experimental validation of the current controller for VSG	77
4.1 Introduction	77
4.2 Implementation on an industrial inverter.....	78
4.3 Experimental validation of the VSG implementation	84
4.4 Conclusion.....	97
Chapter 5. Replicability and portability of the VSG control.....	99
5.1 Introduction	99
5.2 VSG control portability methodology	100
5.3 Implementation on a laboratory-scale prototype system.....	106
5.4 Experimental validation of the methodology on a laboratory-scale prototype system	112
5.5 Conclusion.....	120
5.6 Perspectives	121
Chapter 6. Polymorphic VSG, an advanced control for smart inverter.....	123
6.1 Introduction	123
6.2 Concept and analytic model of the polymorphic VSG.....	124
6.3 Polymorphic VSG model validation	129
6.4 Investigated solutions for the polymorphic integration.....	136
6.5 Comparison between the different advanced solutions	147
6.6 Conclusion.....	149
6.7 Perspectives	149
Chapter 7. General Conclusions and Perspectives	151
7.1 General Conclusion	151
7.2 Perspective of work.....	153
Reference.....	155
Appendixes.....	161
Résumé français étendu.....	192
Résumé	198
Abstract.....	198

Résumé

Les sources classiques d'énergie distribuée (DER) fournissant de l'énergie aux microgrids (généralement des groupes électrogènes diesel) sont progressivement remplacées par des onduleurs basés sur des sources d'énergie renouvelables (RES). Cependant, l'intermittence des sources d'énergie renouvelables pose des problèmes de stabilité majeurs, en particulier dans le contexte des microgrids, notamment parce que ces sources diminuent l'inertie disponible du réseau électrique. Par conséquent, les stratégies de contrôle traditionnelles pour les onduleurs, qui interfacent les différents DER connectés aux micro-réseaux électriques, doivent être adaptées.

Le générateur virtuel synchrone (VSG) est l'une des solutions les plus populaires pouvant participer à l'augmentation de l'inertie des microgrids et pouvant être intégré dans les études de stabilité traditionnelles car il présente des similitudes avec une machine synchrone. Le VSG étant encore un concept récent, principalement pris en compte pour l'intégration de la DER dans un réseau, diverses problématiques demeurent non résolues (certaines d'entre elles sont abordées dans ce manuscrit). De plus, les différentes solutions trouvées dans la littérature ne prennent pas en compte les aspects industriels et pratiques de son développement (également pris en compte dans cette thèse industrielle).

Cette thèse est dédiée aux onduleurs basés sur le VSG et à leur intégration dans des microgrids à forte pénétration d'énergie renouvelable variable. Cette thèse a été réalisée grâce à la coopération de deux laboratoires, G2Elab et Gipsa-Lab, en collaboration avec Schneider Electric et son équipe de R & D, Power Conversion.

Abstract

The classical distributed energy resources (DER) supplying energy to microgrids (usually diesel generator-sets) are progressively supplanted by supplier based on renewable energy sources (RES). However, the intermittency of RES leads to major stability issues, especially in the context of microgrids, notably because these sources usually decrease the available inertia of the grid. Hence, the traditional control strategies for inverters, interfacing the various DERs connected to the microgrid, needs adapting.

The virtual synchronous generator (VSG) is one of the most popular solution that can participate in increasing the microgrids inertia and that could be integrated into traditional stability studies because it presents similarities with a synchronous machine. As the VSG is still a recent concept, mostly considered for the DER integration in microgrid, various problematics remain unresolved (some of which are addressed in this manuscript). In addition, the different solutions that can be found in the literature do not consider the industrial and practical aspect of its development (also considered in this industrial thesis).

This thesis is dedicated to the VSG-based inverters and their integration in microgrids with a high level of variable renewable energy penetration. This PhD have been carried out thanks to the cooperation between two laboratories, G2Elab and Gipsa-Lab, in collaboration with Schneider Electric and its R & D team, Power Conversion.

Remerciements

Cette thèse est la réalisation d'un rêve de jeune fille, d'une fille qui se rêvait d'être « ingénieur en énergie renouvelable » et qui a découvert, au fil de recherches sur le sujet et de ses études supérieures, que le développement des énergies renouvelables, notamment leur insertion dans les réseaux électriques, nécessite encore de nombreux travaux de recherches pour résoudre les différents problèmes rencontrés.

Je tiens à remercier les personnes qui m'ont encadré durant cette thèse, en commençant par mes deux directeurs de thèse, HADJSAID Nouredine et MAZEN Alamir, ainsi que l'ensemble des mes encadrants académiques, Lauric GARBUIO et Vincent DEBUSCHERES. Vous avez tous su me conseiller scientifiquement, quel que soit le domaine, mais aussi humainement afin de faire de cette thèse une aventure que j'ai pu entreprendre avec joie. Vous avez tous fait en sorte que les meilleures conditions soient réunies pour que je réussisse cette thèse malgré les difficultés rencontrées et les sujets très variés qui ont pu être traités dans cette thèse. Je remercie aussi grandement le G2Elab de m'avoir accueillie pendant ma thèse et d'avoir mis à ma disposition tous les éléments qui m'ont permis de réaliser mes travaux dans les meilleures conditions. Je remercie aussi le Gipsa-Lab qui m'a ouvert ses portes lors de mes visites « éclairs » mais très importantes (pour que Mazen puisse répondre à mes nombreuses questions :-D).

Ensuite, je suis très reconnaissante à l'entreprise Schneider Electric de m'avoir fait confiance et permise de réaliser cette thèse et par la même occasion mon rêve de jeune fille. Je remercie Miao-Xin Wang de m'avoir accepté dans son équipe et permis d'utiliser le laboratoire Microgrid afin notamment d'effectuer la validation expérimentale de la solution développée durant ma thèse. Je tiens particulièrement à remercier Mustapha pour toute l'aide qu'il a su m'apporter pendant la thèse et son encadrement dans la réalisation de ce projet. Merci encore pour ton soutien et les conseils que tu as su me donner.

Je tiens également à avoir un mot pour mes collègues de Schneider Electric de l'équipe Power Conversion, avec qui j'ai eu trois années incroyables, que ce soit au laboratoire Darlington, au 2^{ème} étage ou en dehors avec les sorties au lac en été et les raclettes en hiver.

Je remercie Merouane et Jean qui m'ont montré la voie en soutenant l'année où j'ai commencé ma thèse. Pour n'en citer que certains mais parmi les meilleurs avec qui j'ai pu travailler dans l'équipe qui m'a intégré, Alain, Pierre-Yves, Lionel, puis ensuite Chaouki qui a

réussi son BTS et sa licence avec brio, Thomas et Michaël en alternance à l'ENSE3, Antoine qui soutient pendant que j'écris ses mots, Kepa qui va aussi bientôt finir son doctorat, et enfin Jérôme en reprise d'étude et dont je souhaite la réussite. Alain, je m'excuse encore pour avoir fait tomber le labo pendant mes tests mais on a réussi à récupérer des bons résultats expérimentaux malgré tout :-).

Je remercie aussi les collègues qui ont quitté notre équipe et auxquels je souhaite le meilleur pour la suite, Caroline et Grace toujours à Schneider Electric dans d'autres équipes, Sylvain et Yann qui sont partis quand je débute, et les personnes qui nous ont rejoint, Roger, Jérôme et Alain. Je n'oublie bien évidemment pas les personnes avec qui j'ai pu échanger dans Schneider Electric et que j'ai eu plaisir à faire la connaissance, Benoît, Alfredo, Trinidad, David, Jean Louis, Laurent et tant d'autres.

Un grand merci également à tous les membres du G2Elab, permanents et doctorants réunis que j'ai eu la chance de côtoyer. J'ai particulièrement apprécié l'ambiance générale et la bienveillance de mes collègues.

Je remercie les permanents, que ce soit David que j'ai beaucoup embêté au sujet des onduleurs (et vive l'Alsace ! région de rêve), Yvon, Raphaël, Antoine, Cédric, William, Seddik, Gilles, Elise, Cathy et tous ceux que j'oublie de citer mais avec qui j'ai eu l'occasion de discuter et échanger autour d'un café, pendant une réunion, en dégustant un petit dèj du jeudi ou encore durant un des événements du labo et d'Oplat. Merci de tout coeur à toi, Marie-Cécile, pour ton soutien, ta patience et ton écoute surtout à la fin quand je n'en pouvais plus, tu m'as permis de tenir et tu m'as poussé à finir en temps et en heure (et il faut que je récupère la recette des snickers vegan ! :-D).

Je remercie les doctorants du G2Elab, maintenant docteur qui m'ont montré la voie et qui ont toujours mis de l'ambiance au cluster SYREL : Bargahv, Stephan, Félix, Nikolaos, Laurène, Carla, Kevin. Sachez qu'on a rajouté quelques images sur vos murs en plus de celles qui y étaient déjà. Mahana, le bureau n'est plus le même depuis que tu es parti et il faut aussi qu'on arrive à trouver un moyen de continuer nos soirées jeux de plateaux que ce soit à Paris, à Grenoble ou derrière un écran.

Je souhaite aussi le meilleur aux doctorants, et futurs docteurs, que j'abandonne alors qu'ils sont en cours de route dans leur thèse : Ali, Kim, Pierre, Mamadou, Lalitha, Rafael. Je vous souhaite de très bons résultats, des belles découvertes et une superbe soutenance, et surtout de commencer la rédaction dans les meilleures conditions.

Aleksandr, Andy, Candela, Jean-Pierre, Jonathan, je vous souhaite le meilleur pour votre début de thèse et pour les trois loooooongues années qu'ils vous restent à vivre, subir mais aussi explorer et surtout rêver :-D. J'espère de tout coeur que vous garderez l'habitude de fêter les anniversaires et les petits déjeuner du jeudi comme il se doit : avec joie, bonheur et surtout plaisir pour vos papilles.

Un dernier petit mot aussi à Marcos qui m'a grandement aidé à la fin de thèse et que j'ai traumatisé avec différents logiciels, une multitude de versions différentes mais surtout des dinosaures comme Matlab R7... Merci encore pour tout le travail que tu as pu faire. Enfin, je ne sais pas si ce que tu as appris avec moi te sert régulièrement mais j'espère que tu gardes de bons souvenirs du G2Elab et de Grenoble.

Merci encore à tous pour toute la bonne ambiance que ce soit à Schneider Electric ou au G2Elab. Je remercie tous ceux que j'oublie et que j'ai eu la chance de marquer (mais aussi de traumatisé :-P).

Des remerciements sincères et attentionnés également à mes amis. Votre soutien fut très important pour moi et votre présence pendant cette épreuve prouve bien l'importance de notre amitié.

Je tiens à remercier ma famille, mon grand frère, Guillaume, et tout particulièrement mes parents qui m'ont soutenu, poussé à toujours faire de notre travail notre plus grande joie et surtout qui m'ont laissé réaliser mon rêve de jeunesse, être ingénieur et permettre une meilleure intégration des énergies renouvelables. Je remercie mes grands-parents et mon oncle qui ont fait un long chemin pour venir me voir soutenir et partager ce moment.

Je garde toujours le meilleur pour la fin et donc je tiens à remercier tout particulièrement mon conjoint et partenaire depuis plus de 6 ans, Arthur. Faire une thèse est une aventure avec de nombreuses péripéties, dont à certains moments on n'arrive plus à discerner la fin. Mais vivre au quotidien avec un doctorant est loin d'être une tâche aisée, c'est aussi une épreuve. Arthur, toi qui m'as supporté pendant les joies mais aussi pendant les difficultés, tu as su me remotiver et m'encourager alors que je ne pensais plus pouvoir y arriver. Je te remercie d'avoir été là et je te souhaite le meilleur pour ton aventure de doctorant qui commence aussi.

Illustrations

Figure 1.1: Previous VSG control scheme extract from [23].	3
Figure 2.1: Stator and rotor circuits of a synchronous machine [45]	9
Figure 2.2: Static synchronous machine model phasor diagram	19
Figure 2.3: Schematic representation of $\mathcal{L}_d(s)$ magnitude for the SM models.	22
Figure 2.4: Schematic representation of $\mathcal{G}(s)$ magnitude for the SM models.	23
Figure 2.5: Schematic representation of $\mathcal{L}_q(s)$ magnitude for the SM models.	24
Figure 2.6: Output current i^d for the different models during the scenario described in Table 1	25
Figure 2.7: Output current i^q for the different models during the scenario described in Table 1	25
Figure 2.8: Output current i^q during an impact of load for the different models.	26
Figure 2.9: Output three-phases currents supplying a high inductive load for reduced model.	26
Figure 2.10: Output three-phases currents supplying a high inductive load for complete model.	27
Figure 2.11: Output frequency in p.u. for the different models during the scenario described in Table 1.	27
Figure 2.12: RMS output voltage for the different models during the scenario described in Table 1.	28
Figure 2.13: Output current magnitude for the different models during a short-circuit.	29
Figure 2.14: Non-linear load scheme.	31
Figure 2.15: Output three phase voltages supplying a non-linear load for (a) complete, (b) reduced and (c) static models.	32
Figure 2.16: Grid RMS voltage after a load impact with the static model VSG and a generator set in parallel.	33
Figure 3.1: Inverter single line schema.	41
Figure 3.2: Current i^d for both state-space and reference models.	45
Figure 3.3: Current i^q for both state-space and reference models.	45
Figure 3.4: Zoom on currents i^d and i^q during a load impact for state-space and reference models.	46
Figure 3.5: Inverter current i_L^d and the synchronous machine current i^d for PI controller.	49
Figure 3.6: Inverter current i_L^q and the synchronous machine current i^q for PI controller.	50
Figure 3.7: Zoom on currents i^d and i_L^d , and i^q and i_L^q during a load impact for PI controller.	50
Figure 3.8: Duty ratio α^d compared to reference α^{d*} for PI controller	51
Figure 3.9: Duty ratio α^q compared to reference α^{q*} for PI controller	51
Figure 3.10: Inverter's three-phase voltages, currents and duty ratios for VSG controlled by PI Controller.	52
Figure 3.11: V Voltage \hat{e}_{fd} compared to e_{fd}	55
Figure 3.12: Voltage \hat{V}_g^d compared to V_g^d	55
Figure 3.13: Voltage \hat{V}_g^q compared to V_g^q	56
Figure 3.14: Zoom on the voltages \hat{e}_{fd} compared to e_{fd} .	56
Figure 3.15: : Zoom on both voltages \hat{V}_g^d and \hat{V}_g^q compared to V_g^d and V_g^q	57

Figure 3.16: Inverter current i_L^d compared to synchronous machine current i^d	58
Figure 3.17: Inverter current i_L^q compared to synchronous machine current i^q	59
Figure 3.18: Zoom on currents i^d and i_L^d , and i^q and i_L^q during a load impact for PI controller and observer.	59
Figure 3.19: Duty ratio α^d compared to reference α^{d*} for PI controller and observer	60
Figure 3.20: Duty ratio α^q compared to reference α^{q*} for PI controller and observer	60
Figure 3.21: Inverter's three-phase voltages, currents and duty ratios for PI controller and an observer.	61
Figure 3.22: off-loaded VSG three-phase inverter's current for PI controller and an observer	61
Figure 3.23: Reference ratio α^{d*} and α^{q*}	64
Figure 3.24: Proposed current controller	67
Figure 3.25: Inverter current i_L^d compared to synchronous machine current i^d	69
Figure 3.26: Inverter current i_L^q compared to synchronous machine current i^q	70
Figure 3.27: Zoom on the currents i^d and i_L^d , and i^q and i_L^q during a load impact for the proposed controller	70
Figure 3.28: Duty ratio α^d compared to reference α^{d*} for the proposed controller	71
Figure 3.29: Duty ratio α^q compared to reference α^{q*} for the proposed controller	71
Figure 3.30: Inverter three phase voltages, currents and duty ratios during a 20 kW load shedding for the proposed controller.	72
Figure 3.31: off-loaded VSG three-phase inverter's current for the proposed controller.	72
Figure 3.32: Inverter three phase voltages, currents and duty ratios during a 20 kW load impact.....	73
Figure 3.33: Inverter three phase voltages, currents and duty ratios during a 20 kVA load impact.....	74
Figure 3.34: Inverter three phase voltages, currents and duty ratios during a short-circuit.	74
Figure 4.1: Schematic of the Typhoon HIL tests.	78
Figure 4.2: Implemented VSG control scheme.	79
Figure 4.3: Fixed-point variable comparison with a single variable.	80
Figure 4.4: Conversion from traditional implementation in Simulink to an adapted DSP code.	80
Figure 4.5: Implemented VSG adapted regulation scheme.	81
Figure 4.6: Measure of the CPU activity on the DSP on the controlled card of the inverter.	82
Figure 4.7: Identification of the sampling block real activity.	82
Figure 4.8: Identification on the measured CPU signal.	83
Figure 4.9: Schneider Electric microgrid installation.....	85
Figure 4.10: Schematic representation for standalone tests.	86
Figure 4.11: VSG behaviour during a start on a 20 kW load.	87
Figure 4.12: VSG behaviour during a load impact of 20 kW.....	87
Figure 4.13: Zoom on the Currents behaviour during a load shedding of 20 kW.	88
Figure 4.14: VSG voltages behaviour during a load shedding of 20 kW.....	88
Figure 4.15: VSG voltage behaviour supplying a 17.5 kVAr load.	89
Figure 4.16: VSG current behaviour supplying a 17.5 kVAr load.....	89
Figure 4.17: VSG behaviour supplying a 3 kW single phase motor.	90
Figure 4.18: VSG behaviour supplying a 15 kVA drive connected to a DC machine.	91
Figure 4.19: VSG three-phase currents behaviour supplying a compressor.	91
Figure 4.20: VSG three-phase voltage behaviour supplying a compressor.....	92

Figure 4.21: VSG currents behaviour during phase-phase short-circuit	93
Figure 4.22: VSG voltages behaviour during phase-phase short-circuit	93
Figure 4.23: VSG behaviour during a tri-phases short-circuit.	94
Figure 4.24: Schematic representation of VSG inverter in parallel with other power source supplying a load. ...	95
Figure 4.25: Microgrid voltages for the load impact of a 25 kVA load.	95
Figure 4.26: VSG and generator one phase current supplying a 35 kVA load.....	96
Figure 4.27: Microgrid voltage for a load impact of 40 kVA.	96
Figure 4.28: Output VSG currents for a load impact of 40 kVA.	97
Figure 5.1: Steps to determine the parameters of the SM model, adapted to the inverter's characteristics.	105
Figure 5.2: Schematic diagram of the laboratory-scale prototype system for VSG based PHIL validation.	107
Figure 5.3: Testbench single-line scheme.	109
Figure 5.4: dSPACE® schematic control of the testbench inverter.	109
Figure 5.5: Microgrid single-line diagram for PHIL.	110
Figure 5.6: ITM method for virtual model power interface (adapted for [70]).	110
Figure 5.7: Voltage oscillation problems due to the ITM method.	111
Figure 5.8: Schematic representation for testbench standalone tests.	114
Figure 5.9: Testbench VSG behaviour during a load impact of 4 kW (i.e. 100 %).	114
Figure 5.10: Testbench output voltages for a 5 kHz PWM switching frequency (a) and a 10 kHz PWM switching frequency (b).	115
Figure 5.11: Testbench VSG behaviour under an unbalanced load of 4 kW (i.e. rated power of the VSG).	116
Figure 5.12: Schematic representation for DC variation.	116
Figure 5.13: Impact of the DC variation on the testbench output VSG voltages.	117
Figure 5.14: Schematic representation for testbench microgrid integration tests.....	117
Figure 5.15: Schematic representation for testbench standalone non-linear load.	118
Figure 5.16: RMS behaviour of the VSG supplying a 2 kVA motor in the testbench.	118
Figure 5.17: Microgrid three-phase voltages behaviour after a 12 kW (a) load impact and (b) load shedding. .	119
Figure 5.18: VSG behaviour absorbing the exceeding power in the testbench.	120
Figure 6.1: Scheme of the polymorphic control.	129
Figure 6.2: Test configuration for the polymorphic validation concept.	130
Figure 6.3: Voltages period for both normal and polymorphic VSG during the short-circuit.	131
Figure 6.4: Parameters evolution during a period for both normal and polymorphic VSG during short-circuit.	131
Figure 6.5: Evolution of the currents during short-circuit for both normal and polymorphic VSG.	132
Figure 6.6: Evolution of the optimal parameters during a short-circuit.	133
Figure 6.7: Scheme of the polymorphic control with a parabolic approximation.	139
Figure 6.8: Signal's percentage depending of the inputs number for the PCA.	142
Figure 6.9: Scheme of the polymorphic control based on raw data regression model.	144
Figure 6.10: Scheme of the polymorphic control based on ST and PCA regression model.	144
Figure 6.11: Scheme of the polymorphic control based on the determination of the best combination.	146

Tables

Table 2.1: SM parameters used for SM models comparison.....	20
Table 2.2: Load variations scenario.	24
Table 2.3: THD_V and individual harmonics results at off-load condition.	30
Table 2.4: THD_V and individual harmonics results with nonlinear load.	31
Table 2.5: CPU load depending of the SM model selected.....	35
Table 3.1: Inverter parameters.	41
Table 4.1: Fixed-point value with their range and resolution	80
Table 4.2: CPU load for the proposed controller	84
Table 4.3: THD_V and individual harmonics results with non-linear load.....	90
Table 5.1: Expression of the parameters of the SM model, adapted to the inverter's characteristics.	105
Table 5.2 Testbench characteristics.	111
Table 5.3: Testbench set-up.	112
Table 5.4: Adaptation of the controller's frequency depending of the PWM switching frequency.	112
Table 5.5: SM model parameters adapted to the testbench.	113
Table 5.6: Testbench THD_V and individual harmonics results supplying a non-linear load.....	115
Table 6.1: SM model characteristics and polymorphic VSG characteristics.	130
Table 6.2: Inverter characteristics limits.	130
Table 6.3: Limits reaches number and evolution for both normal and polymorphic VSG.	135
Table 6.4: Time simulation for both normal and polymorphic VSG.	135
Table 6.5: Parameters variations during the different scenarios.	136
Table 6.6: Time simulation for parabola polymorphic VSG and polymorphic VSG for scenario 1.	140
Table 6.7: Limits reaches number and evolution for parabola polymorphic VSG and polymorphic VSG during scenario 1.	140
Table 6.8: Parameters values determination	146
Table 6.9: Time simulation depending of the selected solution.	147
Table 6.10: Limits reaches number depending of the selected solution.....	148
Table 6.11: Evolution of limits reaches number depending of the selected solution.	148

Acronym

	Acronym
AVR	Auto-voltage regulator
CPU	Central processing unit
DER	Distributed energy resources
DSP	Digital signal processor
HIL	Hardware-in-the-loop
ITM	Ideal transformer method
LQR	Linear quadratic regulator
PCA	Principal component analysis
PI	Proportional integrator
PHIL	Power-in-the-loop
PLL	Phase locked loop
p.u.	Per unit
PWM	Pulse width modulation
R & D	Research & development
RES	Renewable energy sources
RMS	Root mean square
ST	Standardisation
SC	Short-circuit
SM	Synchronous machine
THD	Total harmonics distortion
VOC	Virtual oscillator
VSG	Virtual synchronous machine

Chapter 1. General Introduction

1.1 Context

The concept of microgrid considering the integration of distributed energy resources (DER) and loads in an electrical network is not recent [1]. A microgrid is defined as a cluster of distributed power sources interconnected with various loads within clearly identified electrical boundaries [2]. Microgrids can be found in the literature in various sizes and configurations, from a few kVA constituted of a small systems with only one customer to a few GVA, real complex electricals networks with multiple various power sources and customers [3], [4]. A microgrid has also the capacity to operate in either grid-connected mode (connected to the main grid), or in islanded mode (disconnected from the main grid, also called off-grid) [5].

For the past two decades, the microgrids have received substantial attention as possible relevant solution for integration renewable energy sources, for allowing the energy access to remote locations and also ensuring an increase of the system resiliency and reliability. Indeed, in the recent years, the classical DER supplying energy to microgrids (usually diesel generator-sets) are supplanted by supplier based on renewable energy sources (RES). However, the intermittency of RES leads to major stability issues, especially in the context of microgrids, notably because these sources usually decrease the available inertia of the grid [6]. Hence, the traditional control strategies for inverters, interfacing the various DERs connected to the microgrid, needs adapting.

Many advanced controls for RES inverters can be found in the literature and most of the proposed solutions to avoid the microgrid instability are developed to interface the inverters as a voltage source.

An rather theoretical example would be the virtual oscillator, named VOC, which is based on the Van der Pol oscillators, first developed in [7], and permitted to ensure the stability of microgrids with RES inverter associated with various storage [8]–[10]. Other solutions that can be found in the literature rely on (advanced) droop controller giving the inverter the capacity to assure the voltage regulation of the microgrid [11], [12]. However, these advanced controllers for inverters are not yet implemented in industrial solutions. The microgrid stability analysis is not accurate with these new inverters, mainly because the dedicated softwares are incapable to model the impact on the microgrid of these new devices.

The virtual synchronous generator (VSG) is one of the most popular solution that can participate in increasing the microgrids inertia and also easily be integrated into traditional stability studies because it presents similarities with a synchronous machine. The research on VSG inverters started in 2007 with H.-P. Beck and R. Hesse works [13], [14] to try mimicking a synchronous machine with an inverter. Since that publication, the VSG has been mainly developed in researches centre [15], [16]. Other researches emerged with various topologies and terminologies from laboratories in association with companies ([17]–[20]). Different projects, summarized in [21], have shown the many advantages of a VSG inverter for various configurations of microgrids, [22], [23].

The different models that can be found in the literature, even with different configurations ([16], [24], [25]), are based on the following elements:

- A synchronous machine model to determine the current reference of the inverter.
- The representation of the synchronous machine swing equations or mechanical representation.
- An auto-voltage regulator (AVR) in order to regulate the voltage and in some cases, the addition of a droop control
- A frequency control, named Governor, to determine and stabilize the frequency of the system, VSG and microgrid.
- A synchronisation system for grid connection to other grid-forming power sources.
- Sensors to collect the grid's measures (currents, voltage, frequency, ...).

As the VSG is still a recent concept, mostly considered for the DER integration in microgrid, various problematics remain unresolved (some of which will be addressed in this manuscript). In addition, the different solutions that can be found in the literature do not consider the industrial and practical aspect of development (that is also considered in this thesis).

The work presented here is based on the VSG solution developed by Schneider Electric Power Conversion team that is detailed in [23]. The reference VSG model used for this thesis, visible in Figure 1.1, is constituted of:

- A synchronous machine model to define the currents reference.
 - Different current saturations in order to ensure that the inverter follows currents that are included in its power range.
 - A current controller to determine the inverter duty ratios with pulse width modulation (PWM) and that the inverter follows the currents references.
-

In the third chapter, “**Experimental validation of the current controller of the VSG**”, the experimental integration of our proposed controller in an industrial inverter is presented. The first part of the chapter details the adaptations needed for the implementation in the industrial inverter, a Connex CL 25 kVA Schneider Electric. Then, the second part presents the experimental results of the VSG with our proposed controller, with in mind its integration in a real microgrid.

In the next chapter, “**Replicability and portability of the VSG control**”, the notion of portability of the VSG control is developed. Thanks to the proposed current controller, developed in the dq-frame in per units, and in association with a methodology that adapts the synchronous machine parameters to the inverter characteristics, the replicability and portability of the VSG-based controller is discussed. The developed solutions are experimentally validated on another inverter integrated in a laboratory-scale prototype.

Finally, the last chapter, “**Polymorphic VSG, an advanced control for smart inverter**”, proposes a self-tuning VSG, named “polymorphic VSG”. It is analytically detailed and validated in simulation in a first part. The proposed solution is an advanced control for VSG based on the self-tuning of the synchronous machine parameters that permits avoiding the inverter’s deterioration during harsh events. Then, in a second part, the implementation of the polymorphic VSG in an industrial inverter (with limited computational power) is discussed, different solutions are investigated in order to make possible a future implementation of the polymorphic control such constrained environment, for its economic viability.

The manuscript ends with a general conclusion that exposes the most pertinent results and some future research work.

1.3 Principal Contributions

The principal contributions developed in this thesis are presented below:

- C1. Highlighting of the necessity to develop standards that are adapted to the grid-forming inverter-based generation solution, especially the VSG, as neither the synchronous machine, the generator set, nor the inverter standards are adapted to the developed solution.
 - C2. A standardisation tests set proposition for the industrialization for a VSG-based inverter and other grid-forming inverters to ensure the standalone proper operation of the device and its capacity to operate in parallel of other grid-forming power supplies connected to the network.
 - C3. A solution to improve the closed loop VSG system stability thanks to the integration of a state observer in presence of unknown and unpredictable loads variation without the addition of virtual impedances to stabilise the system.
-

- C4. A new controller, based on the association of a LQR (Linear Quadratic Regulator) with an integrator and a state observer, better adapted to its integration in an industrial inverter's card.
- C5. A possibility to increase the portability and replicability of the VSG-based control to different power inverters thanks to a methodology that adapts the SM model parameters of the VSG control to the inverter's characteristics and the proposed controller that can be easily adapted to various power reference
- C6. An advanced VSG controller, named polymorphic control, that permits the VSG to modify and adapt the synchronous machine's parameters automatically in order to avoid its deterioration during harsh events as short-circuit or important load impact happening in the microgrid.
- C7. A methodology and solutions to simplify the integration of the polymorphic VSG in an industrial inverter.

1.4 List of publications during the thesis

1.4.1 Patent

- ➔ A. Moulichon, M. Alamir, L. Garbuio, M. A. Rahmani, D. Gualino, V. Debusschere, N. Hadjsaid and M. X. Wang. "Adjustment of parameter values of a control rule of a generator". RUE-2346, No IDEAS:2018- 0000691, 1st filling number: 1910910. 02-10-October 2019. (scope: U.E, China and U.S.A)
- ➔ A. Moulichon, M. Alamir, M. A. Rahmani, L. Garbuio, M. X. Wang, V. Debusschere and N. Hadjsaid. "Control method of a generator". GRE-3364, No IDEAS:2018-0000092, 1st filling number: 1858434. 18-09-September 2018. (scope: U.E, China and U.S.A)

1.4.2 Publication

1.4.2.1 International journal papers

- ➔ A. Moulichon, M. Alamir, M. A. Rahmani, V. Debusschere, L. Garbuio, M. X. Wang and N. Hadjsaid, "New Observer-Based Current Controller for Virtual Synchronous Generator in presence of unknown and unpredictable loads", IEEE Transactions on Smart Grid, 2020 (in submission).
 - ➔ A. Moulichon, V. Debusschere, L. Garbuio, M. A. Rahmani, M. Alamir and N. Hadjsaid, "Standardization Tests for the Industrialization of grid-friendly Virtual Synchronous Generators", Bulletin of the Polish Academy of Sciences: Technical Sciences, 2020 (in submission - 05-Dec-2019).
-

1.4.2.2 International conference papers

- ➔ A. Moulichon, V. Debusschere, L. Garbuio, M. A. Rahmani, and N. Hadjsaïd, “*A Simplified Synchronous Machine Model for Virtual Synchronous Generator Implementation*”, IEEE Power Energy Society General Meeting, 2019, Atlanta.
-

Chapter 2. Synchronous Machine models for standardized and grid-friendly Virtual Synchronous Generators

2.1 Introduction

Multiple synchronous machine (SM) models exist for an implementation in the controller of VSGs. Initial works on VSG [26] used SM models constituted of all the equations representing the electrical dynamics, in dq or abc- axis, including the flux linkages and damper windings effects. It can be found for example in the VISMA project ([18], [27]), as an integrated solution with photovoltaic panels [28], and finally applied to the STATCOM technology in [29]. However, this model has two main limitations. The first one is that as this model tends to represent exactly a SM, which means that the VSG will have the same intrinsic problems as a real SM even if the inverter does not have the same electrical and dynamical capabilities in terms of maximal output current and inertia. The second main limitation is that the implementation could encounter numerical instability in the controller due to the high order of the SM model [28]. This model requires thus simplifications and adaptations to deal with the computational limitation of the controller to ensure its numerical stability, within operational constraints regarding its grid integration. This is the scope of the current chapter.

Hence, a possibility to avoid those issues while implementing a model of VSG in a digital controller would be a simplification based on the emulation of a virtual impedance, which is like a real SM impedance while conserving a dynamic electrical model. A study on the emulation of a virtual impedance as a SM model can be found in [30]. In this study, two controls, based on the voltage to

current or the current to voltage models, are compared to determine which solution have the better performances to represent a simplified SM. In the same spirit, the synchronverter was developed also based on an emulated impedance [16]. The model based on the emulation of a virtual impedance is also considered to control wind turbines in order to improve their integration to the grid [31]. Finally, in [24], a SM model is applied and detailed in the context of Smart Grids. This model simplifies the high-order SM in removing the dampers windings, without saturation and without considering the creation of linkages fluxes or linkages currents in the rotor and stator.

In this context, it is possible to consider more basic SM models [25]. For example, the so-called “algebraic” model, used in various projects with or without improvements [32], [33], an autonomous power management to improve the VSG performances, is based on the SM’s steady state representation instead of Park’s equations. The possibility to only consider the quasi-static model instead of the entire dynamic model is also considered to increase the performances by avoiding the creation of oscillations [34]. As this model only considers the static elements of a SM, it is based only on the steady-state phasor voltage diagram.

Studies have been conducted to characterise the dynamic model of the association of a VSG and a droop controlled in an inverter in order to compare both operations, [35], [36]. Then, various solutions of droop control were also implemented in VSGs [36], [37] which opened the subject of self-synchronisation, as VSGs are not typically the only power sources in microgrids [38]. To ensure the stability of microgrids, the VSG solution must then be able to be parallelized with other power sources (similar ones or not). In addition, as the SM model used for the VSG is virtual, it is possible to study its self-tuning [39], [40]. The above solutions never considered the characteristics of the industrial inverter and computational limitations of the microcontroller used to control the inverter. Indeed, in order to transfer VSGs from research and development to industrialization, the scalability must be at the centre of the preoccupations, as increasing the capabilities of microcontroller will significantly impact the economic viability of future VSG solutions.

The VSG is implemented, with its local control, in a microcontroller of an industrial inverter. For the comparison of the impact of the SM models on the VSG performance, the SM and generators standards are considered as there are no specifications or standards yet for the VSG. The SM is an established solution, requirements and specifications are well developed in term of design and performances [41]–[44]. In addition, in the microgrids context, the VSG is not the only power supply solution. This is the reason why a parallelism study on the VSG with similar or different power sources must be considered to finalize the study. To conclude, the choice of the SM model is based on its capacity to be operational on industrial microcontrollers with its local control and its compliance with SM standards, within the limitations of the inverter.

Hence, in this chapter, three SM models, representing various precisions levels (a complete, a reduced and a simplified one), are detailed and implemented in a digital signal processor. The three models are submitted to tests based on the generators sets standards and which represent a contribution to a reference for VSG solutions (aiming at standardization). The capacity of the three resulting VSGs to operate in parallel with other power sources in a microgrid is then studied. Finally, each model is implemented in the control board of an industrial inverter to assess their relevance in a constrained environment with limited computational power. The goal is ultimately to compare models in a joint perspective of developing grid-friendly VSG-based inverters and a set a test to prove that compatible with future possible standards.

2.2 The dq-transformation

Before starting the study of the impact of the selected SM models on the VSG operational characteristics, the definition of the dq-transformation of the complete SM model (and its controller as detailed in this thesis) is reminded. In addition to the detailed dq-axis expression, the derivation of the variables from the abc- axis to the dq-axis is also reminded as it is a major function of the studied models, SM and controllers, that will be implemented in the inverter supporting the VSG.

2.2.1 Definition of the dq-transformation

The model is based on the P. Kundur, Power System Stability and Control, Chapter Synchronous Machine [45].

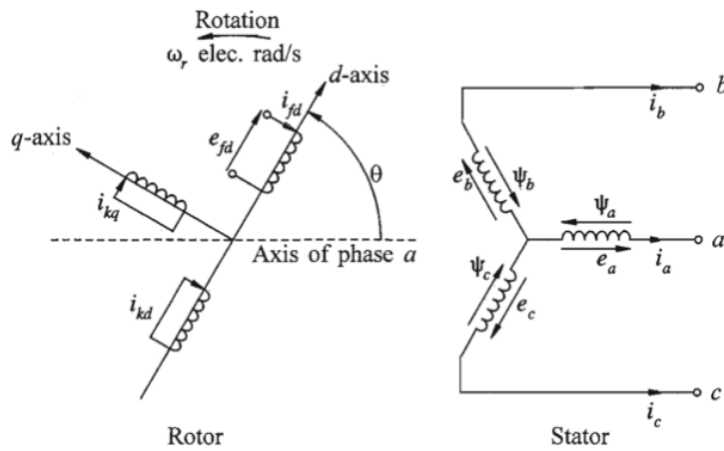


Figure 2.1: Stator and rotor circuits of a synchronous machine [45]

Where the indices are:

- a, b, c : stator phase windings
- fd : field winding
- kd : d-axis of the damping circuit
- kq : q-axis of the damping circuit
- $k = 1, 2, \dots, n$ with n the number of damping circuits
- θ : angle between the d-axis and the phase a (electrical rad)
- ω_r : rotor angular velocity (electrical rad/s)

To simplify the problem, the dq0 variables are used instead of the abc phase variables. The abc to dq transformation is defined by:

$$X_{dq0} = T \cdot X_{abc} \text{ where } T = \frac{2}{3} \cdot \begin{bmatrix} \cos(\theta) & \cos\left(\theta - \frac{2\pi}{3}\right) & \cos\left(\theta + \frac{2\pi}{3}\right) \\ -\sin(\theta) & -\sin\left(\theta - \frac{2\pi}{3}\right) & -\sin\left(\theta + \frac{2\pi}{3}\right) \\ \frac{1}{2} & \frac{1}{2} & \frac{1}{2} \end{bmatrix} \quad \text{eq 2.1}$$

Where the vector $X_{abc}, X_{abc} \in \mathbb{M}_{3,1}$ represents three-phase variable in the abc-axis and the vector $X_{dq0}, X_{dq0} \in \mathbb{M}_{3,1}$ represents the same variable in the dq0-axis. The matrix T is the transfer matrix from abc to dq0-axis.

$$X_{abc} = T^{-1} \cdot X_{dq0} \text{ where } T^{-1} = \begin{bmatrix} \cos(\theta) & -\sin(\theta) & 1 \\ \cos\left(\theta - \frac{2\pi}{3}\right) & -\sin\left(\theta - \frac{2\pi}{3}\right) & 1 \\ \cos\left(\theta + \frac{2\pi}{3}\right) & -\sin\left(\theta + \frac{2\pi}{3}\right) & 1 \end{bmatrix} \quad \text{eq 2.2}$$

Now that the dq0-axis is presented, it possible to described how a variable (a current, a voltage or a flux) can be derivate from the abc-axis to the dq0-axis.

2.2.2 Derivation in dq Transformation

The values of the 0 axis are neglected as the system is considered balanced. A perspective research could be the integration of the homopolar axis of the reference dq0 in the models, which may improve the VSG performances when supplying unbalanced loads. So, the new matrix to convert an element from the abc-axis to the dq-axis is now:

$$X_{abc} = T^{-1} \cdot X_{dq} \text{ where } T^{-1} = \begin{bmatrix} \cos(\theta) & -\sin(\theta) \\ \cos\left(\theta - \frac{2\pi}{3}\right) & -\sin\left(\theta - \frac{2\pi}{3}\right) \\ \cos\left(\theta + \frac{2\pi}{3}\right) & -\sin\left(\theta + \frac{2\pi}{3}\right) \end{bmatrix} \quad \text{eq 2.3}$$

with the derivation, eq 2.3 become:

$$\frac{d}{dt}(X_{abc}) = \frac{d}{dt}(T^{-1} \cdot X_{dq}) \quad \text{eq 2.4}$$

$$\text{hence,} \quad \frac{d}{dt}(X_{abc}) = T^{-1} \cdot \frac{d}{dt}(X_{dq}) + \frac{d}{dt}(T^{-1}) \cdot X_{dq} \quad \text{eq 2.5}$$

concerning the derivation of T^{-1} :

$$\frac{d}{dt}(T^{-1}) = \frac{d\theta}{dt} \cdot \frac{d(T^{-1})}{d\theta} = \omega_r \cdot T^{-1} \begin{bmatrix} 0 & -1 \\ 1 & 0 \end{bmatrix} \quad \text{eq 2.6}$$

hence, combining eq 2.5 and eq 2.6:

$$\frac{d}{dt}(X_{abc}) = T^{-1} \cdot \frac{d}{dt}(X_{dq}) + \omega_r \cdot T^{-1} \cdot \begin{bmatrix} 0 & -1 \\ 1 & 0 \end{bmatrix} \cdot X_{dq} \quad \text{eq 2.7}$$

multiplying eq 2.7 by the matrix T :

$$T \cdot \frac{d}{dt}(X_{abc}) = T \cdot T^{-1} \cdot \frac{d}{dt}(X_{dq}) + T \cdot T^{-1} \cdot \begin{bmatrix} 0 & -\omega_r \\ \omega_r & 0 \end{bmatrix} \cdot X_{dq} \quad \text{eq 2.8}$$

as $T \cdot T^{-1} = \mathbb{I}_2$, eq 2.7 becomes:

$$T \cdot \frac{d}{dt}(X_{abc}) = \frac{d}{dt}(X_{dq}) + \begin{bmatrix} 0 & -\omega_r \\ \omega_r & 0 \end{bmatrix} \cdot X_{dq} \quad \text{eq 2.9}$$

And finally, the derivation in the dq-axis is:

$$\frac{d}{dt}(X_{dq}) = T \cdot \frac{d}{dt}(X_{abc}) + \begin{bmatrix} 0 & \omega_r \\ -\omega_r & 0 \end{bmatrix} \cdot X_{dq} \quad \text{eq 2.10}$$

2.3 Synchronous machine models definition

In order to study the impact of the choice of the SM model on the VSG performances and behaviour, three different SM models are studied. The three models considered for our study have been selected for the next reasons:

- The models are present in the literature and have been tested in many research projects.
- Their precision compared with a real SM depends on
 - Time dependency, time response phenomena
 - Number of variables and parameters that define the model

The first selected SM model is the most detailed one for two reasons. First, it is the most precise model, which means that the VSG will have a behaviour very similar to a real generator set (apart from the short-circuit current). Second, this SM model is the initial version implemented in the VSG developed in Schneider Electric and used as a reference for this thesis. This model is named the “complete” model.

The second model is the simplest one: a static model without time dependency, only represented by an impedance, to conclude on the necessity to consider transitory event for an acceptable VSG behaviour. This model is named the “static” model.

Thirdly, a SM model for the VSG is proposed. This model has time dependency but also simplified equations of the SM. This model is named the “reduced” model. The three models are detailed below, starting with the most complete one, then the reduced version and finally the static model. That hybrid version will prove to be a relevant compromise as the rest of the chapter will tell.

For the three SM models characterisations, considered the notation below:

- e^d and e^q the instantaneous stator phase to neutral voltages on dq-axis.
- e_{fd} field voltage.
- i^d and i^q the instantaneous stator currents on dq-axis
- i_{fd}, i_{1d} and i_{1q} the instantaneous field and dampers currents.
- ψ_d and ψ_q are the instantaneous stator fluxes.
- ψ_{fd}, ψ_{1d} and ψ_{1q} are the instantaneous field and dampers fluxes.
- R_s the armature resistor for each phase.
- R_{fd}, R_{1d} and R_{1q} the rotor circuit resistances.
- L_{ad} and L_{aq} the mutual inductances between stator windings.
- L_{afd}, L_{a1d} and L_{a1q} mutual inductances between stator and rotor windings.
- L_{ffd}, L_{11d} and L_{11q} the self-inductances of rotor.

2.3.1 Complete synchronous machine model

2.3.1.1 Hypothesis

The SM considered here is a salient-pole machine ($p = 2$), the “kq” notation is replaced by the “dq” notation for easier reading as there only one damping. The hypotheses for modelling this SM are:

- The stator windings are sinusoidally distributed along the air-gap as far as the mutual effects with the rotor are concerned;
- The stator slots cause no appreciable variation of the rotor inductances as a function of the rotor position;
- Magnetic hysteresis is negligible;
- Magnetic saturation is negligible.

2.3.1.2 Complete model definitions

The per unit stator voltage, equations for the complete model are:

$$\begin{aligned} e^d &= \frac{1}{\omega_{base}} \cdot \frac{d(\psi_d)}{dt} - \psi_q \cdot \omega_r - R_s \cdot i^d \\ e^q &= \frac{1}{\omega_{base}} \cdot \frac{d(\psi_q)}{dt} + \psi_d \cdot \omega_r - R_s \cdot i^q \end{aligned} \quad eq\ 2.11$$

where ψ_d and ψ_q are the stator fluxes, i^d and i^q the stator currents, e^d and e^q the stator voltages, R_s the armature stator resistor, ω_r the rotor electrical angular velocity and ω_{base} its base value.

The per unit rotor voltage equations for the complete model are:

$$\begin{aligned} e_{fd} &= \frac{1}{\omega_{base}} \cdot \frac{d(\psi_{fd})}{dt} + R_{fd} \cdot i_{fd} \\ 0 &= \frac{1}{\omega_{base}} \cdot \frac{d(\psi_{1d})}{dt} + R_{1d} \cdot i_{1d} \\ 0 &= \frac{1}{\omega_{base}} \cdot \frac{d(\psi_{1q})}{dt} + R_{1q} \cdot i_{1q} \end{aligned} \quad eq\ 2.12$$

where ψ_{fd} , ψ_{1d} and ψ_{1q} are the field and dampers fluxes, i_{fd} , i_{1d} and i_{1q} the field and dampers currents, e_{fd} the field voltage, R_{fd} , R_{1d} and R_{1q} the field and dampers resistors.

The per unit stator flux equations, extract from [45] (page 87), are defined as:

$$\begin{aligned} \psi_d &= -(L_{ad} + L_l) \cdot i^d + L_{ad} \cdot i_{fd} + L_{ad} \cdot i_{1d} \\ \psi_q &= -(L_{aq} + L_l) \cdot i^q + L_{aq} \cdot i_{1q} \end{aligned} \quad eq\ 2.13$$

where L_{ad} and L_{aq} are the mutual stator standard inductances and L_l the linkage inductance.

Similarly, the per unit rotor flux linkage equations are:

$$\begin{aligned}\psi_{fd} &= L_{ffd} \cdot i_{fd} + L_{f1d} \cdot i_{1d} - L_{ad} \cdot i^d \\ \psi_{1d} &= L_{f1d} \cdot i_{fd} + L_{11d} \cdot i_{1d} - L_{ad} \cdot i^d \\ \psi_{1q} &= L_{11q} \cdot i_{1q} - L_{aq} \cdot i^q\end{aligned}\tag{eq 2.14}$$

where L_{ffd} , L_{f1d} and L_{11q} are the field and dampers self-inductances.

2.3.1.3 Standard and physical parameters

The mutual inductances L_{f1d} and L_{ad} are assumed to be equal [45], consequently, all mutual inductances located on the d-axis are equal. The rotor circuit per unit leakage inductances, L_{fd} , L_{1d} and L_{1q} are defined by:

$$\begin{aligned}L_{fd} &= L_{ffd} - L_{f1d} \\ L_{1d} &= L_{11d} - L_{f1d} \\ L_{1q} &= L_{11q} - L_{aq}\end{aligned}$$

The parameters used in these equations are the fundamental parameters which characterise the electrical machine. However, they cannot be directly determined from measurements so standard values are used instead. The different physical parameters can be found in any datasheet. The link between the physical parameters and the standard values in the d-axis are defined by:

$$\begin{aligned}L_d &= L_{ad} + L_l ; \\ L'_d &= \frac{L_{ad} \cdot L_{fd}}{L_{ad} + L_{fd}} + L_l ; \\ L''_d &= \frac{L_{1d} \cdot L_{ad} \cdot L_{fd}}{L_{ad} \cdot L_{fd} + L_{ad} \cdot L_{1d} + L_{1d} \cdot L_{fd}} + L_l ; \\ T'_{d0} &= \frac{L_{ad} + L_{fd}}{R_{fd}} ; \\ T''_{d0} &= \frac{1}{R_{1d}} \cdot \left(L_{1d} + \frac{L_{fd} \cdot L_{ad}}{L_{ad} + L_{fd}} \right) ; \\ T'_d &= \frac{1}{R_{fd}} \cdot \left(L_{fd} + \frac{L_{ad} \cdot L_l}{L_{ad} + L_l} \right) \text{ and} \\ T''_d &= \frac{1}{R_{1d}} \cdot \left(L_{1d} + \frac{L_l \cdot L_{ad} \cdot L_{fd}}{L_{fd} \cdot L_{ad} + L_{fd} \cdot L_l + L_{ad} \cdot L_l} \right)\end{aligned}$$

where L''_d , L'_d and L_d are respectively the subtransient, transient and steady state reactances on d-axis. T''_{d0} and T'_{d0} are respectively the subtransient and transient time response in open circuit on d-axis. T''_d and T'_d are respectively the subtransient and transient time response in short-circuit on d-axis.

Concerning the q-axis, air is the predominant environment. The air environment does not influence the fluxes for both the transient and the permanent states. Hence, it is supposed that: $L_q = L'_q$. Thus:

$$L_q = L'_q = L_l + L_{aq} ;$$

$$L_q'' = L_l + \frac{L_{aq} \cdot L_{1q}}{L_{aq} + L_{1q}} ;$$

$$T_{q0}'' = \frac{L_{ad} + L_{1q}}{R_{1q}}.$$

where L_q'' , L_q' and L_q are respectively the subtransient, transient and steady state reactances on q-axis. T_{q0}'' is the subtransient time response in open circuit on d-axis.

So, the conversion from physical parameters to standard parameters is defined by:

$$L_{ad} = L_d - L_l ;$$

$$L_{fd} = \frac{L_l \cdot L_{ad} - L_d' \cdot L_{ad}}{L_d' - L_l - L_{ad}} ;$$

$$R_{fd} = \frac{L_{ad} + L_{fd}}{T_{do}'} ;$$

$$L_{1d} = \frac{(L_d'' - L_l) \cdot L_{ad} \cdot L_{fd}}{(L_l - L_d'') \cdot L_{fd} + (L_{fd} + L_l - L_d'') \cdot L_{ad}} ;$$

$$R_{1d} = \frac{1}{T_{d0}''} \left(L_{1d} + \frac{L_{fd} \cdot L_{ad}}{L_{ad} + L_{fd}} \right) ;$$

$$L_{aq} = L_q - L_l ;$$

$$L_{1q} = \frac{L_{aq} \cdot (L_l - L_q'')}{L_q'' - L_l - L_{aq}} \text{ and}$$

$$R_{1q} = \frac{L_{aq} - L_{1q}}{T_{q0}''}.$$

2.3.1.4 Complete SM Equations

To simplify the equations, a new variable is defined:

$$\mathfrak{L} = L_{ad} \cdot L_{fd} + L_{ad} \cdot L_{1d} + L_{fd} \cdot L_{1d}$$

The rotor flux linkage equations, eq 2.14, and the standard parameters defined in 2.3.1.3, the per unit rotor current equations are defined by:

$$i_{fd} = \frac{L_{1d} \cdot L_{ad} \cdot i^d + (L_{1d} + L_{ad}) \cdot \psi_{fd} + L_{ad} \cdot \psi_{1d}}{\mathfrak{L}}$$

$$i_{1d} = \frac{L_{fd} \cdot L_{ad} \cdot i^d - L_{ad} \cdot \psi_{fd} + (L_{fd} + L_{ad}) \cdot \psi_{1d}}{\mathfrak{L}} \quad \text{eq 2.15}$$

$$i_{1q} = \frac{\psi_q + L_{aq} \cdot i^q}{L_{1q} + L_{aq}}$$

Concerning the stator flux equations, the stator current i_d and i_q can be defined as:

$$\begin{aligned} i^d &= -\frac{1}{L_d''} \cdot \psi_d + \frac{L_{ad}}{\Omega \cdot L_d''} L_{1d} \cdot \psi_{fd} + \frac{L_{ad}}{\Omega \cdot L_d''} L_{fd} \cdot \psi_{1d} \\ i^q &= -\frac{1}{L_q''} \cdot \psi_q + \frac{\frac{L_{aq}}{L_{aq} + L_{1q}}}{L_q''} \cdot \psi_{1q} \end{aligned} \quad \text{eq 2.16}$$

The currents determined in eq 2.16 and eq 2.17 are substituted in the equations eq 2.11 and eq 2.12. So, the complete model is defined by the fluxes equations below based on [45]:

$$\begin{aligned} \dot{\psi}_d &= \omega_{base} \cdot [e_d + \omega_r \cdot \psi_q - a_1 \cdot \psi_d + a_2 \cdot \psi_{fd} + a_3 \cdot \psi_{1d}] \\ \dot{\psi}_q &= \omega_{base} \cdot [e_q - \omega_r \cdot \psi_d - a_4 \cdot \psi_q + a_5 \cdot \psi_{1q}] \\ \dot{\psi}_{fd} &= \omega_{base} \cdot [e_{fd} + a_6 \cdot \psi_d - a_7 \cdot \psi_{fd} + a_8 \cdot \psi_{1d}] \\ \dot{\psi}_{1d} &= \omega_{base} \cdot [a_9 \cdot \psi_d + a_{10} \cdot \psi_{fd} - a_{11} \cdot \psi_{1d}] \\ \dot{\psi}_{1q} &= \omega_{base} \cdot [a_{12} \cdot \psi_q - a_{13} \cdot \psi_{1d}] \end{aligned} \quad \text{eq 2.17}$$

with the different coefficients, sorting by lines:

$$\begin{aligned} a_1 &= \frac{R_s}{L_d''} ; a_2 = \frac{R_s \cdot L_{ad} \cdot L_{1d}}{\Omega \cdot L_d''} ; a_3 = \frac{R_s \cdot L_{ad} \cdot L_{fd}}{\Omega \cdot L_d''} \\ a_4 &= \frac{R_s}{L_q''} ; a_5 = \frac{R_s \cdot L_{aq}}{L_q'' (L_{aq} + L_{1q})} \\ a_6 &= \frac{L_{1d} \cdot L_{ad} \cdot (L_{ad} + L_{fd})}{T_{do}' \cdot \Omega \cdot L_d''} ; a_7 = \frac{\Omega \cdot L_d'' + L_{ad}^2 \cdot (L_l + L_{1d})}{T_{do}' \cdot \Omega \cdot L_d''} ; a_8 = \frac{L_{ad} \cdot L_l \cdot (L_l + L_{1d})}{T_{do}' \cdot \Omega \cdot L_d''} \\ a_9 &= \frac{L_d' - L_l}{T_{do}'' \cdot L_d''} ; a_{10} = \frac{L_l \cdot L_{ad}}{T_{do}'' \cdot L_d'' (L_{ad} + L_{fd})} ; a_{11} = \frac{L_d'}{T_{do}'' \cdot L_d''} \\ a_{12} &= \frac{L_{aq}}{T_{qo}'' \cdot L_d''} ; a_{13} = \frac{1 + \frac{L_{aq}^2}{L_q'' \cdot (L_{aq} + L_{1q})}}{T_{qo}''} \end{aligned}$$

And concerning the SM current

$$\begin{aligned} i^d &= -c_1 \cdot \psi_d + c_2 \cdot \psi_{fd} + c_3 \cdot \psi_{1d} \\ i^q &= -c_4 \cdot \psi_d + c_3 \cdot \psi_{1q} \end{aligned} \quad \text{eq 2.18}$$

With the coefficients

$$\begin{aligned} c_1 &= \frac{1}{L_d''} ; c_2 = \frac{L_{ad} \cdot L_{1d}}{\Omega \cdot L_d''} ; c_3 = \frac{L_{ad} \cdot L_{fd}}{\Omega \cdot L_d''} \\ c_4 &= \frac{1}{L_q''} ; c_5 = \frac{L_{aq}}{L_q'' \cdot (L_{aq} + L_{1q})} \end{aligned}$$

The so-called “complete” model is constituted of five equations for the fluxes, eq 2.17, and two equations for the output currents, eq 2.18, requiring to characterize 16 parameters [45], [23].

The next model presented is the proposed reduced model which requires less parameters, as detailed below.

2.3.2 Reduced model

2.3.2.1 Hypothesis for the reduced model

The SM in this study is a non-salient pole machine ($p = 2$). The hypotheses for this SM model are:

- The stator windings are sinusoidally distributed along the air-gap as far as the mutual effects with the rotor are concerned;
- The stator slots cause no appreciable variation of the rotor inductances as a function of the rotor position;
- Magnetic hysteresis is negligible;
- Magnetic saturation is negligible.

In addition, to these hypotheses, the SM model is also reduced through the next hypotheses:

- The dampers are neglected so there are no “1d” and “1q” data or variable.
- The synchronous machine’s imperfections X_l is equal to 0.
- The synchronous machine’s homopolar flux is not considered (it was also not simulated in the complete mode though).

2.3.2.1 Standard and physical parameters concerning the reduced model

The mutual inductance L_{f1d} are neglected as there is no damper. Hence, the rotor circuit per unit leakage inductance L_{fd} is introduced by:

$$L_{fd} = L_{ffd} - L_{ad}$$

As the dampers are neglected, there is no sub-transient parameters, only the permanent and transient parameters are present in the equations. Hence, the physical parameters are defined as:

$$\begin{aligned} L_d &= L_q = L_{ad} \\ L'_d &= L_d - \frac{L_d^2}{L_{ffd}} \\ T'_{d0} &= \frac{L_{ffd}}{R_{fd}} \text{ and} \\ T'_d &= \frac{L_{ffd}}{R_{fd}} \cdot \left(1 - \frac{L_d^2}{L_{ffd} \cdot L_d} \right) \end{aligned}$$

where L'_d and L_d are respectively transient and steady state reactances on d-axis, T'_{d0} and T'_d the transient time response respectively in open circuit and in short-circuit.

The link between the physical parameters and the standard ones is given by the equations below:

$$\begin{aligned} L_{ad} &= L_d = L_q \\ L_{fd} &= \frac{L'_d \cdot L_d}{L_d - L'_d} \\ R_{fd} &= \frac{L_d + L_{fd}}{T'_{do}} \end{aligned}$$

2.3.2.2 Reduced model definition

The per unit stator voltage equations for the reduced model, considering the described hypothesis, is defined by the following equations:

$$\begin{aligned} e^d &= \frac{1}{\omega_{base}} \cdot \frac{d(\psi_d)}{dt} - \psi_q \cdot \omega_r - R_s \cdot i^d \\ e^q &= \frac{1}{\omega_{base}} \cdot \frac{d(\psi_q)}{dt} + \psi_d \cdot \omega_r - R_s \cdot i^q \end{aligned} \quad eq \ 2.19$$

where ψ_d and ψ_q are the stator fluxes, i^d and i^q the stator currents, e^d and e^q the stator voltages, R_s the armature stator resistor, ω_r the rotor electrical angular velocity and ω_{base} its base value.

The per unit rotor voltage equation is:

$$e_{fd} = \frac{1}{\omega_{base}} \cdot \frac{d(\psi_{fd})}{dt} + R_{fd} \cdot i_{fd} \quad eq \ 2.20$$

where ψ_{fd} is the field fluxes, i_{fd} the field current, e_{fd} the field voltage, R_{fd} the rotor resistor.

The per unit stator flux equations are:

$$\begin{aligned} \psi_d &= -L_d \cdot i^d + L_d \cdot i_{fd} \\ \psi_q &= -L_q \cdot i^q + L_q \cdot i_{1q} \end{aligned} \quad eq \ 2.21$$

The per unit rotor flux linkage equation is:

$$\psi_{fd} = L_{ffd} \cdot i_{fd} - L_d \cdot i^d \quad eq \ 2.22$$

2.3.2.3 Reduced SM model

With the flux ψ_{fd} equation, eq 2.22, and the standard parameters, the per unit rotor current equation is defined by:

$$i_{fd} = \frac{-\psi_d + \psi_{fd}}{L_{fd}} \quad eq \ 2.23$$

Concerning the stator fluxes equation, eq 2.21, the current i_d and i_q can be defined as:

$$\begin{aligned} i^d &= -\frac{L_{ffd}}{L_{fd} \cdot L_d} \cdot \psi_d + \frac{1}{L_{fd}} \psi_{fd} \\ i^q &= -\frac{1}{L_q} \cdot \psi_q \end{aligned} \quad \text{eq 2.24}$$

The currents eq 2.23 and eq 2.24 are substituted in the voltage equations, eq 2.19 and eq 2.20, hence, the stator fluxes equations are defined by:

$$\begin{aligned} \frac{d\psi_d}{dt} &= \omega_{base} \left[e^d + \omega_r \cdot \psi_q - R_s \cdot \frac{L_{ffd}}{L_d \cdot L_{fd}} \cdot \psi_d + \frac{R_s}{L_{fd}} \cdot \psi_{fd} \right] \\ \frac{d\psi_q}{dt} &= \omega_{base} \left[e^q - \omega_r \cdot \psi_d - \frac{R_s}{L_q} \cdot \psi_q \right] \end{aligned}$$

Concerning the rotor flux, the equation is now:

$$\frac{d\psi_{fd}}{dt} = \omega_{base} \cdot \left[e_{fd} - \frac{R_{fd}}{L_{fd}} \cdot \psi_{fd} + \frac{R_{fd}}{L_{fd}} \cdot \psi_d \right]$$

To conclude, the reduced SM model is determined by the equations:

$$\begin{aligned} \dot{\psi}_d &= \omega_{base} \cdot \left[e^d + \omega_r \cdot \psi_q - R_s \cdot \frac{L_{fd} + L_d}{L_d \cdot L_{fd}} \cdot \psi_d + R_s \cdot \frac{1}{L_{fd}} \cdot \psi_{fd} \right] \\ \dot{\psi}_q &= \omega_{base} \cdot \left[e^q - \omega_r \cdot \psi_d - R_s \cdot \frac{1}{L_q} \cdot \psi_q \right] \\ \dot{\psi}_{fd} &= \omega_{base} \cdot \left[e_{fd} + \frac{R_{fd}}{L_{fd}} \cdot \psi_d - \frac{R_{fd}}{L_{fd}} \cdot \psi_{fd} \right] \end{aligned} \quad \text{eq 2.25}$$

And the reduced SM currents:

$$\begin{aligned} i^d &= -\frac{L_{fd} + L_d}{L_d \cdot L_{fd}} \cdot \psi_d + \frac{1}{L_{fd}} \cdot \psi_{fd} \\ i^q &= -\frac{1}{L_q} \cdot \psi_q \\ i_{fd} &= -\frac{1}{L_{fd}} \cdot \psi_d + \frac{1}{L_{fd}} \cdot \psi_{fd} \end{aligned} \quad \text{eq 2.26}$$

It can be noted that even if the L_d reactance and L_q reactance are equal, the notation differentiation is kept for the comparison between the different models. Hence, the reduced model is characterised by three fluxes equations, eq 2.25, two output currents equations, eq 2.26, and only requires four parameters to be determined.

The last SM model considered in this study is even less detailed, as presented the following section.

2.3.3 Static model

2.3.3.1 Hypothesis

The SM considered in this study is a non-salient pole machine (number of poles, $p = 4$). The hypotheses for this static SM model are:

- The stator windings are sinusoidally distributed along the air-gap as far as the mutual effects with the rotor are concerned;
- The stator slots cause no appreciable variation of the rotor inductances with rotor position;
- Magnetic hysteresis is negligible;
- Magnetic saturation is negligible.

In addition, to these hypotheses, the SM model is also reduced using the following additional hypotheses:

- Non-salient pole machine
- The dampers are neglected so there are no “1d” and “1q” data or variable.
- The SM’s imperfections X_l is equal to 0.
- The SM’s homopolar flux is not simulated (it was not simulated in both precedent models).

In complement,

- No flux-saturation
- Static model, no time constant.

2.3.3.2 Static model Equations

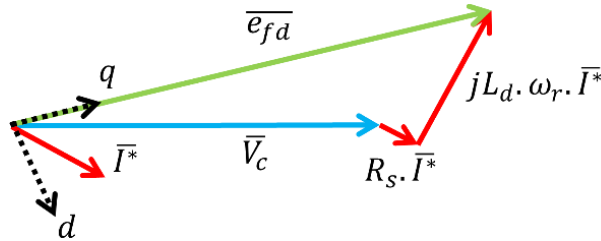


Figure 2.2: Static synchronous machine model phasor diagram

Figure 2.2 present the phasor diagram of the static SM model. Based on this diagram, the static SM currents are defined by:

$$\begin{aligned}
 i^d &= \frac{\omega_r \cdot L_d \cdot (e_{fd} - e^q) - R_s \cdot e^d}{R_s^2 + (\omega_r \cdot L_d)^2} \\
 i^q &= \frac{-\omega_r \cdot L_d \cdot e^d + R_s \cdot (e_{fd} - e^q)}{R_s^2 + (\omega_r \cdot L_d)^2}
 \end{aligned}
 \tag{eq 2.27}$$

The reactance $\omega_r \cdot L_d$ is generally superior to the resistance R_s , so, as $R_s \ll \omega_r \cdot L_d$ the equation can be simplified in eq 2.27 and become:

$$\begin{aligned} i_d &= \frac{(e_{fd} - e^q)}{\omega_r \cdot L_d} \\ i_q &= \frac{-e^d}{\omega_r \cdot L_d} \end{aligned} \quad \text{eq 2.28}$$

In the end, the static model is represented by two currents equations and is based on only one parameter: L_d .

2.4 Synchronous machine models comparison

Previous studies on the impact of the SM model have been done and can be found in the literature. [15], [21], [46]. In [15], a VSG is compared to a droop controller. The topologies that can be found in the literature are detailed in [21] but without comparing the presented solution. Some pros and cons of various SM models are presented in [46], but the models are not compared directly with the same tests.

To conclude, these studies do not propose a complete comparison between the various models and never consider industrial performances or limits to the implementation of the VSG on an actual commercial inverter. In addition, these studies do not consider that the VSG is implemented in industrial solutions as well as integrated in a microgrid. The comparison with industrial performances and standards has never been done on the VSG depending on the implemented model to the best of our knowledge. Indeed, VSGs are developed to be a plug-and-play solution for microgrids with a high share of renewables, having a positive impact on the stability of the microgrid during large load variations and renewables fluctuations.

Hence, for the proposed comparison of the impact of the SM models on the VSG performances, the SM and generators standards are considered as there are no specifications or standards yet for VSGs. The SM is an established solution, requirements and specifications are well developed in term of design and performances [41]–[44]. So, the frequency-response characteristics, an assessment of the stability of the models and a harmonics analysis are conducted to compare the three SM models for an implementation in a VSG-based inverter.

Table 2.1: SM parameters used for SM models comparison.

Parameter	Value (p.u.)	Time response	Value (ms)
X_d	1.93	T''_d	7
X''_d	0.077	T''_q	7
X'_d	0.154	T''_{qo}	50
X_q	1.16	T''_{do}	14
X''_q	0.162	T'_d	80
R_s	0.10	T'_{do}	1000
X_l	0.06		
X_0	0.06		

Concerning the frequency-response characteristics study, only the SM models are studied. For the other tests, the SM model is implemented in the VSG control, with the proposed controller that is defined in this thesis that can be found in Chapter 3. Hence, the VSG control is visible in Chapter 4 (4.2 – p 78) and define in Figure 4.2. In

Table 2.1 can be found the different values of the SM parameters that are used for the comparison study between the SM models and their impact on the VSG inverter behaviour.

Note that those considered tests as a first step of a standard for VSG as well as series of criteria to define grid-friendly inverted-based generators (with or without a VGS implemented). So, even more than the test results, the tests themselves and their definition represent the core contribution of this chapter.

2.4.1 Frequency-response characteristics

The study of the three models' frequency-response characteristics provides an insight on the dynamic characteristics of each model.

$$\begin{aligned}\Delta\psi_d(s) &= \mathcal{G}(s) \cdot \Delta e_{fd} - \mathcal{L}_d(s) \cdot \Delta i_d(s) \\ \Delta\psi_q(s) &= -\mathcal{L}_q(s) \cdot \Delta i_q(s)\end{aligned}\tag{eq 2.29}$$

Where $\mathcal{G}(s)$ is the stator to field transfer function, $\mathcal{L}_d(s)$ is the d-axis inductance and $\mathcal{L}_q(s)$ is the q-axis inductance, Δe_{fd} is a variation of the field voltage, Δi^d is a variation of the stator d-axis current and Δi^q is a variation of the stator q-axis current.

2.4.1.1 Static model

Concerning the static model, there is no time dependency, so the characteristic of this model is constant.

$$\mathcal{L}_d(s) = L_d; \mathcal{G}(s) = \frac{L_d}{R_{fd}}; \mathcal{L}_q(s) = L_q.\tag{eq 2.30}$$

2.4.1.2 Reduced model

Concerning the simplified model, in the d-axis, the parameters $\mathcal{L}_d(s)$ and $\mathcal{G}(s)$ are defined, with $T'_{do} > T'_d$, by the equations:

$$\begin{aligned}\mathcal{L}_d(s) &= L_d \cdot \frac{1 + sT'_d}{1 + sT'_{do}} \\ \mathcal{G}(s) &= \frac{L_d}{R_{fd}} \cdot \frac{1}{1 + sT'_{do}}\end{aligned}\tag{eq 2.31}$$

In the q-axis, the equations of $\mathcal{L}_q(s)$ is characterized by:

$$\mathcal{L}_q(s) = L_q\tag{eq 2.32}$$

2.4.1.3 Complete Model

For the complete SM model, extracted from [45], the parameters $\mathcal{L}_d(s)$ and $\mathcal{G}(s)$ are defined, considering that $T'_{do} > T'_d > T''_{do} > T''_d > T_{kd}$, by the equations below :

$$\mathcal{L}_d(s) = L_d \frac{(1 + sT'_d) \cdot (1 + sT''_d)}{(1 + sT'_{do}) \cdot (1 + sT''_{do})} \quad \text{eq 2.33}$$

$$\mathcal{G}(s) = \frac{L_d}{R_{fd}} \cdot \frac{\left(1 + \frac{L_{1d}}{R_{1d}}\right)}{(1 + sT'_{do}) \cdot (1 + sT''_{do})}$$

And the $\mathcal{L}_q(s)$ equation is characterized by:

$$\mathcal{L}_q(s) = L_q \frac{(1 + sT'_q) (1 + sT''_q)}{(1 + sT'_{qo}) (1 + sT''_{qo})} \text{ with } T''_{qo} > T'_q \quad \text{eq 2.34}$$

2.4.1.4 $\mathcal{L}_d(s)$ Characterisation

Figure 2.3 shows that during the steady and the transient state, both the complete and the reduced models present a similar frequency-response. The function $\mathcal{L}_d(s)$ is equal to L_d at frequencies below T'_{do} as well as during a transient event, for frequencies above T'_d for the reduced model and in the interval $[T'_d T''_{do}]$ for the complete model. The main difference comes from the absence of sub-transient characteristic for the reduced model compared to the complete one.

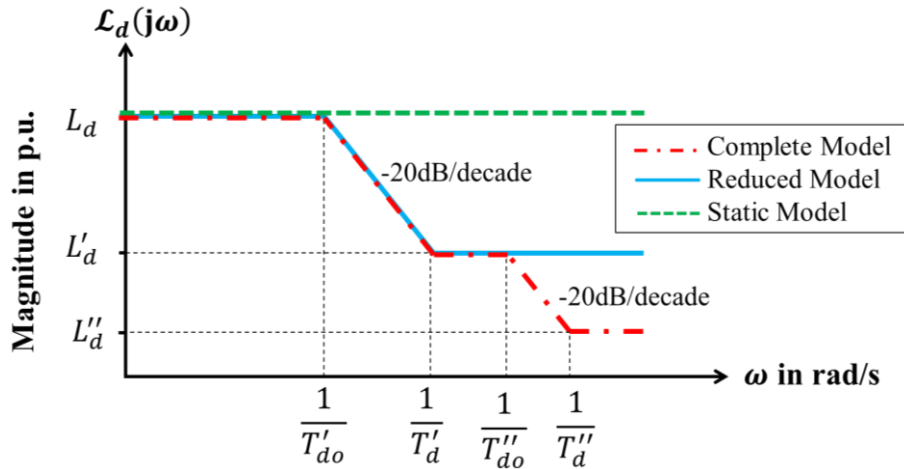


Figure 2.3: Schematic representation of $\mathcal{L}_d(s)$ magnitude for the SM models.

Figure 2.3 also highlights the fact that the harmonics values in high frequencies depends on L'_d for the proposed reduced model and not L''_d as for the complete model [45]. Therefore, as the value of L'_d is higher than L''_d , the individual harmonics and the total harmonic distortion of voltage (THD_V) will be higher for the reduced model. Hence, a study of the harmonics is necessary in order to verify that the standards are respected.

Figure 2.3 highlights finally the fact that the q-axis inductance $\mathcal{L}_q(s)$ for the static model undergoes no variation as there is no time-dependency for this model. The harmonics values of this model will be

higher than for the complete or reduced models as the harmonics values in high frequencies depends on L_d . As $L_d \gg L'_d > L''_d$, the harmonics standards may not be acceptable for this model.

2.4.1.5 $\mathcal{G}(s)$ Characterisation

The d-axis stator flux response to a Δe_{fd} voltage modification with the transient time constant T'_{do} is assessed.

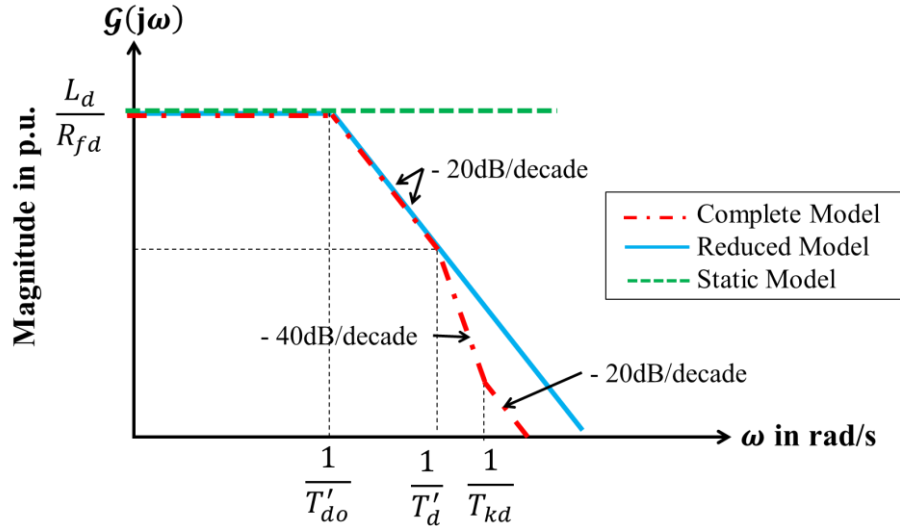


Figure 2.4: Schematic representation of $\mathcal{G}(s)$ magnitude for the SM models.

The Figure 2.4 shows that both the complete and the simplified models present the same behaviour during steady and transient states. It can be noted that the effective gain of the field voltage on the d-axis flux in high frequencies drops off more rapidly for the reduced model than for the more complete one as there is no modelling of the sub-transitory.

The Figure 2.4 highlights the fact that the q-axis inductance $\mathcal{G}(s)$ for the static model undergoes no variation as there is no time-dependency for this model. It can be noted that, contrary to the reduced model and the complete models, the effective gain of the excitative model is constant and presents the same impact.

2.4.1.6 $\mathcal{L}_q(s)$ Characterisation

Figure 2.5 highlights the fact that the q-axis inductance $\mathcal{L}_q(s)$ undergoes no variation as there is no time-dependency in both the reduced and the static model. This means that the variations of $\mathcal{L}_q(s)$ are only affected by the dampers.

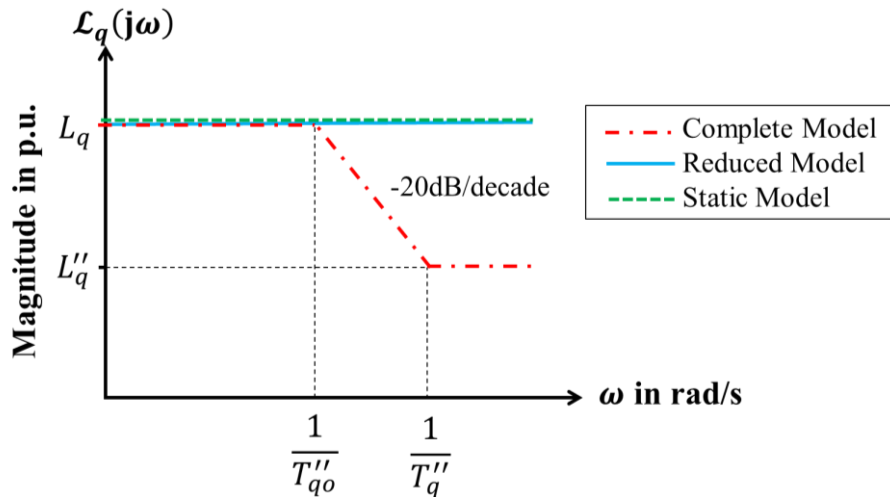


Figure 2.5: Schematic representation of $\mathcal{L}_q(s)$ magnitude for the SM models.

2.4.2 System stability

The VSG is developed to be a plug-and-play solution for (islanded) microgrids with a high share of renewables, having a positive impact on microgrids stability during large load variations and renewables fluctuations.

2.4.2.1 Models stability comparison with load variations

In order to validate the frequency and voltage stabilities, three test cases have been selected and chained in a complete scenario, described in Table 2.2: active and reactive power variations and short-circuits. For this scenario, the three models are implemented in the VSG control.

Table 2.2: Load variations scenario.

Time (s)	Load Impact
0	Off-loading
1	25 % of active power
2	100 % of active power
3	120 % of active power
4	Off-loading
5	30 % of reactive power
6	30 % of reactive and 30 % of active power
7	Off-loading
8	Tri-phases short-circuit of 50 ms
9	Stop

The classic active and reactive power load variations are linked to the general SM model validation and the characteristics of a VSG component integrated in a microgrid. Those specific tests are defined based on the standard [43]. Indeed, in a microgrid, the power variations can be significant depending on

the load variation but also on the production variations. It is the reason why an increase of 75 % of the load and a decrease of 100 % are considered in the scenario proposed in Table 2.2. The overload of the SM is a standard test, included by default in the scenarios presented in Table 2.2, with a load of 120 % of active power based on [44].

The production of reactive power is a necessity to both supply the reactive loads and validate the SM model. In addition, based on the droop control which ensures the voltage stability, the reactive power plays an important part in the voltage stability. Hence, the reactive load variation in the scenario presented in the table are 30 % of reactive power and 30 % of both active and reactive power.

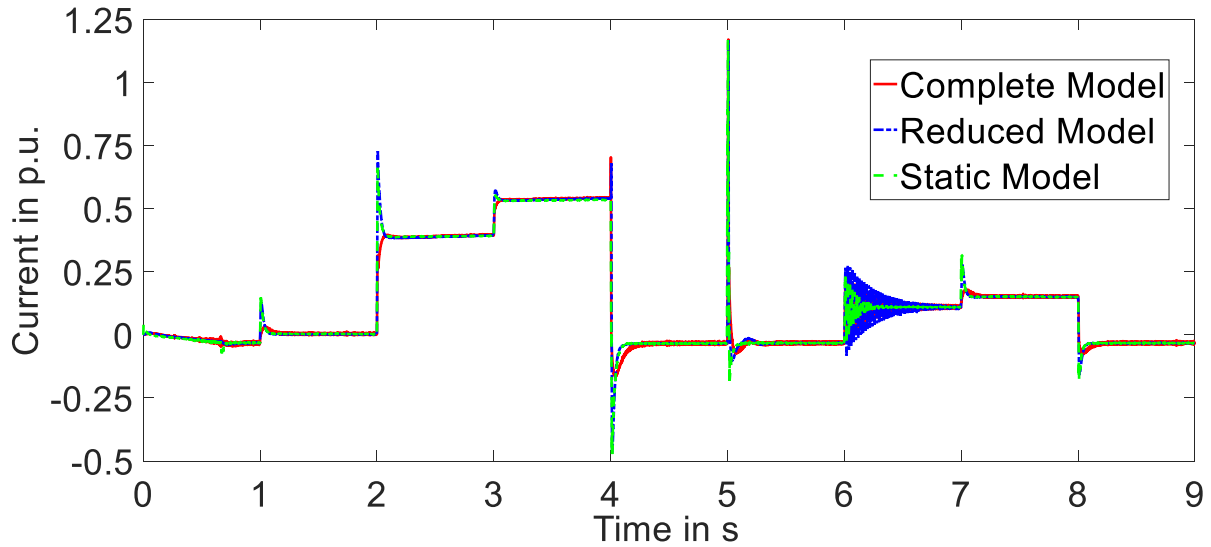


Figure 2.6: Output current i^d for the different models during the scenario described in Table 1.

Figure 2.6 and Figure 2.7 present the output currents for the three models based on the scenario presented in Table 2.2. The three models are stable during the load variations, overload and highly reactive power load that are necessary for the standards validation.

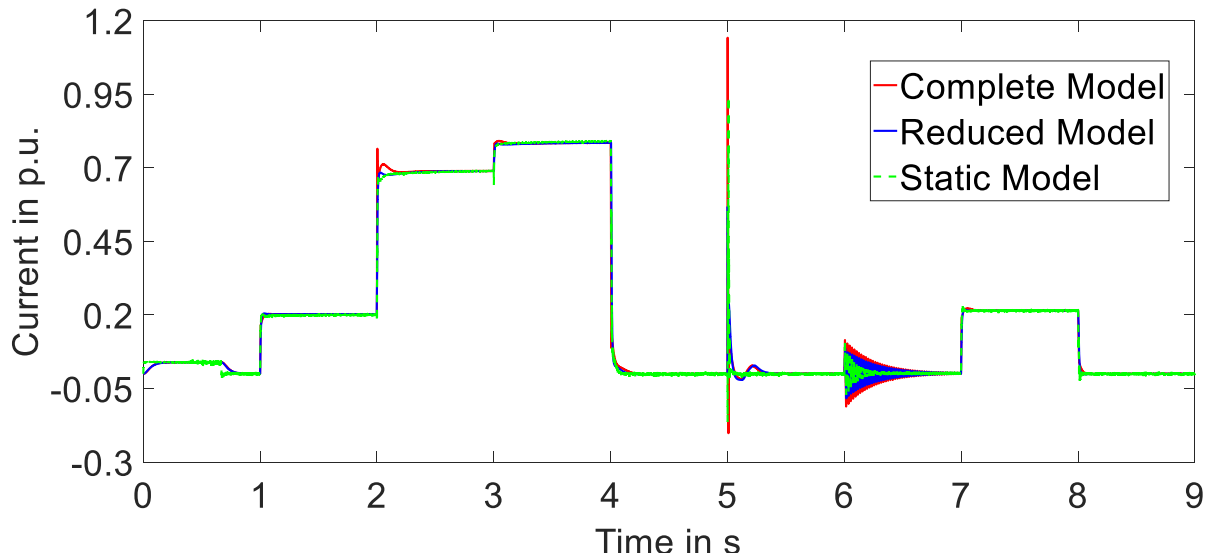


Figure 2.7: Output current i^q for the different models during the scenario described in Table 1.

As expected, the differences between the models are visible during the transient and sub-transient events as it can be seen in Figure 2.8. When initiating the transient responses, the models' differences reduce rapidly until the steady state is reached. All models present a similar behaviour in steady state. The static model is subject to noticeable oscillation during load variations, while the other models, with the help of the transient and sub-transient characteristics, are less impacted by step load variations.

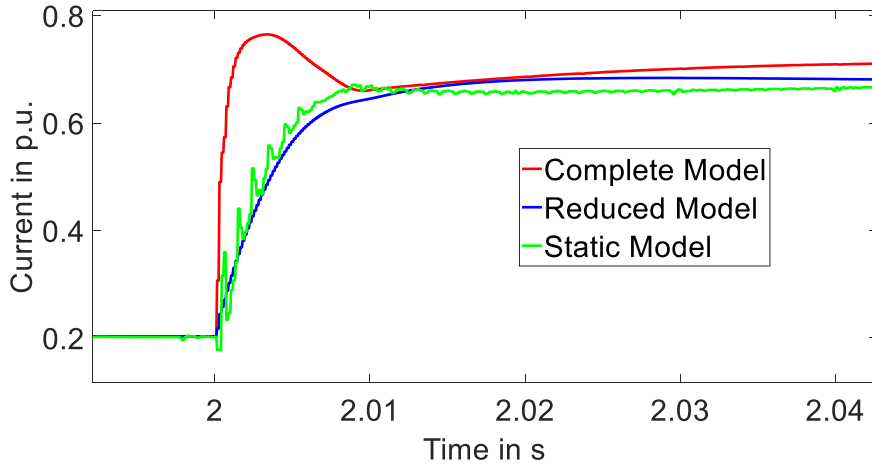


Figure 2.8: Output current i^q during an impact of load for the different models.

A notable difference between the three models can be seen in the output three-phases current in response to a highly inductive load, as it can be seen in Figure 2.6 and Figure 2.7 at $t = 6$ s. Due to the high inductance, an output DC-current is created, both the reduced and the static models stabilize more rapidly than the complete one. Indeed, as the complete model is characterised by sub-transient and transient phenomena, the dissipation of the DC currents created by the inductive elements connected the grid have a more important time response for the complete model than for the reduced and static models.

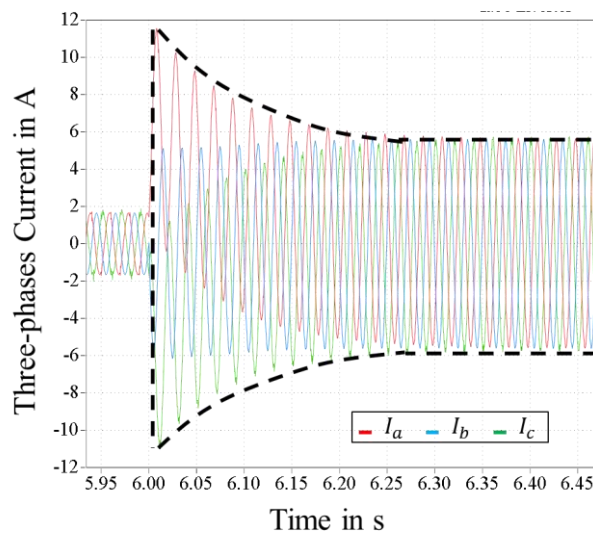


Figure 2.9: Output three-phases currents supplying a high inductive load for reduced model.

Figure 2.9 highlights that the time response to eliminate the output DC-current for the reduced model is about 25 ms (the static model is in the same range). Even after 45 ms, the output DC current produced by the high inductive load is still not eliminated in the case of the complete model (Figure

2.10). Indeed, as discussed before, the simplified models are less sensible to high frequency variations, which explains the difference in the time response after the creation of a DC-component in the output currents or voltages.

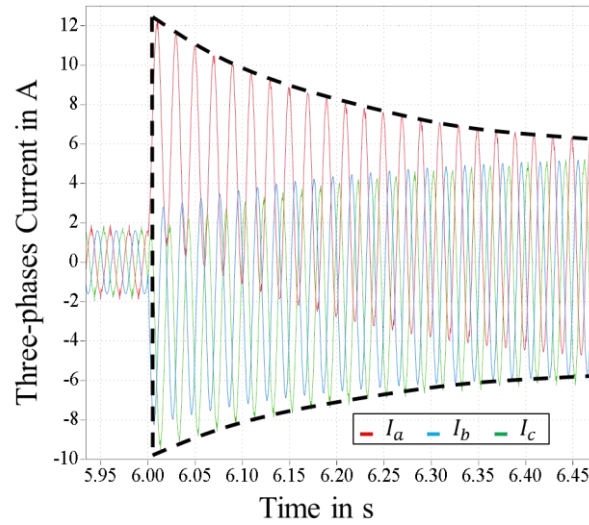


Figure 2.10: Output three-phases currents supplying a high inductive load for complete model.

Figure 2.11 details the mechanical frequency variation of the three models during the scenario described in Table 1. It can be noted that the frequency deviation is similar for the complete and the reduced models. The static model frequency deviations are more important. This high frequency deviations for the static model could be considered in the context of a grid's protection determination to avoid inopportune load-shedding due to the high frequency variations.

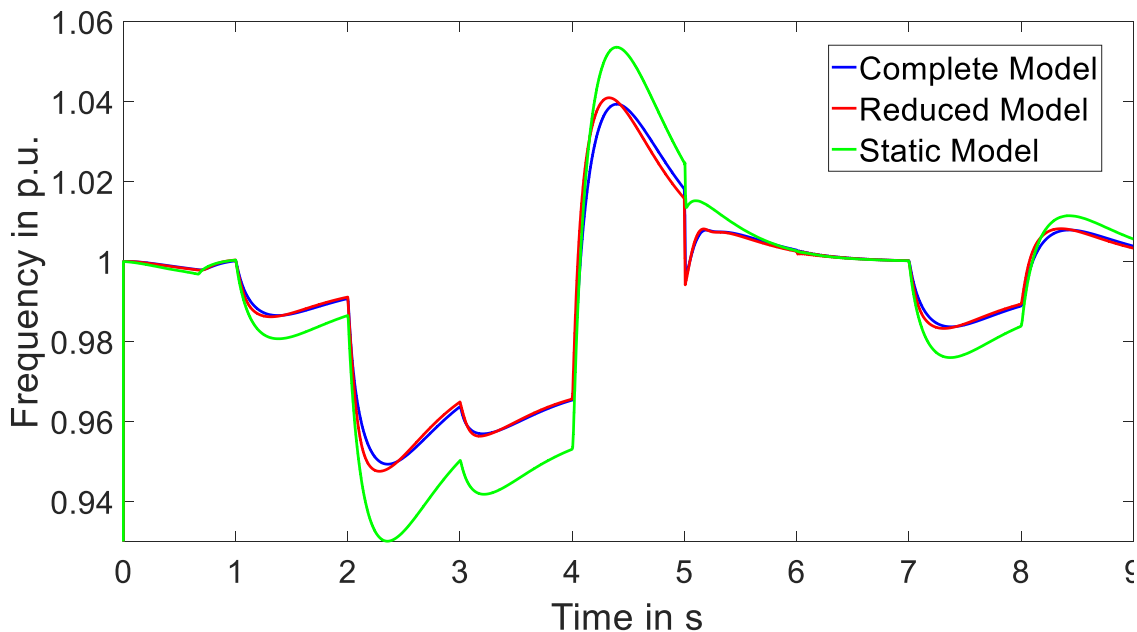


Figure 2.11: Output frequency in p.u. for the different models during the scenario described in Table 1.

Figure 2.12 represents the root mean square (RMS) output voltage of the three models with the same scenario. The complete and reduced models have similar responses. The static model is different especially during highly inductive load variations and short-circuits. It can be noted that the RMS output

voltage of the static model is less impacted by load variations than the other more complete models as it is opposed to voltage variations. However, the transient voltage characteristics of the static model do not respect the standards described in [43].

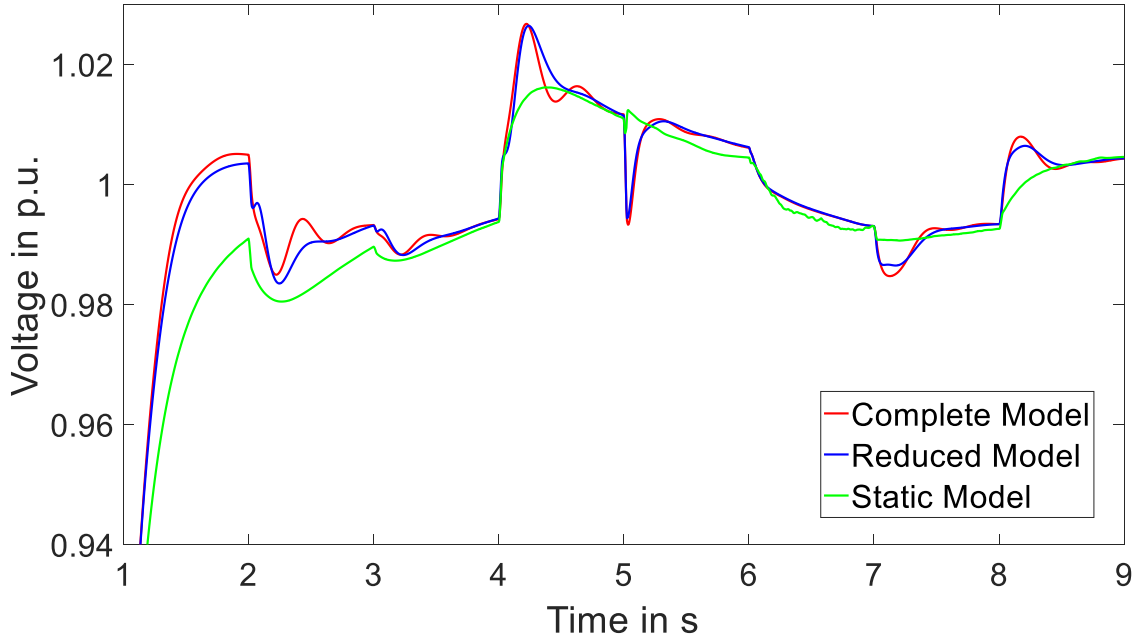


Figure 2.12: RMS output voltage for the different models during the scenario described in Table 1.

To conclude, all the models are stable during the scenario described in Table 2.2. However, it has been noted that the static model is clearly less performant in this context and does not respect the SM standards expected for industrial applications. In addition, the frequency deviation is important with the static model, which means that the microgrids over/under frequency protection devices must be (re)configured adequately (with higher tolerances for instance) to include these deviations and avoid inappropriate load-shedding as the DER protections were not considered.

A perspective that is highlighted by the frequency deviation of the static model and the problem that could be imposed to the grid is the impact of the protection on the stability of the microgrid. Indeed, it could be interesting in further researches to consider similar scenarios with classical DER protections as there were not considered in the different simulations.

2.4.2.2 Short-circuit Currents

The other main difference between the models appears during the short-circuit events as it can be seen Figure 2.6 and Figure 2.7. Indeed, the maximal short-circuit current $I_{sc}^{complete}$ for the complete model (A), considering E_n the phase-phase nominal voltage (V), is:

$$I_{sc}^{complete}(\max) = 2 \cdot \frac{E_n}{X_d''} \quad \text{eq 2.35}$$

For the reduced model, the short-circuit current depends only on the transient inductance. Hence, by analogy with eq 2.35, the maximal short-circuit current $I_{sc}^{reduced}$ (A) is defined by:

$$I_{sc}^{reduced}(\max) = 2 \cdot \frac{E_n}{X'_d} \quad eq\ 2.36$$

Similarly, as the static model only has steady-states components, the maximum short-circuit current I_{sc}^{static} (A) is determined by:

$$I_{sc}^{static}(\max) = 2 \cdot \frac{E_n}{X_d} \quad eq\ 2.37$$

Based on the SM characteristics, the d-axis sub-transient, transient and steady-state inductances are taken as $X''_d \leq X'_d \ll X_d$. Hence, $I_{sc}^{static} \ll I_{sc}^{reduced} \leq I_{sc}^{complete}$ as it can be seen in Figure 2.13. The short-circuit output current magnitude of the complete and reduced models are similar, as the sub-transient inductance X''_d and transient inductance X'_d are comparable and negligible compared to X_d . In this context, the current magnitude during the short-circuit is reduced as expected.

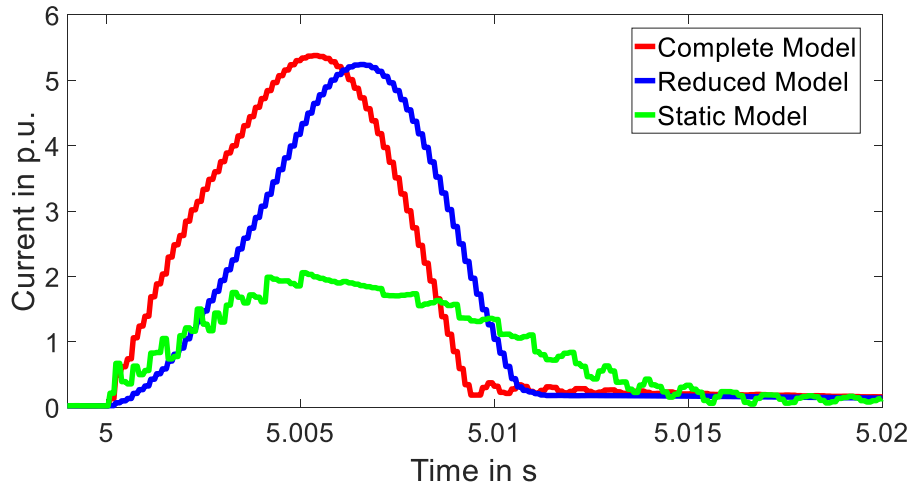


Figure 2.13: Output current magnitude for the different models during a short-circuit.

However, these three models are implemented in an inverter, whose output current is limited between 1.5 to 2.5 times the nominal output current, and cannot reproduce the short-circuit current of a real SM. Indeed, as the objective is not to oversize inverters, the inverter is selected based on its power to ensure the microgrid stability and not for its short-circuit current capability. Hence, if the VSG tries to follow the real SM short-circuit currents, it could:

- Destabilize the VSG model as the output current references are not reachable by the inverter. Since the references are too important comparing to the possible inverter's output current, the inverter will saturate. With the saturation, there is a high possibility that the inverter remains unstable even when the short-circuit is cleared. In this case, the VSG will be disconnected from the microgrid. This may lead to the instability of the microgrid, but not due to the original faulty event.
- Deteriorate the inverter as it is not capable to produce such currents in case where the protections are not triggered.
- Trigger the protections and disconnect the VSG, with all the problems that this can cause on the microgrid stability (losing a power source, short-circuit non-detection, etc.).

To conclude, it is an advantage for the static model, regarding the implementation in the controller of the inverter and more specifically its sizing (and indirectly its stability through non-linear operation).

2.4.3 Harmonics

Finally, a harmonics analysis is conducted as it is linked to the standards validation tests, whose protocols are defined in [41] and in [43].

The Total Harmonic Distortion of Voltage (THD_V) must not exceed 5 % of rated voltage and the individual voltage harmonics must be lower than 3 % of the rated voltage at rated speed and voltage on open-circuit and on non-linear load [41]. The THD_V is calculated based on [41]:

$$THD_V (\%) = \frac{\sqrt{V_2^2 + V_3^2 + \dots + V_{n-1}^2 + V_n^2}}{V_1} \times 100 \quad eq \ 2.38$$

With V_k is the RMS voltage of k^{th} harmonic of 50 Hz and $n = 100$ and V_1 the fundamental.

2.4.3.1 Harmonic at off-load Condition

For this test, the VSG is off loaded in order to extract the THD_V produce by the VSG with the different SM models.

Table 2.3: THD_V and individual harmonics results at off-load condition.

	THD_V in % of rated voltage < 5 %			
	Complete Model	Reduced Model	Static Model	
THD_V	0.41	0.26	3.24	
Individual Harmonic value in % of rated voltage < 3 %				
Harmonic value	3	5	7	11
Complete Model	0.10	0.11	0.13	0.08
Reduced Model	0.20	0.12	0.10	0.09
Static Model	2.28	0.82	0.79	0.41

Table 2.3. details the harmonics value of the three models. Both the complete and the reduced models have similar harmonics content and respect the standards. The static model still respects the standards but produces much more harmonics than the other two models. This is due to the influence of L_d in the high frequencies, as L_d is big compared to L'_d and L''_d .

2.4.3.2 Non-Linear Load Harmonic Tests

A non-linear load is connected to VSG with the reduced model. Below in Figure 2.14, the representation of the non-linear resistive load connected to the VSG:

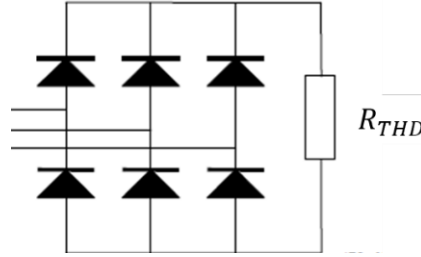


Figure 2.14: Non-linear load scheme.

In the standards, the value of the resistance is chosen for a power factor of 0.8, so:

$$R_{THD} = 1.872 \cdot \frac{E^2}{S \cdot \cos(\phi)} \quad \text{eq 2.39}$$

With E the phase-phase nominal voltage, S the nominal apparent power of the system and $\cos(\phi)$ the power factor at 0.8.

Table 2.4 shows the harmonics analyses of the three models connected to the non-linear load. The complete and the reduced model both respect the standards. The static model does not respect the standards anymore as the total harmonic distortion of voltage exceeds 5 %. In addition, the static model individual voltage harmonics for the 3rd harmonic exceeds 3 % of the rated output voltage. This result is expected as the reactance L_d is taken into account in the characterisation of the harmonics and as $L_d \gg L'_d > L''_d$, the value of the harmonics is too important.

Table 2.4: THD_V and individual harmonics results with nonlinear load.

	THD_V In % of rated voltage < 5 %			
	Complete Model	Reduced Model	Static Model	
THD_V	3.81	3.92	7.92	
Individual Harmonic value in % of rated voltage < 3 %				
Harmonic value	3	5	7	11
Complete Model	2.37	1.31	0.59	0.33
Reduced Model	2.75	1.53	0.86	0.42
Static Model	3.64	1.15	0.73	0.45

Figure 2.15 shows the output three phase voltages of the VSG in per unit (p.u.) with the different models when supplying the non-linear load R_{THD} .

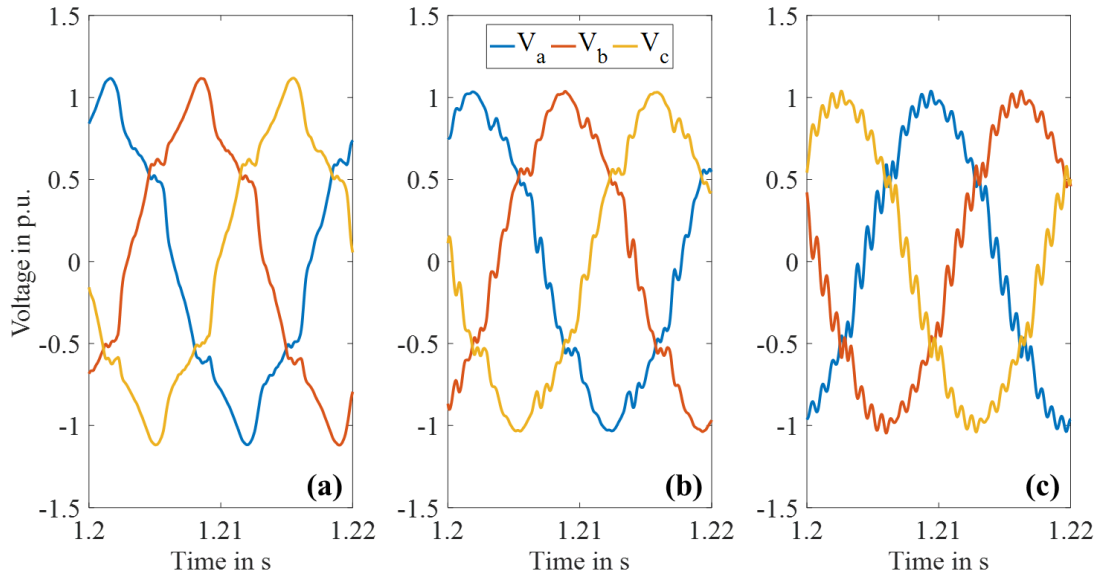


Figure 2.15: Output three phase voltages supplying a non-linear load for (a) complete, (b) reduced and (c) static models.

With Figure 2.15, the reader can clearly see the deterioration of the output three phase voltages between the complete, reduced and static models. Even if the voltage distortion of the complete model, on Figure 2.15 (a), seems more important than the voltage distortion of the reduced or static model, Figure 2.15 (b) and Figure 2.15 (c), the quantity of harmonics distortion is more important for the static model.

2.4.3.3 Conclusion of the Harmonic Creation

To conclude on the harmonics production of the VSG with the three SM models, both the complete and reduced models respect the standards. The static model produces a high quantity of harmonics, which does not respect the standards. This important production of harmonics could impact the supplied load depending on the load's characteristics and its sensibility.

2.4.4 Parallel Operation

The VSG being developed to be a plug-and-play solution, it must be able to operate correctly in parallel with other power sources in a microgrid. As show in [47], the microgrid instabilities can be exacerbated by the resonance among generators and VSGs. Hence, it is necessary to verify the impact of the different SM model on the VSG parallel stable operation. So, the notion of parallel operation is mandatory to validate a potential industrial certification.

As the complete model is the most accurate one compared to a real generator set, a VSG based on the complete model can be put easily and without any problem in parallel with similar or other power sources. However, this is not the case of the reduced or the static model-based VSG. For the parallelism study of the three models, the encountered problems have been divided in two categories, depending on the power sources put in parallel with the VSG.

2.4.4.1 Operation in parallel with an identical VSG

For the static and the reduced models, as there are no damper windings, to avoid any risk of oscillation between multiple identical power sources, some modifications are necessary. The oscillation period of the solution without damper must be considered for the frequency controller of the VSG and the governor, to avoid the creation of oscillations. The considered oscillation period is defined by the equation extracted from [48]:

$$T(s) = \frac{2 \cdot \pi}{p} \cdot \sqrt{\frac{10 \cdot J \cdot \omega_{base}}{E \cdot I_{sc}}} \quad eq\ 2.40$$

With ω_{base} the base angular velocity (rad/s), p the number of poles of the SM, E the grid voltage (V), J the moment of inertia (kg.m²), I_{sc} the short-circuit current (A). The maximum short circuit current I_{sc} is defined depending on the SM model.

This oscillation period $T(s)$ will permit to adapt the time response of the governor in order to avoid the creation of the oscillation between similar VSG with the reduced or static model. The governor's time-response must be adapted in regard to the oscillating time between the same SM models or different power sources. This modification concerns the time response of the voltage and frequency controllers, and only impacts the VSG solution before integration in a microgrid [49].

2.4.4.2 Operation in parallel with other power sources

As the static model does not have transient characteristics, during a load variation, the voltage is instantly modified and imposed by the static VSG. In addition, as showed in Figure 2.12, the voltage variations of the static model are completely different from what can be expected from a SM as it does not respect the expected standards. Indeed, the voltage produced by the genset have sub-transient and transient characteristics which are opposed to the instantly modified voltage of the static VSG. Hence, oscillations appear as each power source try to impose the voltage in the microgrid as it can be seen in Figure 2.16.

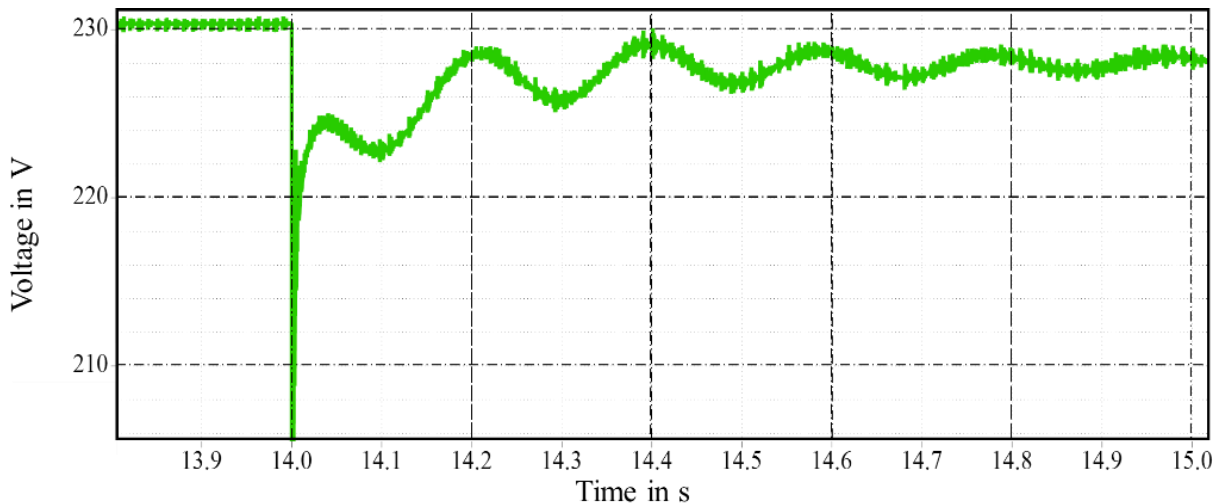


Figure 2.16: Grid RMS voltage after a load impact with the static model VSG and a generator set in parallel.

In addition to the problem of voltage oscillations, the frequency deviation is noticeable with the static model compared to the other SM models as identified in Figure 2.11. During a load impact, the VSG with the static model will have a frequency deviation largely different from the other power sources connected to the microgrid which could result in high frequency and powers variations.

However, the solution proposed in [25] to avoid voltage oscillations requires major modifications to all the other power sources connected to the microgrid. An advanced solution of AVR and governor is proposed in [50] in order to minimize the voltage and frequency oscillations. The solution was validated in simulation and in experimentation but without considering the computation limitations of the industrial inverter, which is the focus of the next section.

To conclude, for a genset in parallel with a VSG based on the static model, the control must be adapted because the voltage is imposed by the model of the VSG as it was identify in [25]. If not dealt with, this problem could generate voltage instability and reduce the operational performances of the considered microgrid with high frequency oscillation. However, concerning the static VSG, the problem is more complicated. Indeed, there is a creation of oscillations as each power source tries to impose this output voltage. This voltage oscillation creates an oscillation in the output current and frequency.

2.4.5 Implementation on a digital controller of an industrial inverter

As the VSG must be a plug-and-play solution, the idea is ultimately to study the integration of the three SM models in a Digital Signal Processor (DSP) of an industrial inverter, a Schneider Electric SOLAR grid-tie inverter, Conext CL 25.

For the discretization and implementation in the DSP, the Euler forward method is used, resolving the differential systems of equations of the SM defined by $\dot{y} = f(y)$ thanks to [23], considering T_s as the sampling time and k a time sept:

$$y(k) = y(k - 1) + T_s \cdot f(y(k - 1)) \quad \text{eq 2.41}$$

The discretized model is implemented with MATLAB Simulink® using the “Embedded Coder” toolbox of MATHWORKS®, and “Code Composer Studio” toolkit.

To compare the three SM models, the DSP’s central processing unit (CPU) load is reported in Table 2.5. All the CPU load cannot be used for the VSG model, in order to ensure a proper operation of the controller (only 70 %-75 % of the CPU load can be used to avoid any overloading, and errors production that could destabilize the controller).

The exact methodology to implement the VSG software in the controlled card of the industrial inverter is detailed in Chapter 4 (4.2.2 – p81) with the presentation of the experimental results of our proposed controller, himself presented in Chapter 3. In this part, only the CPU load of the VSG with the three models is detailed.

Table 2.5: CPU load depending of the SM model selected.

Model	CPU load in %
Complete Model	76.61 %
Reduced Model	69.42 %
Static Model	62.60 %

Table 2.5 details the CPU load used by the three SM models implemented in the DSP. The complete model uses more CPU load than to the reduced or static model. It can be noted that, considering the industrial inverter computation capability and limitation, the complete model is not adapted, as the VSG will be unstable.

The complete model can be implemented in an industrial inverter; however, no other features could be added to the solution. Hence, the advantage to have a virtual model that could be modified is lost due to the high CPU load used for this model. With the reduced model, the CPU load is still important, but below 70 %, which ensures a proper operation of the controller in the industrial inverter but still limits the capacity to integrate additional functions. For the static model, the CPU load is clearly reduced compared to the complete model, showing that the model will have no implementation problems.

To conclude, only the reduced and static models could be implemented in an industrial inverter presenting a limited capability of computational power in order to insure a proper operation of the VSG model. The reduced model is a good compromise solution in the context of this work with good performances and the possibility to implement advanced controls. For example, the reduced model will be considered as the SM reference for the advanced controller that will be explained in Chapter 6 (6.2 – p123). In this chapter, the VSG will take advantage of its virtual characteristics to improve its performances.

2.5 Conclusion

Three SM models for the implementation of a VSG in an industrial inverter are detailed, characterised, compared with respect to various test cases (load variations, short-circuit events), tested in the context of real SM and generators sets standards and operated in parallel with other power sources as in a real microgrid. The three SM models are a “complete” one, constituted of the all dynamic electrical equations, a “reduced” model constituted of a virtual impedance, and a “static” model based on the SM’s steady state.

The standardisation proposal tests are constituted of active and reactive power load impacts, short-circuit in standalone or parallel configurations and total harmonics distortions. The tests are designed to ensure that any VSG solution (independently from the implemented SM model) can be integrated in a microgrid, once respecting the proposed standards. The set of tests proposed in this chapter for the standardisation of grid-friendly VSG is a first step that would necessitate to more precisely define thresholds regarding for example harmonics analysis (maybe allowing to consider a basic model in some configurations) as well as requirements for additional modification of power sources that are integrated in parallel with VSG solutions. To conclude, as highlighted in the chapter, a much needed work would be to determine jointly the requirements for both the VSG solution and its protection, including the protection scheme of the concerned (micro-)grid.

It shows that the static SM model is too simplified for the industrial context. Indeed, this model presents multiple disadvantages: high frequencies variations that could create inappropriate load-shedding if the protections of the grid are not adapted, no respect of the voltage standards which increases the difficulty of parallelism with other power sources and high productions of harmonics which can be destructive for sensible loads. In addition, the static model has the disadvantage to encounter difficulties to be parallelized with another power sources, trying to impose instantly a new voltage after a load impact as the model does not have any time dependency. The model has some advantages: the output short-circuit current is lower than for a real SM and the computational burden for its implementation is low on a DSP. Thanks to the low CPU load, it will be possible to add an improved controller or solutions that will smooth the disadvantages of this model. To conclude on the static model, it can be easily implemented in inverter but have a real impact on the stability of the microgrid. Some precaution must be considered if integrated to a microgrid and put in parallel with other power sources.

The complete model is the most realistic one. It respects the SM and generator standards and has a limited production of harmonics when supplying load. This model also has no problem to be parallelized with other power sources. However, a first problem is the output currents during a short-circuit that must be saturated otherwise the inverter could be damaged. A second problem is the difficulty to be implemented in a real industrial inverters' DSP. Hence, the complete SM model could not be easily industrialised without extra costs on the selection of the industrial solution. This means that this solution could only be implemented in a performant inverter and so more expensive one. Its integration in a microgrid is a real plug and play solution as it have no problems to be put in parallel with other powers sources and validates the entire SM standards.

Then, considering an industrial inverter, the proposed reduced model is the most adapted one, presenting a good compromise between CPU load and performances. This model mimics a SM with the best compromise between details and ease of operation. The parallelized operation has been resolved easily in just choosing the adapted voltage and frequency controllers to avoid the risk of oscillation between this VSG and other power sources. The proposed reduced model of SM is the most adapted to a VSG implementation in an industrial inverter as it respects the generator standards and can be operated in parallel with other power sources while being still relatively "light" for the inverter's DSP.

Now that the impact of the SM model on the behaviour and on the performances of the VSG connected to an islanded microgrid considering analytics models and industrial standards has been studied, in Chapter 3 will be studied the controller of the VSG is constructed to follow the reference currents provided by the SM model.

2.6 Perspective

A perspective of development for further researches could be the integration of the homopolar axis of the reference $dq0$, which have been neglected in this study, for the different models and also its consideration for the VSG controller to may be improve the VSG performance when supplying unbalanced loads.

A perspective that is highlight by the frequency deviation of the static model and the problem that could impose to the grid is the impact of the protection on the microgrid. Indeed, it could be interesting in further researches to considered similar scenarios as described taking into account the classical DER protections.

A possible perspective could be to apply the same methodology of tests to other SM models that can be found in the literature as a reference for VSG solution. Indeed, the three SM models detailed above have been selected as they represent various precision levels and also are the most used models, but different SM representations are also considered as reference for the VSG output currents.

Chapter 3. Evolution of the current controllers for the VSG

3.1 Introduction

One of the most frequently used solutions as VSG software is the multi-loop control architecture that implements the three different regulations, namely: current, voltage and frequency [51], [52]. Concerning the current regulations, many other solutions have also been implemented such as traditional solutions based on PI (proportional integrator) with addition of resonant controller [52], [53] or a robust H_∞ method [54], fuzzy control [55] to cite but some alternatives.

An element that can be noted is that the different controllers are developed to increase both the performance of the VSG but also to minimise the creation of oscillation at the output of the inverter. As described in [28], the different oscillations are caused partly by resonances above the lines frequency which then destabilize the controlled system. A state-space methodology have been used in [40] to develop an optimized controller to avoid the creation of such oscillations. However, as the entire configuration of the microgrid must be implemented in this controller, this restriction limits the controller as it needs to be modified each time the microgrid architecture evolves.

Astonishingly enough, the use of an observer has never been attempted to improve the performances of the controller. In this chapter, firstly, the methodology to implement an observer is detailed to avoid the model instabilities. Then, the advantage of this observer is proved by testing two

different configurations of PI controller, previous controller used, without and with the proposed state observer.

Finally, even if the observer stabilizes and improves the performance of the PI controller, the performance can still be improved. Hence, the proposed solution in this contribution is a combination of a controller based on the state-space model of the SM adapted to the grid-connected inverter and a state observer to reconstruct the load's characteristics supplied by the VSG.

In this chapter, the entire model used to define the different controllers is described. More precisely, in a first section, the previous controller used in Schneider Electric VSG is presented. Then, in order to solve the controller's stability problems, a state observer is added to increase the VSG performances during harsh events. However, even with the observer, the previous controller is not optimal when the VSG supplies high inductive loads or during short-circuit as oscillations appear at the VSG outputs. Finally, a new controller is proposed to improve the performance of the VSG which is created as an extension of the state vector.

3.2 System's state-space model analytic description

As explained before, in this section, the objective is to detail the reference model that will be used to create our different controllers.

Firstly, the inverter grid connected to the grid is detailed to create a state-space model considering a complete SM based VSG that have been detailed in Chapter 2 (2.3.1.2 – p 12). Then, this state-space model is compared to a simulated model to conclude on the quality of the state-space model.

Note that the equations below are expressed in dq-axis in order to reduce the computation time when implemented in the real industrial inverter. Indeed, in abc-axis, all steady state signals are sinusoidal. In dq-axis, the steady state signals are constant. In addition, the working in dq-axis reduces the number of unknowns from three (a, b, c) to two (d, q) as the homopolar axis is not considered (noted 0 axis).

As the derivation from abc-axis to dq-axis have been already detailed in Chapter 2 (2.2 – p 9), the derivation developments are not detailed in this section. Just as a reminder, the derivation in the dq-axis is defined by the equation:

$$\frac{d}{dt}X_{dq} = T \cdot \frac{d}{dt}X_{abc} + \begin{bmatrix} 0 & \omega_r \\ -\omega_r & 0 \end{bmatrix} \cdot X_{dq} \quad \text{eq 3.1}$$

The different equations are also developed in p.u.. In order to simplify the notation, the notation *p.u.* is implicit as all the equations in dq-axis that will be detailed below are also in p.u.. The different controllers detailed below are calculated in p.u. in order to improve the feasibility and portability to other inverters. Indeed, with the controller calculated in p.u., it is not necessary to modify the controller's parameters when implemented in another inverter with different characteristics.

The replicability and portability of the VSG on inverters with different characteristics will be approached in Chapter 5. Replicability and portability of the VSG control (p99).

3.2.1 Description of the inverter model

3.2.1.1 Hypothesis and Schematic of the Inverter Model

Figure 3.1 represents the inverter connected to the grid. The single line voltage V_C is noted as e^d and e^q in the dq-axis, V_C represents the voltage the inverter must produce for grid. The voltage V_i is the output inverter voltage with $V_i = \alpha \cdot \frac{V_{DC}}{2}$, α the single line inverter's duty ratio and V_{DC} the DC voltage as detailed in Figure 3.1. Depending of the microgrid topology, the resistor R_g could be neglected if the microgrid lines are short, hence R_g is not considered as equal to zero. The resistor R_f is also not neglected for inverter's model even if R_f could be neglected in comparison with the value of R_L , in order to have the most complete model.

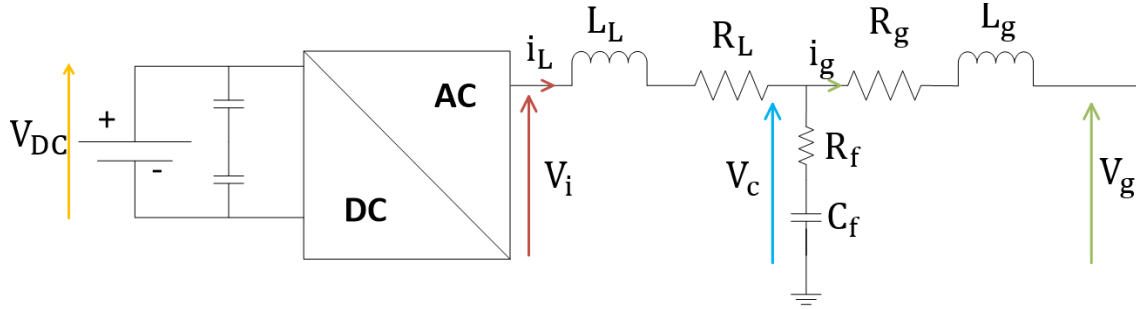


Figure 3.1: Inverter single line schema.

The inverter used as a reference is a SOLAR grid-tie inverter rated to 25 kVA /20 kW for three-phase voltages of 230 V_{AC}, phase-neutral, at a frequency of 50 Hz and supplied by a continuous voltage of 750 V_{DC}. The different inverter parameters that can be seen in Figure 3.1 are detailed.

Table 3.1: Inverter parameters.

Parameter	Characteristics	Value
L_L	Inverter's inductance	870 mH
R_L	Inverter's resistor	7.1 m Ω
L_g	Grid's inductance	60 mH
R_g	Grid's resistor	1 m Ω
C_f	Capacitive filter's inductance	152 μ F
R_f	Capacitive filter's resistor	1 m Ω
V_{DC}	Input DC voltage	750 V

3.2.1.2 Inverter's analytic model description

For determination of currents i_L and i_g , the equations are described below:

$$V_i = L_L \cdot \frac{d(i_L)}{dt} + R_L \cdot i_L + V_C$$

$$V_C = L_g \cdot \frac{d(i_g)}{dt} + R_g \cdot i_g + V_g$$

Therefore, the single line inverter current i_L and the single line grid current i_g are dynamically defined by:

$$\frac{d(i_L)}{dt} = \frac{V_i - V_C}{L_L} - \frac{R_L}{L_L} \cdot i_L \quad \text{eq 3.2}$$

$$\frac{d(i_g)}{dt} = \frac{V_C - V_g}{L_g} - \frac{R_g}{L_g} \cdot i_g \quad \text{eq 3.3}$$

So, the inverter current defined in eq 3.2, in dq-axis and in p.u., is i_L^d and i_L^q . The inverter currents i_L^d and i_L^q are determined by:

$$\begin{aligned} i_L^d &= \omega_{base} \cdot \left(\omega_r \cdot i_L^q + \frac{V_i^d - e^d}{L_L} - \frac{R_L}{L_L} \cdot i_L^d \right) \\ i_L^q &= \omega_{base} \cdot \left(-\omega_r \cdot i_L^d + \frac{V_i^q - e^q}{L_L} - \frac{R_L}{L_L} \cdot i_L^q \right) \end{aligned} \quad \text{eq 3.4}$$

and, similarly, the grid current determined in eq 3.3 is defined by i_g^d and i_g^q in dq-axis and in p.u.. The grid currents equations i_g^d and i_g^q are:

$$\begin{aligned} i_g^d &= \omega_{base} \cdot \left(\omega_r \cdot i_g^q + \frac{e^d - V_g^d}{L_g} - \frac{R_L}{L_g} \cdot i_g^d \right) \\ i_g^q &= \omega_{base} \cdot \left(-\omega_r \cdot i_g^d + \frac{e^q - V_g^q}{L_g} - \frac{R_L}{L_g} \cdot i_g^q \right) \end{aligned} \quad \text{eq 3.5}$$

The single line filter voltage V_C is determined thanks to both currents:

$$\begin{aligned} i_L - i_g &= C_f \frac{d[V_C - R_f \cdot (i_L - i_g)]}{dt} \\ i_L - i_g &= C_f \frac{d(V_C)}{dt} - C_f \cdot R_f \frac{d(i_L - i_g)}{dt} \end{aligned}$$

hence, the voltage V_C is defined by the equation:

$$\frac{d(V_C)}{dt} = \frac{i_L - i_g}{C_f} + R_f \cdot (i_L - i_g)$$

considering eq 3.4 and eq 3.5, the single line filter voltage \dot{V}_C is determined by the equation:

$$\dot{V}_C = \frac{i_L - i_g}{C_f} - \frac{R_f \cdot R_L}{L_L} \cdot i_L + \frac{R_f \cdot R_g}{L_g} \cdot i_g + \frac{R_f}{L_L} \cdot V_i + \frac{R_f}{L_g} \cdot V_g - R_f \cdot \left(\frac{1}{L_L} + \frac{1}{L_g} \right) \cdot V_C$$

The dq-axis filter voltage e^d and e^q in p.u. are defined by:

$$\begin{aligned} e^d &= \omega_{base} \cdot \left(\omega_r \cdot e^q + \frac{i_L^d - i_g^d}{C_f} - \frac{R_f \cdot R_L}{L_L} \cdot i_L^d + \frac{R_f \cdot R_g}{L_g} \cdot i_g^d + \frac{R_f}{L_L} \cdot V_i^d + \frac{R_f}{L_g} \cdot V_g^d - R_f \left(\frac{1}{L_L} + \frac{1}{L_g} \right) \cdot e^d \right) \\ e^q &= \omega_{base} \cdot \left(-\omega_r \cdot e^d + \frac{i_L^q - i_g^q}{C_f} - \frac{R_f \cdot R_L}{L_L} \cdot i_L^q + \frac{R_f \cdot R_g}{L_g} \cdot i_g^q + \frac{R_f}{L_L} \cdot V_i^q + \frac{R_f}{L_g} \cdot V_g^q - R_f \left(\frac{1}{L_L} + \frac{1}{L_g} \right) \cdot e^q \right) \end{aligned} \quad eq\ 3.6$$

3.2.2 State-space model description

The proposed controller is based on the concatenation of the complete synchronous machine, detailed before in Chapter 2 (2.3.1.2 – p 12) and the inverter models. To simplify the model and to rewrite it in state-space framework, the assumption $\omega_r = 1$ is used. This assumption is relevant since the dynamic frequency variations in an electrical grid is limited to less than 10 % of the nominal value. In the remainder below, we will see if the hypothesis of $\omega_r = 1$ can be considered. This assumption is a posterior validated later in this chapter, see the section 3.2.3 (p 44).

Hence, with the hypothesis $\omega_r = 1$, the equations eq 3.4, eq 3.5 and eq 3.6 can be defined as a state-space model. This state-space model in dq-axis and p.u. is:

$$\begin{aligned} \dot{X}_{SYS} &= A_{SYS} \cdot X_{SYS} + B_{SYS} \cdot U_{SYS} + G_{SYS} \cdot W_{SYS} \\ Y_{SYS} &= C_{SYS} \cdot X_{SYS} \end{aligned} \quad eq\ 3.7$$

where X_{SYS} is the regulated system's states, U_{SYS} is the regulated system's command, W_{SYS} is the system's exogenous inputs and finally Y_{SYS} is the regulated system's outputs.

$$\begin{aligned} X_{SYS} &= [\psi_d \quad \psi_q \quad \psi_{fd} \quad \psi_{1d} \quad \psi_{1q} \quad i_L^d \quad i_L^q \quad e^d \quad e^q \quad i_g^d \quad i_g^q]^t, X_{SYS} \in \mathbb{M}_{11,1} \\ U_{SYS} &= \begin{bmatrix} V_i^d \\ V_i^q \end{bmatrix}, U_{SYS} \in \mathbb{M}_{2,1}; W_{SYS} = \begin{bmatrix} e_{fd} \\ V_g^d \\ V_g^q \end{bmatrix}, W_{SYS} \in \mathbb{M}_{3,1} \text{ and } Y_{SYS} = \begin{bmatrix} i^d \\ i^q \end{bmatrix}, Y_{SYS} \in \mathbb{M}_{2,1}, \end{aligned}$$

the matrixes A_{SYS} , B_{SYS} , G_{SYS} and C_{SYS} , $A_{SYS} \in \mathbb{M}_{11,11}$; $B_{SYS} \in \mathbb{M}_{11,2}$; $G_{SYS} \in \mathbb{M}_{11,3}$ and $C_{SYS} \in \mathbb{M}_{2,11}$, are given below:

$$A_{SYS} = \omega_{base} \cdot \begin{bmatrix} A_{MS} & A_E \\ \mathbb{O}_{6,5} & A_{LCL} \end{bmatrix} \text{ with } A_{MS} = \begin{bmatrix} -a_1 & \omega_r & a_2 & a_3 & 0 \\ -\omega_r & -a_4 & 0 & 0 & a_5 \\ a_6 & 0 & -a_7 & a_8 & 0 \\ a_9 & 0 & a_{10} & -a_{11} & 0 \\ 0 & a_{12} & 0 & 0 & -a_{13} \end{bmatrix}, A_E = \begin{bmatrix} \mathbb{O}_{2,2} & \mathbb{I}_2 & \mathbb{O}_{2,2} \\ \mathbb{O}_{3,2} & \mathbb{O}_{3,2} & \mathbb{O}_{3,2} \end{bmatrix},$$

$$A_{LCL} = \begin{bmatrix} -\frac{R_L}{L_L} & \omega_r & -\frac{1}{L_L} & 0 & 0 & 0 \\ -\omega_r & -\frac{R_L}{L_L} & 0 & -\frac{1}{L_L} & 0 & 0 \\ \left(\frac{1}{C_f} - \frac{R_f \cdot R_L}{L_L}\right) & 0 & -R_f \cdot \left(\frac{1}{L_L} + \frac{1}{L_g}\right) & \omega_r & -\left(\frac{1}{C_f} - \frac{R_f \cdot R_g}{L_g}\right) & 0 \\ 0 & \left(\frac{1}{C_f} - \frac{R_f \cdot R_L}{L_L}\right) & -\omega_r & -R_f \cdot \left(\frac{1}{L_L} + \frac{1}{L_g}\right) & 0 & -\left(\frac{1}{C_f} - \frac{R_f \cdot R_g}{L_g}\right) \\ 0 & 0 & \frac{1}{L_g} & 0 & -\frac{R_g}{L_g} & \omega_r \\ 0 & 0 & 0 & \frac{1}{L_g} & -\omega_r & -\frac{R_g}{L_g} \end{bmatrix};$$

$$B_{SYS} = \omega_{base} \cdot \begin{bmatrix} 0 & 0 \\ 0 & 0 \\ 0 & 0 \\ 0 & 0 \\ 0 & 0 \\ \frac{V_{DC}}{2 \cdot L_L} & 0 \\ 0 & \frac{V_{DC}}{2 \cdot L_L} \\ \frac{R_f \cdot V_{DC}}{2 \cdot L_L} & 0 \\ 0 & \frac{R_f \cdot V_{DC}}{2 \cdot L_L} \\ 0 & 0 \\ 0 & 0 \end{bmatrix}; \quad G_{SYS} = \omega_{base} \cdot \begin{bmatrix} 0 & 0 & 0 \\ 0 & 0 & 0 \\ 1 & 0 & 0 \\ 0 & 0 & 0 \\ 0 & 0 & 0 \\ 0 & 0 & 0 \\ 0 & 0 & 0 \\ 0 & \frac{R_f}{L_g} & 0 \\ 0 & 0 & \frac{R_f}{L_g} \\ 0 & -\frac{1}{L_g} & 0 \\ 0 & 0 & -\frac{1}{L_g} \end{bmatrix};$$

$$C_{SYS} = \begin{bmatrix} -c_1 & 0 & c_2 & c_3 & 0 & 0 & 0 & 0 & 0 & 0 & 0 & 0 & 0 \\ 0 & -c_4 & 0 & 0 & c_5 & 0 & 0 & 0 & 0 & 0 & 0 & 0 & 0 \end{bmatrix}$$

3.2.3 State-space model validation

Before designing the current controllers for the VSG inverter, the complete model, concatenation of the complete SM model and grid connected inverter model, has to be validated since the state-space model is our reference for the different controllers described in this chapter. The inputs of the model in dq-axis for the validation can be seen in Appendix 2 (p163) and will be used for the entire chapter.

The reference model used for the validation is described in Appendix 1 (p161). The reference model is the concatenation of a SM model and the output filter of the inverter in Simulink®.

The link between the SM model and the inverter output filter is the capacitor voltages, V_c in single line or e^d and e^q in dq-axis. In addition, to validate our hypothesis on $\omega_r = 1$ considered for the state-space model, electrical rotor velocity ω_r used for the reference will be considered variable in order to represent the different load impacts on the frequency.

Concerning the state-space model validation, the inputs are both the inverter voltages e^d and e^q , the grid voltages V_g^d and V_g^q , and the voltage e_{fd} . The electrical rotor velocity ω_r is considered as constant and equal to 1 p.u..

As the objective of the SM model implemented in the VSG is to give the current reference, only the currents i^d and i^q will be considered in this section. It can be noted that the other variables of the state-space system are visible in Appendix 3 (p165). Below, Figure 3.2 and Figure 3.3 represent the SM output currents i^d and i^q from both the state-space model, in red, and the reference model, in blue.

In Figure 3.2 and Figure 3.3, one can observe high currents peaks and oscillations currents. The currents peaks are caused by the different load impacts. The current oscillations are due to the inductive characteristics of the load.

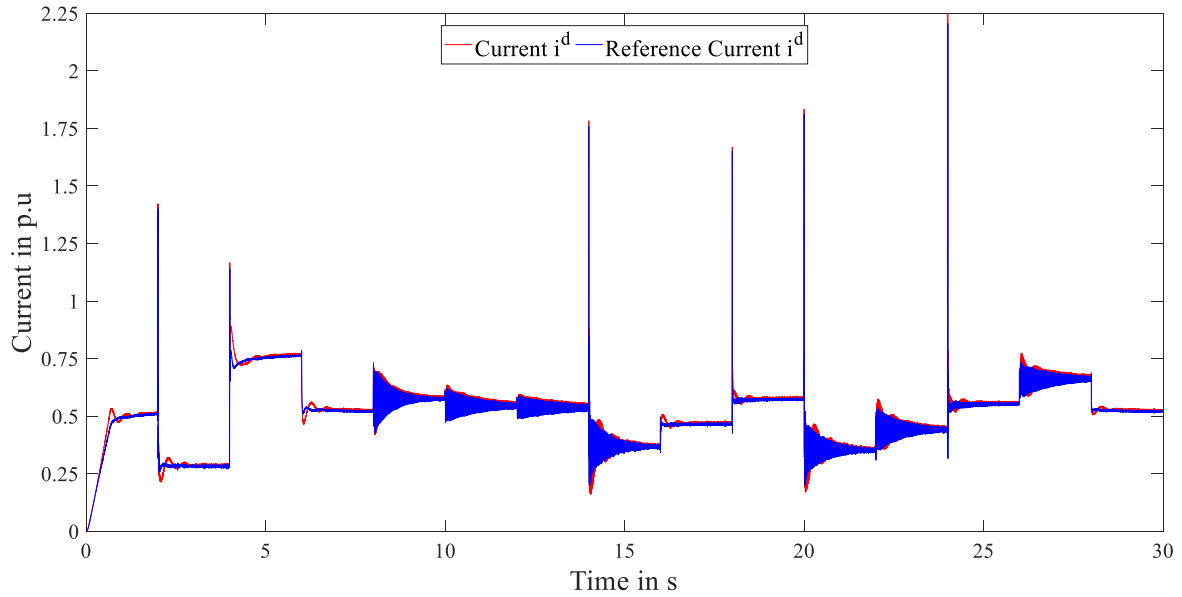


Figure 3.2: Current i^d for both state-space and reference models.

Figure 3.2 and Figure 3.3 show that the state-space model is accurate as far as i^d is concerned in steady-state. Figure 3.4 show that the state-space model is accurate, even with the hypothesis on ω_r as the state-space model dynamic follow the reference during a load impact.

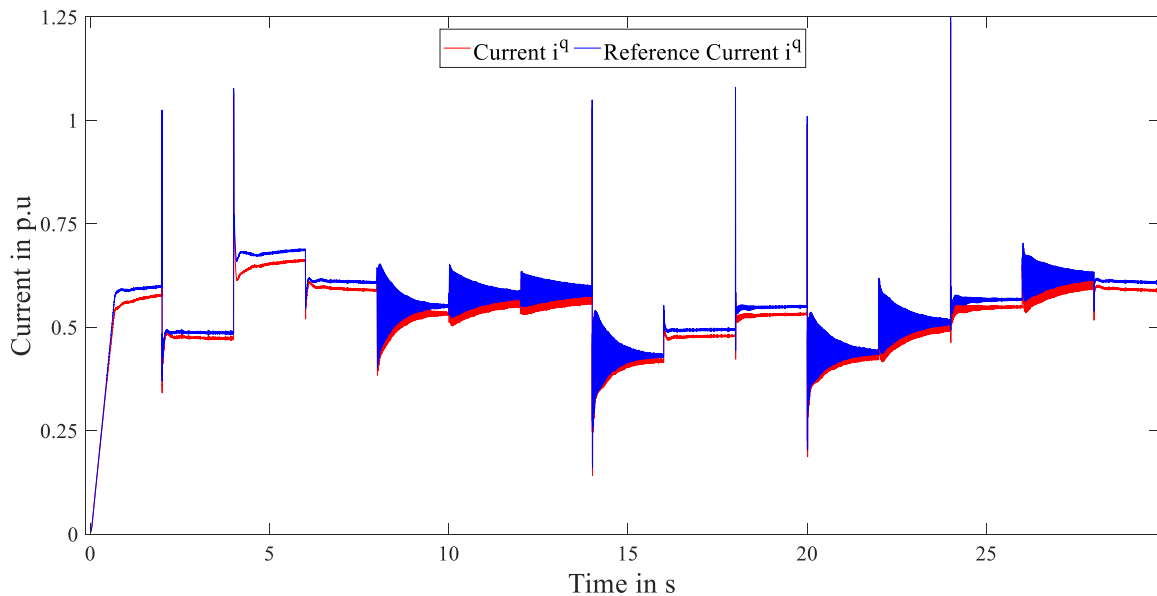


Figure 3.3: Current i^q for both state-space and reference models.

Thanks to the high current variations to which both models are submitted, it can be said that the state-space model follows the reference model even during harsh events. In addition, these different events, high peaks and oscillations of currents, will permit to observe the different controllers reactions to high variations on the references.

Concerning the current i^q on Figure 3.3, it can be noted an offset of -5 % between the state-space and the reference model. This i^q offset in steady-state will be removed with the closed-loop system thanks to the addition of a feedback in the controller.

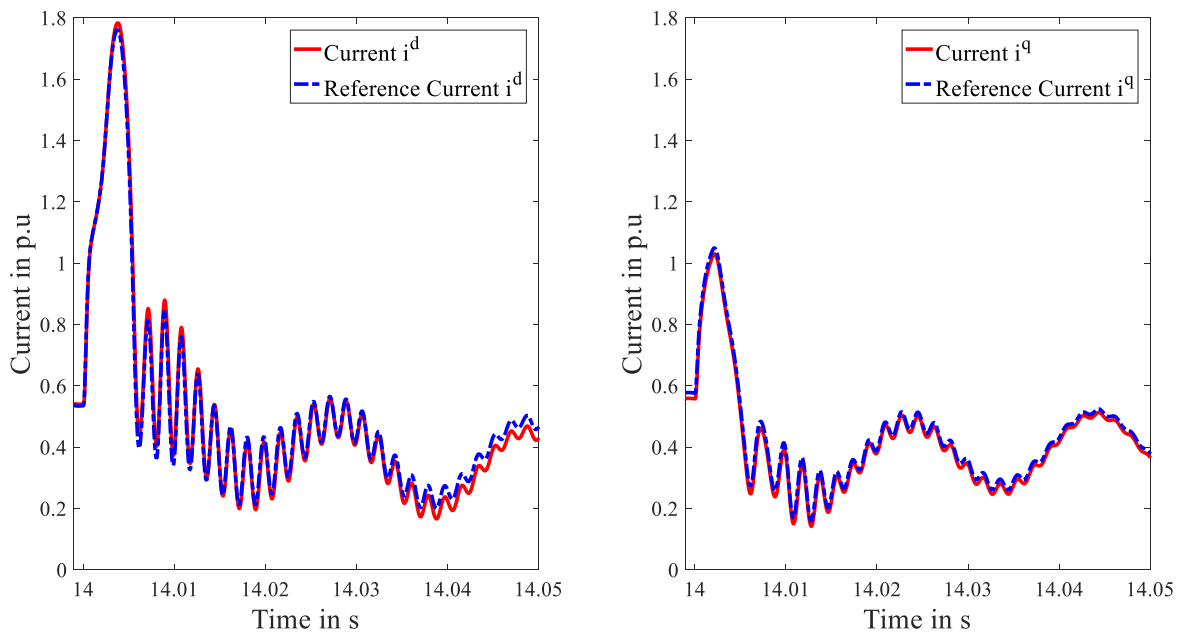


Figure 3.4: Zoom on currents i^d and i^q during a load impact for state-space and reference models.

Figure 3.2, Figure 3.3 and Figure 3.4 validate the state-space model and hypothesis that ω_r could be considered fixed and equal to 1 p.u. as the velocity used for the reference varies as it can be seen in Appendix 2 (p163).

To conclude, as the state-space model has been validated, it's possible to build, simulate and integrate different controllers based on this model for the VSG.

3.3 Simple PI Controller as the current controller of VSG

In the VSG model described in [23], the current controller implemented was a PI controller. The current controller has to force the inverter output current i_L^d and i_L^q to follow the SM model currents i^d and i^q by giving the duty ratios of the inverter.

In this section, the analytic PI controller model is described based on the previous state-space model that have been validated. Then, this PI controller model is tested on one scenario thanks to the state-space equations. Finally, this controller will be integrated in the VSG control for the final validation and some basic but necessary tests.

3.3.1 PI controller analytic model

As the PI controller forces the inverter to follow the SM model currents i^d and i^q , a new variable ε is defined. The new variable ε output is defined as the difference between the inverter's currents, i_L^d and i_L^q , compared to the synchronous machine's currents i^d and i^q . Hence, the variable, $\varepsilon \in \mathbb{M}_{2,1}$ is defined as follows:

$$\begin{aligned} \varepsilon &= \begin{bmatrix} i^d - i_L^d \\ i^q - i_L^q \end{bmatrix} = (C_{SYS}^s - [\mathbb{O}_{2,5} \quad \mathbb{I}_2 \quad \mathbb{O}_{2,4}]) \cdot X_{SYS} \\ \varepsilon &= C_\varepsilon \cdot X_{SYS} \end{aligned} \quad eq \ 3.8$$

With $C_\varepsilon = (C_{SYS}^s - [\mathbb{O}_{2,5} \quad \mathbb{I}_2 \quad \mathbb{O}_{2,4}])$, $C_\varepsilon \in \mathbb{M}_{2,11}$, the model is now defined by:

$$\begin{aligned} \dot{X}_{SYS} &= A_{SYS} \cdot X_{SYS} + B_{SYS} \cdot U_{SYS} + G_{SYS} \cdot W_{SYS} \\ \varepsilon &= C_\varepsilon^s \cdot X_{SYS} \end{aligned} \quad eq \ 3.9$$

The PI controller determines the inverter duty ratios that force the inverter currents to follow the SM currents. The link between the inverter voltage V_i^d and V_i^q and the inverter duty ratio α^d and α^q is given by the equations below:

$$\begin{aligned} \alpha^d &= \frac{2}{V_{dc}} \cdot V_i^d \\ \alpha^q &= \frac{2}{V_{dc}} \cdot V_i^q \end{aligned} \quad eq \ 3.10$$

The PI controller applies on the inverter voltage references V_i^{d*} and V_i^{q*} . So, the PI controller is characterised by equations:

$$\begin{bmatrix} V_i^{d*} \\ V_i^{q*} \end{bmatrix} = K_p \cdot \varepsilon + K_i \cdot \varepsilon_{PI} \quad eq \ 3.11$$

Noting the impact of the PI controller on the inverter outputs voltages, the inverter voltage is determined by the equation in dq-axis and p.u:

$$\begin{aligned} V_i^d &= e^d + V_i^{d*} \\ V_i^q &= e^q + V_i^{q*} \end{aligned} \quad eq \ 3.12$$

Considering that the variable ε_{PI} , $\varepsilon_{PI} \in \mathbb{M}_{2,1}$, is defined by the equation:

$$\dot{\varepsilon}_{PI} = \varepsilon \quad eq \ 3.13$$

Thank to eq 3.12 and eq 3.11, the inverter voltage in dq-axis and p.u. is defined by the equation:

$$\begin{bmatrix} V_i^d \\ V_i^q \end{bmatrix} = \begin{bmatrix} e^d \\ e^q \end{bmatrix} + K_p \cdot \varepsilon + K_i \cdot \varepsilon_{PI} \quad \text{eq 3.14}$$

with $K_p \in \mathbb{M}_{2,2}$ and $K_i \in \mathbb{M}_{2,2}$.

Hence, with eq 3.12 and eq 3.4, the inverter currents equations are determined by:

$$\begin{bmatrix} \dot{i}_L^d \\ \dot{i}_L^q \end{bmatrix} = \omega_{base} \cdot \begin{bmatrix} -\frac{R_L}{L_L} & \omega_r \\ -\omega_r & -\frac{R_L}{L_L} \end{bmatrix} \cdot \begin{bmatrix} i_L^d \\ i_L^q \end{bmatrix} + \omega_{base} \cdot \begin{bmatrix} \frac{1}{L_L} & 0 \\ 0 & \frac{1}{L_L} \end{bmatrix} \cdot \begin{bmatrix} V_i^{d*} \\ V_i^{q*} \end{bmatrix} \quad \text{eq 3.15}$$

with eq 3.14, the inverter current is determined by the equations:

$$\begin{bmatrix} \dot{i}_L^d \\ \dot{i}_L^q \end{bmatrix} = \omega_{base} \cdot \left(\begin{bmatrix} -\frac{R_L}{L_L} & \omega_r \\ -\omega_r & -\frac{R_L}{L_L} \end{bmatrix} \cdot \begin{bmatrix} i_L^d \\ i_L^q \end{bmatrix} + \begin{bmatrix} \frac{1}{L_L} & 0 \\ 0 & \frac{1}{L_L} \end{bmatrix} K_p \cdot \varepsilon + \begin{bmatrix} \frac{1}{L_L} & 0 \\ 0 & \frac{1}{L_L} \end{bmatrix} \cdot K_i \cdot \varepsilon_{PI} \right) \quad \text{eq 3.16}$$

As the variable ε is defined in eq 3.8, it's possible to define the inverter current by:

$$\begin{bmatrix} i_L^d \\ i_L^q \end{bmatrix} = \begin{bmatrix} i^d \\ i^q \end{bmatrix} - \varepsilon \quad \text{eq 3.17}$$

replacing 1.14 in 1.13, the equation 1.13 around the steady-state regime is defined by

$$-\varepsilon = -\omega_{base} \cdot \left(\begin{bmatrix} -\frac{R_L}{L_L} & \omega_r \\ -\omega_r & -\frac{R_L}{L_L} \end{bmatrix} \cdot (-\varepsilon) + \begin{bmatrix} \frac{1}{L_L} & 0 \\ 0 & \frac{1}{L_L} \end{bmatrix} \cdot K_p \cdot \varepsilon + \begin{bmatrix} \frac{1}{L_L} & 0 \\ 0 & \frac{1}{L_L} \end{bmatrix} \cdot K_i \cdot \varepsilon_{PI} \right) \quad \text{eq 3.18}$$

$$\text{or, } \varepsilon = \omega_{base} \cdot \left(\begin{bmatrix} -\frac{R_L}{L_L} & \omega_r \\ -\omega_r & -\frac{R_L}{L_L} \end{bmatrix} - \begin{bmatrix} \frac{1}{L_L} & 0 \\ 0 & \frac{1}{L_L} \end{bmatrix} \cdot K_p \right) \cdot \varepsilon - \omega_{base} \cdot \begin{bmatrix} \frac{1}{L_L} & 0 \\ 0 & \frac{1}{L_L} \end{bmatrix} \cdot K_i \cdot \varepsilon_{PI} \quad \text{eq 3.19}$$

The matrix $K_p^{diag} \in \mathbb{M}_{2,2}$, is given by $\omega_{base} \cdot \left(\begin{bmatrix} -\frac{R_L}{L_L} & \omega_r \\ -\omega_r & -\frac{R_L}{L_L} \end{bmatrix} - \begin{bmatrix} \frac{1}{L_L} & 0 \\ 0 & \frac{1}{L_L} \end{bmatrix} K_p \right)$.

The matrix of coefficients K_p as function of K_p^{diag} is then given by:

$$K_p = \left(\omega_{base} \cdot \begin{bmatrix} \frac{1}{L_L} & 0 \\ 0 & \frac{1}{L_L} \end{bmatrix} \right)^{-1} \cdot \left(\omega_{base} \cdot \begin{bmatrix} -\frac{R_L}{L_L} & \omega_r \\ -\omega_r & -\frac{R_L}{L_L} \end{bmatrix} + K_p^{diag} \right) \quad \text{eq 3.20}$$

To conclude, the equations of the PI-controlled system are:

$$\begin{bmatrix} \dot{X}_{SYS} \\ \dot{\varepsilon}_{PI} \end{bmatrix} = \begin{bmatrix} A_{SYS} + B_{SYS} \cdot K_p \cdot C_\varepsilon & B_{SYS} \cdot K_i \\ K_p \cdot C_\varepsilon & \mathbb{O}_{2,2} \end{bmatrix} \cdot \begin{bmatrix} X_{SYS} \\ \varepsilon_{PI} \end{bmatrix} + \begin{bmatrix} G_{SYS} \\ \mathbb{O}_{2,3} \end{bmatrix} \cdot W_{SYS} \quad eq\ 3.21$$

with the model outputs:

$$\begin{bmatrix} V_i^d \\ V_i^q \end{bmatrix} = \left[\left(\left[\mathbb{O}_{2,7} \quad \mathbb{I}_2 \quad \mathbb{O}_{2,2} \right] + K_p \cdot C_\varepsilon \right) \quad K_i \right] \cdot \begin{bmatrix} X_{SYS} \\ \varepsilon_{PI} \end{bmatrix} \quad eq\ 3.22$$

$$\varepsilon = \left[K_p \cdot C_\varepsilon \quad \mathbb{O}_{2,2} \right]$$

3.3.2 Simulation of the closed loop under PI controller

The objective of this section is to determine and validate the parameters K_p^{diag} and K_i before the implementation in the entire VSG model in Simulink®. The PI controller parameters that have been implemented in the previous Schneider Electric VSG current controller are:

$$K_p^{diag} = \begin{bmatrix} 3500 & 0 \\ 0 & 3500 \end{bmatrix}.$$

$$K_i = \begin{bmatrix} 300 & 0 \\ 0 & 300 \end{bmatrix}.$$

The different figures below are simulated thanks to the model defined in eq 3.21 and eq 3.22 using the MATLAB® function “*lsim*” and considering the inputs reported in Appendix 2 (p163).

As the objective is to validate the design of the PI controller, only the references currents i^d and i^q and the controlled inverter currents i_L^d and i_L^q are showed. The other variables of the model are not relevant to show except the duty ratios α^d and α^q in order to check the feasibility of the controller. Indeed, the duty ratios of the inverter should not be greater than 1p.u. in order to avoid the saturation of the inverter. If the inverter duty ratios are saturated, it impacts the voltage e^d and e^q by creating overvoltages.

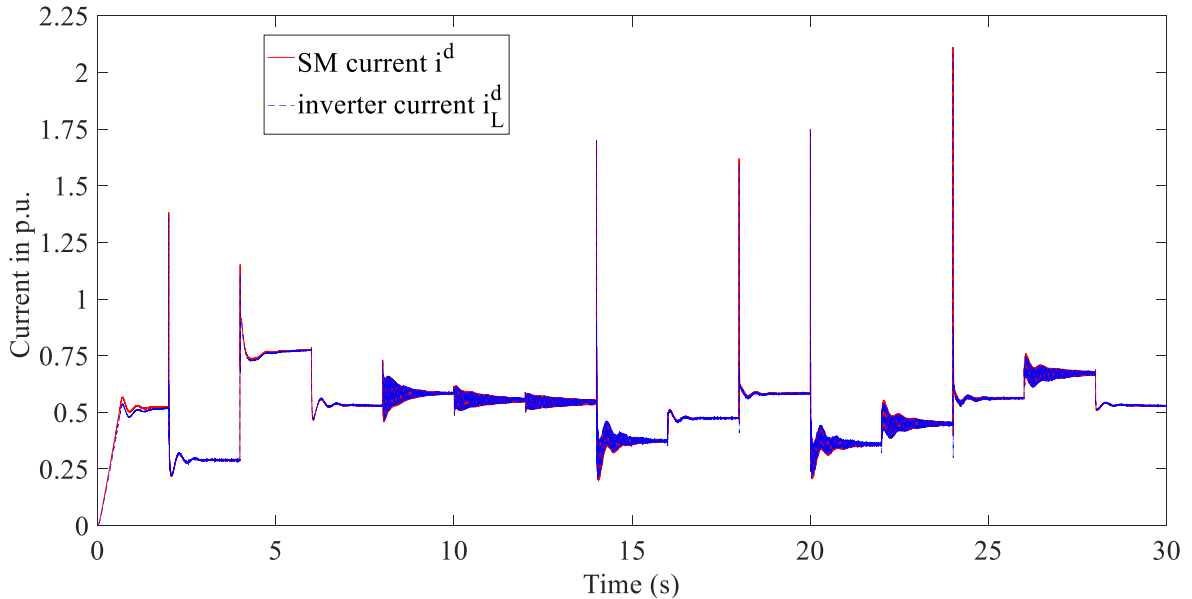


Figure 3.5: Inverter current i_L^d and the synchronous machine current i^d for PI controller.

Figure 3.5 and Figure 3.6 show that the output inverter's currents i_L^d and i_L^q follow the reference SM currents i^d and i^q with accuracy during the steady-state even during the high peaks of currents. It can be noted that during the steady-state, there is no offset between the inverter currents i_L^d and i_L^q and the reference i^d and i^q thanks to the integrator of the PI controller.

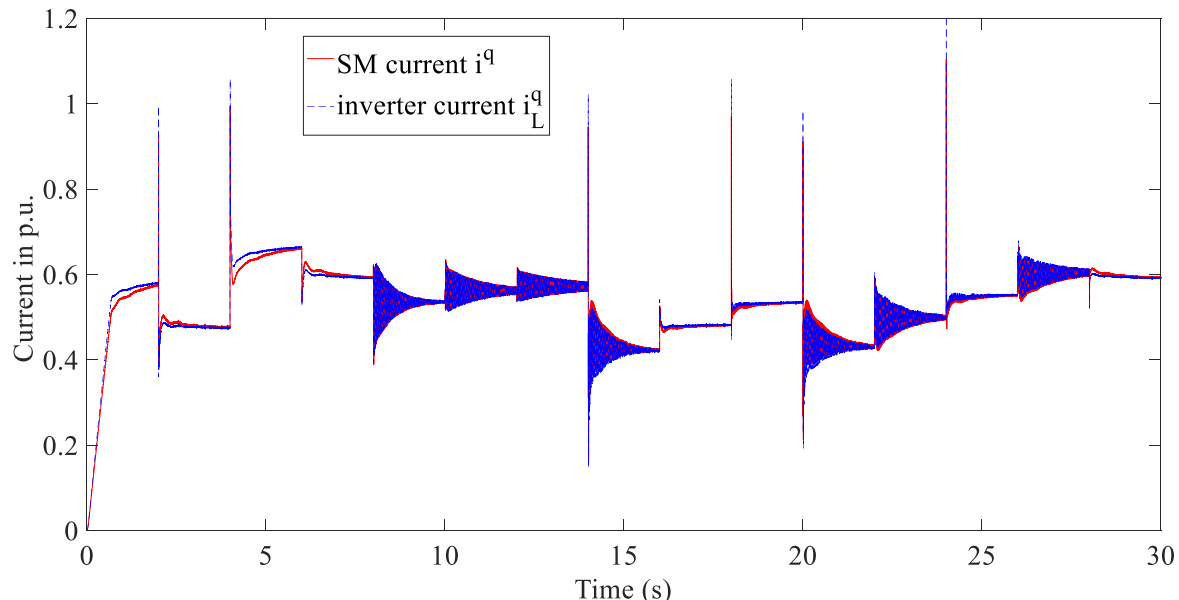


Figure 3.6: Inverter current i_L^q and the synchronous machine current i^q for PI controller.

Figure 3.7 shows that the PI controller can follow the references even if the references show high oscillations due to the application of a high inductive load at $t = 20$ s. It can be noted that the inverter currents follow the entire synchronous machine, even the high oscillations due to the inductive characteristics of the load as visible in Figure 3.7.

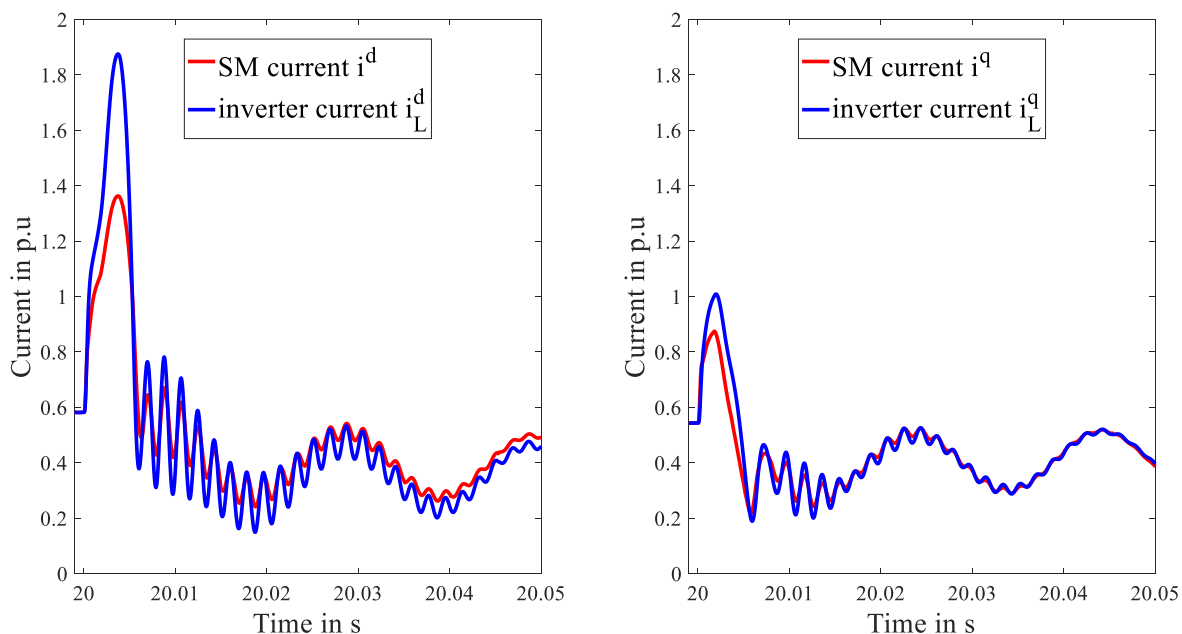


Figure 3.7: Zoom on currents i^d and i_L^d , and i^q and i_L^q during a load impact for PI controller.

Figure 3.8 and Figure 3.9, below, show that the duty ratios α^d and α^q determined by the PI control follow the reference duty ratios α^{d*} and α^{q*} required by the controller. Also, the duty ratios are in the range $[-1 ; 1]$ so the inverter's saturation is not reached with the PI controller solution.

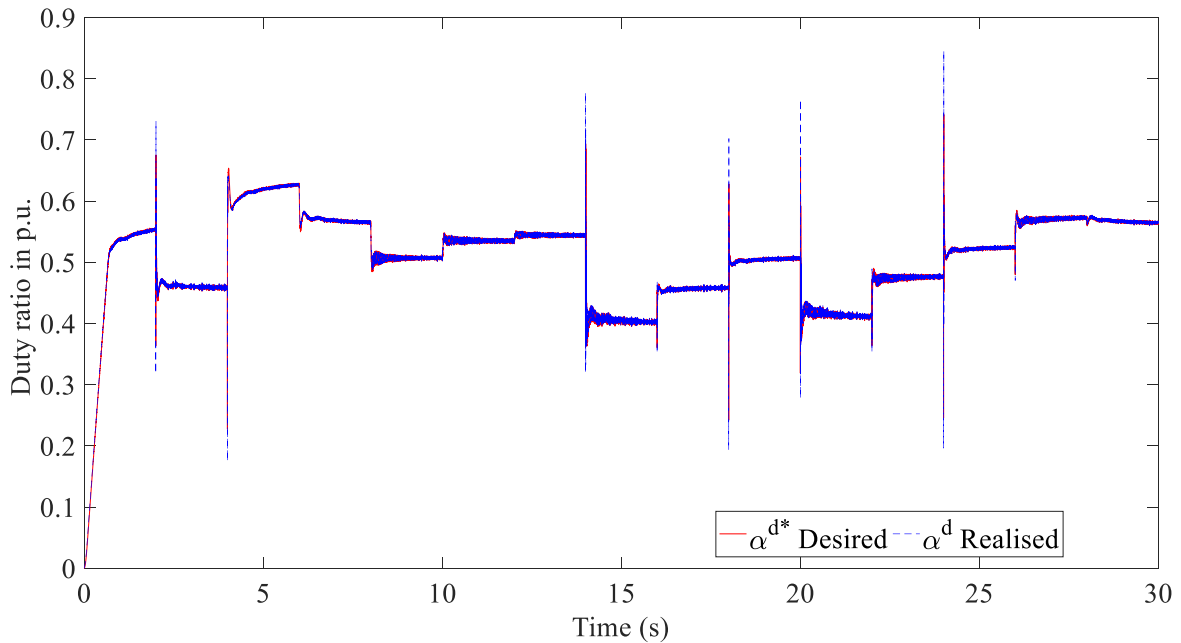


Figure 3.8: Duty ratio α^d compared to reference α^{d} for PI controller.*

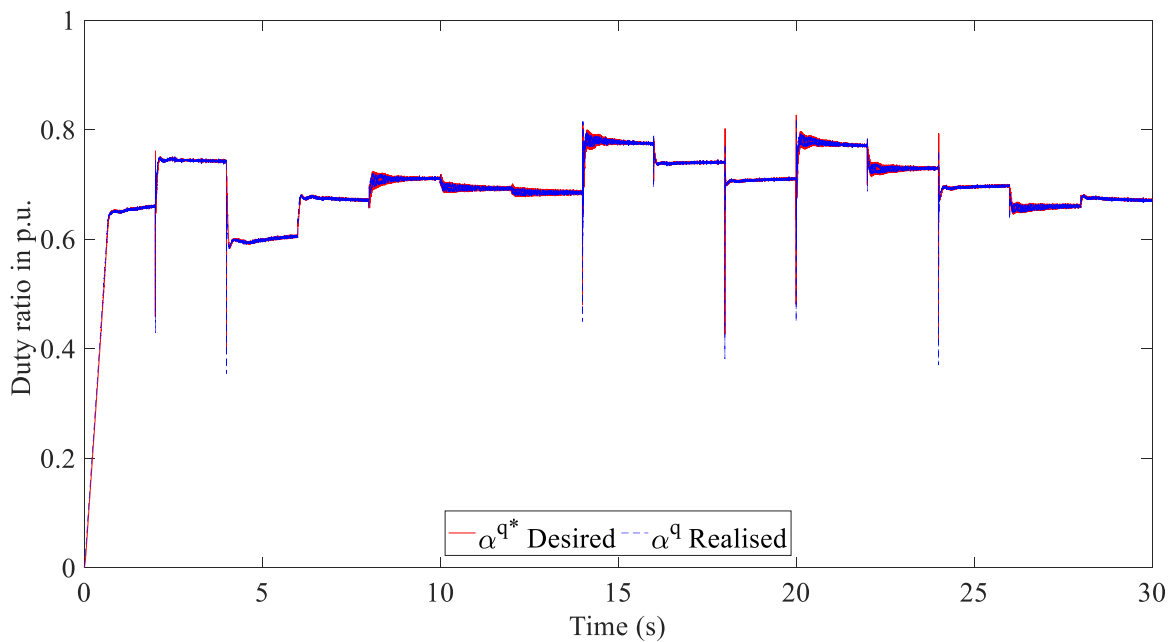


Figure 3.9: Duty ratio α^q compared to reference α^{q} for PI controller.*

3.3.3 Results with the PI controller integrated in the VSG control

The PI controller is added to the VSG control. The inverter used in the simulation of the VSG-based inverter is a 25 kVA, 400 V phase-phase nominal voltage for a nominal current of 36 A and a maximal output current of 60 A.

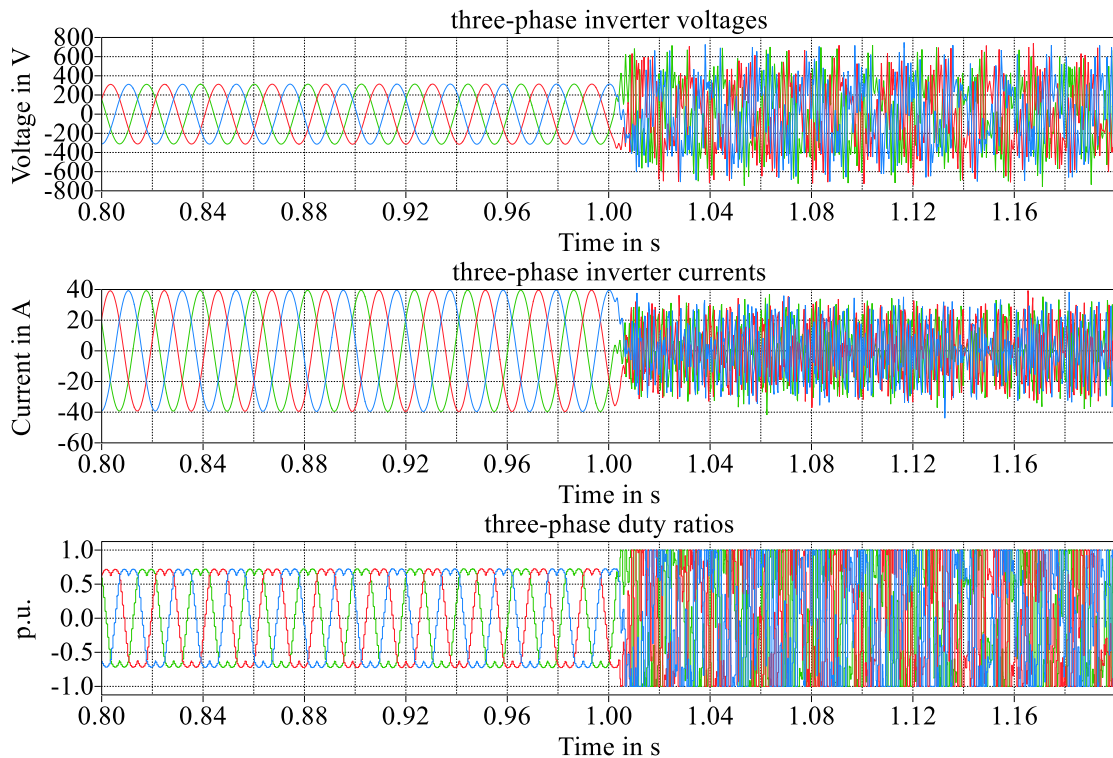


Figure 3.10: Inverter's three-phase voltages, currents and duty ratios for VSG controlled by PI Controller.

When integrated with the VSG control in closed loop, the PI controller is unstable during different tests, when the load is highly inductive or capacitive, and also during a load shedding as it can be seen in the Figure 3.10. On Figure 3.10, the VSG controlled by the PI controller is supplying a 20 kW load and at $t = 1$ s, the load is removed. Figure 3.10 shows that the PI controller integrated in the VSG is unstable when the VSG is off-loaded which is a major problem for the VSG development.

Other tests were also done on the VSG in closed-loop with the PI controller and these tests show that the system is unstable if the load is under 70 % of VSG active power or more than 30 % of VSG reactive power. Moreover, another test fail that can be noted is the short-circuit case. Indeed, during short-circuit, the inverter saturation is often reached. The problem is that even after the disappearance of the short-circuit, the closed loop PI controller behaviour cannot reach again a stable state.

The main problem with the closed-loop system with the PI controller is that control does not take into account phenomena that can destabilise the closed-loop system [28]:

- DC-current build-up with the controller feedback due to computation errors in the model or sensors errors;
- Super-synchronous oscillation due to the load characteristics such as a highly inductive load, an open-circuit VSG or a current-sink.

3.3.4 Conclusion on the PI controller for VSG

In this section, the previous controller used, a PI, for the VSG is presented, analytically detailed and validate in state-space. Then, the PI controller is implemented in the VSG, but the closed loop model is unstable even when the VSG is off-loaded.

In order to stabilize the closed loop PI controller, a common solution is the addition of some virtual impedances as described in [23] based on the methodology developed in [28]. However, these virtual impedances addition to the implemented system causes two main problems: an increasing complexity of the VSG model and a delicate tuning of the virtual impedances parameters requirement. In addition, the virtual impedances decrease the global performances of the VSG as they consume virtual active and reactive power. Consequently, due to these various disadvantages, the addition of virtual impedances was not selected as a solution to stabilize the closed-loop model of the VSG inverter.

The original solution developed in this thesis is the use of a state observer to determine the exogenous inputs' load characteristics to avoid the closed loop model instabilities. Therefore, in the following section, the state observer model will be analytically described and validated.

3.4 The original solution to improve the closed loop system stability: integration of a state observer

The addition of an observer has the advantages to possibly improve the VSG performances and avoids the inverter's saturation even during harsh event on the microgrid (example: short-time short-circuit) but also to simplify the VSG's implementation and increase the replicability on other kinds of inverters.

The objective of the observer is to reconstruct, based on the different available measurements, the load variations at the outputs of the inverter characterized by the grid output voltages V_g^d and V_g^q and the grid output currents i_g^d and i_g^q . These estimations enable to face the instability induced by highly inductive loads for example. Indeed, in these cases, oscillations and resonances above the lines frequency [28] might occur which destabilizes the controlled system. In addition, numerical instabilities induced by the high order of the SM models as demonstrated in [28], destabilizes the system. Indeed, DC leakage currents are created at the outputs of the inverter which then are fed to the controller which destabilizes the system within milli-seconds.

Even if the grid voltages are measured at the inputs of the VSG for its synchronisation with other power supplies connected to the microgrid, these measures are not considered for the determination of the grid voltage V_g . Indeed, since the entire controller will be implemented in the dq-axis, a PLL would be necessary in order to convert the abc-axis grid voltage V_g measure in dq-axis. As different studies developed in [56] and in [57], prove the decrease of the performance due to the use of the PLL implemented in the inverter controller, the implementation of a PLL for the controller is avoided regarding the grid voltage V_g .

3.4.1 Observer's analytic model description

As the SM and the AVR are virtual so, the fluxes, the SM currents and the voltage e_{fd} are available for the observer. In addition, the inverter output currents i_L^d and i_L^q , the voltages e_d and e_q are also measured by dedicated sensors. Hence, the outputs vector Y_{meas} considering all measurements, is defined by:

$$Y_{meas} = [i^d \quad i^q \quad \psi_d \quad \psi_q \quad \psi_{fd} \quad \psi_{1d} \quad \psi_{1q} \quad i_L^d \quad i_L^q \quad e^d \quad e^q \quad e_{fd}]^t, Y_{meas} \in \mathbb{M}_{12,1}$$

which can be written in the following form as a linear combination of state and inputs vectors:

$$Y_{meas} = C_{meas} \cdot X_{SYS} + H_{meas} \cdot W_{SYS}$$

$$C_{meas}^s = \begin{bmatrix} C_{SYS}^s \\ \mathbb{I}_9 & \mathbb{O}_{9,2} \\ \mathbb{O}_{1,11} \end{bmatrix} \text{ and } H_{meas} = \begin{bmatrix} \mathbb{O}_{11,3} \\ 0 & 0 & 1 \end{bmatrix}$$

with $C_{meas}^s \in \mathbb{M}_{12,11}$, $H_{meas} \in \mathbb{M}_{12,3}$ and as a reminder $W_{SYS} = \begin{bmatrix} e_{fd} \\ V_g^d \\ V_g^q \end{bmatrix}$, $W_{SYS} \in \mathbb{M}_{3,1}$.

In order to determine exogenous inputs W_{SYS} , W_{SYS} is considered as a constant during multiple periods. With this hypothesis, W_{SYS} is now defined as:

$$W_{SYS}^+ = W_{SYS} \quad eq \ 3.23$$

the model considered for designing the observer becomes:

$$\begin{aligned} \bar{X}_{obs}^+ &= \bar{A}_{obs}^s \cdot \bar{X}_{obs} + \bar{B}_{obs}^s \cdot U_{SYS} \\ Y_{meas} &= \bar{C}_{obs}^s \cdot \bar{X}_{obs} \end{aligned} \quad eq \ 3.24$$

where \bar{X}_{obs} denotes the extended system's state vector, namely $\bar{X}_{obs} = \begin{bmatrix} X_{SYS} \\ W_{SYS} \end{bmatrix}$, $\bar{X}_{obs} \in \mathbb{M}_{14,1}$, with the matrices of eq 1.21 defined below:

$$\bar{A}_{obs}^s = \begin{bmatrix} A_{SYS}^s & G_{SYS}^s \\ \mathbb{O}_{3,11} & \mathbb{I}_3 \end{bmatrix}, \quad \bar{B}_{obs}^s = \begin{bmatrix} B_{SYS}^s \\ \mathbb{O}_{3,2} \end{bmatrix} \quad \text{and} \quad \bar{C}_{obs}^s = [C_{meas}^s \quad H_{meas}^s].$$

With $\bar{A}_{obs}^s \in \mathbb{M}_{14,14}$, $\bar{B}_{obs}^s \in \mathbb{M}_{14,2}$ and $\bar{C}_{obs}^s \in \mathbb{M}_{12,14}$

Fortunately, the new extended model is observable with the SM model defined Chapter 2 (2.3.1.2 – p 12) and the inverter parameters defined in Table 3.1. Therefore, it is possible to compute a matrix gain L_{obs} of a linear state observer based on the methodologies described in [58]. More precisely: the model observer dynamics can be written as follows:

$$\begin{aligned} \hat{\bar{X}}_{obs}^+ &= (\bar{A}_{obs}^s - L_{obs} \cdot \bar{C}_{obs}^s) \cdot \hat{\bar{X}}_{obs} + \bar{B}_{obs}^s \cdot U_{SYS} + L_{obs} \cdot Y_{meas} \\ Y_{meas} &= \bar{C}_{obs}^s \cdot \hat{\bar{X}} \end{aligned} \quad eq \ 3.25$$

Note that $L_{obs}, L_{obs} \in \mathbb{M}_{12,12}$, can also be defined as:

$$L_{obs} = \begin{bmatrix} L_X^X & L_W^X \\ L_X^W & L_W^W \end{bmatrix} \quad eq \ 3.26$$

3.4.2 Closed loop observer simulations

L_{obs} is designed with the function MATLAB® “*dlqr*”. Note that the transposed matrix of M is defined as M^t in the definition of L_{obs} :

$$L_{obs} = dlqr(\bar{A}_{obs}^s, \bar{C}_{obs}^s, Q_{obs}, R_{obs})^t \text{ with } Q_{obs} = 10^{12} \cdot \mathbb{I}_{12} \text{ and } R_{obs} = \mathbb{I}_{12}$$

The different figures below are obtained thanks to the observer model defined in eq 3.25 and the MATLAB® function “*dlsim*” with the inputs that can be find in Appendix 2 (p163).s

The three figures below, from Figure 3.11 to Figure 3.13, show that the observer determines with accuracy the simulated perturbations.

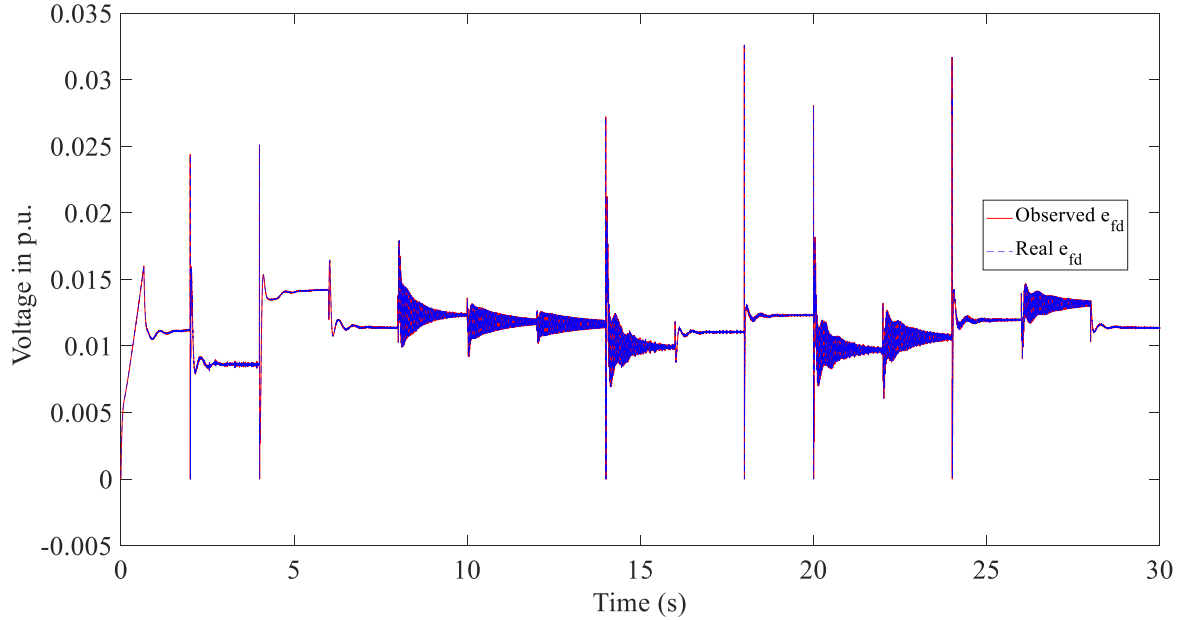


Figure 3.11: Voltage \hat{e}_{fd} compared to e_{fd} .

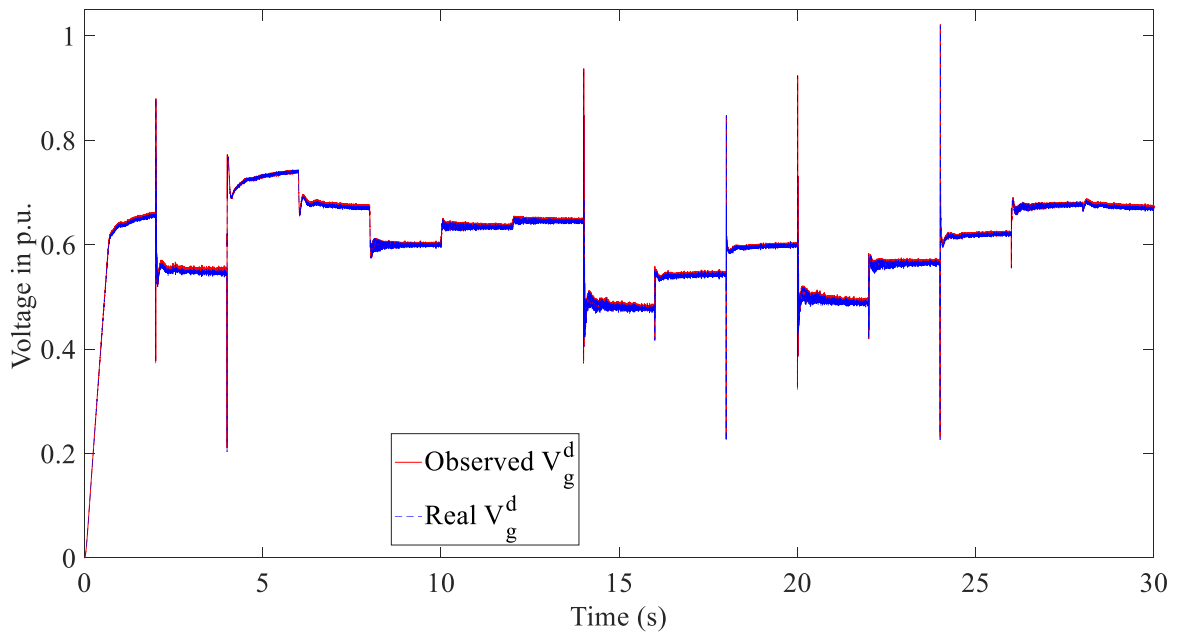


Figure 3.12: Voltage \hat{V}_g^d compared to V_g^d .

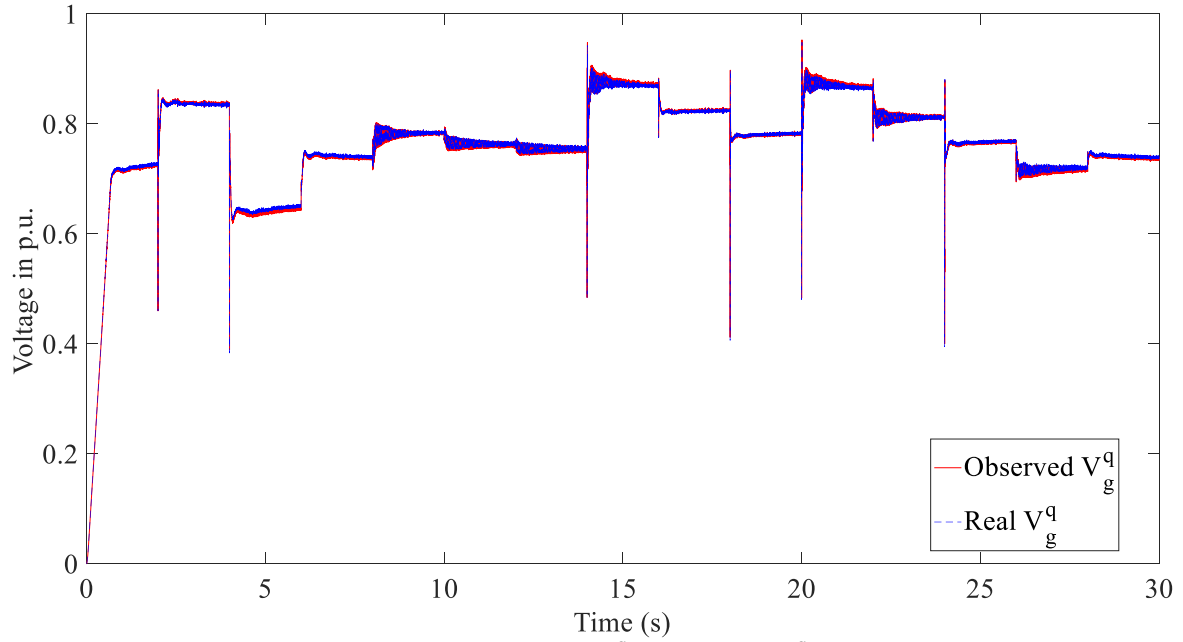


Figure 3.13: Voltage \hat{V}_g^q compared to V_g^q .

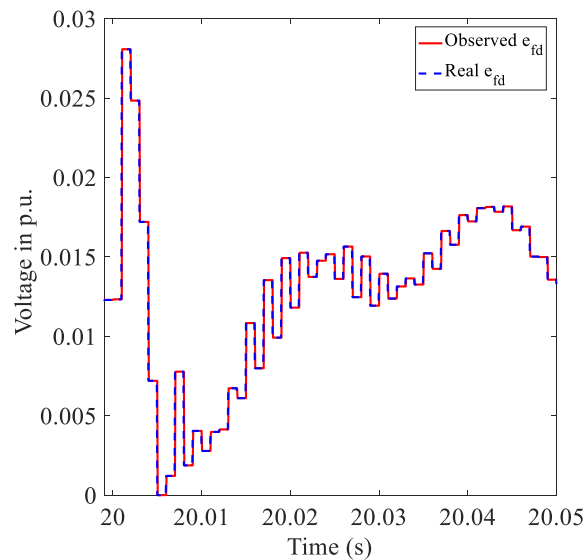


Figure 3.14: Zoom on the voltages \hat{e}_{fd} compared to e_{fd} .

It can be noted that the observer follows efficiently the voltage e_{fd} during the impact of load as depicted in Figure 3.14. Indeed, voltage e_{fd} have a slower dynamic and is sampling at a frequency of 1 kHz, imposed by the VSG controller itself for the voltage stability, rather than the grid voltage V_g^d and V_g^q . The grid voltages are measured at 20 kHz from different sensors. Even with a high variation as it is shown in Figure 3.15, the observer follows with high precision both voltages V_g^d and V_g^q .

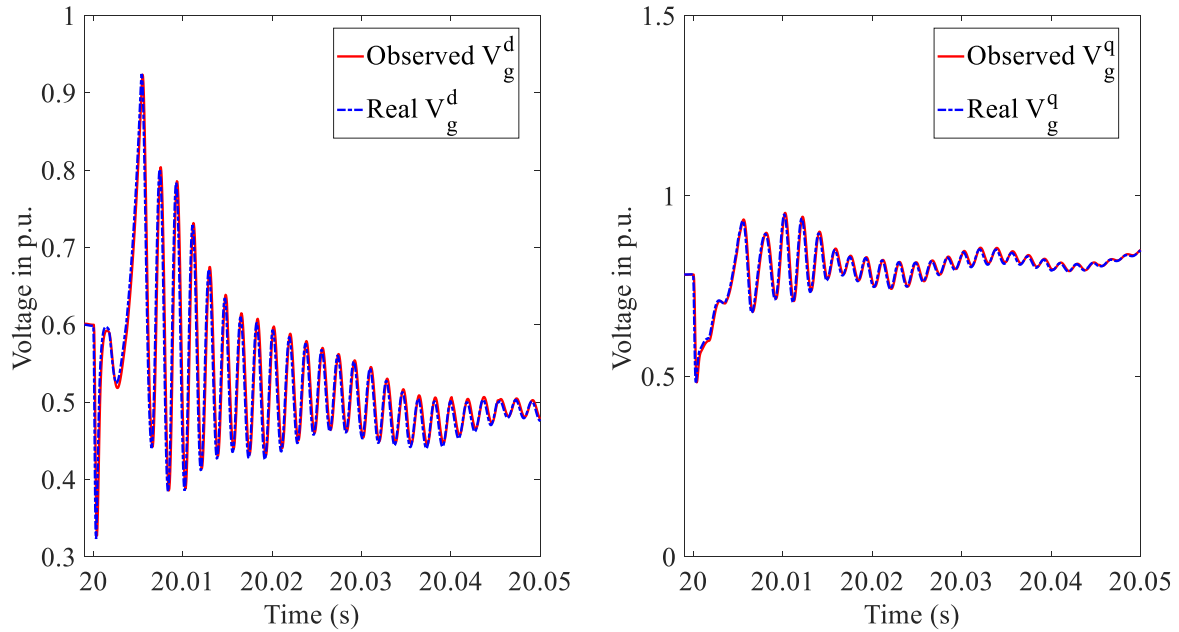


Figure 3.15: Zoom on both voltages \hat{V}_g^d and \hat{V}_g^q compared to V_g^d and V_g^q .

3.4.3 Conclusion on the observer

In section 3.4.1 is described the observer model that will be added to the current controller in order to avoid the instability of the closed loop PI controller as show in 3.3.3. The section 3.4.2, Figure 3.11 to Figure 3.13, validates the analytic model and the parameters of the observer.

The next step is the implementation of this observer together with the previous controller to check the impact of the observer on the closed loop model stability.

3.5 Combined observer and PI controller for VSG current regulation

In this section, the combination PI controller with the state observer is studied. First of all, the analytic model is described. Then, the closed loop system PI and observer is validated with the same input used before and that can be found in Appendix 2 (p163). Finally, to conclude on the advantage of the integration of the observer, the controller PI and observer is implemented in the VSG control in closed loop.

3.5.1 PI controller and state observer analytic model

To improve the performance of the PI controller, an observer is added to the PI controller. The state-space vector is extended to include the state ε_{PI} of the PI controller. So, the controlled states of this system are defined by the equations:

$$U_{SYS} = \begin{bmatrix} \hat{e}_d \\ \hat{e}_q \end{bmatrix} + [K_p \cdot C_\varepsilon \quad \mathbb{O}_{2,3} \quad K_i] \cdot \begin{bmatrix} \hat{X} \\ \hat{\varepsilon}_{PI} \end{bmatrix} \quad eq \ 3.27$$

Combining the state-space system, eq 3.7, with the PI controller equations, eq 3.21 and eq 3.27, converted in discrete state-space and in including the state observer determined in eq 3.25, the PI controller and observer equations are:

$$\begin{bmatrix} \hat{X} \\ \hat{\epsilon}_{PI} \end{bmatrix}^+ = \left(\begin{bmatrix} (\bar{A}_{obs}^s - L_{obs} \cdot \bar{C}_{obs}^s) & \bar{B}_{obs}^s \cdot K_i \\ K_p \cdot C_\epsilon & \mathbb{I}_2 \end{bmatrix} \right) \cdot \begin{bmatrix} \hat{X} \\ \hat{\epsilon}_{PI} \end{bmatrix} + \begin{bmatrix} L_{obs} \\ \mathbb{O}_{2,2} \end{bmatrix} \cdot Y_{meas} \quad eq \ 3.28$$

with the PI controller and observer outputs:

$$\begin{aligned} \epsilon &= [C_\epsilon \quad \mathbb{O}_{2,3} \quad \mathbb{O}_{2,2}] \cdot \begin{bmatrix} \hat{X} \\ \hat{\epsilon}_{PI} \end{bmatrix} \\ U_{SYS} &= [[\mathbb{O}_{2,7} \quad \mathbb{I}_2 \quad \mathbb{O}_{2,2}] + K_p \cdot C_\epsilon \quad \mathbb{O}_{2,3} \quad K_i] \cdot \begin{bmatrix} \hat{X} \\ \hat{\epsilon}_{PI} \end{bmatrix} \\ Y_{meas} &= [\bar{C}_{obs}^s \quad \mathbb{O}_{2,2}] \cdot \begin{bmatrix} \hat{X} \\ \hat{\epsilon}_{PI} \end{bmatrix} \end{aligned} \quad eq \ 3.29$$

3.5.2 Simulations of PI controller and state observer

For the PI Controller with observer validation, the same parameters as before are used:

$$\begin{aligned} K_p^{diag} &= \begin{bmatrix} 3500 & 0 \\ 0 & 3500 \end{bmatrix} \\ K_i &= \begin{bmatrix} 300 & 0 \\ 0 & 300 \end{bmatrix} \end{aligned}$$

similarly concerning the observer:

$$L_{obs} = dlqr(\bar{A}_{obs}^s, \bar{C}_{obs}^s, Q_{obs}, R_{obs})^t \text{ with } Q_{obs} = 10^{12} \cdot \mathbb{I}_{12} \text{ and } R_{obs} = \mathbb{I}_{12}$$

Similar to the study on the PI controller, only the output currents i_L^d and the i_L^q are compared to their references, the SM model i^d and i^q . In addition, the duty ratios are visible in Figure 3.19 and Figure 3.20 to identify the possible system's saturation. The results of the observed states of the system can be seen in Appendix 4 (p169). According to Figure 3.16 and Figure 3.17, the inverter's currents i_L^d and the i_L^q follow the SM current i^d and i^q after stabilisation of the reference signal.

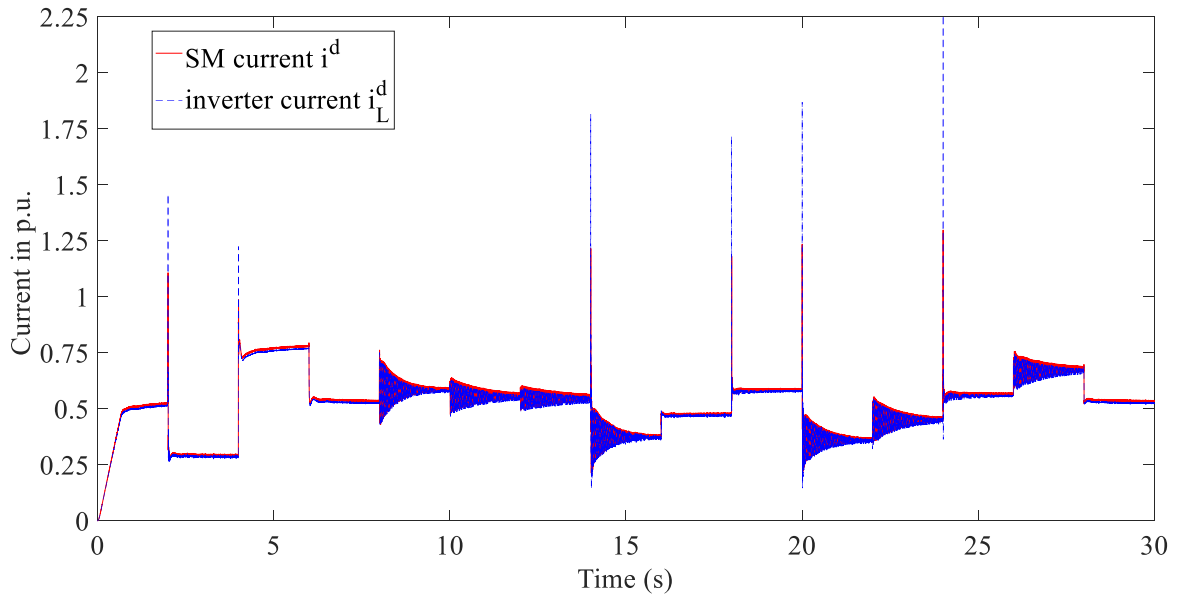


Figure 3.16: Inverter current i_L^d compared to synchronous machine current i^d .

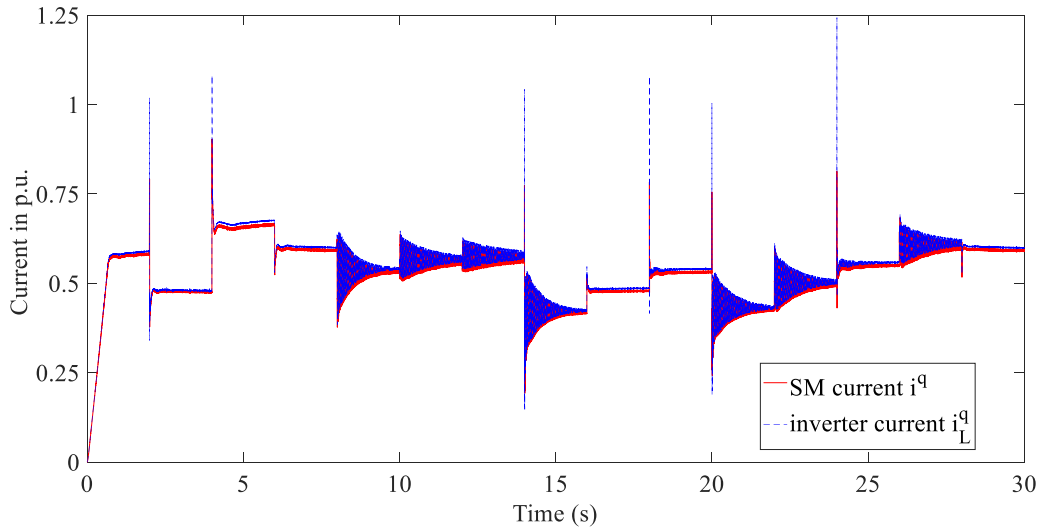


Figure 3.17: Inverter current i_L^q compared to synchronous machine current i^q .

With the observer, the impacts and high oscillation of the current references are smooth which helps avoiding the destabilisation of the system. The differences could be due to the dynamic of the observer which increases the time response of the controlled system due to its dynamic response.

The main form of the current references, i^d and i^q are kept, the peak oscillations are reduced by half. The fact that PI controller and observer does not follow the peak of current as it can be seen in Figure 3.16, Figure 3.17 and Figure 3.18 at time equal 20s, is certainly due to the delay induced by the observer. However, as an inverter can't follow the same output currents of a real synchronous machine, the fact that the PI controller and observer system minimizes the high current peaks is an advantage. Indeed, the emulated SM currents have to be saturated to avoid the deterioration of the inverter in this case.

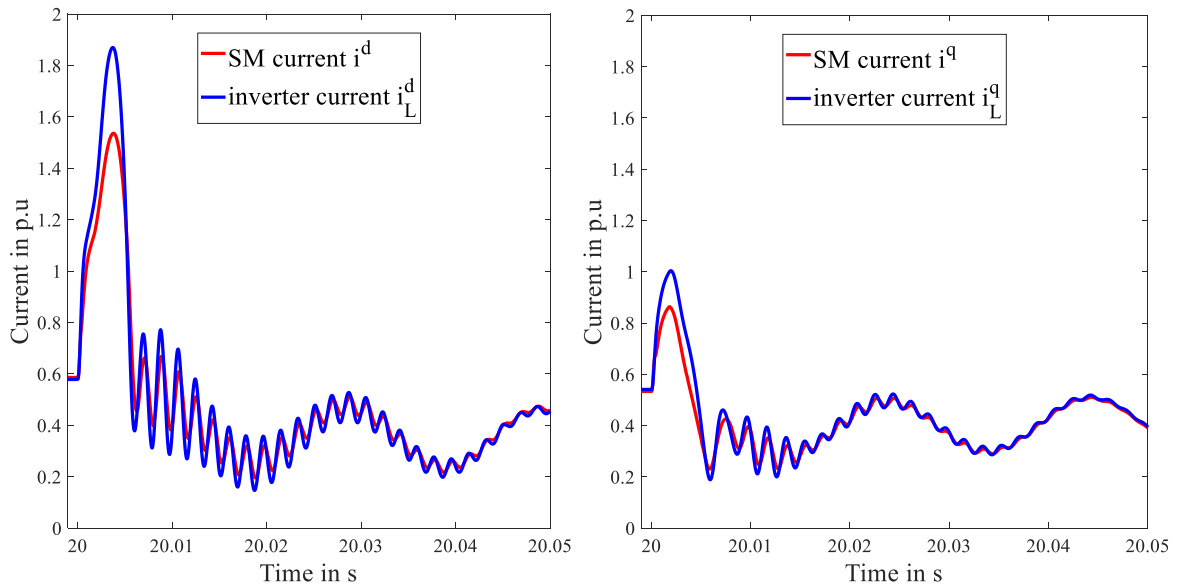


Figure 3.18: Zoom on currents i^d and i_L^d , and i^q and i_L^q during a load impact for PI controller and observer.

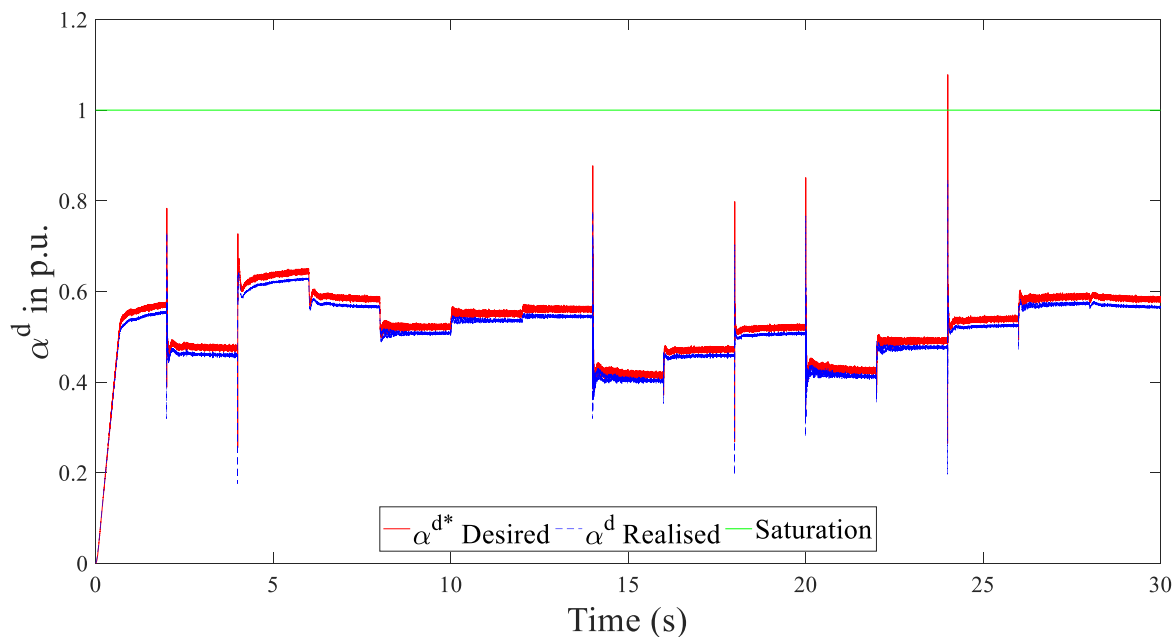


Figure 3.19: Duty ratio α^d compared to reference α^{d*} for PI controller and observer.

Figure 3.19 and Figure 3.20 show that the duty ratios α_d and α_q determined by the PI controller with observer follow the reference duty ratio α_d and α_q calculated before. Also, the duty ratios are in its limits of $[-1 ; 1]$ with one exception.

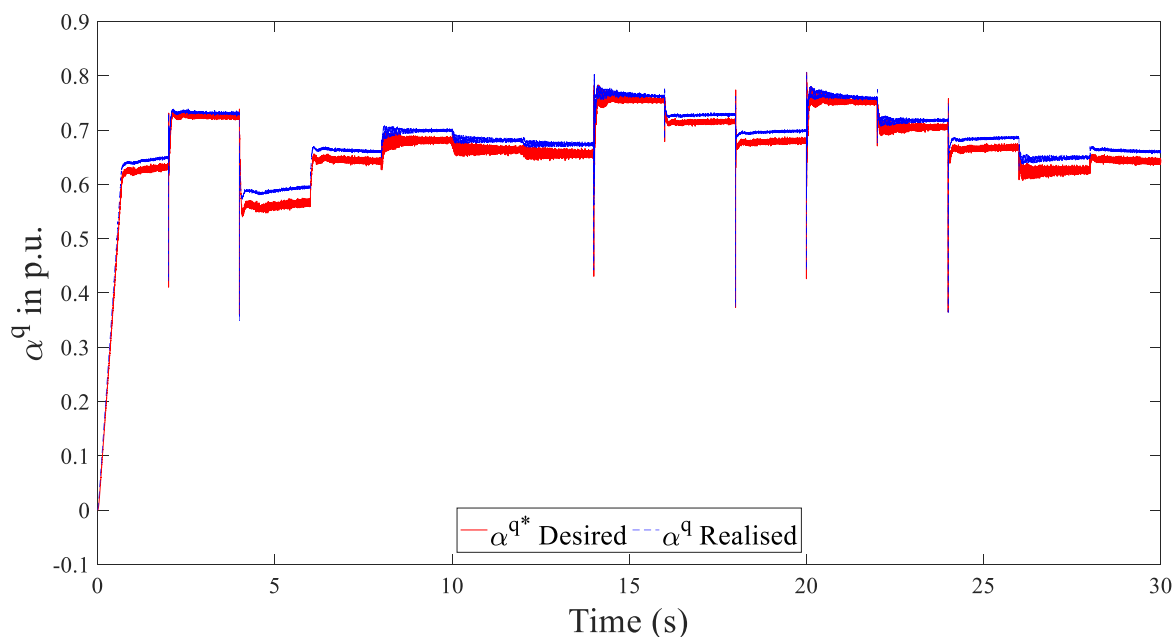


Figure 3.20: Duty ratio α^q compared to reference α^{q*} for PI controller and observer.

3.5.3 PI controller and state observer integrated in the VSG control

Similarly, to the PI controller alone in 3.3.3, the PI controller and observer is integrated in the VSG control in closed loop. The same inverter as in 3.3.3 (p51) is used, a 25 kVA, 400 V phase-phase nominal voltage for a nominal current of 36 A and a maximal output current of 60 A. the same inverter used, a.

On Figure 3.21, the VSG controlled by the PI controller and state observer is supplying a 20 kW load and at $t = 1$ s, the load is removed.

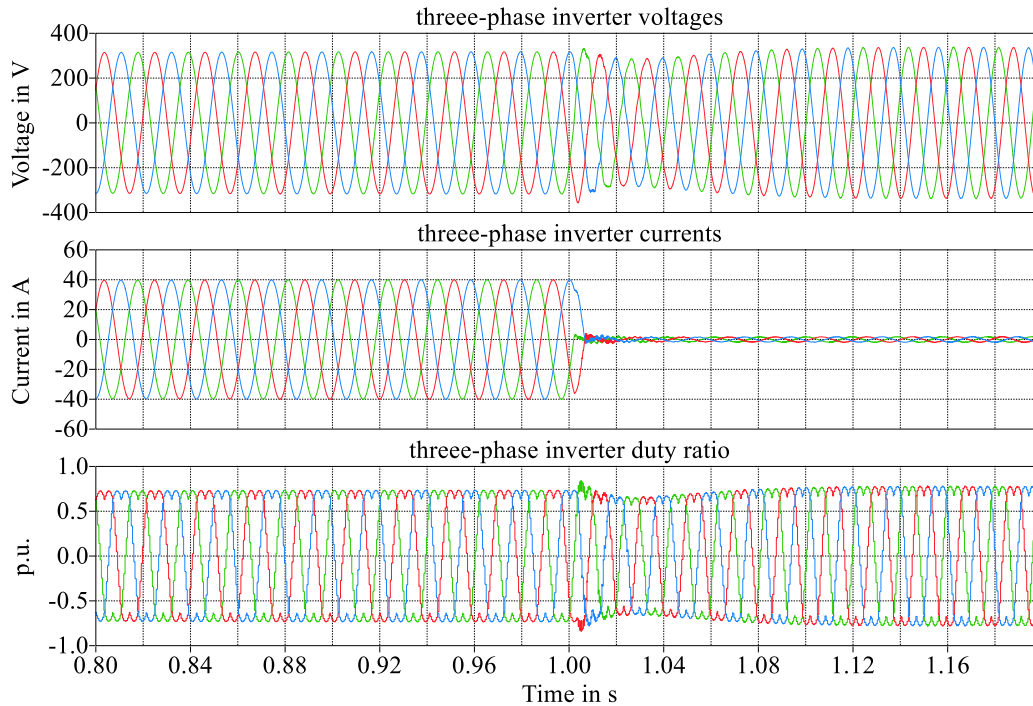


Figure 3.21: Inverter's three-phase voltages, currents and duty ratios for PI controller and an observer.

Figure 3.21 represents the three-phase currents, voltages and duty ratios of the VSG control with the controller based on PI and a state observer. Comparing Figure 3.21 and Figure 3.10, the observer clearly stabilizes the system when submitted to this harsh event.

However, Figure 3.22 shows the three-phase output currents from the VSG controlled by the observer and PI, show that thanks to the observer, the system remains stable, but the three-phase output current is oscillating due to the PI controller under off-loading.

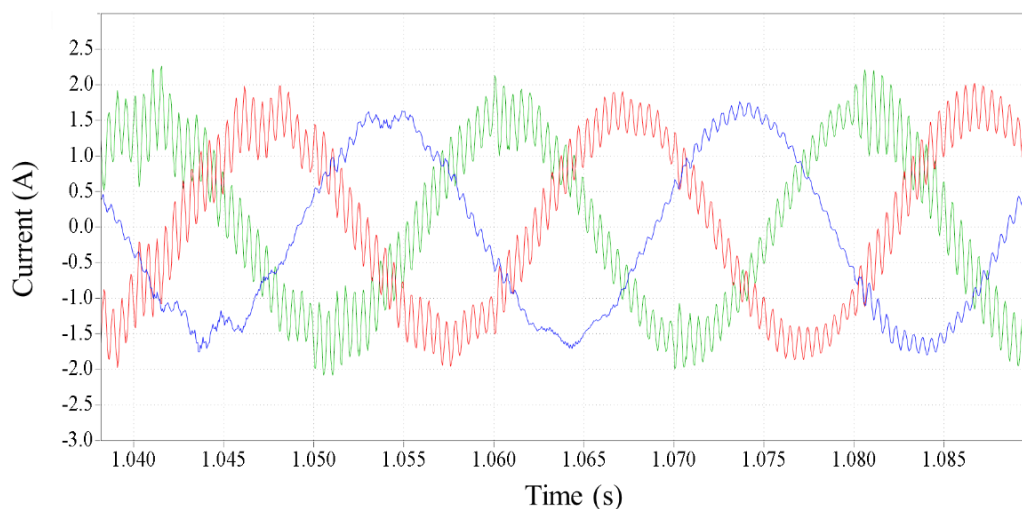


Figure 3.22: off-loaded VSG three-phase inverter's current for PI controller and an observer.

3.5.4 Conclusion on PI controller and observer

With this section, it is possible to say that, as the virtual impedance proposed in [28], the observer permit to avoid the destabilization of the closed loop system under the PI controller. PI controller and observer assure that the inverter output currents i_L^d and i_L^q correctly follow the SM currents i^d and i^q .

However, even if the observer showed improvement when integrated in the VSG, the simple test above shows that the PI controller may not be the most optimized controller for the VSG in closed loop.

3.6 The proposed controller: LQR controller with an integrator and a state observer

As detailed above, even with the addition of a state observer, the PI controller regulation of the inverter output currents is still not satisfactory. As detailed before, many other solutions have also been investigated in literature such as traditional solutions based on Proportional+Resonant controller [52], [53] to avoid the addition of virtual impedances. Also, more complex solutions have been tested such as a robust H_∞ method [54], fuzzy control [55] to cite but some alternatives.

However, none of these controllers cited above have been implemented in a real industrial inverter. Indeed, the fact that the VSG has to be implemented in an industrial inverter brings limits on the controller selection:

- The industrial inverter is limited in terms of memory size and computation capacity.
- Discretisation of the controller at different frequency.
- Simplicity of realisation to increase the portability of the solution.

Hence, the proposed controller is based on a LQR (Linear Quadratic Regulator) with an integrator and a state observer taking into account the different limitations cited above. The proposed controller is directly discretised to ensure the proposed controller implementation feasibility in the industrial inverter.

The proposed controller for VSG is first analytically detailed, and then the proposed controller is implemented in the VSG simulation for final validation similarly to what have been done for the PI controller or PI and observer controller.

3.6.1 LQR with an integrator controller and observer analytic model

In this section, the proposed controller for VSG is detailed: the analytic model considering the integrator section, the adaptation of the output variables depending on the input of the system and finally the LQR current controller.

3.6.1.1 Integrator analytic description

Let us first introduce the integrator that enables to recover long range errors on the steady state that might occur due to modelling errors. Similarly to the PI controller, the integrator is defined as the difference between the inverter's currents, i_L^d and i_L^q , and the synchronous machine's currents i_d and i_q . Hence, the same model described in eq 3.9 as the PI controller is used as reference for our proposed controller.

As a remainder, the state-space model defined in eq 3.9 is:

$$\begin{aligned} X_{SYS}^+ &= A_{SYS}^s \cdot X_{SYS} + B_{SYS}^s \cdot U_{SYS} + G_{SYS}^s \cdot W_{SYS} \\ \varepsilon^s &= C_\varepsilon^s \cdot X_{SYS} \end{aligned}$$

Therefore, in order to ensure disturbance rejection, an integrator state $\varepsilon_{int} \in \mathbb{M}_{2,1}$, is added to the current controller with the following dynamics:

$$\varepsilon_{int}^+ = \begin{bmatrix} \varepsilon_{int}^d \\ \varepsilon_{int}^q \end{bmatrix}^+ = \begin{bmatrix} \varepsilon_{int}^d \\ \varepsilon_{int}^q \end{bmatrix} + \varepsilon \quad \text{eq 3.30}$$

Considering the extended state \bar{X}_{SYS} that is obtained by including ε_{int} , so $\bar{X}_{SYS} = \begin{bmatrix} X_{SYS} \\ \varepsilon_{int} \end{bmatrix}$, the matrix C_ε^s , the model becomes:

$$\begin{aligned} \bar{X}_{SYS} &= \bar{A}_{SYS}^s \cdot \bar{X}_{SYS} + \bar{B}_{SYS}^s \cdot \bar{U}_{SYS} + \bar{G}_{SYS}^s \cdot W_{SYS} \\ \varepsilon &= \bar{C}_\varepsilon^s \cdot \bar{X}_{SYS} \end{aligned} \quad \text{eq 3.31}$$

$$\text{With } \bar{A}_{SYS} = \begin{bmatrix} A_{SYS}^s & \mathbb{O}_{11,2} \\ C_\varepsilon^s & \mathbb{I}_2 \end{bmatrix}, \bar{B}_{SYS} = \begin{bmatrix} B_{SYS}^s \\ \mathbb{O}_{2,2} \end{bmatrix}, \bar{G}_{SYS} = \begin{bmatrix} G_{SYS}^s \\ \mathbb{O}_{2,2} \end{bmatrix} \text{ and } \bar{C}_\varepsilon^s = [C_\varepsilon^s \quad \mathbb{O}_{2,2}].$$

Hence, $\bar{A}_{SYS} \in \mathbb{M}_{13,13}$; $\bar{B}_{SYS} \in \mathbb{M}_{13,2}$; $\bar{G}_{SYS} \in \mathbb{M}_{13,3}$ and $\bar{C}_\varepsilon^s \in \mathbb{M}_{2,13}$.

Once the integrator introduced, the reference values for the controller system have to be defined. This is detailed in the following section.

3.6.1.2 Reference values

In stationary regime, as the value of ε should be minimized, the reference value of $\varepsilon^* = \mathbb{O}_{2,1}$ for an imposed load W_{SYS} is used. In stationary regime, $\bar{X}_{SYS}^{*+} = \bar{X}_{SYS}^*$ and $\varepsilon^* = \mathbb{O}_{2,1} = C_\varepsilon^s \cdot \bar{X}_{SYS}^*$. So, it's possible to define eq 3.31 in stationary regime as:

$$\begin{bmatrix} \bar{G}_{SYS}^s \cdot W_{SYS} \\ \varepsilon^* \end{bmatrix} = \begin{bmatrix} (\mathbb{I}_{13} - \bar{A}_{SYS}^s) & -\bar{B}_{SYS}^s \\ C_\varepsilon^s & \mathbb{O}_{2,2} \end{bmatrix} \cdot \begin{bmatrix} \bar{X}_{SYS}^* \\ U_{SYS}^* \end{bmatrix}$$

As the matrix $\begin{bmatrix} (\mathbb{I}_{13} - \bar{A}_{SYS}^s) & -\bar{B}_{SYS}^s \\ C_\varepsilon^s & \mathbb{O}_{2,2} \end{bmatrix}$ is inversible with the SM model defined Chapter 2 (2.3.1.2 – p 12) and the inverter parameters defined in Table 3.1, the system can be solved to find the vector defined by $\begin{bmatrix} \bar{X}_{SYS}^* \\ U_{SYS}^* \end{bmatrix}$:

$$\begin{bmatrix} \bar{X}_{SYS}^* \\ U_{SYS}^* \end{bmatrix} = \begin{bmatrix} (\mathbb{I}_{13} - \bar{A}_{SYS}^s) & -\bar{B}_{SYS}^s \\ C_\varepsilon^s & \mathbb{O}_{2,2} \end{bmatrix}^{-1} \cdot \begin{bmatrix} G_{SYS}^s & \mathbb{O}_{11,2} \\ \mathbb{O}_{2,3} & \mathbb{I}_2 \end{bmatrix} \cdot \begin{bmatrix} W_{SYS} \\ \varepsilon^* \end{bmatrix} \quad \text{eq 3.32}$$

considering that:

$$\begin{bmatrix} (\mathbb{I}_{13} - \bar{A}_{SYS}^s) & -\bar{B}_{SYS}^s \\ C_\varepsilon^s & \mathbb{O}_{2,2} \end{bmatrix}^{-1} \cdot \begin{bmatrix} G_{SYS}^s & \mathbb{O}_{11,2} \\ \mathbb{O}_{2,3} & \mathbb{I}_2 \end{bmatrix} = \begin{bmatrix} K_W^X & K_\varepsilon^X \\ K_W^U & K_\varepsilon^U \end{bmatrix}$$

to simplify the equations of the current controller, eq 3.32 is decomposed in equations:

$$\begin{aligned}\bar{X}_{SYS}^* &= K_W^X \cdot W_{SYS} + K_\varepsilon^X \cdot \varepsilon^* \\ U_{SYS}^* &= K_W^U \cdot W_{SYS} + K_\varepsilon^U \cdot \varepsilon^*\end{aligned}\quad eq\ 3.33$$

Hence, $K_W^X \in \mathbb{M}_{13,3}$; $K_\varepsilon^X \in \mathbb{M}_{13,2}$; $K_W^U \in \mathbb{M}_{2,3}$ and $K_\varepsilon^U \in \mathbb{M}_{2,2}$

The four new defined matrices in eq 3.33 will help to simplify the equations in forthcoming development of this chapter. The determination of the reference values is now possible thanks to the equations eq 3.10 and the above eq 3.32. The inputs used to determine the reference duty ratios can be found in Appendix 2 (p163) considering that $\varepsilon^* = \begin{bmatrix} 0 \\ 0 \end{bmatrix}$.

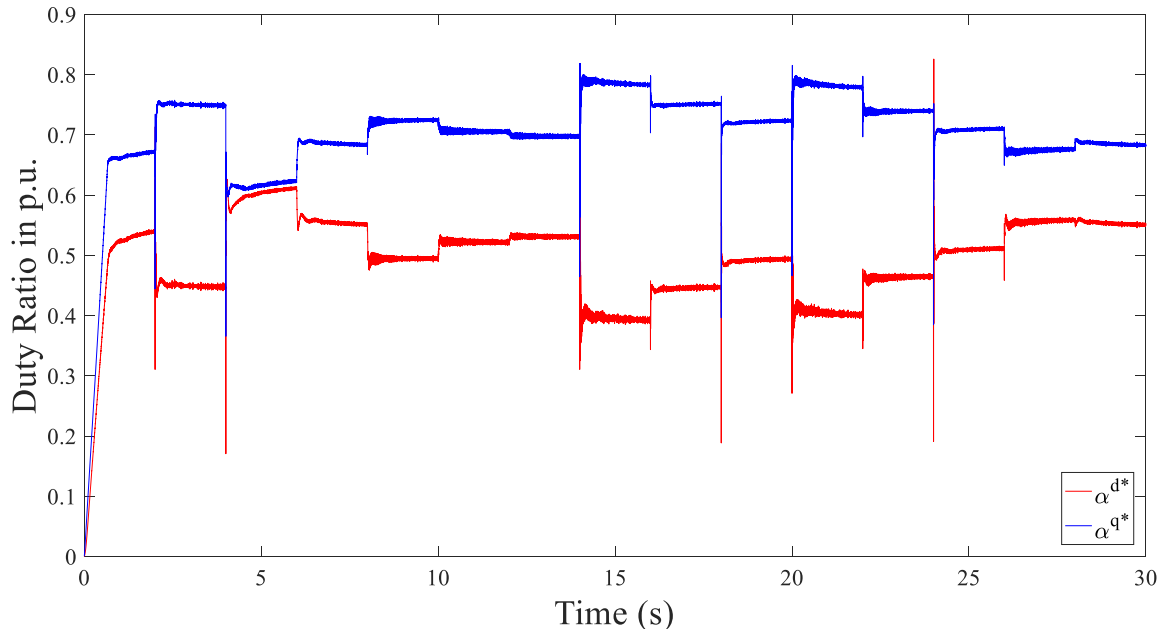


Figure 3.23: Reference ratio α^{d*} and α^{q*} .

The equation eq 3.32 above enables to write eq 3.31 considering the dynamics in terms of the deviation variables as follows:

$$\begin{aligned}(\bar{X}_{SYS} - \bar{X}_{SYS}^*)^+ &= \bar{A}_{SYS}^s \cdot (\bar{X}_{SYS} - \bar{X}_{SYS}^*) + \bar{B}_{SYS}^s \cdot (U_{SYS} - U_{SYS}^*) \\ \varepsilon^s - \varepsilon^* &= \bar{C}_\varepsilon^s \cdot (\bar{X}_{SYS} - \bar{X}_{SYS}^*)\end{aligned}\quad eq\ 3.34$$

or with obvious equation:

$$\begin{aligned}\bar{\varepsilon}_X^+ &= \bar{A}_{SYS}^s \cdot \bar{\varepsilon}_X + \bar{B}_{SYS}^s \cdot \varepsilon_U \\ \varepsilon_Y &= \bar{C}_\varepsilon^s \cdot \bar{\varepsilon}_X\end{aligned}\quad eq\ 3.35$$

With $\bar{\varepsilon}_X = (\bar{X}_{SYS} - \bar{X}_{SYS}^*)$, $\varepsilon_U = (U_{SYS} - U_{SYS}^*)$ and $\varepsilon_Y = (\varepsilon^s - \varepsilon^*)$.

3.6.1.3 Current controller model

The controller will be applied not on the control vector U_{SYS} but on the derivative term of the control vector ΔU , $\Delta U \in \mathbb{M}_{2,1}$. This modification reduces the dynamic rapidity of the system response, but it also permits to minimize the risk of high variations of the system during harsh events.

Hence, the derivative term of the control vector ΔU is defined by:

$$U_{SYS}^+ = U_{SYS} + \Delta U \quad eq\ 3.36$$

The variable ΔU is the input of the system and as $\varepsilon_U = U_{SYS} - U_{SYS}^*$ the new state is $\varepsilon_U^+ = \varepsilon_U + \Delta U$. Hence, the new system including ε_U as a state is defined by combining the equations eq 3.35 and eq 3.36:

$$\begin{aligned} \begin{bmatrix} \overline{\varepsilon_X} \\ \varepsilon_U \end{bmatrix}^+ &= \begin{bmatrix} \overline{A}_{SYS}^s & \overline{B}_{SYS}^s \\ \mathbb{O}_{2,13} & \mathbb{I}_2 \end{bmatrix} \cdot \begin{bmatrix} \overline{\varepsilon_X} \\ \varepsilon_U \end{bmatrix} + \begin{bmatrix} \mathbb{O}_{13,2} \\ \mathbb{I}_2 \end{bmatrix} \cdot \Delta U \\ \varepsilon_Y &= [\overline{C}_\varepsilon^s \quad \mathbb{O}_{2,2}] \cdot \overline{\varepsilon_X} \end{aligned} \quad eq\ 3.37$$

Based on the above centred dynamical model, it is possible to control the inverter's state using a standard LQR design that takes the following form:

$$\Delta U = -K^s \cdot \begin{bmatrix} \overline{\varepsilon_X} \\ \varepsilon_U \end{bmatrix} \quad eq\ 3.38$$

with $K^s \in \mathbb{M}_{2,15}$.

So, combining eq 3.37 and eq 3.38, the controlled system is:

$$\begin{aligned} \begin{bmatrix} \overline{\varepsilon_X} \\ \varepsilon_U \end{bmatrix}^+ &= \underline{A}^s \cdot \begin{bmatrix} \overline{\varepsilon_X} \\ \varepsilon_U \end{bmatrix} \\ \begin{bmatrix} \varepsilon_Y \\ \Delta U \end{bmatrix} &= \begin{bmatrix} \underline{C}^s \\ -K^s \end{bmatrix} \cdot \begin{bmatrix} \overline{\varepsilon_X} \\ \varepsilon_U \end{bmatrix} \end{aligned} \quad eq\ 3.39$$

with $\underline{A}^s = \begin{bmatrix} \overline{A}_{SYS}^s & \overline{B}_{SYS}^s \\ \mathbb{O}_{2,13} & \mathbb{I}_2 \end{bmatrix} - \begin{bmatrix} \mathbb{O}_{13,2} \\ \mathbb{I}_2 \end{bmatrix} \cdot K^s$, $\underline{A}^s \in \mathbb{M}_{15,15}$; $\underline{C}^s = [\overline{C}_\varepsilon^s \quad \mathbb{O}_{2,2}]$, $\underline{C}^s \in \mathbb{M}_{2,15}$.

Hence, considering the definition of the states $\overline{\varepsilon_X}$, ε_U , ε_Y and the characteristics of \overline{X}_{SYS}^* and U_{SYS}^* determined in eq 3.32. The controlled model is defined by the dynamics given by:

$$\begin{aligned} \begin{bmatrix} \overline{X}_{SYS} \\ U_{SYS} \end{bmatrix}^+ &= \underline{A}^s \cdot \begin{bmatrix} \overline{X}_{SYS} \\ U_{SYS} \end{bmatrix} - (\underline{A}^s - \mathbb{I}_{15}) \cdot \begin{bmatrix} K_W^X & K_\varepsilon^X \\ K_W^U & K_\varepsilon^U \end{bmatrix} \cdot \begin{bmatrix} W_{SYS} \\ \varepsilon^* \end{bmatrix} \\ \begin{bmatrix} \varepsilon \\ \Delta U \end{bmatrix} &= \begin{bmatrix} \underline{C}^s \\ -K^s \end{bmatrix} \cdot \begin{bmatrix} \overline{X}_{SYS} \\ U_{SYS} \end{bmatrix} - \left(\begin{bmatrix} \underline{C}^s \\ -K^s \end{bmatrix} \cdot \begin{bmatrix} K_W^X & K_\varepsilon^X \\ K_W^U & K_\varepsilon^U \end{bmatrix} - \begin{bmatrix} \mathbb{O}_{2,3} & \mathbb{I}_2 \\ \mathbb{O}_{2,3} & \mathbb{O}_{2,2} \end{bmatrix} \right) \cdot \begin{bmatrix} W_{SYS} \\ \varepsilon^* \end{bmatrix} \end{aligned} \quad eq\ 3.40$$

3.6.1.4 The complete proposed controller model

The extended system including the observer in which the controlled input is the increment ΔU , is defined by the equations below and visible in Figure 3.24.

$$\begin{aligned}\hat{X}_\Delta^+ &= A_\Delta^s \cdot \hat{X}_\Delta + B_\Delta^s \cdot \begin{bmatrix} Y_{meas} \\ \varepsilon^* \end{bmatrix} \\ Y_\Delta &= C_\Delta^s \cdot \hat{X}_\Delta + D_\Delta^s \cdot \begin{bmatrix} Y_{meas} \\ \varepsilon^* \end{bmatrix}\end{aligned}\quad eq\ 3.41$$

With $X_\Delta = \begin{bmatrix} \bar{X}_{SYS} \\ U_{SYS} \\ W_{SYS} \end{bmatrix}$, $X_\Delta \in \mathbb{M}_{18,1}$; $Y_\Delta = \begin{bmatrix} Y_{meas} \\ \varepsilon \\ \Delta U \end{bmatrix}$, $Y_\Delta \in \mathbb{M}_{13,1}$, and where the different matrices are defined as:

$$L_{obs\Delta} = \begin{bmatrix} L_X^X & \mathbb{O}_{11,4} & L_W^X \\ \mathbb{O}_{4,11} & \mathbb{O}_{4,4} & \mathbb{O}_{4,3} \\ L_X^W & \mathbb{O}_{3,4} & L_W^W \end{bmatrix} \text{ with the different parameters of } L_{obs\Delta} \text{ defined in eq 3.26}$$

$$A_\Delta^s = \begin{bmatrix} \underline{A}^s & (\underline{A}^s - \mathbb{I}_{15}) \cdot \begin{bmatrix} K_W^X \\ K_W^U \end{bmatrix} \\ \mathbb{O}_{3,15} & \mathbb{I}_3 \end{bmatrix} - L_{obs\Delta} \cdot [C_{meas} \quad \mathbb{O}_{12,4} \quad H_{meas}], A_\Delta^s \in \mathbb{M}_{18,18};$$

$$B_\Delta^s = [L_{obs\Delta} \quad (\mathbb{I}_{15} - \underline{A}^s) \cdot \begin{bmatrix} K_\varepsilon^X \\ K_\varepsilon^U \end{bmatrix}], B_\Delta^s \in \mathbb{M}_{18,14};$$

$$C_\Delta^s = \begin{bmatrix} [C_\varepsilon^s \quad \mathbb{O}_{4,2}] & H_{meas}^s \\ \underline{C}^s & -\underline{C}^s \cdot \begin{bmatrix} K_W^X \\ K_W^U \end{bmatrix} \\ -K^s & -K^s \cdot \begin{bmatrix} K_W^X \\ K_W^U \end{bmatrix} \end{bmatrix}, C_\Delta^s \in \mathbb{M}_{14,18} \text{ and}$$

$$D_\Delta^s = \begin{bmatrix} \mathbb{O}_{12,12} & \mathbb{O}_{12,2} \\ \mathbb{O}_{2,12} & \mathbb{I}_2 - \underline{C}^s \cdot \begin{bmatrix} K_\varepsilon^X \\ K_\varepsilon^U \end{bmatrix} \\ \mathbb{O}_{2,12} & -K^s \cdot \begin{bmatrix} K_\varepsilon^X \\ K_\varepsilon^U \end{bmatrix} \end{bmatrix}, D_\Delta^s \in \mathbb{M}_{14,14}$$

Now that the new proposed controller design has been detailed, in the next section, the simulation in closed loop are presented.

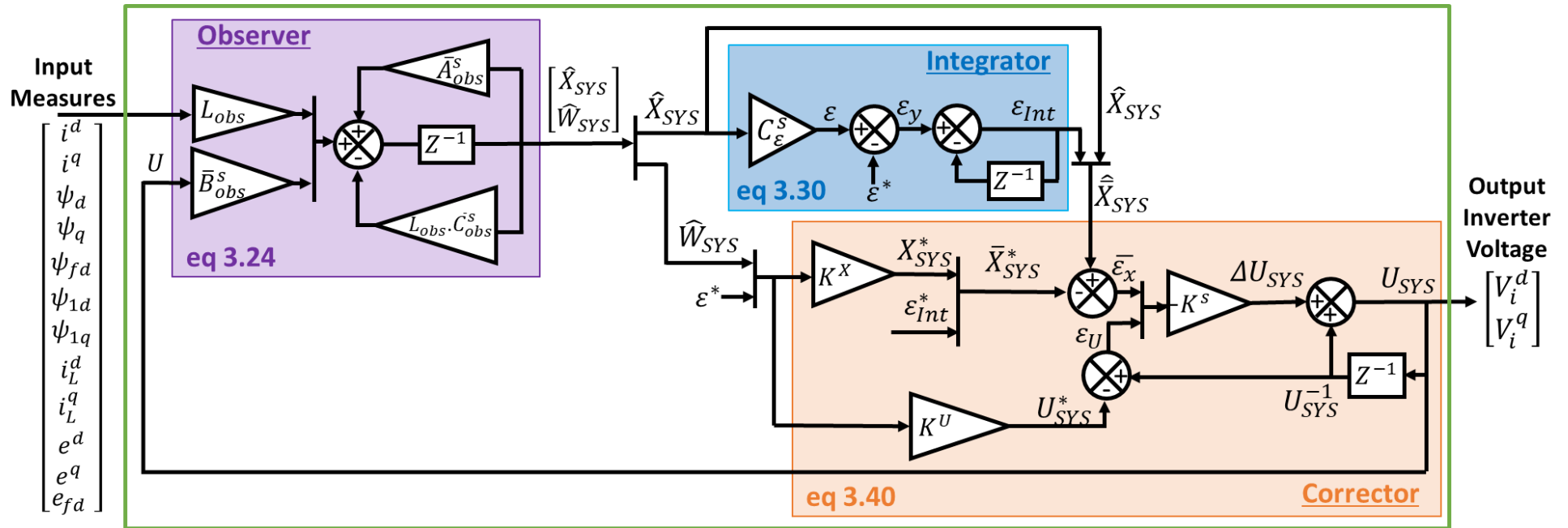


Figure 3.24: Proposed current controller.

With $K^X = [K_W^X \quad K_\epsilon^X]$ (determine in eq 3.33 – p64)

$K^U = [K_W^U \quad K_\epsilon^U]$ (detailed in eq 3.33 – p64)

and $\begin{bmatrix} \alpha^d \\ \alpha^q \end{bmatrix} = \frac{2}{V_{dc}} \cdot \begin{bmatrix} V_i^d \\ V_i^q \end{bmatrix}$ (defined in eq 3.10 – p47)

3.6.2 Simulation of the closed loop with the proposed controller

K^s is designed with the function MATLAB® “*dlqr*”.

$$K^s = dlqr(\underline{A}^s, \underline{B}^s, Q_\Delta, R_\Delta)$$

The matrices are defined by:

$$Q_\Delta = \begin{bmatrix} Q_{X_{SYS}} & \mathbb{0}_{11,2} & \mathbb{0}_{11,2} \\ \mathbb{0}_{2,2} & Q_\varepsilon & \mathbb{0}_{2,2} \\ \mathbb{0}_{2,11} & \mathbb{0}_{2,2} & Q_{U_{SYS}} \end{bmatrix} + 10^{-9} \cdot \mathbb{I}_{15} \text{ where } \begin{cases} Q_{X_{SYS}} = 100 \cdot (\bar{C}_\varepsilon^{s^t} \cdot \bar{C}_\varepsilon^s) \\ Q_\varepsilon = \mathbb{I}_2 \\ Q_{U_{SYS}} = 100 \cdot \mathbb{I}_2 \end{cases} \text{ and } R_\Delta = \mathbb{I}_2$$

Similarly, L_{obs} is also designed with the function MATLAB® “*dlqr*”:

$$L_{obs} = dlqr(\bar{A}_{obs}^{s^t}, \bar{C}_{obs}^{s^t}, Q_{obs}, R_{obs})^t \text{ with } Q_{obs} = 10^{12} \cdot \mathbb{I}_{12} \text{ and } R_{obs} = \mathbb{I}_{12}$$

In Appendix 6 (p173) can be read the methodology follows in order to determine the different values of the proposed controller parameters, $Q_{X_{SYS}}$ and $Q_{U_{SYS}}$. To avoid any overcurrent, the parameter Q_ε is keep as equal to \mathbb{I}_2 . The different parameters values that are described here are the controller parameters that are applied throughout the following chapters, Chapter 4 (p77), Chapter 5 (p99) and Chapter 6 (p123).

In addition, based on these controller parameters values, a robustness study of the proposed controller can be found Appendix 7 (p176) in order to highlight the impact of uncertainties in the determination of the inverter, L_L and R_L , capacitor filter, L_f and R_f , and grid characteristics, L_g and R_g . Finally, in Appendix 8 (p181) can be found an analytic comparison of the different current controllers in closed loop described in this Chapter and the previous controller used by Schneider Electric and described in [23].

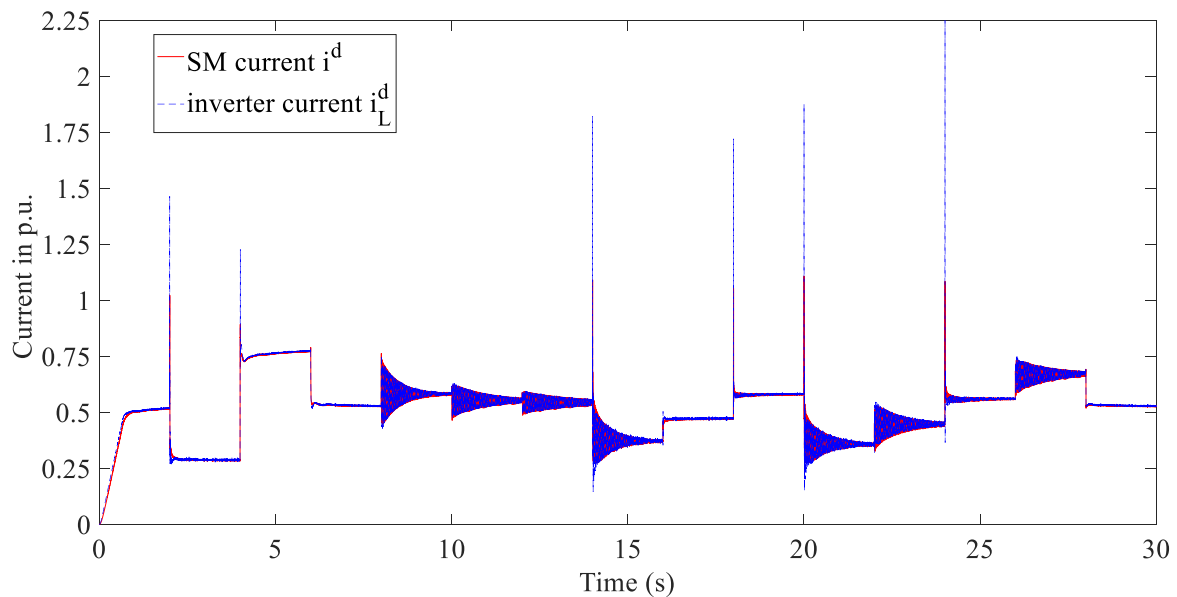


Figure 3.25: Inverter current i_L^d compared to synchronous machine current i^d .

Figure 3.25 to Figure 3.28 are plotted thanks to the function “*dlsim*” of MATLAB® based on the state-space model described in eq 2.41 with the perturbations described in Appendix 2 (p163).

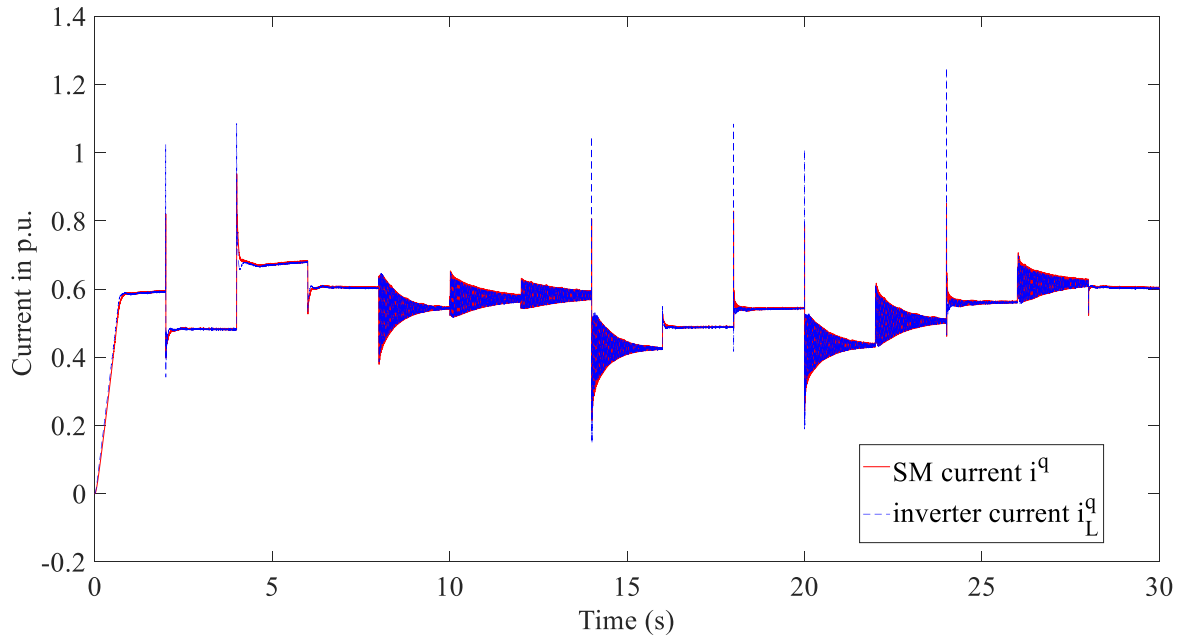


Figure 3.26: Inverter current i_L^q compared to synchronous machine current i^q .

Comparing Figure 3.18 and Figure 3.27, these oscillations are even more reduced with our proposed controller. This is both due to the state observer but also increased by the fact that the controller is applied on the derivative term of the command ΔU and not directly on the command U_{SYS} . Similarly, the maximal outputs currents are also reduced by half with our proposed solution. These maximal currents reduction will minimize the inverter saturation as it can be seen in both Figure 3.28 and Figure 3.29.

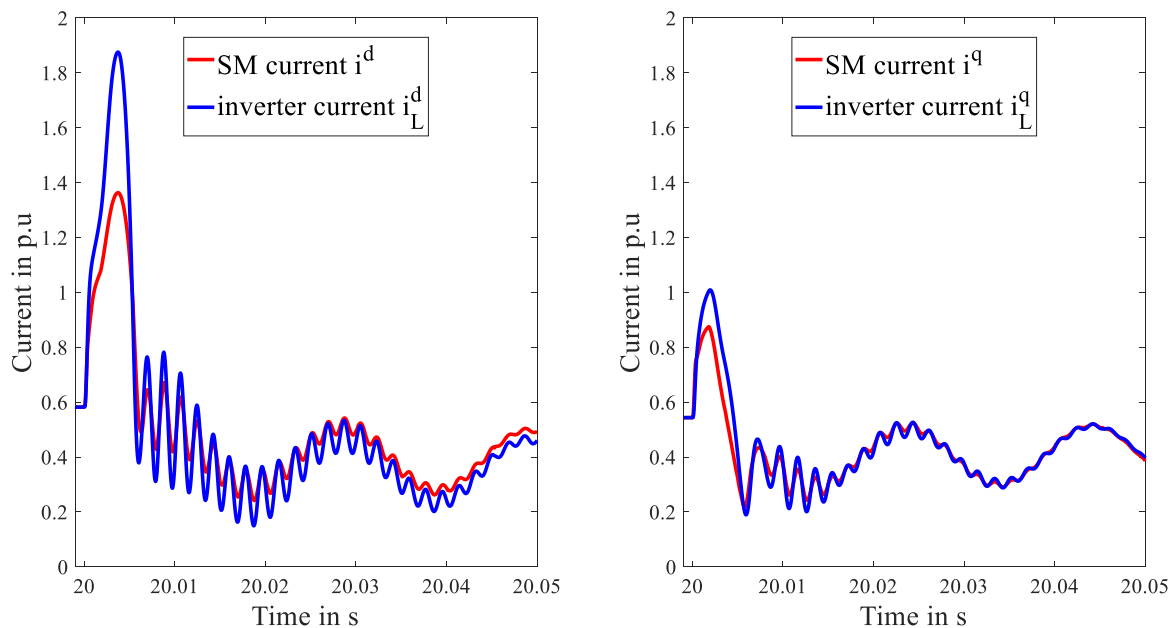


Figure 3.27: Zoom on the currents i^d and i_L^d , and i^q and i_L^q during a load impact for the proposed controller.

Figure 3.28 and Figure 3.29 show that the duty ratios α_d and α_q follow the reference duty ratio α_d and α_q calculated before in Figure 3.23. Also, it can be noticed that the duty ratios are in their limits of $[-1; 1]$ with no saturation thanks to the penalty used on the derivative term ΔU as it was the case with the PI and observer controller in section 3.5.3. It can be noted that the proposed controller helps to minimize the inverter risk of saturation during harsh events.

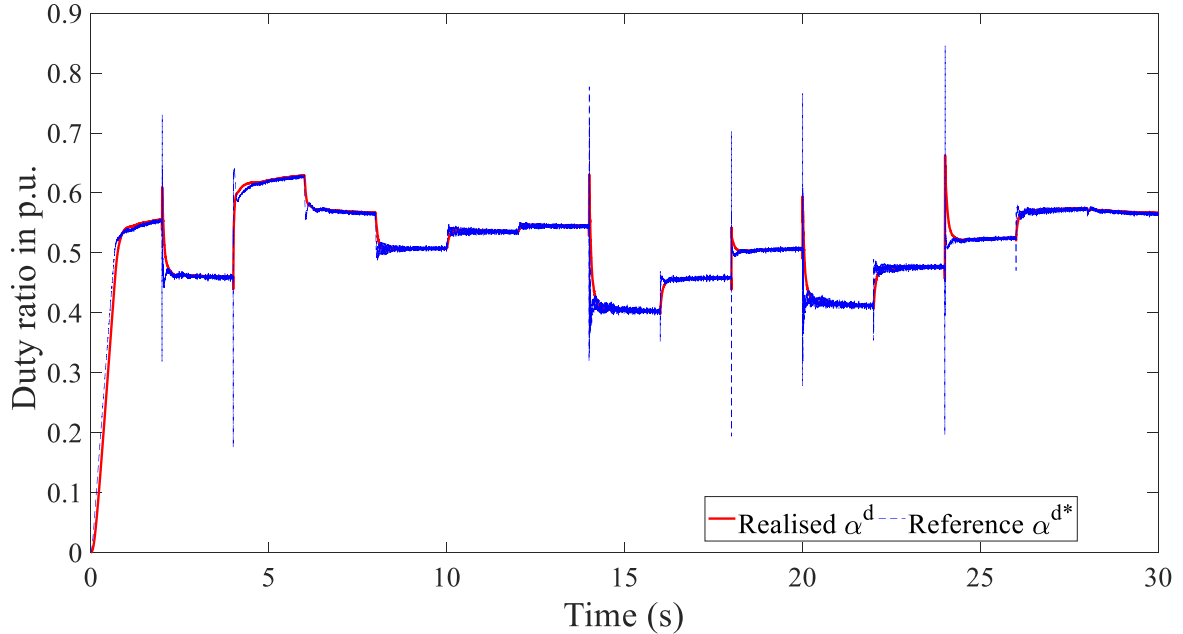


Figure 3.28: Duty ratio α^d compared to reference α^{d} for the proposed controller.*

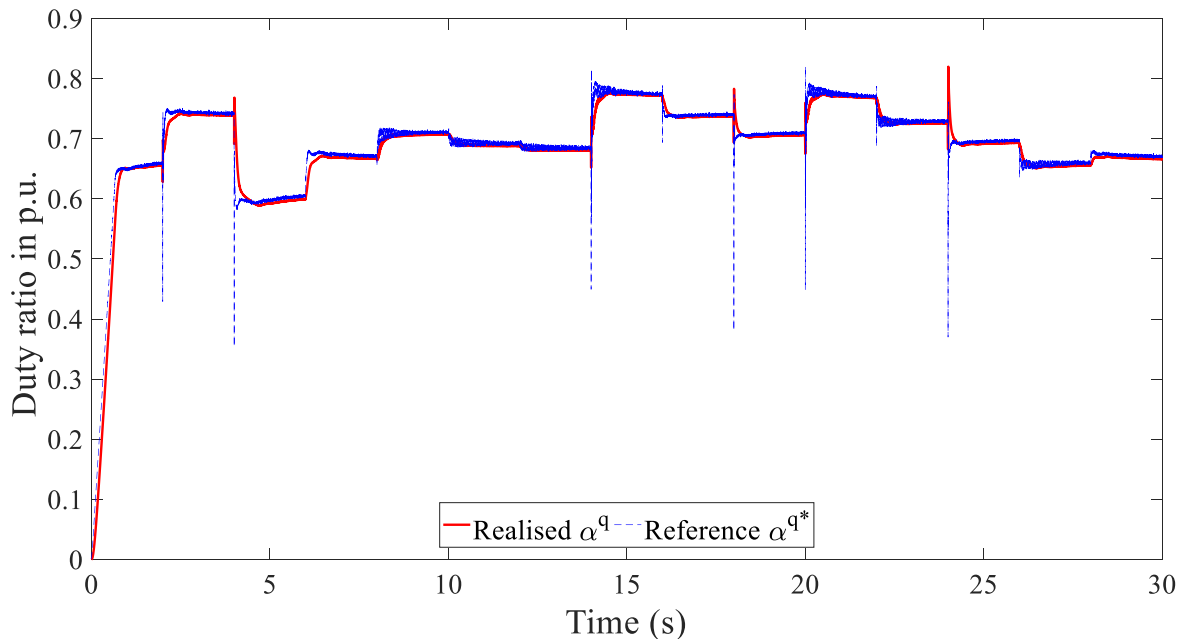


Figure 3.29: Duty ratio α^q compared to reference α^{q} for the proposed controller.*

The results of the observed states of the proposed controller can be seen in the Appendix 5 (p171).

3.6.3 Complete controller simulation integrated in the entire VSG

Similarly, to the PI controller alone in 3.3.3, the PI controller and observer in 3.5.3, the proposed controller is integrated in the VSG control in closed loop. The same inverter as in 3.3.3 (p51) and 3.5.3 (p60) is used, a 25 kVA, 400 V phase-phase nominal voltage for a nominal current of 36 A and a maximal output current of 60 A.

On Figure 3.30, the VSG controlled by the proposed controller is supplying a 20 kW load and at $t = 1$ s, the load is removed.

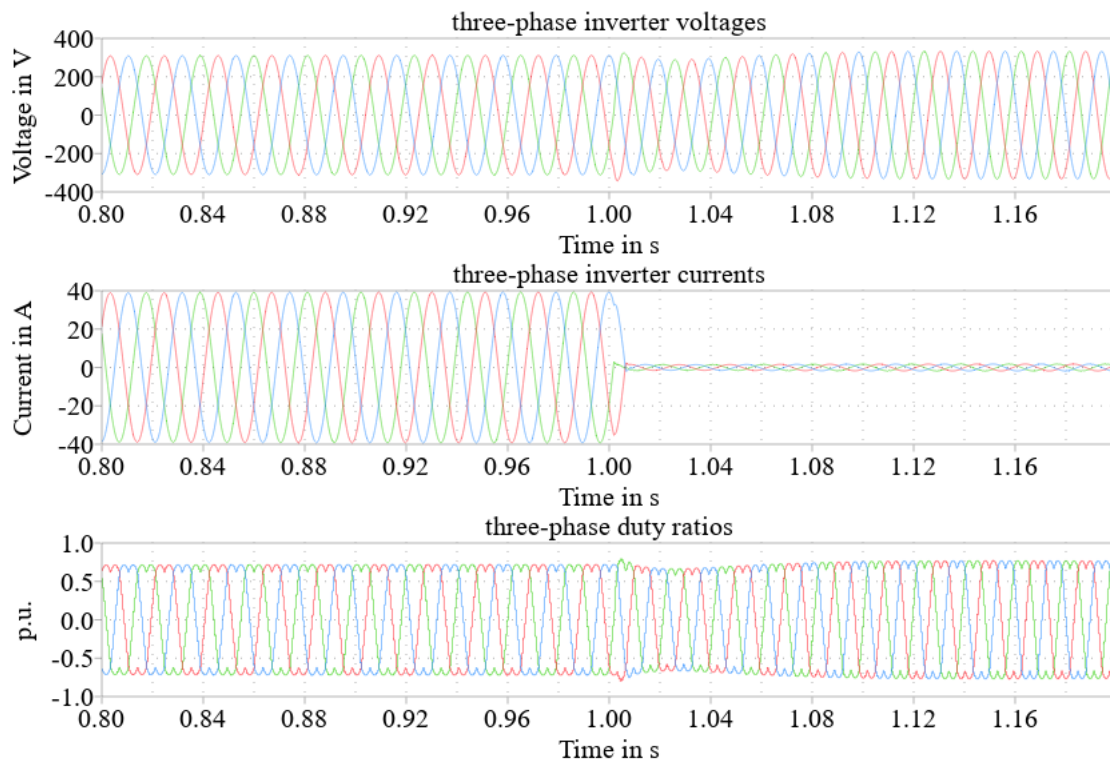


Figure 3.30: Inverter three phase voltages, currents and duty ratios during a 20 kW load shedding for the proposed controller.

Figure 3.30 represents the three-phase currents, voltages and duty ratios of the VSG control with proposed controller. Comparing Figure 3.30, Figure 3.21 and Figure 3.10, the proposed controller has clearly stabilized the system when submitted for harsh event. In comparing Figure 3.31 and Figure 3.22, it can be noted that the VSG three-phase output currents submitted no more oscillation as it was the case with the PI and observer controller.

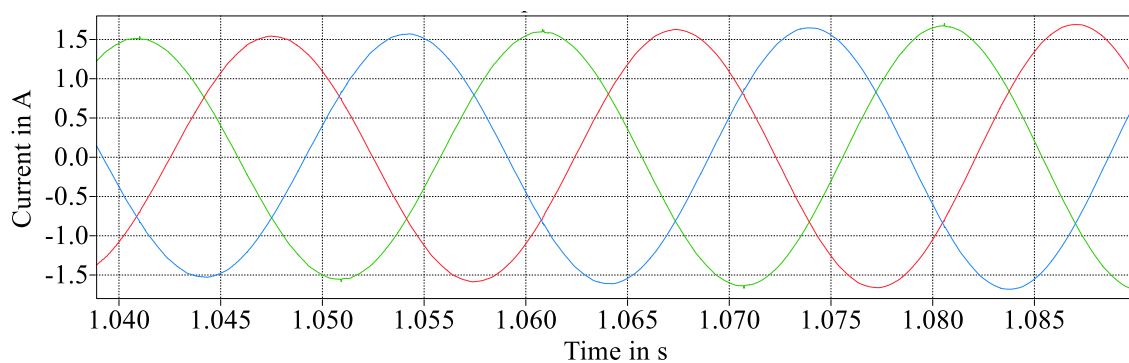


Figure 3.31: off-loaded VSG three-phase inverter's currents for the proposed controller.

In addition of the test above, different tests are also considered as a necessity to validate the VSG model with the proposed controller. In this section, the VSG with the proposed controller is tested for different use cases in order to be sure of the stability and efficiency of the proposed controller once implemented in the VSG control. These tests are mandatory to validate the VSG from an industrial point of view:

- Off-loaded starting and transition to maximal active power load;
- Maximal active power load starting and then transition to off-loaded.

Testing the transition on charge to without charge is necessary because the system can be stable when starting without a charge, but instable after the transition on charge to without charge as it was the case for the PI controller. Then, different load impacts and load shedding, with active and reactive power have to be done in order to conclude on the global VSG model stability. In addition, the short-circuit event has to be validated in simulations to ensure that the VSG is not unstable during or after the short-circuit.

Each load impact is applied at $t = 1$ s.

3.6.3.1 Loads Impact and Shedding

Figure 3.32 and Figure 3.33 show that the proposed controller in closed-loop integrated in the VSG model is stable during and after harsh events as important load variation or highly reactive load.

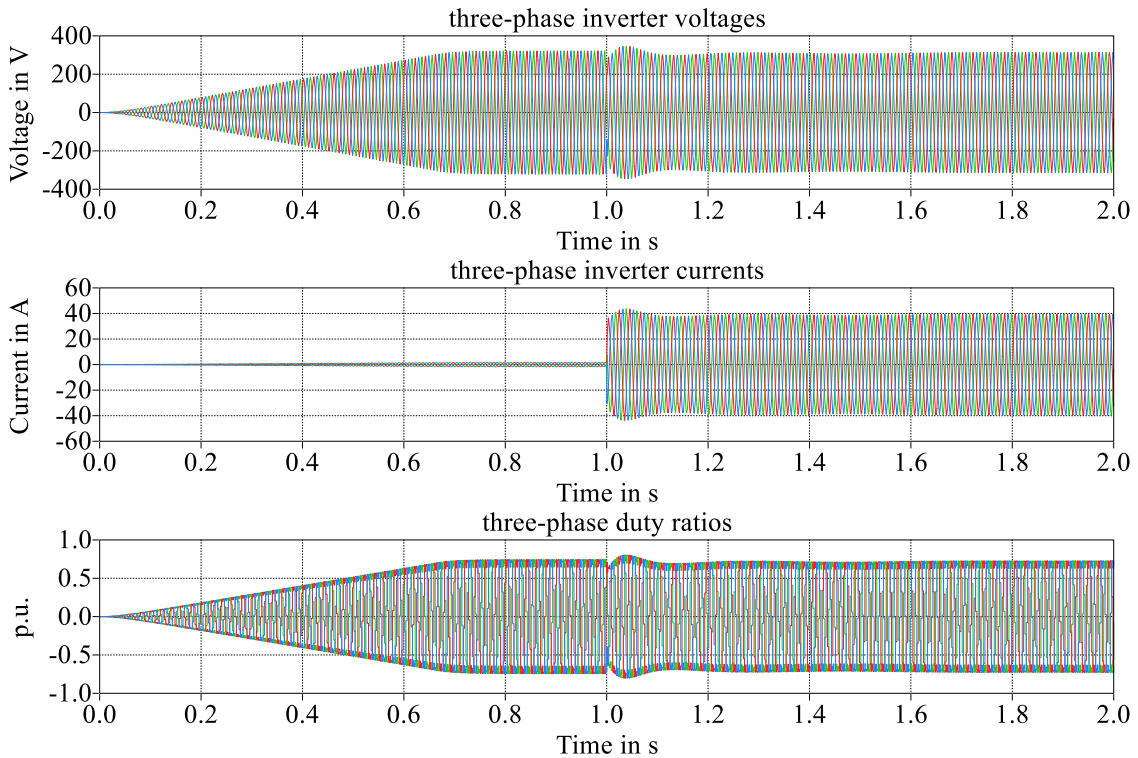


Figure 3.32: Inverter three phase voltages, currents and duty ratios during a 20 kW load impact.

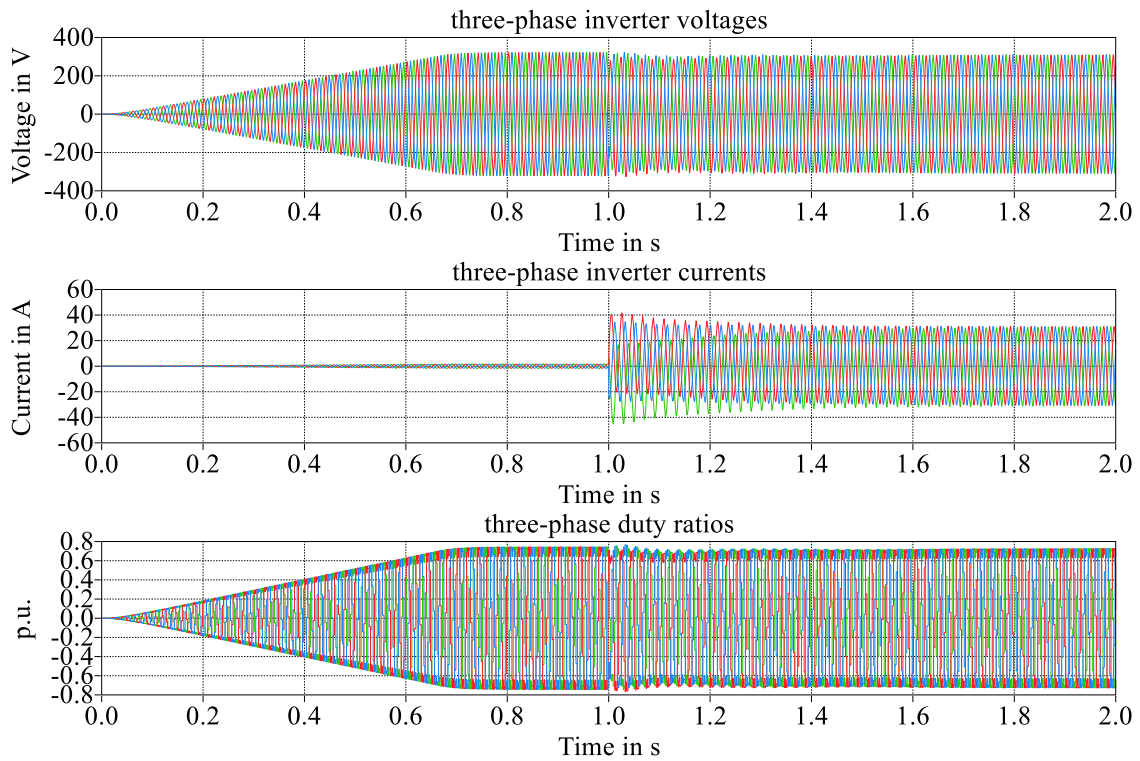


Figure 3.33: Inverter three phase voltages, currents and duty ratios during a 20 kVA load impact

3.6.3.2 Short-Time Short-Circuit

The reader can see that the closed-loop system with the proposed controller is stable during and after the short-circuit.

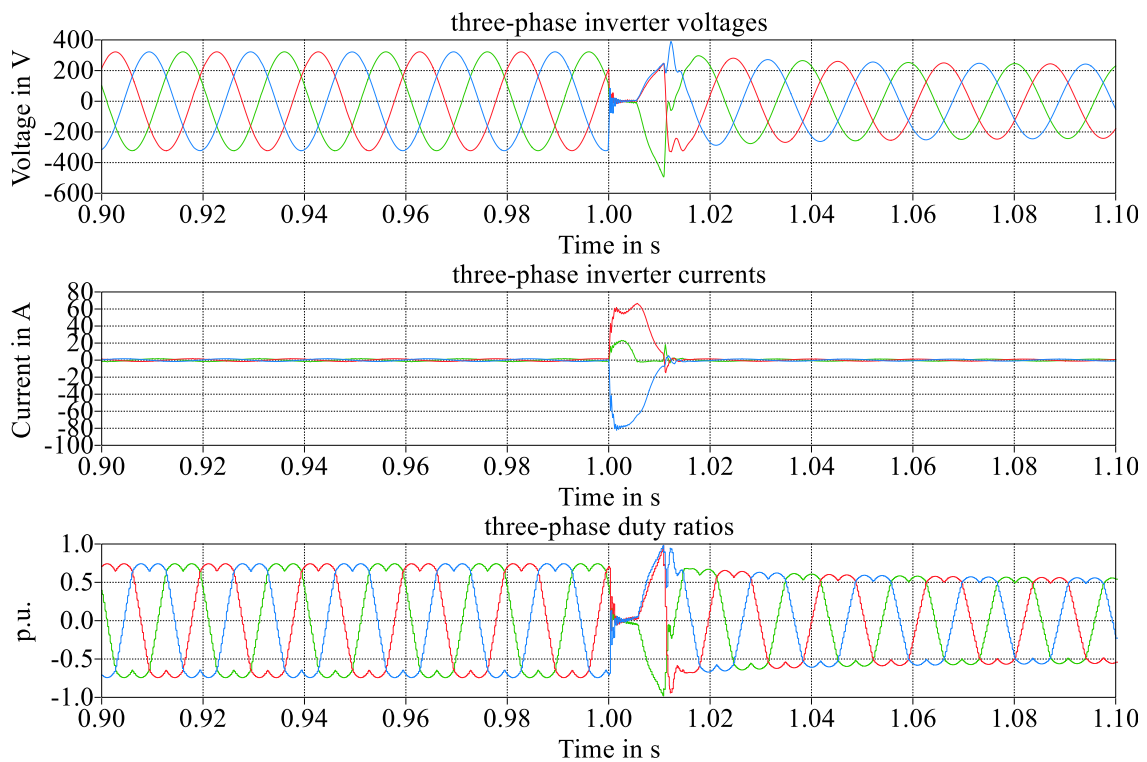


Figure 3.34: Inverter three phase voltages, currents and duty ratios during a short-circuit.

The different simulations, Figure 3.30 to Figure 3.34, show that the proposed controller integrated in the VSG is stable during the different tests described above, the next step is the implementation in the industrial inverter.

3.6.4 Conclusion on the proposed controller

Firstly, the model of the proposed controller is analytically described and summarised with Figure 3.24. Secondly, the state-space model is validated based on the inputs that can be found in Appendix 2 (p163). This study shows that the proposed controller has better performances than the PI controller with observer. It can be noted that the error between the inverter output currents i_L^d and i_L^q in comparison to the SM currents i_d and i_q , have some high values. Indeed, these high error values are due to the proposed model building as the main objective is to follow the SM current but also to avoid the inverter saturation. Finally, the proposed current controller is implemented in the VSG control where it is proved to have better results than the PI and observer controller when implemented in the VSG control.

With this study on the proposed controller, it's possible to say that the LQR with an integrator controller and observer is a performant solution to ensure the VSG model stability even during harsh events as short-circuit.

3.7 Conclusion on the current controllers for VSG

Three different controllers, adapted to the possible implementation in an industrial inverter, have been detailed in this chapter: a PI controller, a PI controller with an observer and finally, our proposed controller, LQR with an integrator controller and observer simulations.

The integration of the PI controller in the VSG control highlights the fact that a simple controller lead to instability due to different perturbations. Indeed, oscillations and resonances above the lines frequency [28] might occur which destabilizes the controlled system. In addition, numerical instabilities are created, due to the high order of the SM models as demonstrated in [28]. Finally, DC leakage currents could be created in output of the inverter which then are reinjected in the controller and destabilize the system in some milli-seconds.

The solution detailed in [28] and also validated in [23] shows that virtual impedances have a real impact on the VSG model stability during harsh events. However, to ensure the stability, virtual impedances were added to the implemented model causing two main problems: increasing complexity of the VSG model and tuning the virtual impedances parameters.

Hence, another solution described in this chapter, to address the problems of oscillations and resonances above the lines frequency and numerical instabilities, is the implementation of an observer. The performance of the observer has been validated with the study on the controller constituted of an observer and an PI. Indeed, contrary to the PI controller alone, PI controller and observer is stable which validated the improving of the observer to resolve the stability problems of the model during harsh events. However, even if the instabilities are suppressed by the used of the observer, in some configurations such as short-circuit or off-loading, the results need to be improved to ensure a good performance of the VSG.

This is the reason why, the LQR proposed controller, with an integrator and an observer, is analytically detailed and tested after being implemented in the VSG control. As the objective is to have a performant controller implementable in an industrial inverter, the LQR controller seems to be the best trade of between performance and simplicity. Indeed, this chapter underlines that the proposed controller is adapted to resolve the instability problems of the VSG, thanks to its observer, and also ensure a good performance of the VSG thanks to its integrator and LQR controller.

In the next chapter, Chapter 4, this proposed controller is implemented in a real industrial inverter for final validation on Schneider Electric microgrid.

3.8 Perspectives and extensions

As the system is considered as balanced, the homopolar elements are not considered. A perspective for further researches could be the integration of the homopolar axis with its consideration in both SM model and proposed controller. It could be interesting to compare the proposed controller without and with homopolar axis especially during unbalanced loads impact.

Another perspective of research that could be mentioned is the state-space model analytic study of the observability and controllability. Indeed, as the entire parameters of the SM and inverter were known, the observability and controllability were easily determined. The analytic study of the controllability and observability may help to determine limitation on the SM parameters and on inverter outputs filter characteristics.

Chapter 4. Experimental validation of the current controller for VSG

4.1 Introduction

The controller developed for the VSG solution has been analytically detailed and validated in simulations in Chapter 3 (3.4 – p 39). The objective of this chapter is to present the experimental integration of our proposed controller in an industrial inverter. Before starting the tests with the industrial inverter, some adaptations were necessary to implement the proposed controller in control card of the industrial inverter, a Schneider Electric inverter Connex CL 25. The inverter is a 25 kVA, 400 V phase-phase nominal voltage for a nominal current of 36 A and a maximal output current of 60 A.

The first step was to implement the proposed controller on the inverter's control card and to use a hardware-in-the-loop (HIL) testbed to emulate the inverter, thus avoiding deteriorations of the system due to bugs in the numerical control. The experimental validation was rapidly moved to the implementation in the real inverter due to two mains elements: the results with the HIL were conclusive and the use of HIL presented limitations, especially for the short-circuit tests.

As the experimental test results on the physical inverter and on the HIL testbed are similar, in this chapter are only presented the results of the implementation on the real inverter. However, the HIL testbench is briefly described as it served as a very flexible prototyping tool and thus is of interest for that matter. Figure 4.1 show a simplified representation of the installation. The entire system, microgrid and inverter, is emulated in the HIL, a Typhoon 602. The emulated inverter is controlled by the control

card based on the “measurements” emulated by the HIL. The control of the loads of the emulated microgrid as well as the visualisation of the measurements is done via the HIL interface.

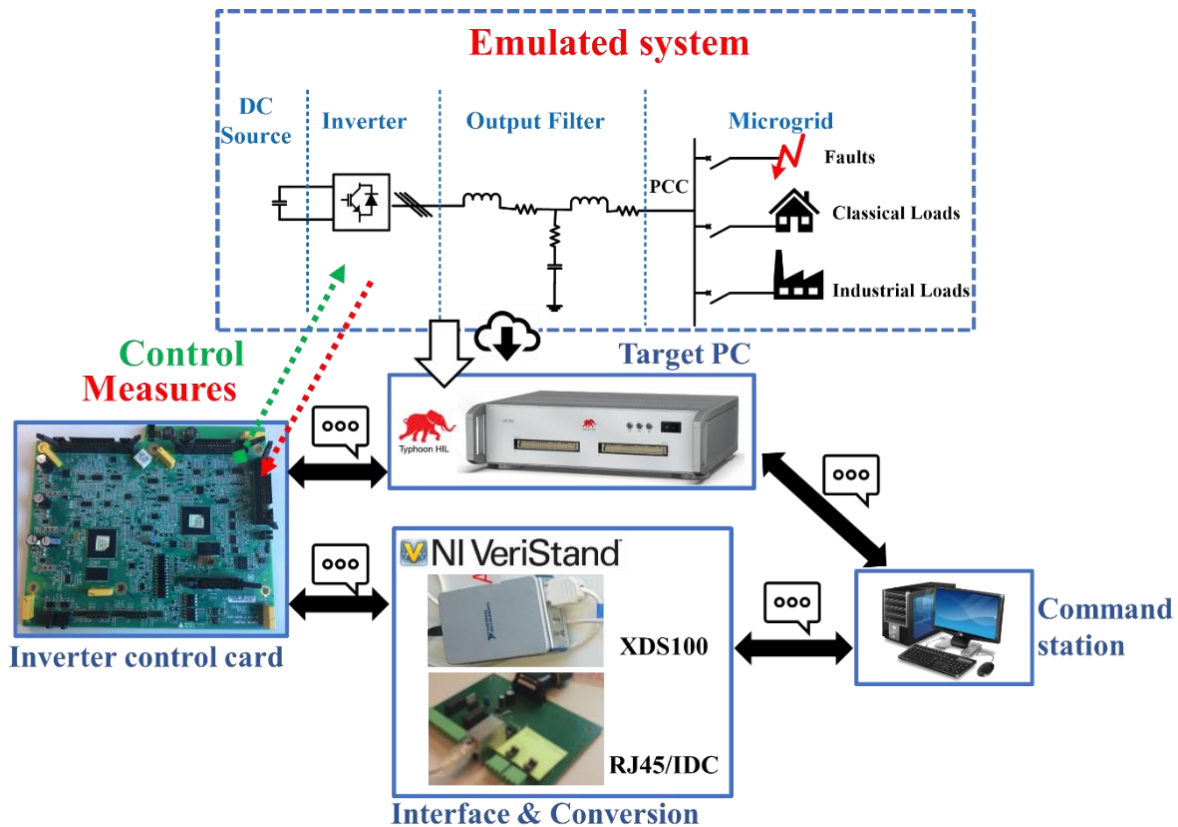


Figure 4.1: Schematic of the Typhoon HIL tests.

Focusing now on the physical inverter experimentation, a first section details the integration of the proposed controller in the industrial inverter control card. Then, a second section presents the experimental results of the VSG with our proposed controller, with in mind its integration in a microgrid. Not all tests are presented in this chapter but only the most significant ones. The selection has been made on criteria of illustrating mainly the robustness of the proposed controller

4.2 Implementation on an industrial inverter

The adaptation of the proposed controller for the implementation in the industrial inverter was a non-negligible work due to the CPU load limit of the DSP. Indeed, the CPU load of the DSP with our proposed controller needs to be below 70 % to 75 % to avoid CPU overloading, and error production that could destabilize the entire VSG controller. The limit of 70 % to 75 % ensures that the DSP has the capability to execute the entire program without any lag. In this section, the necessary controller adaptations are detailed.

4.2.1 Controller adaptation for the implementation in the real inverter

The entire VSG control, considering the proposed controller, is proposed in Figure 4.2 (p79) and the previous one in Figure 1.1 (p3). The control of the VSG has been sampling with three sampling frequencies to minimize the CPU load, as detailed in [23], with:

- **Block sampling at 20 kHz:** for the current regulation, in our case, the proposed controller, and the entire measures (voltages and currents) – in blue.
- **Block sampling at 6.66 kHz:** for the SM model, the reference current saturation and the state observer – in green.
- **Block sampling at 1 kHz:** for the voltage and frequency regulation as well as the different droop control, the inertia and the protections – in orange.

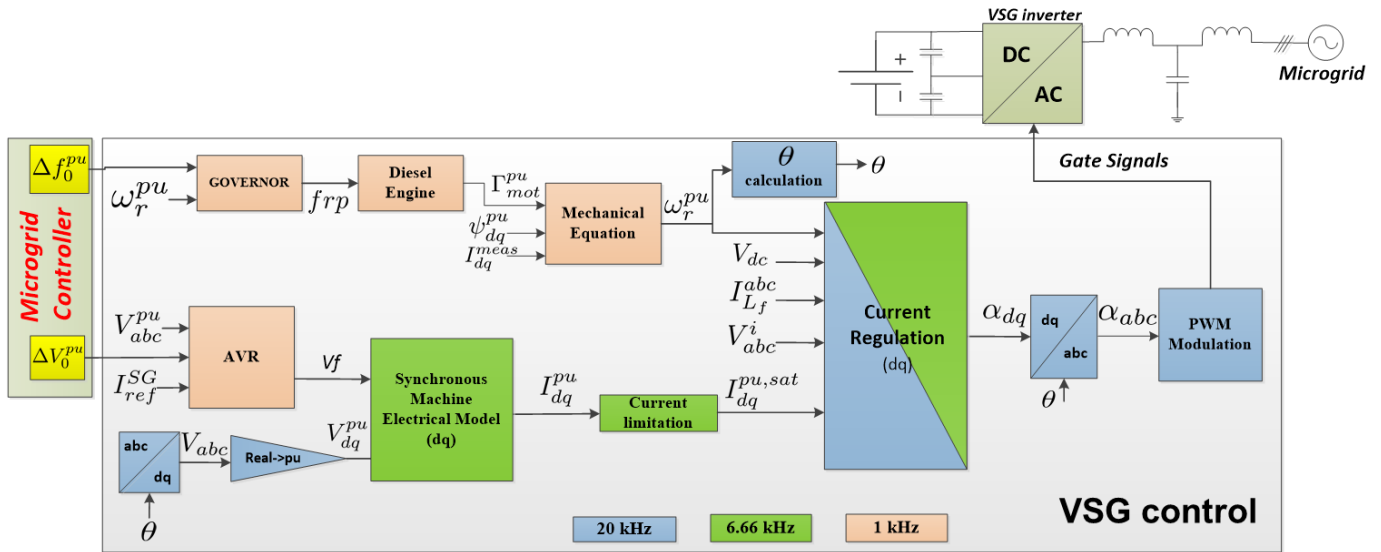


Figure 4.2: Implemented VSG control scheme.

By comparing the VSG global control scheme from Figure 1.1 (p3) and Figure 4.2, it can be noted that the virtual impedances have been removed as well as a current limitation. Indeed, as the state observer helps stabilizing the current controller, even during harsh events as short-circuits, the addition of the virtual impedances is no more necessary to stabilise the close-loop system. In addition, the current limitation at a frequency of 20 kHz has been removed as it was only necessary to ensure the system stability with the virtual impedances which impacted the current reference, causing it to be out of range for the inverter. For the rest, the global VSG controller is not modified.

As the proposed controller is already determined in a discrete representation, there is no adaptation necessary for its integration in the DSP of the inverter's control card.

Firstly, the entire proposed controller, i.e. the LQR controller with integrator and state observer, was implemented in the inverter control at a sampling frequency of 20 kHz. However, the CPU load was overloaded. The controller has been modified to avoid the DSP saturation due to the CPU overloading in order to ensure its proper integration in the DSP.

The first step of the modifications was to convert the format of the numbers of the entire controller from double or single to fixed-point. Fixed-point numbers are highly optimised with a high precision in this DSP. In fixed-point, each variable of the VSG control is determined with a defined number of digits, (32 in our case), when with single or double, the digits limitation is less restrictive. The fixed-point value

is determined by its Q-format where Q represents the number of digits that are used to characterise the fractional part of the number. To summarise, the higher the Q-format, the higher the fractional precision and the lower the maximum value that can be encoded. So, the value of the fixed-point influences the precision of the calculation, the resolution decreases with the decrease of the fixed-point value. An example of two different fixed-point values are visible in Table 4.1.

Table 4.1: Fixed-point value with their range and resolution

Q format	Fixed-point range		Resolution
	Min Value	Max Value	
30	-2	1.999 999 999	9.31323E-10
18	-8192	8191.999 996 185	3.8147E-06

In addition, if a fixed-point value is not precisely determined, the entire controller could become instable. A fixed-point variable cannot contain values outside its limits, meaning that, if a limit is reached, the next value will be on the opposite range, as illustrated in Figure 4.3.

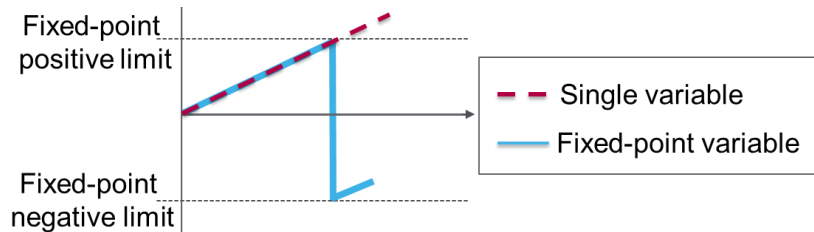


Figure 4.3: Fixed-point variable comparison with a single variable.

In order to ensure that the format of the fixed-point variables have been well set, multiple simulations firstly in single, then in fixed-point, have been run in various configurations to identify exactly the operating ranges of each variables.

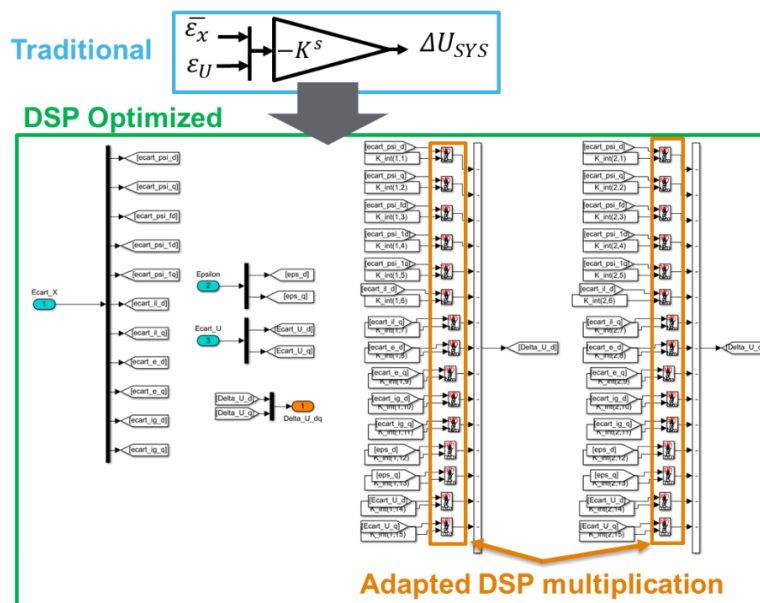


Figure 4.4: Conversion from traditional implementation in Simulink to an adapted DSP code.

The second modification is to convert the entire matrixes of the proposed controller into equations with summations, divisions and multiplications to optimize the DSP's calculations and thus reduce the CPU load. Figure 4.4 is an example of transfer function from Simulink in a more traditional way, compared with its optimized DSP implementation with selected fixed-point values.

These optimized multiplications are adapted to fixed-point values, especially when the two multiplied variables have the same fixed-point value. Hence, the same fixed-point is preferably extended to an entire block of the controller (for example the observer) to increase the global performance of the controller (i.e. decrease the CPU load) taking into account the operating ranges of each variables.

The final step of the modifications is to move the state observer to the block with the sampling frequency of 6.66 kHz from the one with the sampling frequency of 20 kHz. The adapted controller for an implementation on the DSP (considering its restrictions) is shown Figure 4.5 (to compare with Figure 1.1 (p3) for the original one).

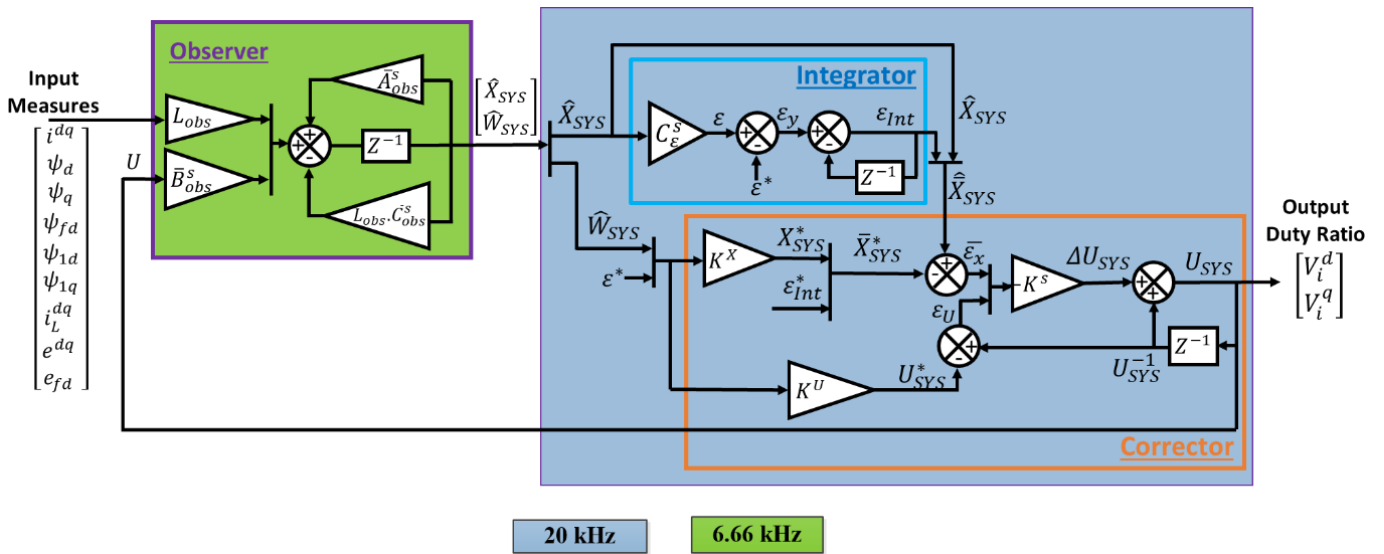


Figure 4.5: Implemented VSG adapted regulation scheme.

Thanks to the presented modifications, the implementation of the proposed controller in the industrial inverter control card is feasible. In the following section, how the CPU load is calculated is explained in order to verify the proper operation of the inverter with the implemented VSG controller.

4.2.2 CPU load measure of the control card of the industrial inverter

As explained before, the CPU load measurement of the industrial inverter's control card is needed to ensure the proper functioning of the VSG controller. Figure 4.6 shows the industrial inverter's control card when measuring the CPU activity at the output of the DSP. Two DSP can be seen on the controller card in Figure 4.6, one for the AC control and the other for the DC control. In our case, only the AC is concerned as it is the only one impacted by our modifications on the VSG controller.

As each sampling block starts by being turned on and ends by been turned off with the same command, the DSP activity of each sampling block is measured based on this characteristic. As the command can be visualized with an oscilloscope via an output port, it is possible to determine when the block is active and thus to determine the sampling period, i.e. the time needed by a block to be executed.

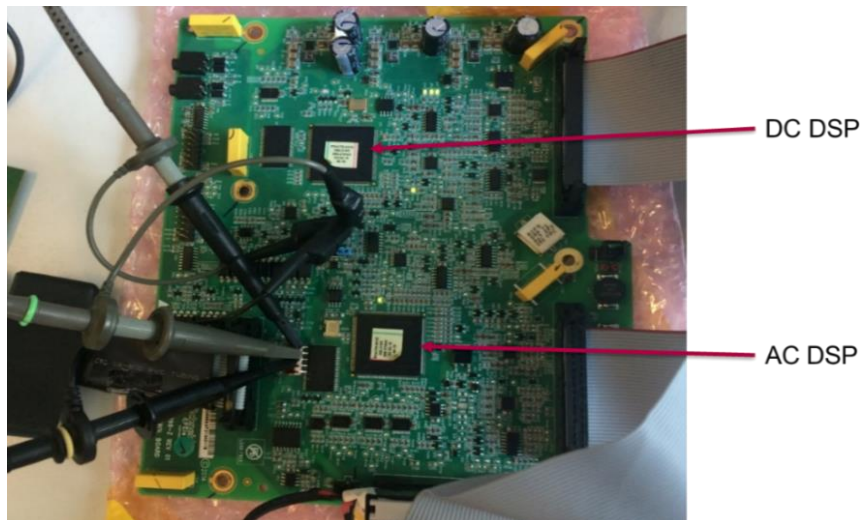


Figure 4.6: Measure of the CPU activity on the DSP on the controlled card of the inverter.

In order to determine the CPU activity of the DSP based on the real activity of each sampling block, it necessary to determine:

- The maximal period of each sampling block.
- The measured activity of each sampling block (on the oscilloscope in our case)
- The time interruption of each sampling block by knowing the priority of each sampling block

The real activity of a sampling block is equal to the measured activity minus the time interruption.

Figure 4.7 shows the real activity of a sampling block (block 2) which is interrupted by the sampling block (block 1). The real activity of sampling block 2 is determined by its measured activity minus the interruption time, i.e. the measured activity of block 1.

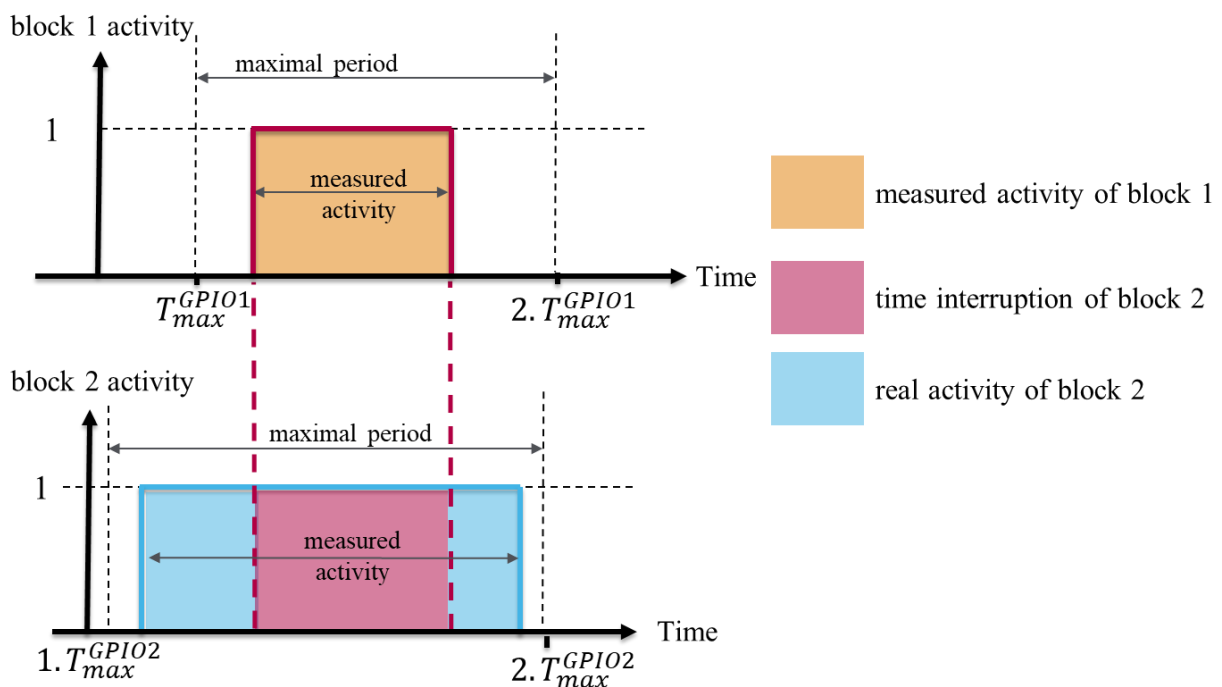


Figure 4.7: Identification of the sampling block real activity.

To determine the CPU load, the real activity of a sampling block is compared to the maximal period of this sampling block which is equivalent to 100 % of the CPU load. The maximal period T_{max} is defined as:

$$T_{max} = \frac{1}{\text{sampling block frequency}} \quad \text{eq 4.1}$$

For example, at a sampling frequency of 20 kHz, the maximal period is defined by:

$$T_{max}^{20 \text{ kHz}} = 1 / 20000 = 50 \mu\text{s}$$

The CPU activity of each sampling block is visible in Figure 4.8:

- In yellow, the 20 kHz sampling block activity.
- In violet, the 6,66 kHz sampling block activity, interrupted only by 20 kHz sampling block
- In green, the 1 kHz sampling block activity, interrupted by both 20 kHz and 6,66 kHz sampling blocks.

In Figure 4.8, the 1 kHz sampling block is interrupted 6 times by the 20 kHz sampling block and 2 times by the 6.66 kHz sampling block. In Figure 4.8, the real activity of the 1 kHz sampling block is highlighted in green, the interruptions are showed with dotted black lines.

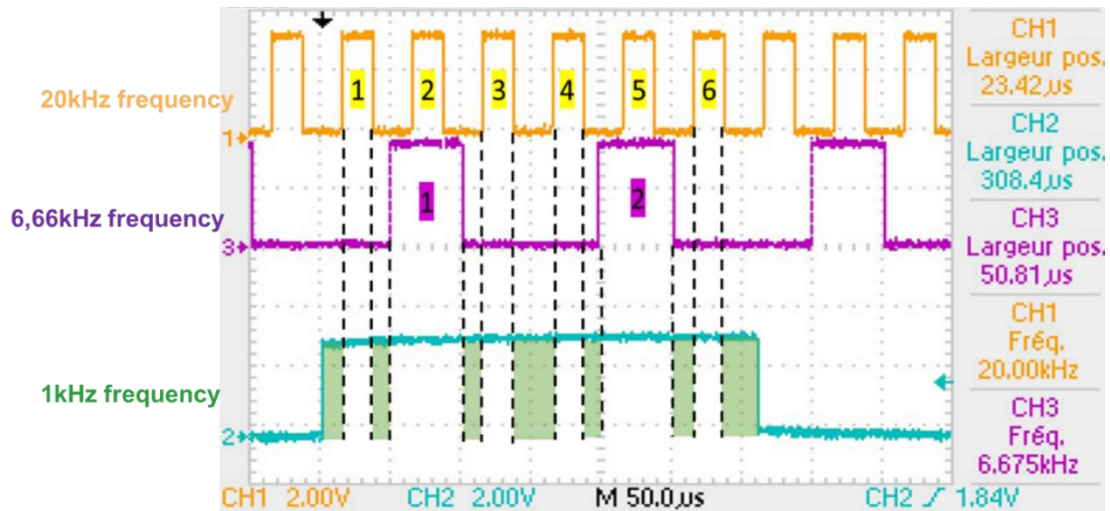


Figure 4.8: Identification on the measured CPU signal.

Hence, the real activity of each sampling block is defined by:

- real activity(20 kHz) = measured activity (20 kHz)
- real activity(6.66 kHz) = measured activity (6.66 kHz) – real activity (20 kHz)
- real activity(1 kHz) = measured activity (1 kHz) – 2×real activity (6.66 kHz) – 6×real activity (20 kHz)

Table 4.2 proposes information concerning the sampling blocks: the real time executed frequency, the maximal period, the measured activity, the real activity and finally the calculated real CPU load for each sampling block. The CPU load is defined by the equation:

$$\text{CPU load (\%)} = \frac{\text{real activity}}{\text{maximal period}} \cdot 100 \quad \text{eq 4.2}$$

Table 4.2: CPU load for the proposed controller

Frequency	Real execution frequency	Maximal period	Measured activity	Real activity	CPU load by sampling block
20 kHz	20000 Hz	1/20000 = 50 μ s	23.42 μ s	23.42 μ s	46.84 %
6.66 kHz	6675 Hz	1/6675 = 150 μ s	50.81 μ s	27.39 μ s	18.50 %
1 kHz	1000 Hz	1/1000 = 1000 μ s	308 μ s	112.7 μ s	11.27 %
				CPU load	76.61 %

It can be noted in Table 4.2 that the CPU load is a little higher than recommended for safety, around 70-75 %, but the VSG control is functional and efficient. Table 4.2 highlights the fact that the main part of the CPU load is used for the 20 kHz sampling block. The CPU load percentages of the 6.66 kHz and 1 kHz sampling blocks are similar, around 15 %. An important part of the 20 kHz sampling block activity is used for the Park transformation: abc-axis conversion to dq-axis for the output inverter currents, output inverter voltages and grid voltages, in addition of the dq-axis conversion to abc for the duty-ratios. The 0 axis of the dq0-axis is not represented, as the system is considered as a three-phase balanced system without neutral. The addition of the 0 axis in the 20 kHz sampling block will thus increase the CPU load even more. To conclude, the proposed controller can be integrated in the inverter DSP in the proposed configuration. Concerning the parameters value of the proposed controller, the same parameters as described in 3.6.2 (p69) and Appendix 6 (p173) are kept.

4.2.3 Assessment of the implementation of the controller

Some adaptations have been made to ensure that the VSG controller can be implemented in the DSP of the industrial inverter control card: conversion into fixed-point, modifications of the matrixial equation with optimized multiplications for the DSP calculation with the selection of the fixed-point value of the variables. Finally, the CPU load of the inverter control card is verified to ensure that the VSG controller will be correctly functioning. Consequently, the controller can be implemented in the industrial inverter card. It was then possible to begin the experimental validation of our proposed controlled, integrated in a real microgrid that is detailed in the next section.

4.3 Experimental validation of the VSG implementation

The VSG is developed to be a plug-and-play solution for microgrids with a high share of renewable sources. its intended function is to improve the stability of microgrids during important load variations and renewables sources fluctuations.

A lot of research has been conducted on the behaviour of VSG supplying power to balanced loads, [25], [59], and unbalanced loads [25], [60]. also considering harmonics [25]. There is currently no standard for VSG, hence, the results of this chapter consist of a first set of tests to define VSG standards. In that context, the VSG's behaviour is also studied in parallel with other power sources, like with other

VSGs, as described in [47], [61] or with other type of sources, like generator sets [19], [52]. The tests proposed in this chapter must be validated before considering the large scale integration of VSG in grids.

4.3.1 Schneider Electric Microgrid Laboratory

The proposed controller for VSG was tested within the Schneider Electric R & D centre in Grenoble (France). This is a dedicated microgrid laboratory which includes several power sources that can be put in parallel on a 100 kVA distribution network at a voltage of 230 V RMS and a frequency of 50 Hz. The power sources are of two kinds: diesel generator sets with three different characteristics (15 kVA, 45 kVA and 50 kVA) and four inverter-based power sources connected through SCHNEIDER SOLAR inverters of 25 kVA. Two of them are in grid-feeding mode (supplied by a DC power source) associated with solar emulators, both operated using a VSG-based control. Several loads are connected to the distribution network: RLC and industrial loads (induction motors, a compressor and a motor controlled by a 15 kVA drive). Finally, a short-circuit cabinet with different combinations is also available. The possible scenarios are: phase-neutral, phase-phase, three phase and phase-ground. A global picture of the laboratory can be seen in Figure 4.9, the complete microgrid single line diagram is proposed in Appendix 9 (p187).

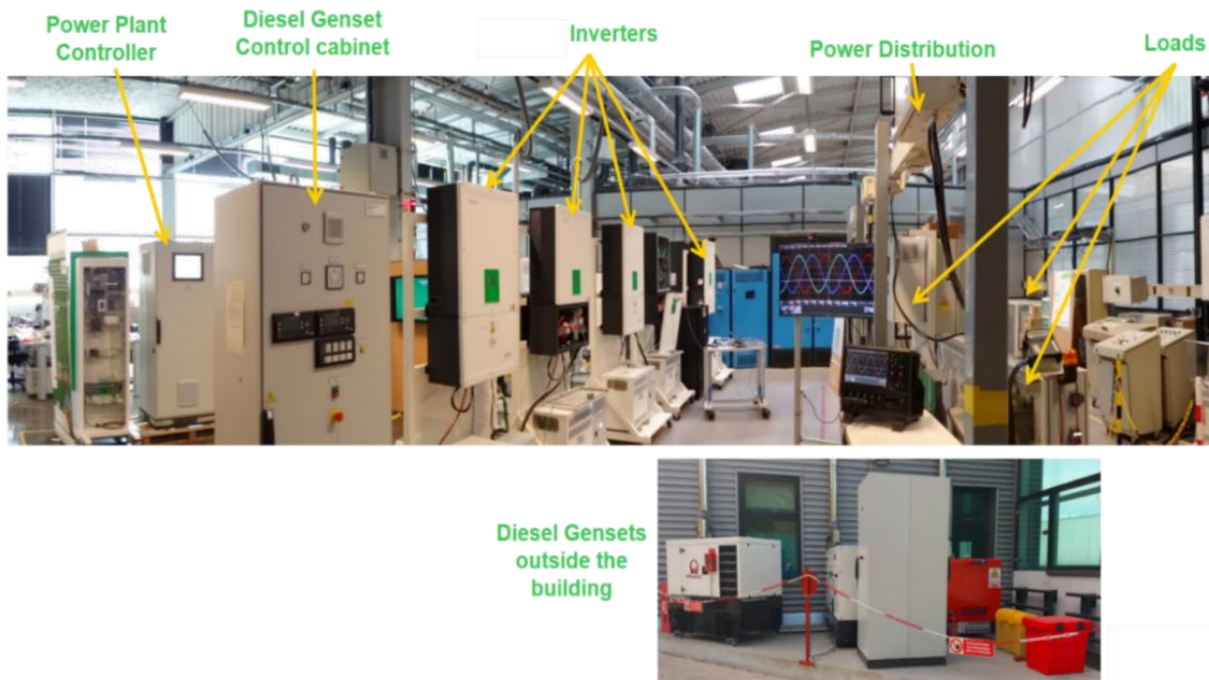


Figure 4.9: Schneider Electric microgrid installation.

4.3.2 Experimental results with the proposed controller

In this section, experimental results under selected scenarios are studied to validate the proposed VSG controller for an application in an industrial context. The validation tests are separated in two sections: one where the VSG is in a standalone mode and one where the VSG is operated in parallel with other power sources (another VSG inverter and/or generator sets). The tests results have been selected based on the different standards validation that can be found in the literature and industrial expectations that have been detailed in Chapter 2 (2.4.2 – p24). Indeed, SM is an established solution, requirements and specifications are well developed in term of design and performances [41]–[44]. As

there is no specification or standards yet on the circulating currents between the inverters, the generator and SM standards are considered as reference to determine the impact of the SM models on the VSG performances. In addition, in the microgrids context, the VSG is not the only power supply solution. This is the reason why a parallelism study with similar or other power sources must be considered to finalize the study.

4.3.2.1 Standalone VSG

In this section, the VSG with the proposed controller represents the unique power source connected to the microgrid. The tests described will ensure that the proposed controller is stable during multiple harsh events as it is represented in Figure 4.10.

As the inverters are supplied by the same DC source, a battery or a super-capacitor, in order to avoid the circulating currents between, each inverter is directly connected to a D-Yn transformer, as it can be seen in in Figure 4.10. In the different tests presented, the currents are measure at the output of the inverter, so before the transformer and after the LCL filter. The voltages measure is done at the grid voltage, after the transformer.

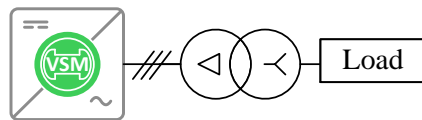


Figure 4.10: Schematic representation for standalone tests.

It can be noted that basic tests such as off-loaded black-start or small load variations are not presented in this section. Indeed, these tests are mandatory to consider the system stable for a possible integration in a microgrid and do not represent a significant added value in the study as they are less difficult to validate than the one presented here.

The dynamic behaviour of the VSG during traditional load impacts but also when starting on maximal load and short-circuit are experimentally investigated to ensure a good integration in a microgrid. In addition, other tests such as the harmonics tests have been selected based on standards validation that can be found in the literature [41]–[44]. With the same consideration, non-linear loads and short-circuits are not commonly tested in the various studies on VSG although they are mandatory before any possible industrial implementation in a microgrid.

- **Starting on maximal load**

As the power supply can be variable in a microgrid, the VSG should be able to start at the maximal load when needed.

This test is conducted to validate that the VSG has the capability to do a black-start with load connected to the microgrid. Hence, for this test, a 20 kW load is connected to the VSG before its starts. It can be noted that the VSG takes about 600 ms to reach the nominal voltage value. The starting time response of the VSG have been adjusted taking into account the risk of load resonance resulting on a possible instability VSG model.

Figure 4.11 shows that the VSG can start properly at its maximal power while supplying the full load and stay stable. It means that the developed solution supports the black start without problem.

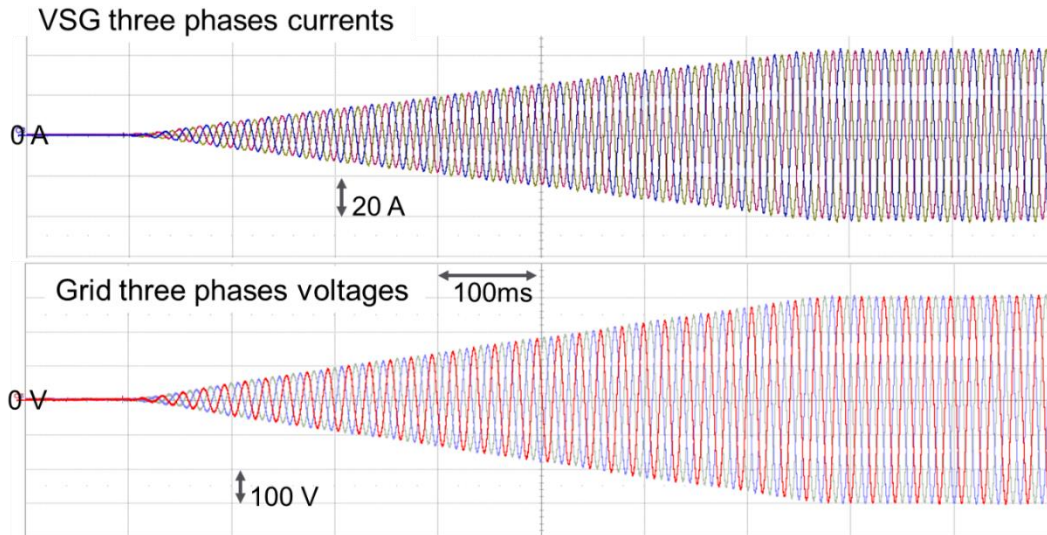


Figure 4.11: VSG behaviour during a start on a 20 kW load.

- **Maximal Power load Impact**

A load variation or the loss of production presents a high probability in microgrids supplied by renewable energies. The objective of this test is to validate the fact that the VSG is stable during harsh load variations.

Figure 4.12 shows the transient dynamic behaviour of a VSG under a resistive 20 kW load impact. The voltages and currents waveforms are the same as a real SM with a sub-transient and transient phenomenon before stabilizing to steady-state as defined in the standard [44].

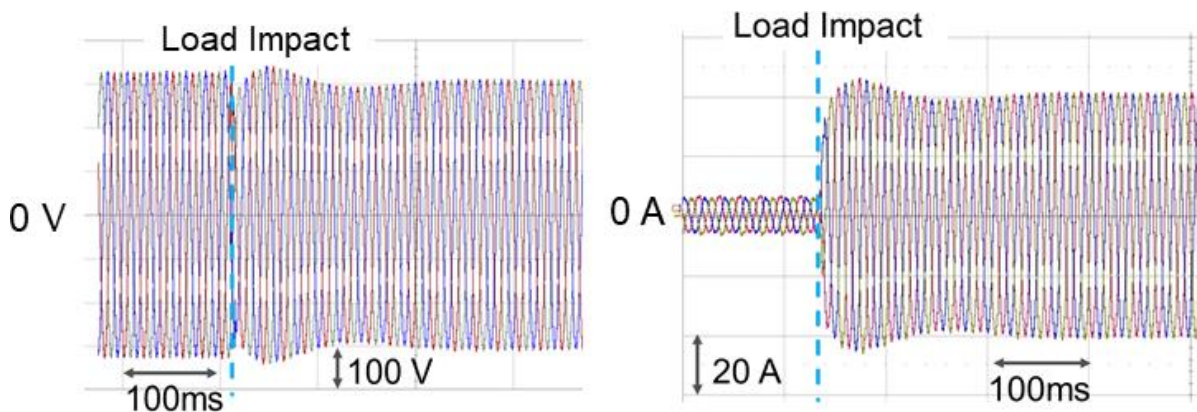


Figure 4.12: VSG behaviour during a load impact of 20 kW.

During the load impact, the output voltages of the VSG decrease until the AVR applied in order to bring back the voltage to its nominal value. Thanks to the AVR and the implemented droop control, the VSG stabilizes to a new voltage value while supplying the 20 kW load.

To conclude, Figure 4.12 shows that the VSG stays stable during load impact equal to its maximal power load.

- **Maximal Power load Shedding**

The objective here is to ensure that the VSG remains stable during a 100 % load shedding. Indeed, with high voltages and currents variations, the inverter saturates, which impacts the voltage quality and could create overvoltage that can deteriorate the loads or components connected to the microgrid.

Figure 4.13 and Figure 4.14 show the transient dynamic behaviour of a VSG under a 20 kW load shedding. On Figure 4.13, the VSG rapidly stabilizes from a production currents of 40A to 2A without incident.

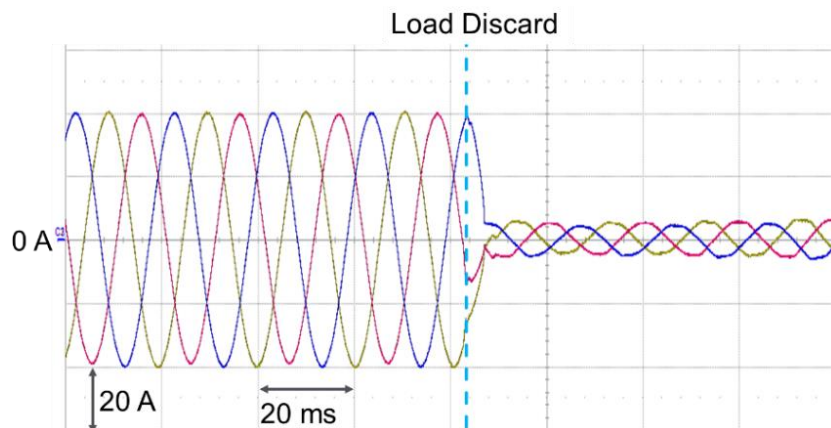


Figure 4.13: Zoom on the Currents behaviour during a load shedding of 20 kW.

Figure 4.14 shows the typical voltages waveforms of a real SM with a sub-transient and transient phenomenon before stabilizing to steady-state as defined in the standard [44].

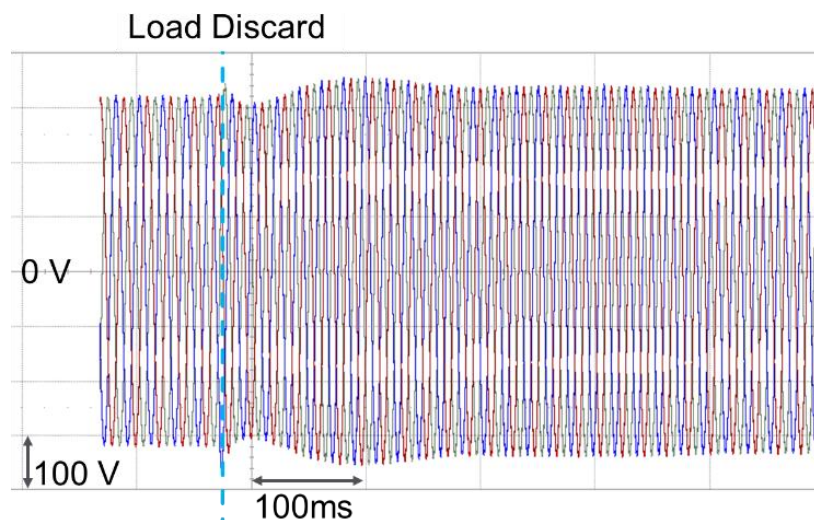


Figure 4.14: VSG voltages behaviour during a load shedding of 20 kW.

Hence, the VSG is capable to remain stable under load shedding equivalent to it maximal power without saturation as it is shown by Figure 4.13 and Figure 4.14.

- **Highly inductive load**

A real SM can't supply a load with a power factor below 0.8 in steady state as it will deteriorate the physical elements of the generator. This is not a problem for the VSG if its model is stable. This is a benefit of the VSG compared to traditional SM-based generation.

Figure 4.15 shows that the voltages produced by the VSG are stable and they also respect the classical waveforms of a SM model.

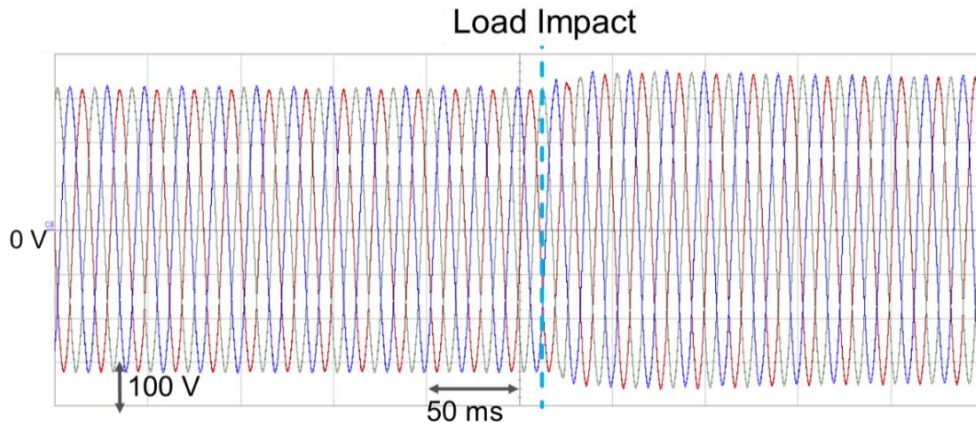


Figure 4.15: VSG voltage behaviour supplying a 17.5 kVAr load.

Figure 4.16 show that the VSG supply correctly the 17.5kVAr load. It can be noted that, during the transition, there is a peak of current that reach the limit output current of the inverter (60A). This high current, visible at the load connection, is due to the voltage variation across the inductor creating a transient DC current. Then, the created DC current is rapidly absorbed until its disappearance.

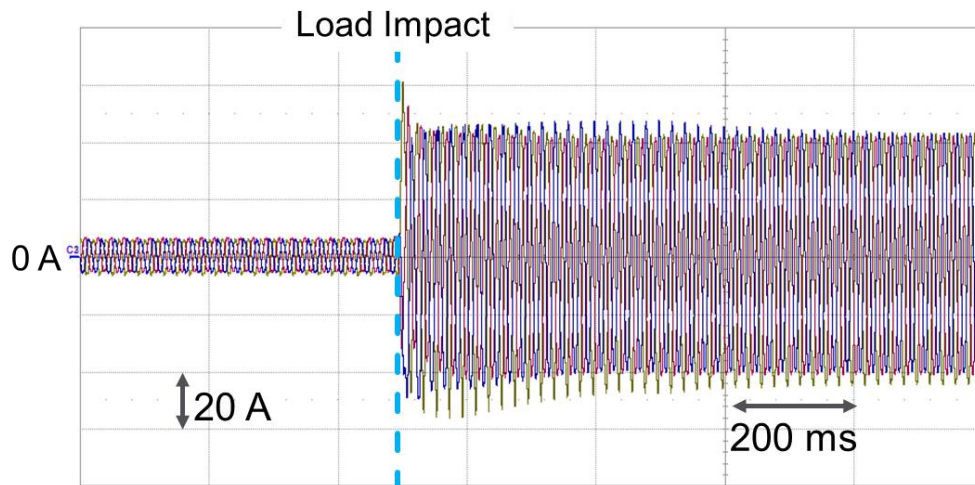


Figure 4.16: VSG current behaviour supplying a 17.5 kVAr load.

This test proposes a 17.5 kVAr impact to verify that the VSG is stable and can supply a load with a power factor near 0 with Figure 4.15 and Figure 4.16. Hence, the VSG is capable to supply any power factor loads and is not limited in power factor as a traditional SM.

- **Harmonics Validation**

A non-linear load is connected to the off-loaded VSG as detailed by the standard [41] and Chapter 2 (2.4.3 – p30).

Table 4.3: THD_V and individual harmonics results with non-linear load.

THD_V In % of rated voltage < 5 %				
THD_V	3.80			
Individual Harmonic value in % of rated voltage < 3 %				
Harmonic value	3	5	7	11
VSG	0.090	0.341	0.237	0.106

It can be noted that the measures on the VSG differ from the one calculated in Chapter 2 (2.4.3 – p30), especially the 3rd individual harmonic. The differences most likely come from the integration of a transformer at the output of the VSG. Indeed, as explained before, a transformer in a D-Yn configuration is connected at the output of the inverter to do an electrical separation between the AC and the DC sides of the inverter. Hence, the D configuration of the transformer avoids the propagation of the 3rd order individual harmonic, which explains the small value of the 3rd order harmonic in comparison to the simulation.

To conclude, the VSG respects the characteristics defined by the norms as the total harmonics distortion is inferior to 5 % and individual harmonics are below 3 %.

- **Non-linear and Unbalanced load**

To consider an industrial development, a VSG should be capable of supplying any load including unbalanced or non-linear loads, especially motors or drives. Indeed, industrial grid-connected or off-grid facilities represent an important percentage of the microgrid loads.

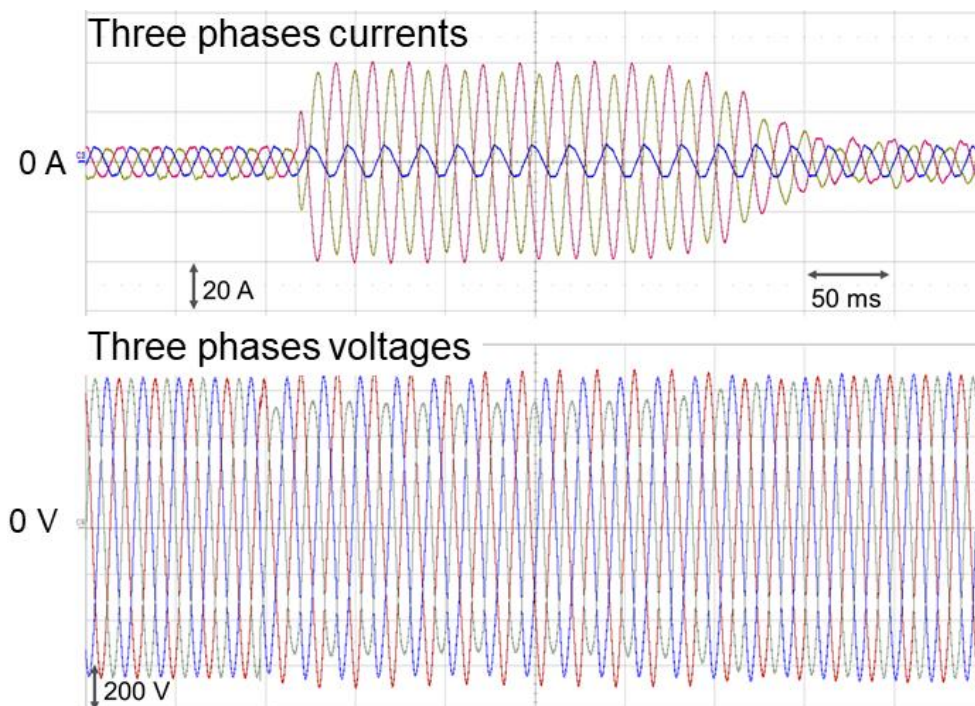


Figure 4.17: VSG behaviour supplying a 3 kW single phase motor.

As the VSG is supplying a highly unbalanced load, a single-phase motor, only two phases are impacted by the load. The currents supplying the motor reach 40 A on two phases when the third stays around 2 A, equal to the off-loaded value. Similarly, the same impact can be seen on the voltage: two phases are more impacted due to the unbalanced load.

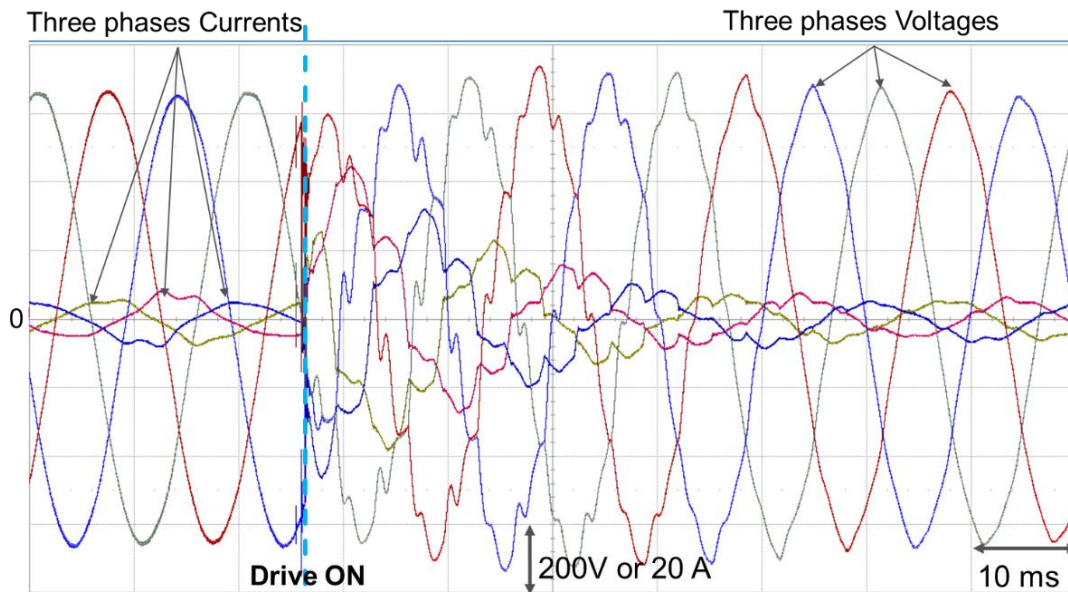


Figure 4.18: VSG behaviour supplying a 15 kVA drive connected to a DC machine.

As the drives are highly non-linear loads, Figure 4.18 shows the high distortion of the VSG output voltages when supplying the 15.5 kVA drive. It can be noted that after the drive connexion, the voltage stabilizes after 50 ms. Similarly to the voltages, the currents are also highly distorted due to the non-linear characteristics of the drive. It can be noted that the voltage distortion is similar to the simulation results presented in Chapter 2 (2.4.3 – p30) with the complete SM model.

Figure 4.17 and Figure 4.18 show that the VSG remains stable supplying significantly unbalanced or non-linear loads such as single phase motor or a drive.

Figure 4.19 and Figure 4.20 show the VSG behaviour supplying a compressor of 5.5 kVA. Firstly, the compressor's starting phase lasts 1.5s which is longer than when the compressor is supplied by a traditional generator.

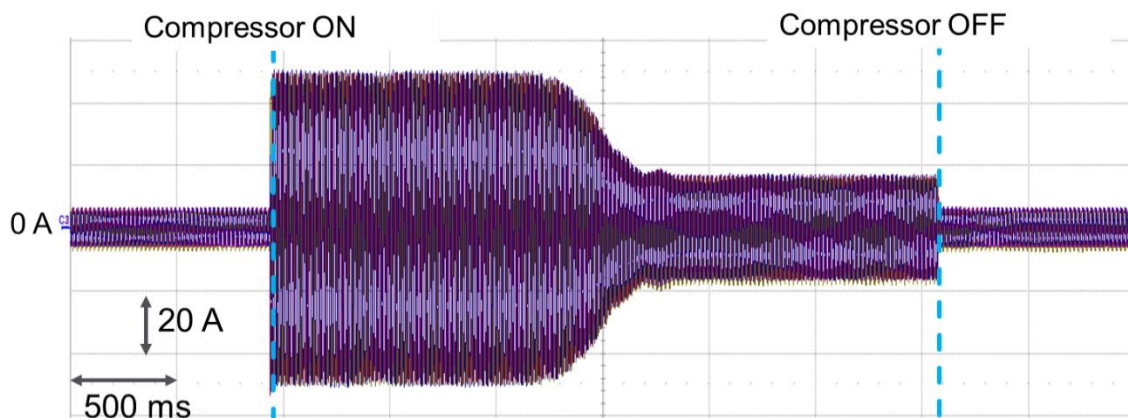


Figure 4.19: VSG three-phase currents behaviour supplying a compressor.

This delay in the starting of the compressor is due to the output inverter current's saturation as it's visible in Figure 4.19. Indeed, an inverter can't supply the same outputs current as a real SM ($2.I_N$ or $3.I_N$) when necessary to start industrial elements like compressors. Inverters are often sized to supply $1,2.I_N$ or $1,5.I_N$ and not more by default. This current limitation must be considered to size the necessary VSG power supply of a microgrid with industrial components, such as compressors or motors.

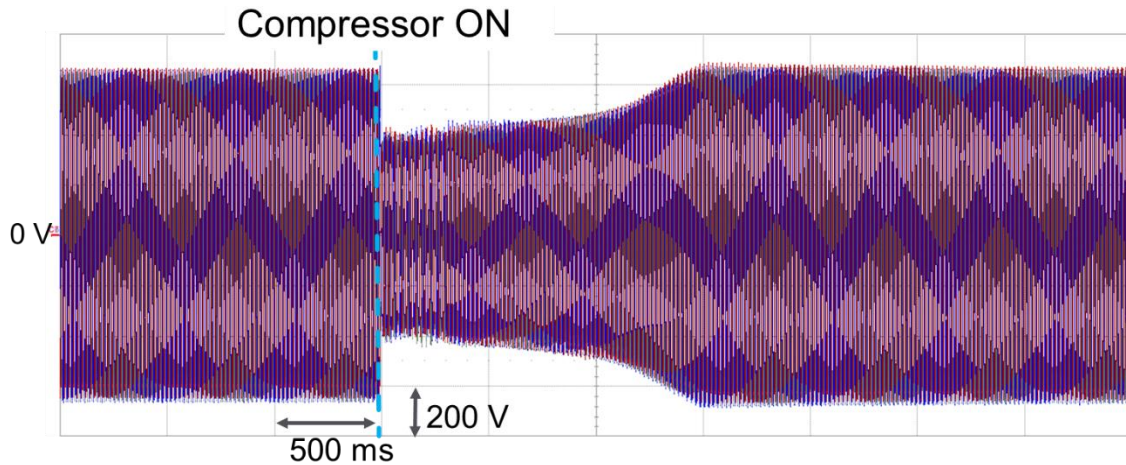


Figure 4.20: VSG three-phase voltage behaviour supplying a compressor.

Secondly, on Figure 4.20, the output inverter voltage drops when the output current limit is reached. Indeed, when the maximal output current is reached, the classical voltage reference can no more be supplied by the inverter. Hence, the voltage droop controller decreases the voltage output references in order to ensure the VSG model stability. This phenomenon also explains why the compressor's starting phase is longer than with a more traditional power supply. Once the currents supplied by the VSG are below the limit, the voltage increases until it reaches the reference. In addition of the current limitation, this protection also needs to be considered when sizing the number of VSG supplying a microgrid with mainly industrial components.

Figure 4.17 to Figure 4.20 show that the VSG with the proposed controller is stable when supplying non-linear or unbalanced loads. These tests also demonstrate one limit of the VSG, when the maximal output current of the inverter is reached. Indeed, the inverter outputs current limitation must be considered in the microgrid's sizing when using VSG, especially if the microgrid is constituted of industrial components and presents strict operational requirements.

- **Short-circuit**

Short-circuits are another test that VSG-based inverter must validate for being considered as acceptable sources for microgrids. Indeed, the maximal output current of inverters is limited between 1.5 to 2.5 times their nominal value and cannot compete with the short-circuit current of a real SM (up to a factor 10). So, inverters present a saturation. In that context, the VSG must remain stable (i.e. connected) during a short-circuit, supplying the current during the time needed for the electrical protections to clear the short circuit.

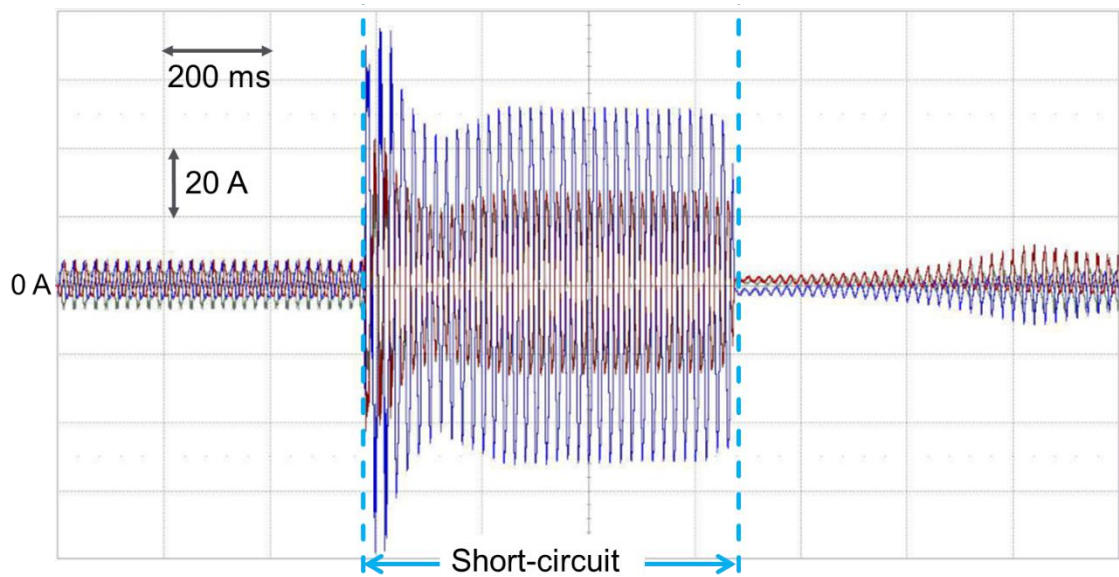


Figure 4.21: VSG currents behaviour during phase-phase short-circuit.

Figure 4.21 shows the VSG output current supplying the phase-phase short-circuit. At the start of the short-circuit, the maximal current is reached until there is a stabilisation after 200 ms. As the short-circuit is phase-phase, in two phases the currents are equal. The third phase is equal to minus the sum of the two others. In addition, on Figure 4.21, during the last 400 ms, the transformer (connected to the VSG) magnetisation currents can be observed.

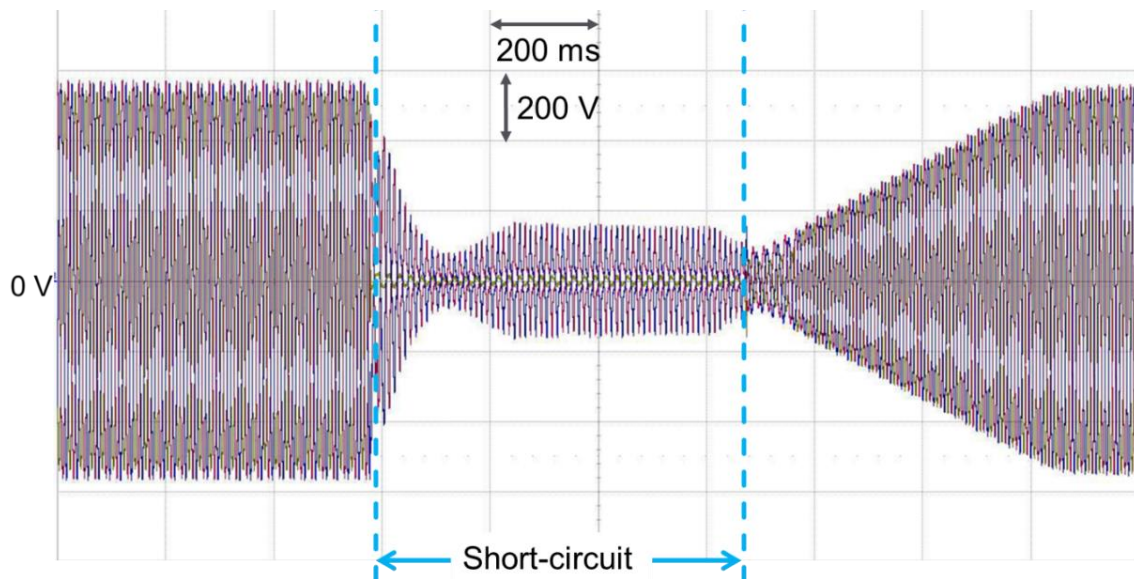


Figure 4.22: VSG voltages behaviour during phase-phase short-circuit.

Figure 4.22 shows the VSG output voltages supplying the short-circuit. It can be noted that the voltage decreases in 200 ms due to the phase-phase short-circuit and the fact that the VSG is a balanced source. In Figure 4.22, after the fault clearance, it can be noted that the voltage increases until it comes back to its nominal value in 600 ms.

Figure 4.23 is a zoom on the beginning of a tri-phases short-circuit. The VSG's voltage is null and current oscillations can be seen due to the output LCL filter and the transformer. Similarly to the phase-

phase short-circuit, the supplying the short-circuit currents stabilize after 15 ms. After the stabilisation, the short-circuit current is equal to the maximal inverter current limits.

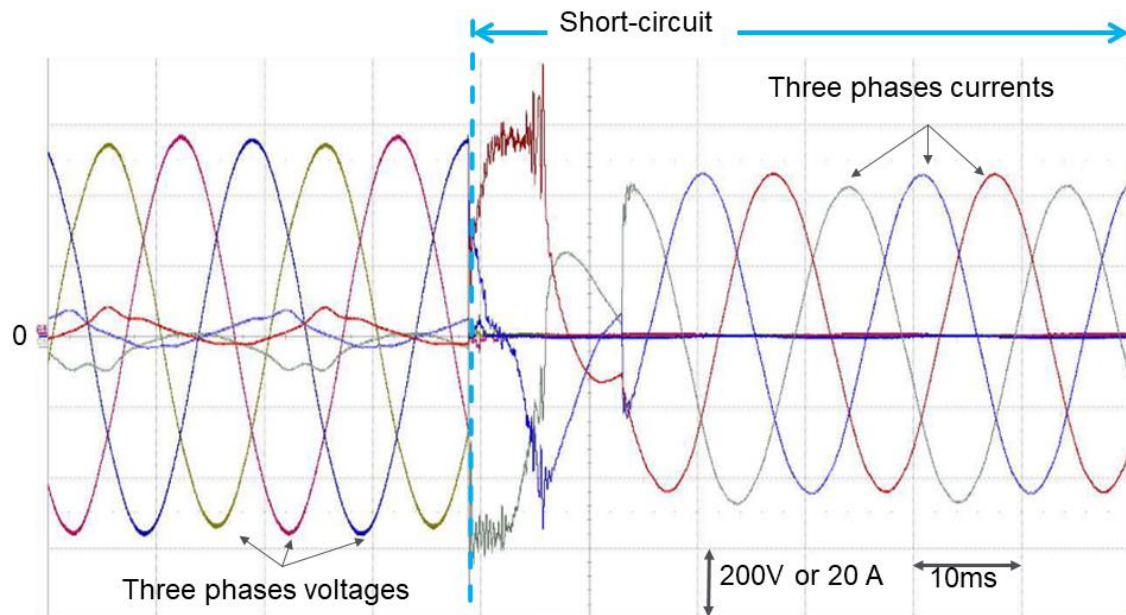


Figure 4.23: VSG behaviour during a tri-phases short-circuit.

Figure 4.21 to Figure 4.23 show that the VSG remains stable during a short-circuit and supplies the short-circuit to help to its detection by the protections.

As it was explained in the Chapter 2 (2.4.2.2 – p28), it can be noted that the output currents of the VSG are limited between 1.2 to 2.5 times the nominal output current and cannot follow the short-circuit current of a real SM. With the output current limit of the inverter, traditional protections using the SM short-circuit current to trigger will not detect this short-circuit. This means that with the increase of inverter-based generators, the detection of short-circuits by the traditional protections will become a problem. Hence, given that the short-circuit prediction is difficult, the VSG must be stable during a short-circuit to help the protection detecting faults. A first possibility to ensure a good detection of the fault may be to include voltage measures to traditional protections in order to overcome the maximal short-circuit current limitation. Another possible solution is to develop standards for the VSG behaviour during short-circuit in order to calibrate the protections based on these VSG performances.

4.3.2.2 VSG in parallel with other power sources

The VSG must be a plug-and-play solution, thus operating correctly in parallel with other power sources in a microgrid. As described in [47], the microgrid instabilities can be exacerbated by the resonance among generators and VSGs. Hence, it is necessary to validate the capacity of our proposed VSG solution to operate in parallel with other power sources, especially in the context of an industrial certification. The previous tests cases, detailed for a standalone VSG, have been conducted to ensure the VSG stability in parallel with other power sources. Two of the most representative examples of parallelisation are selected, which are represented in Figure 4.24, one with another VSG and one with a generator set.

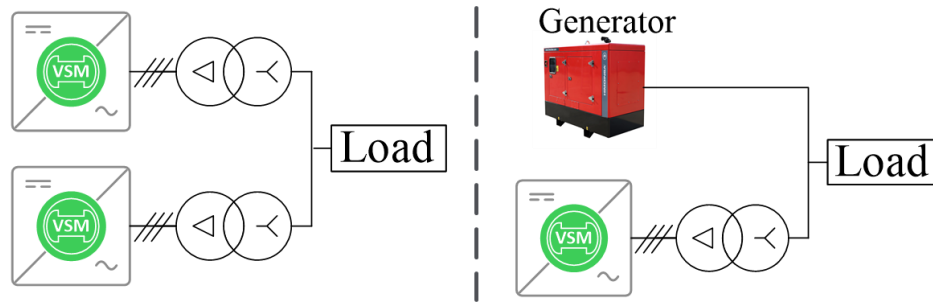


Figure 4.24: Schematic representation of VSG inverter in parallel with other power source supplying a load.

- **Parallel operation with a generator**

In Figure 4.25 and Figure 4.26, a highly inductive 35 kVA load impact on a 20 kVA VSG and 45 kVA generator is conducted.

Figure 4.25 shows the microgrid voltage during the load impact. When the load is connected to the microgrid, the voltage decreases and then rapidly increases to its nominal value thanks to both power sources in the microgrid. The microgrid voltage remains stable without oscillation as both power sources share the load.

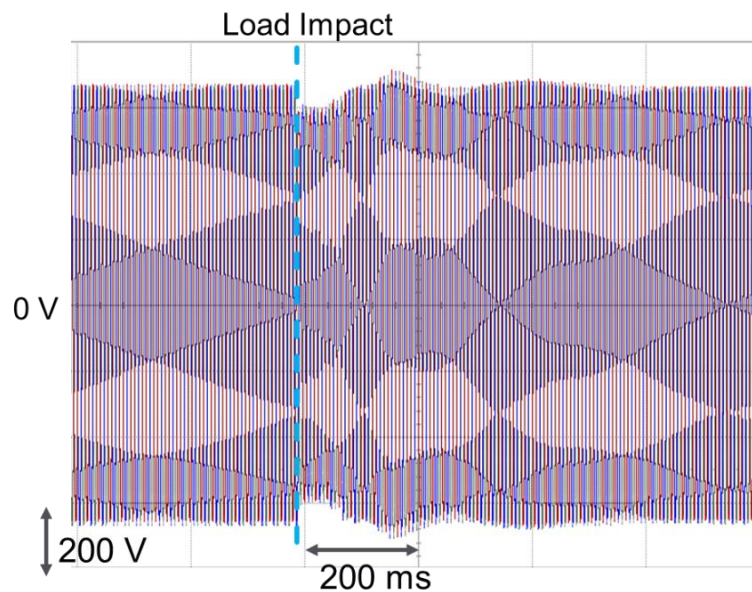


Figure 4.25: Microgrid voltages for the load impact of a 25 kVA load.

Figure 4.26 shows that both power sources supplied the loads throughout the test. When the load is connected to the microgrid, both power sources produce an important current due to the load characteristics. The VSG rapidly absorbs the DC current (in less than 200 ms). This is not the case of the traditional generator which takes more than 400 ms until the DC current disappears with the proposed controlled. After the DC current dissipations for both power sources, the load's current is divided equally between the VSG and the generator.

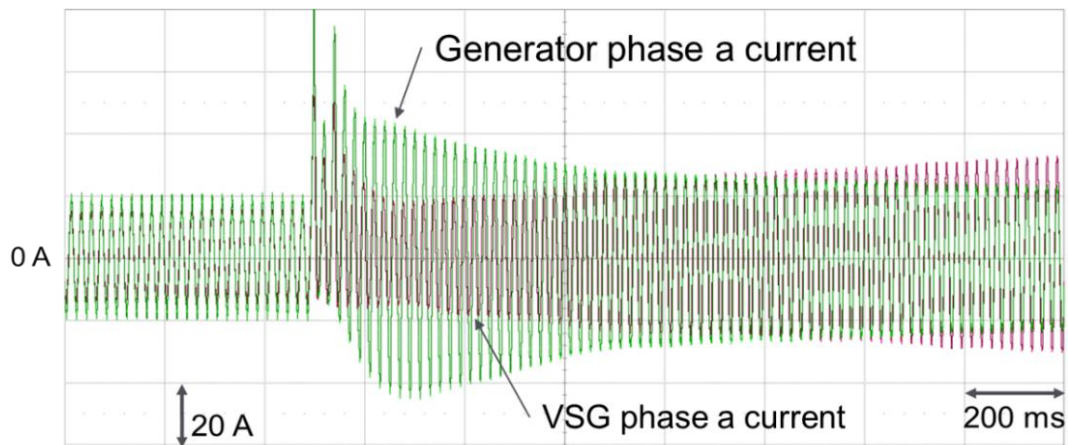


Figure 4.26: VSG and generator one phase current supplying a 35 kVA load.

To conclude on the parallel operation with a generator, the VSG with the proposed control can be put in parallel with other power sources and ensure the microgrid stability.

- Parallel operation with another VSG

Finally, the last presented test is the application of a 40 kVA load on a microgrid constituted of 2 VSG inverters. Figure 4.27 shows that the voltage of the microgrid is stable supplied by both VSGs and is stabilized after 200 ms. This voltage stabilizes more rapidly with two VSG inverters than with a VSG and a generator as the two VSG have similar time responses and behaviour. Similarly, the microgrid voltage behaviour is similar to what can be found in Figure 4.12, presenting the VSG behaviour supplying a 20 kW load. During the load impact, the voltage decreases due to the load addition and then rapidly increases when the effect of the AVR is present, back to its nominal value.

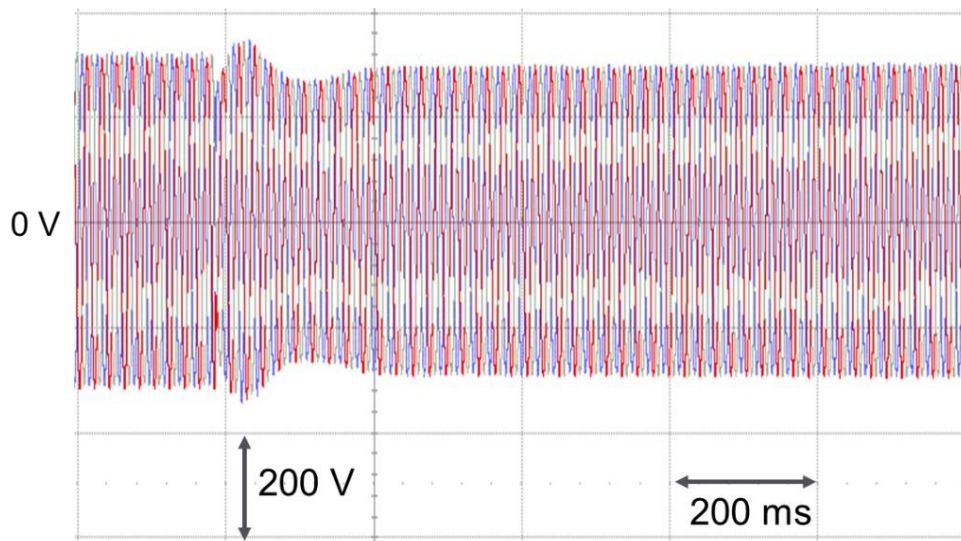


Figure 4.27: Microgrid voltage for a load impact of 40 kVA.

Figure 4.28 shows one VSG output currents during the load impact. It can be noted that the output currents of the VSG present some oscillation after stabilizing around 45 A. The current oscillations are due to the transient behaviour of both VSGs and the fact that their current limit of 55 A is reached. The transient behaviour rapidly stabilises in less than 200 ms.

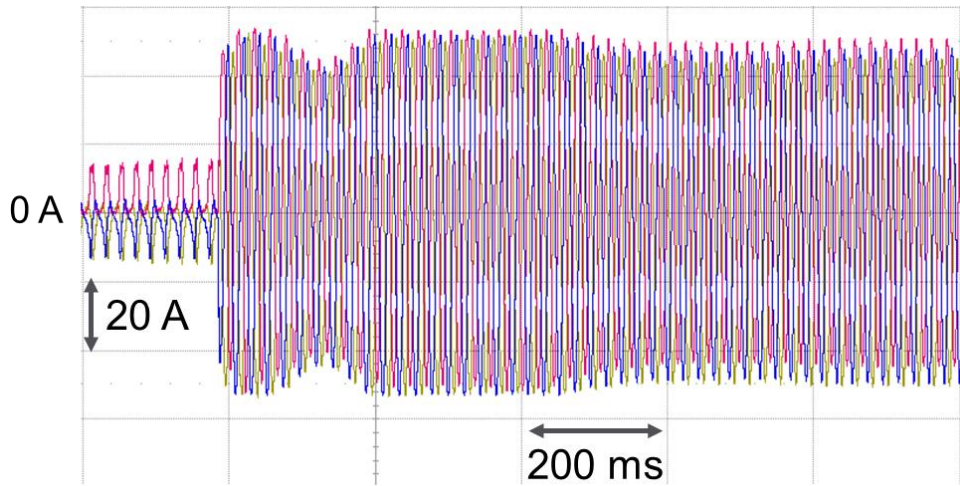


Figure 4.28: Output VSG currents for a load impact of 40 kVA.

To conclude on the parallel operations, the VSG with the proposed control can be put in parallel with other power sources of the same or different nature. The presented tests as well as all other experiments conducted during the PhD were conclusive in that sense.

4.4 Conclusion

In the first section of this chapter, the methodology to adapt the proposed controller for its implementation in a DSP is described. The VSG controller is divided in three parts: a block sampling at 20 kHz for the current controller and measures, a sampling block of 6.66Hz for the SM model and finally, a 1kHz block for the voltage and frequency stability. Firstly, to minimize the CPU load, the entire controller is converted into fixed-point values. In order to determine the optimal fixed-point value for each variable, multiple simulations have been conducted to determine their range. Then the next step of the adaptation was to change the entire matrixial system into optimized DSP multiplications and summations to reduce the calculation time of the DSP. During this stage, the value of the fixed-point elements was selected. Indeed, the DSP multiplications is optimized for similar fixed-point values but applying a small fixed-point value means reducing the precision of the computation. This adapted controller was implemented in the industrial inverter successfully with a CPU load close to the limit but acceptable for a viable control.

Then various experimental results are presented, based on use cases constructed in the microgrids laboratory in the Schneider Electric R & D facility in Grenoble, France. A first step shows the validation of the SM behaviour during traditional resistive load impacts. Contrary to many other studies on VSG, less traditional loads, as non-linear or unbalanced ones were also studied. Indeed, as the industrial development of the VSG is considered and as grid-connected or off-grid facilities generally involves non-linear loads, supplying motors and drives are added to the use cases for the VSG validation. Thanks to the proposed controller, the VSG is stable and capable of supplying highly non-linear or unbalanced loads such as drives or single phase motors as well as survive short-circuits, which are mandatory to guarantee the well-functioning and plug-and-play operation of VSG in microgrids. Two different short-circuits are tested: tri-phase and bi-phases.

Finally, as the VSG parallel operation is mandatory to validate any possible industrial development, the behaviour of the VSG is studied in parallel with a generator set supplying a compressor and in parallel with the same VSG with a more traditional load. The same use-cases were tested in those configurations and showed that the proposed VSG-based controller is a robust solution.

Now that the proposed controller is validated in simulation and in experimentation at the Schneider Electric laboratory, in the next chapter, Chapter 5, will be described a methodology to validate the replicability and portability of the VSG-based controller to other inverters of various characteristics.

Chapter 5. Replicability and portability of the VSG control

5.1 Introduction

Now that the proposed controller has been analytically detailed and validated in simulations and in experimentation at the Schneider Electric laboratory, the objective of this chapter is to assess the portability and replicability of the VSG solution on various inverters with different technical characteristics.

In order to improve the integration of the VSG solution in microgrids, one of the simplest solutions is to implement it on actual inverters as discussed in the previous chapter. However, depending on the size of the selected inverter, two problems can appear. The first one is linked to the SM model used for the VSG. Indeed, depending of the inverter characteristics, the SM model could not be adapted regarding the nominal voltage and the nominal current. The second problem is linked to the controllers, especially the current controller, which must often be entirely reconfigured. Thanks to the fact that the entire control is develop in p.u. and built on the SM model, the proposed controller helps ensuring the portability and replicability of the VSG solution to various inverter as there is no necessity to reconfigure it.

In this chapter, the first section develops the methodology allowing adapting the SM parameters of the VSG model to the inverter's characteristics. The second section presents the laboratory-scale prototype system on which the methodology to replicate the VSG controller is applied to another

inverter. Finally, the experimental results of the VSG with the adapted SM model parameters and the proposed controller are presented when its integration to a microgrid is assessed.

5.2 VSG control portability methodology

The objective of this methodology is to determine the adapted SM parameters for the VSG solution including the proposed controller, based on the inverter's characteristics, that ensure the replicability and portability of the VSG solution.

In addition to develop a SM model adapted to the inverter's limits, the other objective of this methodology is to ensure that the SM model still represents as much as possible a real SM, maintaining the relationship between the SM parameters. Hence, when possible, the relationship between the inverter's characteristics and the parameters of the SM complete model are based on real SM or on what can be generally found in datasheets.

As the complete SM model requires the most important number of parameters, the methodology of replicability is based on this model but can be also applied to determine the parameters of the reduced and static models.

5.2.1 Inverter characteristics

The inverter's characteristics considered for the methodology to determine the SM parameters adapted to the inverter are:

- The maximal inverter currents, I_{ond}^{max} in A;
- The inverter output nominal current, I_n in A.
- The PWM switching frequency, f_{IGBT} in Hz;
- The inverter output nominal voltage, E_n , phase-phase, in V;

The frequency, f_{IGBT} , permits defining the time responses of the SM complete model. The maximal inverter currents and the nominal voltage and current help determining the reactances and the resistors of the SM model.

5.2.2 Parameters for the complete SM model

5.2.2.1 SM complete model hypothesis and characteristics

As described in Chapter 2 (2.3.1 – p12), the following SM parameters must be determined:

- Reactances: $X_d, X'_d, X''_d, X_q, X'_q, X''_q, X_2, X_l, X_0$
- Stator resistor: R_s
- Time constants: $T'_d, T''_d, T'_{do}, T''_{do}, T'_q, T''_q, T_a$

These SM parameters must respect the following relations [45], [62], [63]:

$$\begin{aligned}
X_d &\geq X_q \geq X'_q \geq X'_d \geq X''_q \geq X''_d \\
T'_{do} &\geq T'_d \geq T''_{do} \geq T''_d \\
T'_{qo} &\geq T'_q \geq T''_{qo} \geq T''_q
\end{aligned} \tag{eq 5.1}$$

In addition of the relationship defined eq 5.1, the SM model should also be based on the equations extracted from [45], [62], [63]:

$$\text{In the d-axis: } \frac{T'_{do}}{T'_d} = \frac{X_d}{X'_d} \tag{eq 5.2}$$

$$\frac{T''_{do}}{T''_d} = \frac{X'_d}{X''_d} \tag{eq 5.3}$$

$$\text{the q-axis: } \frac{T''_{qo}}{T''_q} = \frac{X'_q}{X''_q} = \frac{X_q}{X''_q} \tag{eq 5.4}$$

5.2.2.2 SM complete model reactances

To determine the impedances of the d-axis, X_d, X'_d, X''_d , the maximal current produced by the inverter I_{ond}^{max} and the nominal characteristics of the inverter are used. In order to link the inverter characteristics to the d-axis reactance of the SM model, X_d, X'_d, X''_d , the SM short-circuit currents equation is considered. The short-circuit current SM characteristics is defined by the equation:

$$\begin{aligned}
I_{sc}(t) = E_n &\left[\frac{1}{X_d} + \left(\frac{1}{X'_d} - \frac{1}{X_d} \right) \cdot e^{-t/\tau'_d} + \left(\frac{1}{X''_d} - \frac{1}{X'_d} \right) \cdot e^{-t/\tau''_d} \right] \cos(\omega \cdot t + \psi) \\
&+ \frac{E_n}{2} \left[\left(\frac{1}{X''_d} - \frac{1}{X'_d} \right) \cdot e^{-t/\tau_a} \right] \cos(\psi) + \frac{E_n}{2} \left[\left(\frac{1}{X''_d} - \frac{1}{X'_d} \right) \cdot e^{-t/\tau_a} \right] \cos(2\omega \cdot t + \psi)
\end{aligned} \tag{eq 5.5}$$

With ψ the phase angle (rad), and ω the angular velocity (rad/s).

- **Reactance X_d**

Contrary to the SM, the maximal inverter current is usually limited between 1.5 to 2 times the nominal current. Hence, the selected solution for the sizing of the X_d parameter is based on the permanent short-circuit current, to simplify the short-circuit detection by the inverter's protection. Hence, the link between the maximal inverter output current and the SM short-circuit characteristics is:

$$I_{sc}(t = \infty) = I_{ond}^{max} \tag{eq 5.6}$$

Considering $t = \infty$, the SM short-circuit current $I_{sc}(t = \infty)$ is defined by

$$I_{sc}(t = \infty) = \frac{E_n}{X_d} \tag{eq 5.7}$$

So, considering eq 5.6 and eq 5.7, the reactance X_d is defined by:

$$X_d = \frac{E_n}{I_{ond}^{max}} \tag{eq 5.8}$$

However, the value of the reactance, obtained thanks to eq 5.7, is closer to X_d^{sat} than X_d . The ratio between the reactance X_d and X_d^{sat} , depending on the power of the modelled SM, can vary between 1.5 to 4. In order to ensure imposing maximal output current of the inverter during a short-circuit, the parameter X_d has to be a high value, hence, the ratio between X_d^{sat} and X_d is fixed as:

$$X_d^{sat} = \frac{1}{4} \cdot X_d \quad eq\ 5.9$$

Hence,

$$X_d(\Omega) = 4 \cdot \frac{E_n}{I_{ond}^{max}} \quad eq\ 5.10$$

In p.u.

$$X_d(p.u.) = 4 \cdot \frac{E_n}{I_{ond}^{max}} \cdot \frac{1}{Z_{base}} \quad eq\ 5.11$$

- **Reactance X_d''**

To determine the reactance X_d'' , the SM maximal short-circuit current is used. The maximal SM short-circuit current is determined for $t = 0$ in eq 5.5:

$$I_{sc}(t = 0) = 2 \cdot \frac{E_n}{X_d''} \quad eq\ 5.12$$

so, the reactance X_d'' is defined by:

$$X_d'' = 2 \cdot \frac{E_n}{I_{sc}(t = 0)} \quad eq\ 5.13$$

The maximal SM current during a short-circuit could reach up to 15 times the SM nominal current. For our methodology, the maximal SM current during the short-circuit is fixed to 15 times the maximal inverter's current. The fact that the inverter cannot reach the same sub-transitory current is dealt with the saturation of the current's reference.

$$I_{sc}(t = 0) = 15 \cdot I_{ond}^{max} \quad eq\ 5.14$$

Hence, with hypotheses eq 5.14 and eq 5.13, the reactance X_d'' is determined by the equation:

$$X_d'' = 2 \cdot \frac{E_n}{15 \cdot I_{ond}^{max}} \quad eq\ 5.15$$

In p.u.:

$$X_d''(p.u.) = 2 \cdot \frac{E_n}{15 \cdot I_{ond}^{max}} \cdot \frac{1}{Z_{base}} \quad eq\ 5.16$$

- **Reactance X'_d**

In order to determine X'_d and link its value to the inverter's characteristics, the relationship between the reactances X'_d and X''_d has been used. Indeed, in traditional SM, the value of the reactance X'_d is slightly superior to the reactance X''_d . Based on the SM characteristics that can be found in different datasheet concerning the impedances X'_d and X''_d , X'_d can be defined as:

$$X'_d = 2 \cdot X''_d \quad \text{eq 5.17}$$

- **Reactance X_q**

As the complete model is considered for the replicability methodology, a salient-pole SM is considered, where the reactance X_d is largely superior to the reactance X_q , from 2 to 10 times. In order to avoid an oversalient machine, the parameters X_q is selected as:

$$X_q = \frac{X_d}{2} \quad \text{eq 5.18}$$

- **Reactance X''_q**

In order to link X''_q to the inverter characteristics, it was chosen to link reactance X'_d and reactance X''_q as both due the dampers element. The variation between the parameters X''_q and X''_d are include between a range of 1.5 and 3. As it was identified in Chapter 2 (2.4.1 – p21), the value of X''_q and X''_d influence the value of the harmonics, hence, the reactance X''_q is selected in order to minimise the value of the output harmonics as:

$$X''_q = 1.5 \cdot X''_d \quad \text{eq 5.19}$$

- **Stator winding resistor R_s**

Following the model of a SM, the stator winding resistor R_s and the reactance X_2 are defined by the two following equations:

$$R_s = \frac{X_2}{T_a} \quad \text{eq 5.20}$$

with

$$X_2 = \frac{(X''_d + X''_q)}{2} \quad \text{eq 5.21}$$

The parameter T_a having usually the same order of magnitude as the time response T''_d , the variable is defined as:

$$T_a = T''_d \quad \text{eq 5.22}$$

Hence, combining eq 5.20, eq 5.21 and eq 5.22, the stator winding resistor is defined by:

$$R_s = \frac{(X_d'' + X_q'')}{2 \cdot T_d''} \quad \text{eq 5.23}$$

- **Reactance X_0 and X_l**

As both reactances X_0 and X_l represent the SM model's imperfections, in order to avoid unnecessary losses and improve the behaviour of the VSG, the solution is to consider that both reactance equal to zero. Hence:

$$X_l = X_0 = 0 \quad \text{eq 5.24}$$

5.2.2.3 SM complete model time response

- **Time response T_d'' and T_q''**

The PWM switching frequency is used to determine the sub-transient time responses T_d'' and T_q'' (knowing that $T_d'' = T_q''$ due to dampers characteristics of the SM). The controller frequency can be identical to the PWM switching frequency. To ensure the model stability, enough calculation points are necessary. So, the coefficient multiplying the PWM switching frequency to obtain the SM sub-transient time response needs to be important enough to ensure the discreet model stability. However, the coefficient between the PWM switching frequency and the time response should not be too high in order to ensure a time response that satisfies the SM time response standards and the microgrid fast stability recovery after a load impact. Hence, the definition of the times responses T_d'' and T_q'' is chosen as:

$$T_d'' = T_q'' = 50 \cdot \frac{1}{f_{IGBT}} \quad \text{eq 5.25}$$

- **Time response T_{qo}''**

Knowing X_q'' , X_d'' and T_q'' , the response time T_{qo}'' can be determined thanks to the equation eq 5.3:

$$T_{qo}'' = T_q'' \cdot \frac{X_q}{X_q''} \quad \text{eq 5.26}$$

- **Time response T_d' and T_{do}'**

Thanks to eq 5.2 and eq 5.11, the relationship between T_{do}' and T_d' is:

$$T_{do}' = 30 \cdot T_d' \quad \text{eq 5.27}$$

However, to determine T_d' or T_{do}' , another relationship is necessary to fix one of the two parameters. The time response T_d' is often included between $2 \cdot T_d''$ to $10 \cdot T_d''$ in the SM characteristics. Similarly to the time responses T_d'' and T_q'' , the coefficient has to ensure the stability of the discreet SM

model (i.e. limit the risk of saturation) and also not reduce too much the time response of the system after a load impact. Hence, the time response T'_d is chosen as:

$$T'_d = 4 \cdot T''_d \quad \text{eq 5.28}$$

5.2.3 Methodology

To conclude, Table 5.1 and Figure 5.1 recapitulate the relationships between the inverter's characteristics and the SM parameters that are adapted for an implementation in any inverter, depending on its characteristics.

Table 5.1: Expression of the parameters of the SM model, adapted to the inverter's characteristics.

Parameters in p.u.	Time response in s
$X_d = \frac{E_n}{I_{ond}^{max}} \cdot \frac{1}{Z_{base}}$	$T''_d = T''_q = 50 \cdot \frac{1}{f_{IGBT}}$
$X''_d = 2 \cdot \frac{E_n}{15 \cdot I_{ond}^{max}} \cdot \frac{1}{Z_{base}}$	$T''_{qo} = T''_q \cdot \frac{X_q}{X''_q}$
$X'_d = 2 \cdot X''_d$	$T'_d = 4 \cdot T''_d$
$X_q = \frac{X_d}{2}$	$T'_{do} = 30 \cdot T'_d$
$X''_q = 1.5 \cdot X''_d$	
$R_s = \frac{(X'_d + X''_q)}{2 \cdot T''_d}$	
$X_l = 0$	
$X_0 = 0$	

Figure 5.1 highlights the different links between the inverter characteristics and the methodology based on the complete model. It can be noted that hypotheses are necessary in order to determine the entire parameters based on the inverter characteristics.

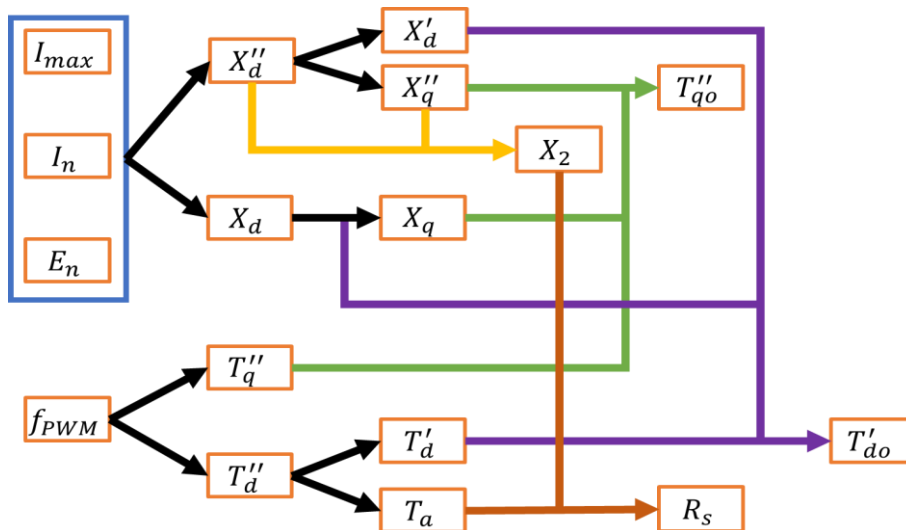


Figure 5.1: Steps to determine the parameters of the SM model, adapted to the inverter's characteristics.

Once the link between the parameter of the SM model and the inverter's characteristics is defined, the next step is to implement the VSG-based controller, using the proposed methodology, on more than one inverter to insure the replicability.

5.3 Implementation on a laboratory-scale prototype system

A power-in-the-loop (PHIL) approach has been used in order to validate the methodology to adapt the parameters of the SM model to the characteristic of any inverter, as the transfer of the VSG-based control to another inverter (different from the initial Schneider Electric installation) required significant material and human investments. To that purpose, in the facilities of the G2Elab, a laboratory-scale prototype has been built to develop and validate, for various scenarios, control strategies that enhance the capabilities of inverter-based generation systems notably used for renewable energies such as photovoltaic [64]–[66], wind turbines [67], [68] or microgrid controllers [69].

5.3.1 Description of the laboratory-scale prototype system

The complete schematic diagram of the prototype used to replicate the VSG on another inverter and validate the methodology developed in the previous section is described in Figure 5.2. The testbench is constituted of two main systems: the VSG-based inverter and the microgrid used to validate the portability of the control to another inverter. Each system can be divided in two layers: software and hardware.

In Figure 5.2, two software layers that can be seen, one for the inverter control and one for the emulated microgrid, represented with their associated real-time digital simulators, dSPACE® and RT-LAB®. Due to the entire testbench configuration, both simulators, dSPACE® and RT-LAB®, are simultaneously employed but at different frequencies. The emulated microgrid is controlled at a fixed frequency of 20 kHz. Concerning the inverter, the VSG control and the PWM switching frequency have been tested for two frequencies, 10 kHz and 5 kHz. Those two main parts are detailed in the subsection below.

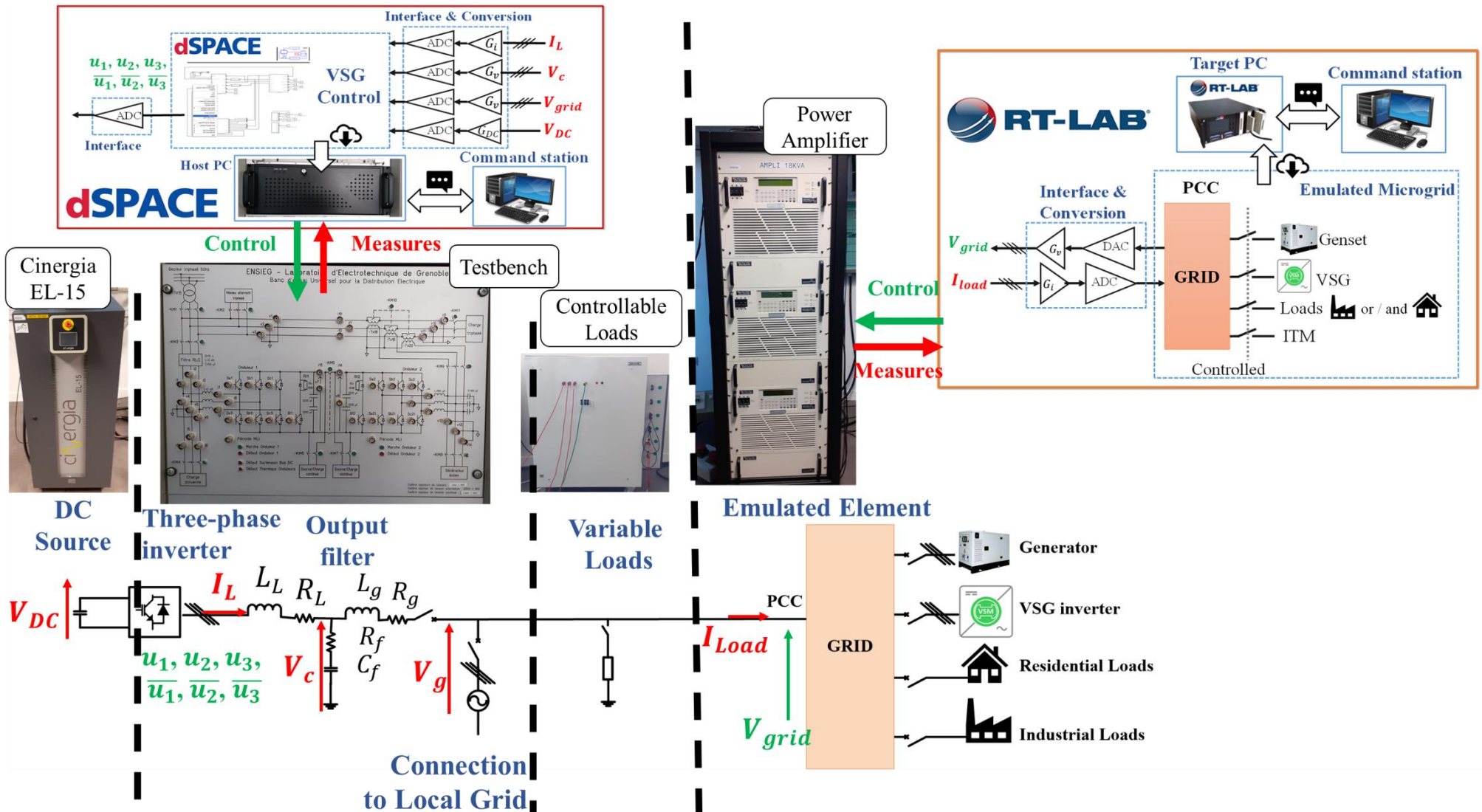


Figure 5.2: Schematic diagram of the laboratory-scale prototype system for VSG based PHIL validation.

5.3.1.1 Testbench inverter

The testbench inverter hardware, visible in Figure 5.3, consists of:

- A three-phase inverter;
- An output LCL filter;
- A controllable DC source;
- A switch for the connexion to the microgrid.

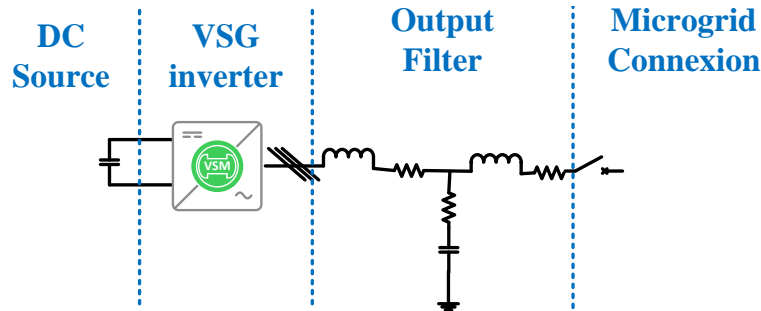


Figure 5.3: Testbench single-line scheme.

In order to command the testbench inverter, the VSG control is implemented in an industrial computer with dSPACE® thanks to the VSG model built in MATLAB®/SIMULINK® as it can be seen in Figure 5.4. All the elements of the testbench can be connected and disconnected remotely from the command station.

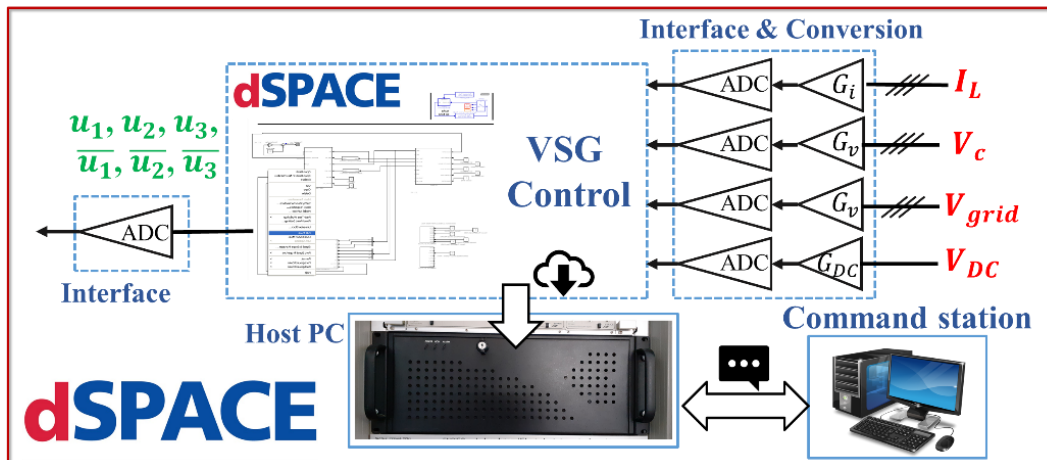


Figure 5.4: dSPACE® schematic control of the testbench inverter.

5.3.1.2 Microgrid description

The hardware part of the microgrid consists of a connexion to the local distribution grid, actual loads that can be modulated to create unbalanced operation, the power interface that controls the power amplifier which is used to emulate the microgrid. The emulated microgrid's model is developed using MATLAB®/Simulink® and then integrated in the RT-LAB® platform at a frequency of 20 kHz. The emulated microgrid contains traditional, industrial, non-linear and unbalanced loads, two different power sources, a diesel engine generator and a VSG inverter. To validate the real VSG-based inverter stability during fault, there is the possibility to create faulty conditions at the point of coupling.

To resume, the microgrid, represented in Figure 5.5, is constituted of:

- Real and emulated, balanced and unbalanced loads;
- Emulated industrial and no-linear loads such as a 2 kVA motor;
- Other power sources: an emulated VSG of 4 kVA, an emulated generator of 4 kVA and the possible connection to the local distribution grid (national French grid);
- Faults generation capabilities in both emulated and real microgrid.

All the elements of the microgrid can be connected and disconnected remotely from the command station as it is showed in Figure 5.5, with the help of switches.

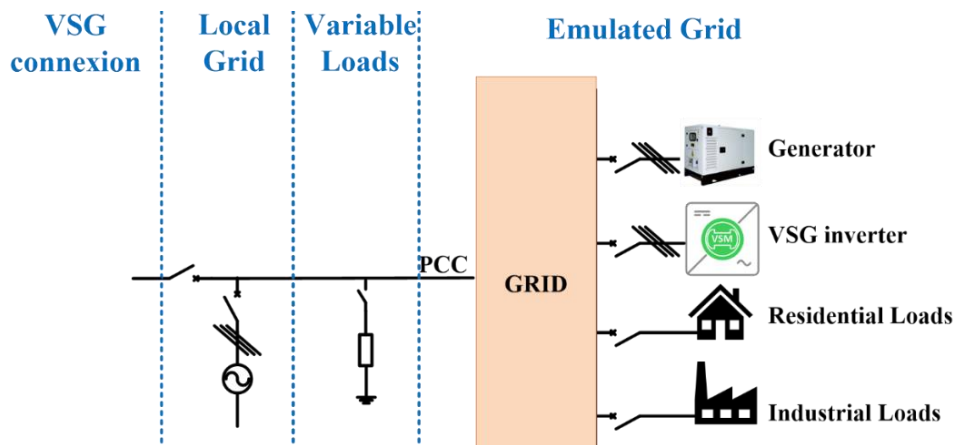


Figure 5.5: Microgrid single-line diagram for PHIL.

In addition, a retroaction is implemented in the emulated microgrid connected at the microgrid's point of common connexion (PCC), based on the measured output currents of the power amplifier, to link the emulated microgrid to the real loads and VSG inverter. Hence, during a load impact, the voltage of the microgrid is directly impacted thanks to the retroaction on the current. The methodology is named "ideal transformer method" (ITM), detailed in [70] and schematically represented in Figure 5.6 (adapted for [70]).

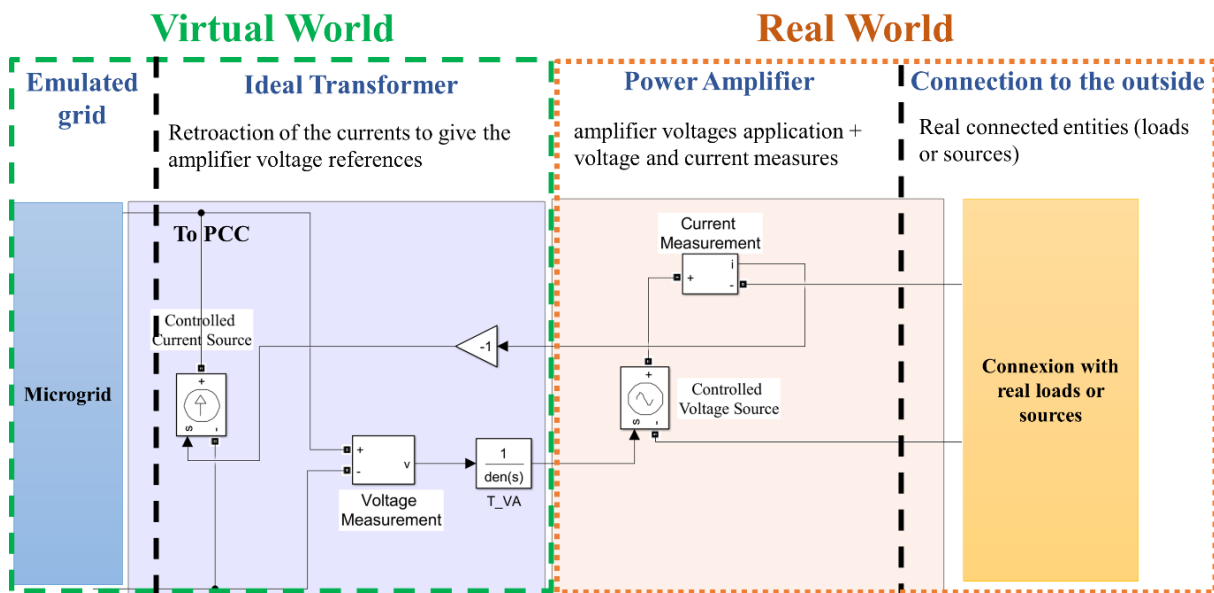


Figure 5.6: ITM method for virtual model power interface (adapted for [70]).

The ITM methodology permits to link the emulated microgrid to the real world however, some problems could appear. Indeed, if the measured currents injected in the ITM are different from the real currents for some reason (measures errors, discreet delay, ...), high frequency voltage oscillations could appear and in some extreme cases destabilize the system.

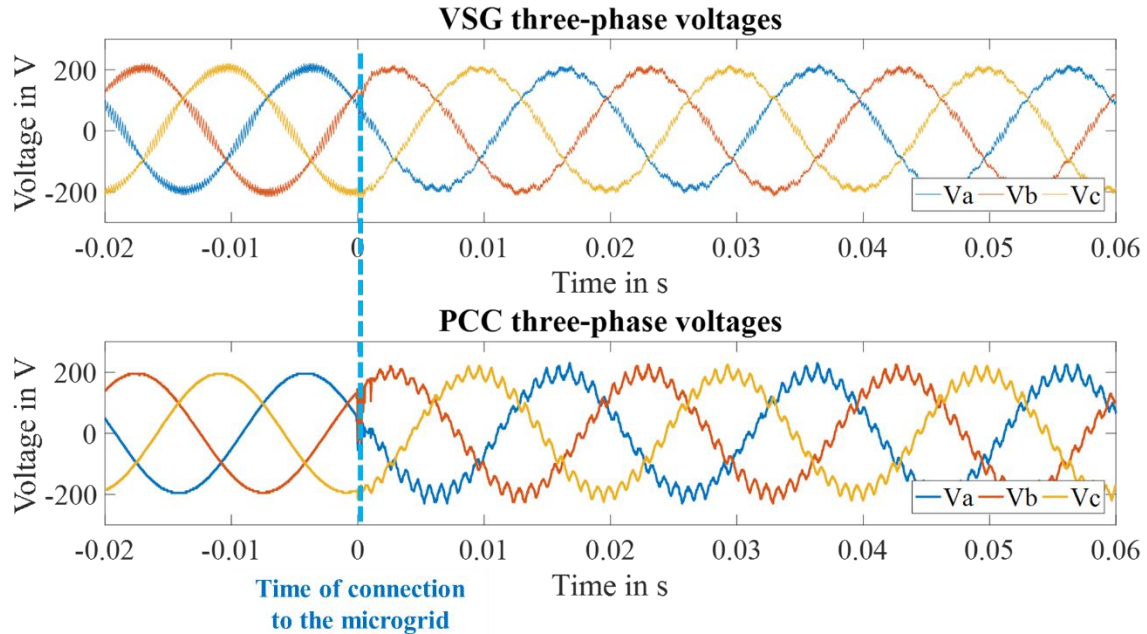


Figure 5.7: Voltage oscillation problems due to the ITM method.

Figure 5.7 show the connection of the VSG to the microgrid only constituted of the emulated VSG without any load. The creation of voltage oscillations can be noted, due to the problem described above with the ITM. When a load is connected to the microgrid, the voltage oscillation disappears as the measure errors become negligible before the actual current, thus impacting less the ITM.

5.3.2 Testbench characteristics

The limitations of the testbench are summarized in Table 5.2.

Table 5.2 Testbench characteristics.

Parameters	Value
Maximal apparent Power S_{max}	5 kVA
Maximal output three-phase voltage E_{max} (phase-phase)	400 V
Maximal output current I_{ond}^{max}	20 A
Maximal PWM switching frequency f_{PWM}	10 kHz
Maximal DC voltage V_{DC}	800 V

The local distribution grid is connected to the testbench via a transformer imposing the microgrid's voltage and frequency. Hence, in order to beneficiate from that connexion, the microgrid's voltage reference is imposed at 240 V and the frequency at 50 Hz. As the microgrid's voltage is limited, so is

the DC voltage. In addition, to limit the risk of material deterioration, the VSG-based inverter's maximal power, thus maximal current, are also limited. Concerning the PWM switching frequency, the testbench is limited to 10 kHz, explaining why only two frequency have been tested for the PWM and maximal controller frequency, 10 kHz and 5 kHz. Table 5.3 details the characteristics of the laboratory-scale prototype system that was used to validate the portability and replicability of the VSG controller.

Table 5.3: Testbench set-up.

Parameters	Value
Apparent Power S_n	4 kVA
Nominal output voltage E_n (phase-phase)	240 V
Maximal output current I_{ond}^{max}	15 A
Nominal output current I_n	10 A
PWM switching frequency f_{PWM}	10 kHz or 5 kHz
DC input voltage V_{DC}	450 V
Frequency f	50 Hz

5.4 Experimental validation of the methodology on a laboratory-scale prototype system

Now that the laboratory-scale prototype system has been presented, in this section, the experimental results are studied in order to validate the replicability of the proposed controller and the methodology to determine the SM parameters of the VSG. Like in the Chapter 4 (4.3.2 – p85), the validation tests are separated in two sections: a standalone mode and a grid-connected one, where the VSG is integrated to the microgrid. Like for the chapter experimentation, the tests result in this section are based on the literature and industrial expectations as well as on the laboratory-scale prototype system limitations.

5.4.1 VSG model characteristics with the methodology

For the current controller, the SM parameters are determined using the matrixes presented in Chapter 3 (3.6 – p 62). In addition, the control's frequencies of the VSG controller are also adapted to the PWM frequency as it can be seen in Table 5.4.

Table 5.4: Adaptation of the controller's frequency depending of the PWM switching frequency.

PWM frequency	20 kHz	10 kHz	5 kHz
Current Controller	20 kHz	10 kHz	5 kHz
Synchronous machine model	6.66 kHz	3.33 kHz	1.66 kHz
AVR, governor and swing equations	1 kHz	1 kHz	1 kHz

Following the methodology resumed in Table 5.1, the adapted SM parameters established considering the testbench's characteristics are defined in Table 5.5.

Table 5.5: SM model parameters adapted to the testbench.

Parameters	Value (p.u.)	Time response	$f_{IGBT} = 10 \text{ kHz}$	$f_{IGBT} = 5 \text{ kHz}$
			Value (ms)	
$X_d = \frac{E_n}{I_{ond}^{max}} \cdot \frac{1}{Z_{base}}$	3.7712	$T_d'' = 50 \cdot \frac{1}{f_{IGBT}}$	5	10
$X_d'' = 2 \cdot \frac{E_n}{15 \cdot I_{ond}^{max}} \cdot \frac{1}{Z_{base}}$	0.1257	$T_q'' = 50 \cdot \frac{1}{f_{IGBT}}$	5	10
$X_d' = 2 \cdot X_d''$	0.2514	$T_{qo}'' = T_q'' \cdot \frac{X_q}{X_q''}$	50	100
$X_q = \frac{X_d}{2}$	1.8856	$T_d' = 4 T_d''$	20	40
$X_q'' = 1.5 \cdot X_d''$	0.1886	$T_{do}' = 30 T_d'$	600	1200
$R_s = \frac{(X_d'' + X_q'')}{2 \cdot T_d''}$	0.10			
X_l	0			
X_0	0			

5.4.2 Validation tests

In order to validate the methodology and the portability on various inverters, the proposed controller, detailed in 3.6 (p62) and 4.2.1 (p79), is tested on the testbench with two different PWM switching frequencies, 5 kHz and 10 kHz. Both systems, with different frequencies, is tested with the same parameters value as described in 3.6.2 (p69) and Appendix 6 (p173) to validate the replicability of the proposed controller.

Even with different PWM switching frequencies, both VSG have similar behaviour, as the SM model is similar in terms of reactances. The main different between both models is the time response: the VSG with a PWM switching frequency of 5 kHz is slower than the other one. However, as the performances of both models are similar, only the VSG with a PWM switching frequency of 5 kHz is presented in this section, keeping in mind that it is the less performant one.

5.4.2.1 Standalone VSG

In this section, the VSG implemented in the testbench represents the unique power source connected to the microgrid. The tests described in this section illustrates that the proposed controller and the methodology developed in this chapter permit to ensure the portability of the VSG control. In that experiment, it was implemented on a 4 kVA inverter. Figure 4.10 represents the generic schematic of the tests conducted in the standalone application with the testbench.

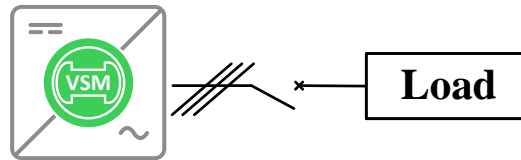


Figure 5.8: Schematic representation for testbench standalone tests.

- **Load impact**

Figure 5.9 shows the transient dynamic behaviour of a VSG under a 4 kW load impact (i.e. 100 %) realised with the real loads.

The voltages and currents waveforms are similar to the one of a real SM. During the load impact, the three-phase voltage decreases almost immediately then stabilizing at their nominal voltage value. Similarly, during the load impact, the current rapidly increases before stabilizing. To conclude, the VSG is able to cope with a significant load impact, equal to its maximal power.

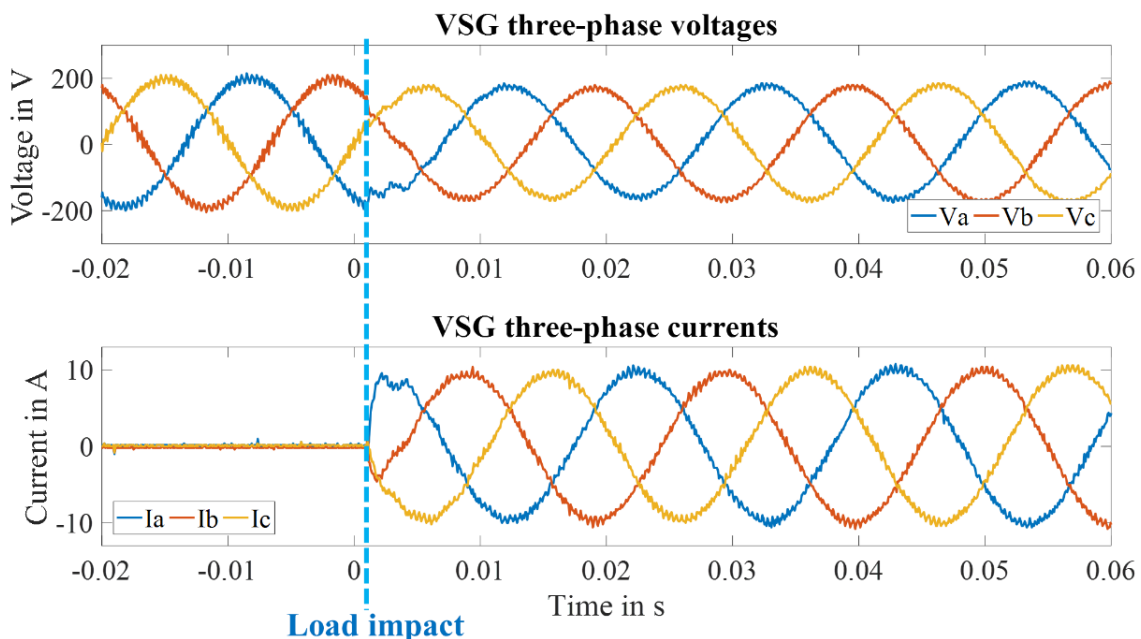


Figure 5.9: Testbench VSG behaviour during a load impact of 4 kW (i.e. 100 %).

On Figure 5.9, high frequency oscillations can be noted on the output voltage. Figure 5.10 shows a focus on the output voltages for both PWM switching frequencies, 5 kHz and 10 kHz. It can be noted that the VSG with the 5 kHz PWM switching frequency is more subject to high frequency oscillations. The first reason is that the output filter of the testbench is optimised for a switching frequency of 10 kHz and not 5 kHz.

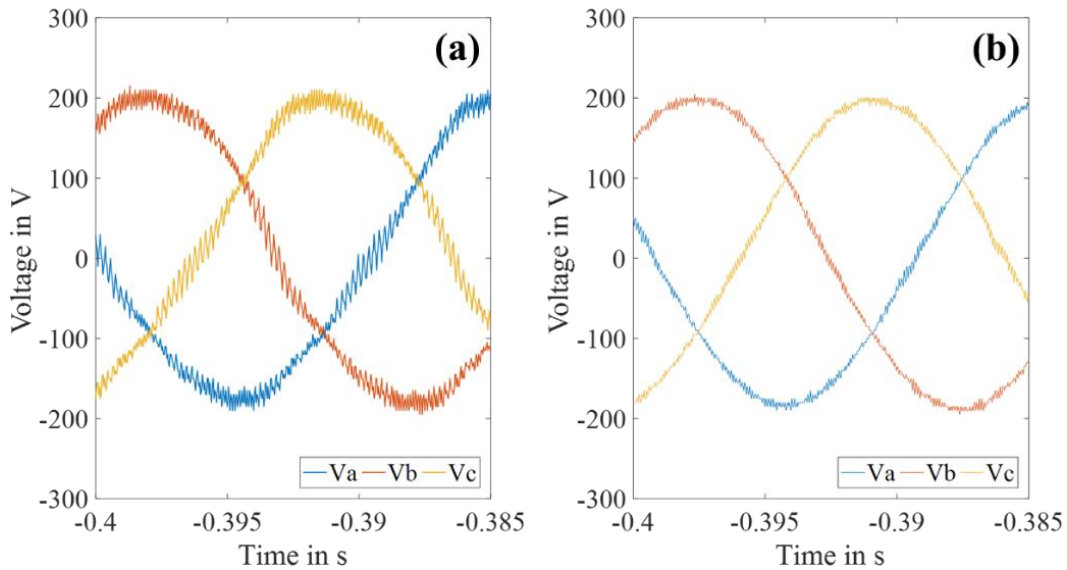


Figure 5.10: Testbench output voltages for a 5 kHz PWM switching frequency (a) and a 10 kHz PWM switching frequency (b).

Even if the output filter of the testbench is not optimized to filter the 5 kHz of the PWM, Table 5.6 shows that the harmonics standards are still respected. The non-linear load, a diode bridge connected to a resistor, is calculated based on the standards, [41] and [43], defined as in Chapter 2 (2.4.3 – p30).

Table 5.6: Testbench THD_V and individual harmonics results supplying a non-linear load.

	THD_V In % of rated voltage < 5 %			
	5 kHz PWM		10 kHz PWM	
THD_V	3.62		2.45	
Individual Harmonic value in % of rated voltage < 3 %				
Harmonic value	3	5	7	11
5 kHz PWM	0.56	1.45	0.79	0.47
10 kHz PWM	0.02	1.29	0.48	0.25

- **Unbalanced load**

In order to validate the behaviour of the VSG supplying power to an unbalanced load, one phase (the c phase) of a 4 kW load is disconnected (note that 4 kW is the rated power of the VSG). In Figure 5.11 can be observed the behaviour of the VSG supplying that load.

As the phase c of the load is disconnected, the voltage of that phase is clearly impacted and the current null. The voltage of the phases a and b, as the VSG supplies the load, are relatively impacted. The voltage of phases a and b decrease and stabilize to a value (200 V) smaller than the nominal one due to the implementation of a droop control. It can be noted that the output currents of the phases a phase b are in opposition. The VSG tested in the testbench is stable while supplying an unbalanced load.

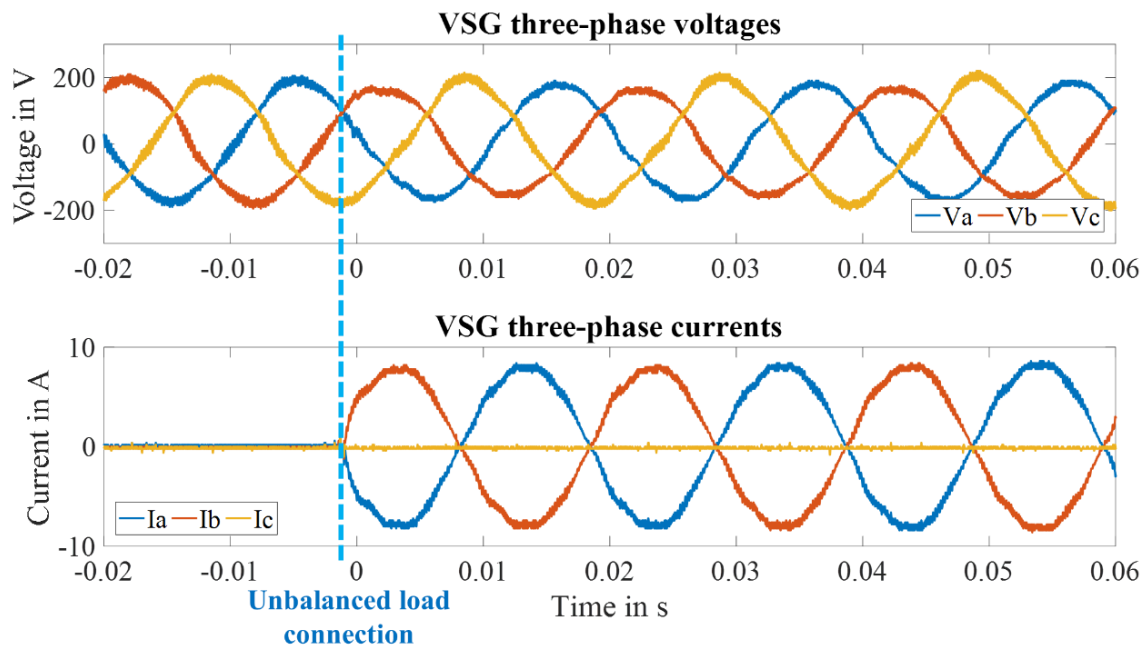


Figure 5.11: Testbench VSG behaviour under an unbalanced load of 4 kW (i.e. rated power of the VSG).

- DC variation

The objective of this test is to analyse the sensitivity of the VSG controller to a decrease of the input DC voltage. As the testbench is supplied by a controllable DC source and not a real storage, it is possible to modify the DC voltage reference V_{DC} as it can be seen in Figure 5.12.



Figure 5.12: Schematic representation for DC variation.

Due to the capacitor used to filter the DC voltage's variations, high variations will be filtered by the component. Hence, in this test, the VSG is supplying a 4 kVA load when the DC voltage of the VSG is reduced by 25 % of its nominal value. The DC voltage decreases from 450 V to 350 V to represent a decrease of the power storage. As the protection of the DC source restrains voltage variations, the DC voltage decrease is done in 0.08 s, which equivalent to an important unloading of the storage.

Figure 5.13 shows the input DC voltage variations and the three-phase output voltage of the VSG when supplying a 4 kVA load. This voltage is not impacted by the decrease of the DC voltage as highlighted by the RMS voltage value also in Figure 5.13. With a variation of 25 % of the DC voltage, the VSG inverter is still capable to produce its maximal power. However, 25 % of variation was found to be the experimental limit of stability of the VSG, as the DC voltage is then below 1.5 times the AC voltage (the inverter saturation is reached).

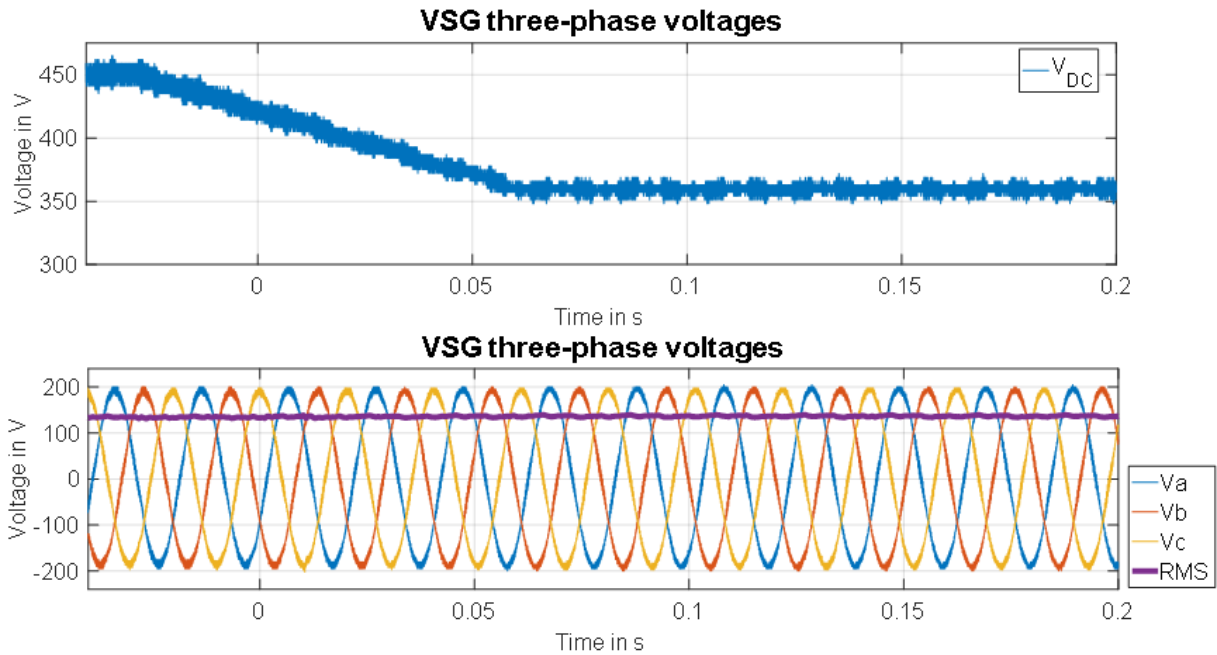


Figure 5.13: Impact of the DC variation on the testbench output VSG voltages.

To conclude, the VSG behaviour remains stable (without saturation) for a DC voltage variation of up to 25 % of its nominal value, equivalent of 150 % of the AC nominal voltage value.

5.4.2.2 VSG integrated in a microgrid

In this section, the VSG is integrated in a basic microgrid to validate its parallel operation. Figure 5.14 represents the schematic of the tests described below. As each element of the microgrid, real or emulated, can be connected or disconnected for different tests configurations thanks to real or emulated, controllable interrupters. The two emulated power sources connected to the microgrid can be a generator set and another VSG, each power source with the same power as the testbench VSG: 4 kVA.

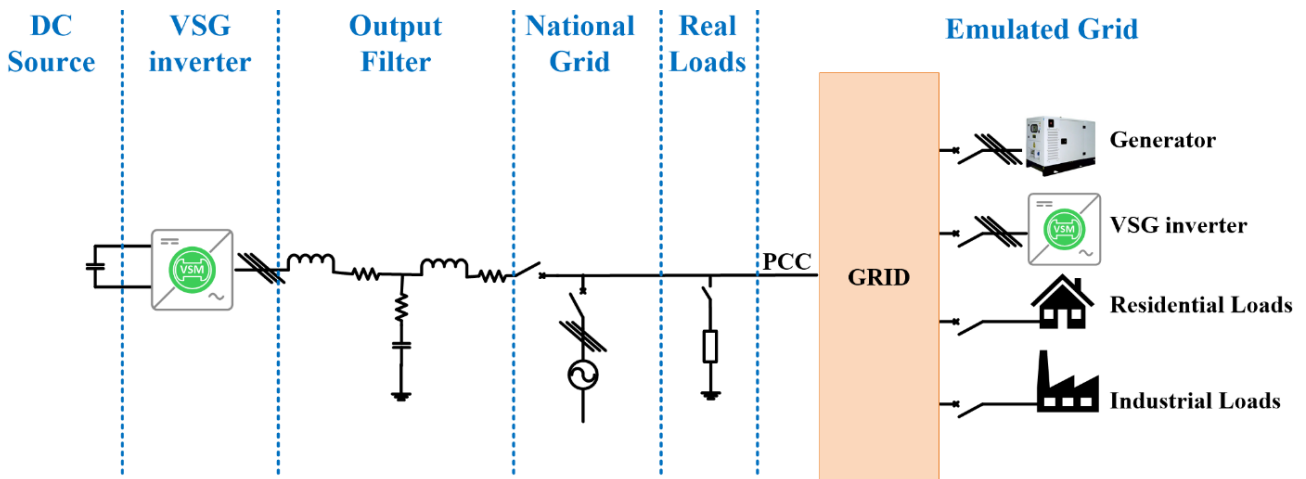


Figure 5.14: Schematic representation for testbench microgrid integration tests.

- **Non-linear load**

To validate the behaviour of the VSG controller facing non-linear loads, an emulated 2 kA three-phase motor, is directly connected to the inverter. The motor is realised on the emulated microgrid and is the only load connected as it can be seen in Figure 5.15.

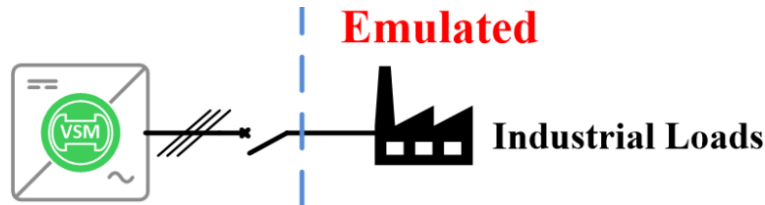


Figure 5.15: Schematic representation for testbench standalone non-linear load.

Figure 5.16 represents the RMS output voltages and currents of the VSG supplying power to the motor. It can be noted that as the maximal output current of the VSG is reached, hence the output voltage is reduced in order to avoid the deterioration of the inverter as explained in Chapter 4 (4.3.2 – p85). Due to the measured high current, the saturation protection rapidly reacts, explaining why the RMS output voltage drops to nearly zero. Then, as the current decreases back to the maximal value of the VSG controller (i.e. the saturation limit), the voltage drop stabilizes around 50 V.

During the first instants of the motor connexion, the VSG produces a peak of currents of around 20 A, which is greater than the maximum current of the inverter. The high current value could be created by a resonance in the LCL output filter of the testbench. Another more probable possibility would be that the peak of current is the work of the ITM due to the difference between the real and the measured currents during the integration in the emulated microgrid.

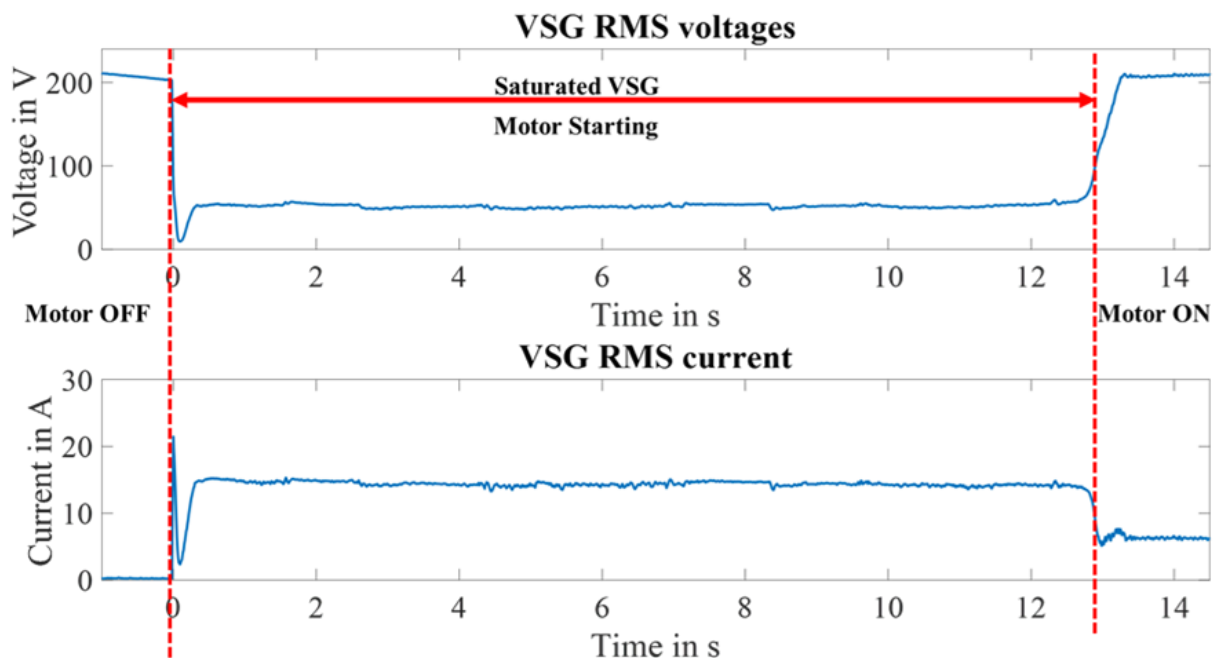


Figure 5.16: RMS behaviour of the VSG supplying a 2 kVA motor in the testbench.

The saturation of the current to the maximal value of the VSG (14 A) and the resulting reduced output voltage causes the starting of the motor to last about 13 s. This emulation time is longer than starting time of the actual motor tested in Chapter 4 (4.3.2 – p85). This could be explained by the ratio

of power between the motor and the VSG. In this experiment, that power ratio is of 50 % while in Chapter 4 (4.3.2 – p85) the power ratio was of 25 %.

To conclude, the VSG is capable of supplying a non-linear load but with some limitations, as already discussed in Chapter 4 (4.3.2 – p85). Some specifications must be considered when non-linear loads are added in a microgrid supplied by VSG if constraints exist on time constants.

- **Load impact and load shedding**

The objective of this test is to validate the parallel operations of the VSG control without creating oscillation that could destabilize the microgrid. During this test, a 12 kW load is connected to the microgrid constituted of the three power sources: a real VSG, an emulated VSG and a generator.

The three-phase voltage of the microgrid is shown in Figure 5.17 during the load impact and the load shedding (100 % of the load). It can be noted that the voltage rapidly returns to its nominal value after the two tests without creation of oscillation between the three power sources as shown by the RMS voltage value that remains stable. The voltage drop shown in Figure 5.17 during a load impact or a load shedding, are linked to the different source times responses. If the VSG possess a faster time response, maybe the voltage drop may be less important, however, that also means the VSG inverter will have to supply the entire loads with the risk of saturation.

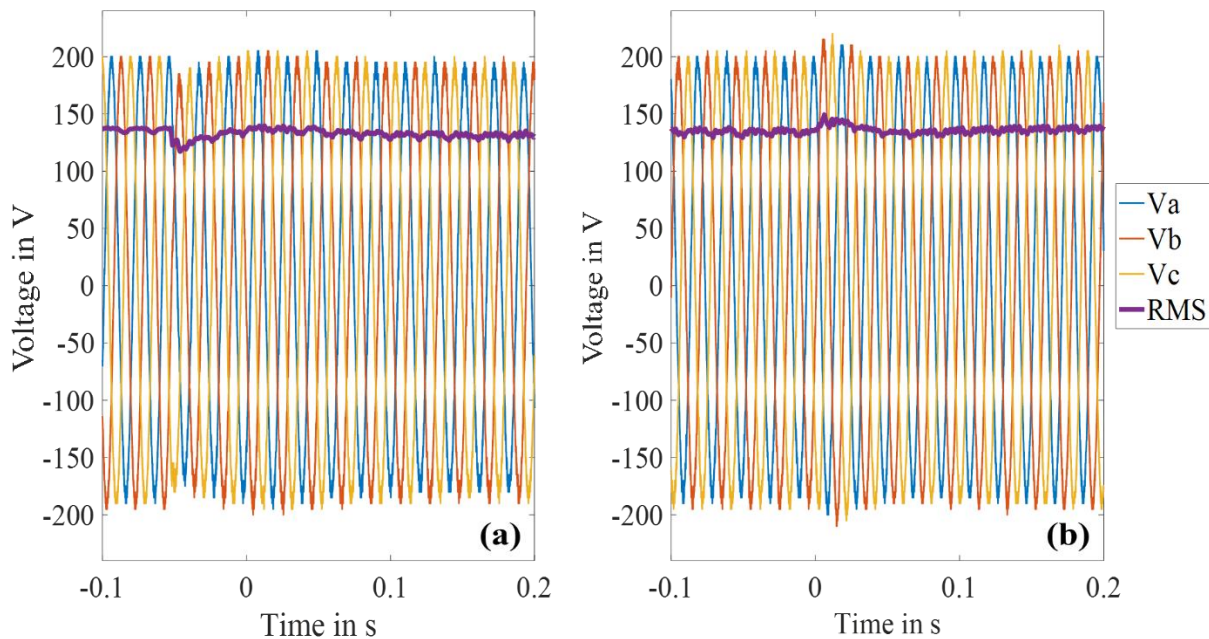


Figure 5.17: Microgrid three-phase voltages behaviour after a 12 kW (a) load impact and (b) load shedding.

To conclude, the parallel operation is validated as there is no creation of voltage oscillation during a 100 % load impact on the microgrid.

- **Power absorption**

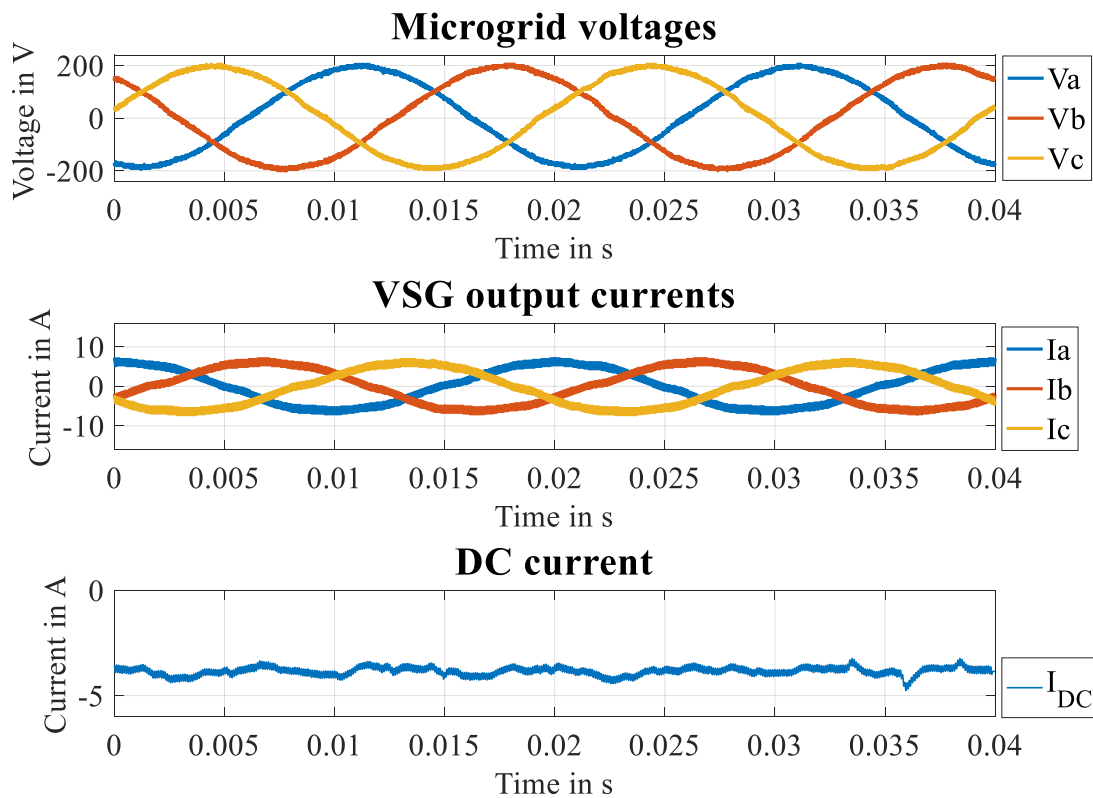


Figure 5.18: VSG behaviour absorbing the exceeding power in the testbench.

As the production on the microgrid is more important than the consumption, in order to avoid an overvoltage and a significant frequency deviation, the VSG should be able to absorb exceeding power. For this test, the production is considered maximal with a low consumption to represent the worst case scenario in the configuration of a microgrid with high penetration of renewable energies.

Figure 5.18 shows the microgrid's three-phase voltage, the testbench VSG output currents and the DC current of the real VSG. The microgrid voltage and the output voltage of the VSG are in opposition. This phenomenon is due to the fact that the VSG is absorbing the microgrid exceeding power as it can be seen with the negative VSG DC current. It can be noted that the microgrid's voltage is close to its nominal value (200 V) even with an over production of 4 kVA in the microgrid.

5.5 Conclusion

In the first section of this chapter, the methodology to adapt the SM model implemented in the VSG control of any inverter depending on its characteristics is described. The methodology to determine the most adapted SM parameters and the proposed controller have been tested with different scales of platforms and different inverter's PWM switching frequencies. In order to validate both the detailed methodology and the proposed controller replicability, various experimental results are presented.

The laboratory-scale prototype system that has been used to test the VSG control deployed in the testbench of the G2Elab is presented. In order to validate both the methodology and the portability of the proposed controller, the VSG-based inverter is tested in both standalone and parallel operations, integrated in a basic microgrid. In the standalone operation, the VSG control is stable for step-like load

impact (equivalent to the inverter's maximal power), unbalanced and non-linear loads connection. In addition, the impact of the DC voltage variations on the VSG behaviour is studied.

To finalise the validation of the transfer of the VSG controller to another inverter, the VSG-based inverter is integrated in a basic microgrid connecting multiple power sources to a load. Different use-cases have been tested, such as load impacts, to conclude on the microgrid's stability thanks to the integration of the proposed VSG solution. In addition, as the VSG is a two-way power source, it is able to absorb the exceeding production avoiding a possible overvoltage in the microgrid.

With both standalone and parallel studies, it can be concluded that the methodology and the proposed controller permits to increase the potential of portability and replicability of the VSG controller to different power inverters.

In the next chapter, the virtual part of the VSG will be studied in order to increase its performance by modifying the SM model parameters to avoid the inverter's deterioration during harsh events.

5.6 Perspectives

A first perspective of research is the impact of the SM model on the VSG behaviour with in mind the discretisation of the SM model and the standards that have to be respected. Indeed, in order to ensure that the model is stable when implemented in discreet controllers, the time responses of the SM model must be short enough. However, standards and major microgrid configurations naturally favour a rapid VSG to ensure the system's stability (in frequency and voltage).

Another perspective is the amelioration of the ITM methodology in order to improve the emulated microgrid with a low consumption. Indeed, as it was show in this chapter, the difference between the measured current injected in the ITM and the real current has an impact on the quality of the microgrid's three-phase voltage (presenting high frequency oscillations). A possible amelioration could come from an experimentation with an industrial load in order to analyse more in details the behaviour of the VSG in that case.

To improve the DC source of the laboratory-scale prototype, the idea would be to change it for a more controllable one that emulates a PV production or a real DC storage. A perspective of research is to improve the performance of the VSG when subject to even larger load variations than the ones presented in this chapter. The first perspective is to consider the storage to limit the output power produced by the VSG. The other perspective is to adapt and modify the SM of the VSG model depending of the storage instantaneous characteristics.

Chapter 6. Polymorphic VSG, an advanced control for smart inverter

6.1 Introduction

The virtual characteristics of the VSG control have only been used in the recent years. Indeed, the main objective of the first studies on VSG inverters was to show the advantage of the VSG solutions integrated in a microgrid, [18], [26], [27]. Nowadays, thanks to the virtual characteristics of the VSG control, the parameters of the system can be adapted: self-tuning offline depending on the microgrid configuration or during operations when the microgrid submits harsh events. The self-tuning VSG inverter is used as a grid-forming inverter that enables to minimize the risks of voltage oscillations or frequency oscillations thanks to a control based on virtual inertia [39], [71]–[73]. Recently, in addition to the SM inertia, the damping coefficient considered in the swing equation is also adapted during operations to improve the VSG performances as it has been developed in [74], [75].

In the literature, the concept of self-tuning or adapting VSG parameters are mainly considered as solutions to improve the VSG performances in order to decrease the voltage or frequency oscillations in a microgrid during harsh events such as during a short-circuit or an islanding. In addition, the parameters that are generally considered are linked to the swing equation: the inertia of the SM model, the damping coefficient. The SM parameters are rarely considered except in [40] where only one parameter of the SM model is controlled. However, even if online self-tuning VSG has been developed, some considerations have to be taken into account to enable the development of this VSG adapted parameters in an industrial context. Unfortunately, the application of the VSG self-tuning concept has never been applied to avoid the inverter deterioration that can occur.

Hence, in a first section of this chapter, the concept of polymorphic VSG, self-tuning SM parameters that enable to minimise the inverter deterioration is explained, analytically detailed and

validated in simulation. Then, in a second part, as an objective is the development of the polymorphic VSG in industrial inverter, different solutions are investigated in order to make possible a future implementation of the polymorphic control in the inverter control card. The problem mainly lies in the computation time and the memory burden that need to be contained at the price of a small drop in the performance and the corresponding gain.

6.2 Concept and analytic model of the polymorphic VSG

6.2.1 Polymorphic VSG concept

The polymorphic VSG concept is to optimize the set of virtual SM parameters in order to limit or, in the best case, avoid, the deterioration of the inverter caused by overshoot of currents, voltages or inverter duty ratio saturations. The main problem when a limit is reached or overreached, is that the VSG control does not return in stable states and stays in instable states. Then, the fact that the inverter reaches its limits means that its internal components, like the switches, rapidly deteriorate, minimizing the lifetime. In addition, there is also the possibility that the internal protection of the inverter trigger, disconnected the inverter creating the loss of a power source in the microgrid.

The polymorphic control is based on a predictive control: the repetitive solution of an open loop optimal control problem that follows the different steps below:

- At each decision instant, given the current state an optimal sequence of parameter values us obtained through the minimisation of a cost function that expresses penalties on the constraint satisfaction and the quality of the regulation.
- The optimal sequence is found using a dedicated solver. This is an optimal sequence of control actions.
- The first actions in this optimal sequence is applied over the sampling period.
- At the beginning of the next sampling period, the new optimisation problem is defined given the new value of the state vector.

This process continues indefinitely leading to a state feedback.

In the context of polymorphic VSG, the control signal is represented by the value of the machine's parameters over the next prediction horizon. As explained in Chapter 2 (2.4.5 – p34), the reduced SM model is the most adapted for VSG-based inverter as it shows a good trade-off between CPU load and performances for industrial inverters. Hence, the polymorphic VSG has been developed based on the reduced model that can be found in Chapter 2 (2.3.2.2 – p17). The polymorphic VSG adapts the following set of SM parameters: the d-axis transient and steady-state impedances, L'_d and L_d , the q-axis steady-state impedance, L_q , the stator resistor R_s and finally, the transient open-circuit time response T'_{do} .

Hence, the reference and constant set of SM parameters $p^{ref}, p^{ref} \in \mathbb{M}_{5,1}$ and the candidate values of the SM parameter $p^k, p^k \in \mathbb{M}_{5,1}$, at a decision instant k , are noted:

$$p^{ref} = \begin{bmatrix} L_d^{ref} \\ L_d'^{ref} \\ L_q^{ref} \\ R_s^{ref} \\ T_{do}'^{ref} \end{bmatrix} \text{ and } p^k = \begin{bmatrix} L_d^k \\ L_d'^k \\ L_q^k \\ R_s^k \\ T_{do}'^k \end{bmatrix}.$$

As the reduced model is a non-salient pole machine, the reactance L_d and the reactance L_q should be equal. However, in order take full advantage of the virtual characteristics of the VSG, the non-salient pole machine is not respected for the resolution of the optimal control problem. This fact will help in simplifying the resolution of the solution of the underlying optimisation problem as both d-axis and q-axis become independent.

Now that the concept of the polymorphic VSG have been detailed as well as the methodology for the resolution of the optimisation problem, in the following sections, the different elements that define the predictive control on the set of SM parameters are detailed: the model used for the determination of the predicted profiles, the cost function, the control parameterization, the set of admissible values of the decision variables and finally the proceeding to solve the underlying optimization problem.

6.2.2 Optimisation problem constraints definitions

In order to determine the predictive profiles and the constraints of the optimisation problem, the model develops and details in Chapter 3 (3.6.1 – p62) is used. The proposed controller is adapted to include the reduced SM model instead of the complete SM model. The same coefficient values for K^S and L_{obs} are kept but adapted to the reduction of SM model. In Appendix 10 (p189), the reader can find the state-space model adaptation as the controller adaptation is not the main subject of this chapter. Considering the adapted proposed controller to the SM model used, the state-space model is defined as:

$$\begin{aligned} \hat{X}_\Delta^+ &= A_\Delta^s \cdot \hat{X}_\Delta + B_\Delta^s \cdot \begin{bmatrix} Y_{meas} \\ \varepsilon^* \end{bmatrix} \\ Y_\Delta &= C_\Delta^s \cdot \hat{X}_\Delta + D_\Delta^s \cdot \begin{bmatrix} Y_{meas} \\ \varepsilon^* \end{bmatrix} \end{aligned} \quad \text{eq 6.1}$$

where the vectors are defined as:

$$\begin{aligned} X_\Delta &= [\psi_d \quad \psi_q \quad \psi_{fd} \quad i_L^d \quad i_L^q \quad e^d \quad e^q \quad i_g^d \quad i_g^q \quad \varepsilon^d \quad \varepsilon^q \quad U_{SYS}^d \quad U_{SYS}^q \quad e_{fd} \quad V_g^d \quad V_g^q]^t, \\ Y_{meas} &= [i^d \quad i^q \quad \psi_d \quad \psi_q \quad \psi_{fd} \quad i_L^d \quad i_L^q \quad e^d \quad e^q \quad e_{fd}]^t \text{ and } \varepsilon^* = \mathbb{O}_{2,1}, \\ Y_\Delta &= [i^d \quad i^q \quad \psi_d \quad \psi_q \quad \psi_{fd} \quad i_L^d \quad i_L^q \quad e^d \quad e^q \quad e_{fd} \quad \varepsilon^d \quad \varepsilon^q \quad \Delta U^d \quad \Delta U^q]^t \end{aligned}$$

with $X_\Delta \in \mathbb{M}_{16,1}$, $Y_{meas} \in \mathbb{M}_{10,1}$ and $Y_\Delta \in \mathbb{M}_{14,1}$. The different matrixes A_Δ^s , B_Δ^s , C_Δ^s , and D_Δ^s , are detailed in Appendix 10 (p189).

Thanks to the state-space model defined in eq 6.1 and a Euler forward method, the predicted profiles of the state vector \hat{X}_Δ can be determined, in dq and p.u. for a given input state vector and a set of SM parameters during the prediction horizon, both considered as constant over the prediction horizon.

It can be noted that the vector Y_{meas} appears in the model since an observer is incorporated that uses the sensors information in order to observe the current and voltage values of the load-related term. In order to avoid the consideration that Y_{meas} is constant during the prediction and as the command is one of the variables of interest to avoid the inverter saturation, the predicted command is applied to the system at the next step in order to determine an evolution of the variable in Y_{meas} during the prediction.

As the model in eq 6.1 is a discrete model, the prediction horizon is divided in time steps equal to the current controller sampling time. Hence, considering a horizon prediction of N steps, defined as $[0; N]$, with 0 as the first prediction step and N as the last prediction step, has a prediction horizon time equal to N times the current controller's sampling time and not the polymorphic control. Indeed, the polymorphic control has a sampling time different than the current controller, hence to ensure the model stability, the current controller sampling is used to define two consecutive steps of the prediction horizon.

The set of SM parameters is considered as constant during the entire prediction as the state-space matrixes are set of SM parameters functions. Since the polymorphic control main objective is to avoid the creation of overcurrents, overvoltages or the inverter duty ratio saturations, the predicted profiles that are considered in the resolution of the optimisation problem, are based on the characteristics:

- The inverter output currents, i_L^d and i_L^q .
- The inverter output voltages, e^d and e^q .
- The inverter output duty ratio, α^d and α^q ($\alpha^d = \frac{2}{V_{DC}} \cdot U_{SYS}^d$ and $\alpha^q = \frac{2}{V_{DC}} \cdot U_{SYS}^q$).

With the predicted profiles, it's possible to determine the voltage and current overshoots and the inverter saturation as the difference between the interested variables modules and their respective limits. Hence, considering the state vector input \hat{X}_Δ^0 at a decision instant k , for an instant m included in the prediction horizon $[0; N]$ with a set of SM parameters p^k , the voltage and current overshoots and the inverter saturation can be determined as:

$$\begin{aligned}
 V_E(m, \hat{X}_\Delta^0, p^k) &= \sqrt{e^d(m, \hat{X}_\Delta^0, p^k)^2 + e^q(m, \hat{X}_\Delta^0, p^k)^2} - e_{max} \\
 V_{i_L}(m, \hat{X}_\Delta^0, p^k) &= \sqrt{i_L^d(m, \hat{X}_\Delta^0, p^k)^2 + i_L^q(m, \hat{X}_\Delta^0, p^k)^2} - i_{max} \\
 V_\alpha(m, \hat{X}_\Delta^0, p^k) &= \sqrt{\alpha^d(m, \hat{X}_\Delta^0, p^k)^2 + \alpha^q(m, \hat{X}_\Delta^0, p^k)^2} - \alpha_{max}
 \end{aligned} \tag{eq 6.2}$$

Where the elements, $V_E(m, \hat{X}_\Delta^0, p^k)$, $V_{i_L}(m, \hat{X}_\Delta^0, p^k)$ and $V_\alpha(m, \hat{X}_\Delta^0, p^k)$ represent, respectively the overvoltage, the overcurrent and the saturation for a given instant m during the prediction horizon for a set of SM parameters p^k during the decision instant k considering a state vector input \hat{X}_Δ^0 . The inverter physical limits are defined as e_{max} the maximal output voltage limit, i_{max} the maximal output duty ratio limit, α_{max} the maximal duty ratio limit.

Hence, considering a state vector input \hat{X}_Δ^0 at a decision instant k with a set of SM parameters p^k , the voltage and current overshoots and saturation during the prediction horizon $[0; N]$ can be determined as:

$$V_E^{[0;N]}(\hat{X}_\Delta^0, p^k) = \begin{bmatrix} V_E(0, \hat{X}_\Delta^0, p^k) \\ V_E(1, \hat{X}_\Delta^0, p^k) \\ \vdots \\ V_E(N, \hat{X}_\Delta^0, p^k) \end{bmatrix}, V_E^{tot} \in \mathbb{M}_{N,1} \quad eq\ 6.3$$

$$V_{i_L}^{[0;N]}(\hat{X}_\Delta^0, p^k) = \begin{bmatrix} V_{i_L}(0, \hat{X}_\Delta^0, p^k) \\ V_{i_L}(1, \hat{X}_\Delta^0, p^k) \\ \vdots \\ V_{i_L}(N, \hat{X}_\Delta^0, p^k) \end{bmatrix}, V_{i_L}^{tot} \in \mathbb{M}_{N,1} \quad eq\ 6.4$$

$$V_\alpha^{[0;N]}(\hat{X}_\Delta^0, p^k) = \begin{bmatrix} V_\alpha(0, \hat{X}_\Delta^0, p^k) \\ V_\alpha(1, \hat{X}_\Delta^0, p^k) \\ \vdots \\ V_\alpha(N, \hat{X}_\Delta^0, p^k) \end{bmatrix}, V_\alpha^{tot} \in \mathbb{M}_{N,1} \quad eq\ 6.5$$

with $V_E^{[0;N]}(\hat{X}_\Delta^0, p^k)$, $V_{i_L}^{[0;N]}(\hat{X}_\Delta^0, p^k)$ and $V_\alpha^{[0;N]}(\hat{X}_\Delta^0, p^k)$ characterise the voltage and current overshoots as well as the inverter saturation, the optimisation problem solution of the polymorphic control is the set of SM parameters that enables $V_E^{[0;N]}(\hat{X}_\Delta^0, p^k)$, $V_{i_L}^{[0;N]}(\hat{X}_\Delta^0, p^k)$ and $V_\alpha^{[0;N]}(\hat{X}_\Delta^0, p^k)$ to be equal to zero.

Now that the voltage and current overshoots as well as the inverter saturation are characterised depending of the state vector inputs and the applied set of SM parameters, considered constant during the entire prediction, it's possible to define the optimisation problem

6.2.3 Polymorphic VSG: optimisation problem

The optimisation problem decision vector is the set of SM parameters p^k , constituted of the five SM parameters L_d^k , $L_d'^k$, L_q^k , R_s^k and $T_{do}'^k$, constant over the prediction horizon. The set of parameters p^k is the solution that minimizes the variation of the optimised parameters set compared to the value of the nominal reference parameters p^{ref} , constituted of the reference SM parameters, L_d , L_d' , L_q , R_s and T_{do}' . The constraint of this optimisation problem is that the solution p^k removes the voltage and current overshoots and saturation.

In order to guarantee the boundedness of the solution and avoid too large values, the range of the set of admissible parameters p^k is limited by a coefficient V_{lim} , $V_{lim} \in \mathbb{M}_{1,1}$. Hence, the domain of possible value of the admissible parameters p^k , \mathbb{J} , is defined as:

$$\mathbb{J} := \left[\frac{L_d^{ref}}{V_{lim}}; L_d^{ref} \cdot V_{lim} \right] \times \left[\frac{L_d'^{ref}}{V_{lim}}; L_d'^{ref} \cdot V_{lim} \right] \times \left[\frac{L_q^{ref}}{V_{lim}}; L_q^{ref} \cdot V_{lim} \right] \\ \times \left[\frac{R_s^{ref}}{V_{lim}}; R_s^{ref} \cdot V_{lim} \right] \times \left[\frac{T_{do}'^{ref}}{V_{lim}}; T_{do}'^{ref} \cdot V_{lim} \right] \quad eq\ 6.6$$

In addition of these constraints on the range of p^k , the set of SM parameters variations between two successive sampling is also added to the cost function in order to avoid untimely SM parameters oscillations. Finally, slack variables, are added to the optimisation problem decision vector and constraints in order to enable to derive a feasible optimisation problem. The different slack variables noted $\varepsilon_E, \varepsilon_{i_L}$ and ε_α , are also added to the cost function to minimise their value.

So, the optimisation problem decision vector of this new optimisation problem, at decision instant k , are the set of SM parameters $p^k, p^k \in \mathbb{M}_{5,1}$, the slack variables $\varepsilon_E^k, \varepsilon_E^k \in \mathbb{M}_{N,1}$ for the relaxation on the voltage, the slack variables $\varepsilon_{i_L}^k, \varepsilon_{i_L}^k \in \mathbb{M}_{N,1}$ for the relaxation on the current, the slack variables $\varepsilon_\alpha^k, \varepsilon_\alpha^k \in \mathbb{M}_{N,1}$ for the relaxation on the saturation. The different element of the decision vector, $p^k, \varepsilon_E^k, \varepsilon_{i_L}^k$ and ε_α^k are constant over the prediction horizon. To simplify the notation in the optimisation problem, the variable ε is defined as:

$$\varepsilon = \begin{bmatrix} \varepsilon_E^k \\ \varepsilon_{i_L}^k \\ \varepsilon_\alpha^k \end{bmatrix}, \varepsilon \in \mathbb{M}_{3 \times N, 1}$$

With the solution of the optimisation problem is defined as:

$$S^k = \begin{bmatrix} p^k \\ \varepsilon \end{bmatrix}, S^k \in \mathbb{M}_{3 \times N + 5, 1}$$

Hence, the optimisation problem that is implemented in the polymorphic control is defined as:

$$\begin{aligned} \min_{p^k \in \mathbb{J}, \varepsilon \geq \mathbb{0}_{3 \times N, 1}} & \sum_{i=1}^5 \left| \frac{p^{ref}(i) - p^k(i)}{p^{ref}(i)} \right|^2 + \beta \cdot \sum_{i=1}^5 \left| \frac{p^{k-1}(i) - p^k(i)}{p^{ref}(i)} \right|^2 + \mu \cdot \sum_{i=1}^{3 \cdot N} \varepsilon^2(i) \\ \text{under:} & \begin{bmatrix} V_E^{[0; N]}(\hat{X}_\Delta^0, p^k) \\ V_{i_L}^{[0; N]}(\hat{X}_\Delta^0, p^k) \\ V_\alpha^{[0; N]}(\hat{X}_\Delta^0, p^k) \end{bmatrix} - \varepsilon \leq \mathbb{0}_{3 \cdot N, 1} \end{aligned} \quad \text{eq 6.7}$$

where p^{ref} is the reference set of SM parameters, p^k the candidate values of the SM parameter at the decision instant k constant for the prediction horizon $[0; N]$, p^{k-1} is the previous applied set of parameters at the decision instant $k - 1$, the domain \mathbb{J} is defined in eq 6.6, the parameters $\varepsilon_E^k, \varepsilon_{i_L}^k$ and ε_α^k are the slack decision variables and the elements β, V_{lim} and μ are adjusting coefficients for the cost function.

- The term $\left\| \frac{p^{ref} - p^k}{p^{ref}} \right\|$ penalizes the variation of the candidate values parameters set compared to the value of the nominal reference parameters.
- The term $\left\| \frac{p^k - p^{k-1}}{p^{ref}} \right\|$ and the coefficient $\beta, \beta \in \mathbb{M}_{1,1}$ penalizes the variations between two successive values.

- The coefficient $\mu, \mu \in \mathbb{M}_{1,1}$ and the vectors $\varepsilon_E, \varepsilon_{i_L}, \varepsilon_\alpha$ are called relaxation variables. The coefficient μ and the vectors $\varepsilon_E^k, \varepsilon_{i_L}^k, \varepsilon_\alpha^k$ enable to derive a feasible optimisation problem.
- To finish, the coefficient V_{lim} guarantees the boundedness of the solution and avoid too large values.

The optimisation problem is solved using a Nonlinear Programming (NLP) solver CasADi with the function “*nlpsoI*” [76]. In order to increase the problem resolution rapidity, if an optimization is necessary (violation occurred), a hot start initial guess is used, namely, the previous applied solution at the decision instant $k - 1$, $p^{k-1}, \varepsilon_E^{k-1}, \varepsilon_{i_L}^{k-1}$ and ε_α^{k-1} , is the starting points of the optimisation problem at the decision instant k .

The Figure 6.1 summarises the inputs of the polymorphic control, the state-space vectors inputs, \hat{X}_Δ^0 and the previous instant applied solution of the optimisation problem S^{k-1} . The outputs of the polymorphic control are the solution of the optimisation problem S^k .

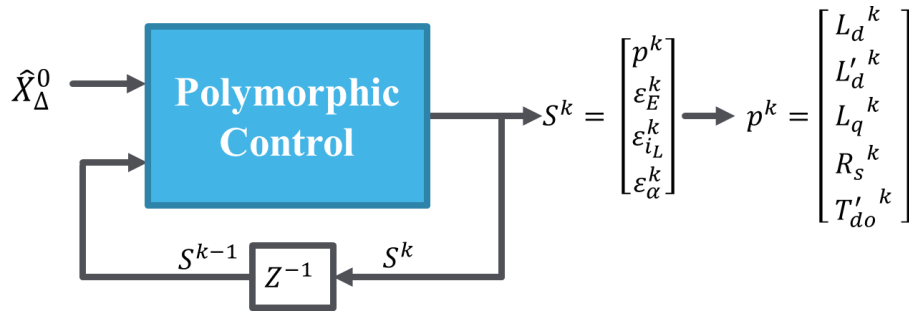


Figure 6.1: Scheme of the polymorphic control.

Now that the concept of the polymorphic VSG is presented and that the open loop optimal control problem is detailed considered for the polymorphic VSG based on predictive control, the polymorphic VSG is tested and integrated in a microgrid.

6.3 Polymorphic VSG model validation

The objective of this section is to highlight the impact of the polymorphic VSG on the risk of overcurrent, overvoltage and saturation by the inverter when integrated in a microgrid. This section is dedicated to the validation of the polymorphic VSG principle. The concern of real-time implementation in an inverter is studied in a later section.

First, in order to understand the polymorphic VSG behaviour during harsh events that could lead to a deterioration of the inverter, an example is detailed in comparison with a traditional VSG, also using the same SM reduced model. Then, both traditional VSG and polymorphic VSG inverters are compared for different scenarios to conclude on the global advantages of the advanced control.

Table 6.1: SM model characteristics and polymorphic VSG characteristics.

SM parameter	Value	Unit	Polymorphic parameter	Value	Unit
L_d^{ref}	1.93	p.u.	Control frequency	1000	Hz
$L_d'^{ref}$	0.154	p.u.	Current controller frequency	20000	Hz
L_q^{ref}	1.16	p.u.	Prediction horizon length N	20	-
R_s^{ref}	0.11	p.u.	Prediction horizon time	1	ms
$T_{do}'^{ref}$	1000	ms	V_{lim}	10	-

In Table 6.1 can be found the different parameters that have been used, the reduced model parameters for both traditional and polymorphic VSG, and the polymorphic control characteristics. Table 6.2 presents the inverter bound on the current, the voltage and the duty ratio that are considered for the polymorphic control and that will be used to determine the number of constraint violations.

Table 6.2: Inverter characteristics limits.

Characteristics	Value	Unit
Duty ratio limit	1	-
Voltages limit	750	V
Currents limit	60	A

In the next section, an example of the polymorphic VSG behaviour is presented during a phase-neutral short-circuit and compared to the traditional VSG. For the comparison, both traditional and polymorphic VSG inverters use the exact same SM model: the reduced SM model that can be found in Chapter 2 (2.3.2.2 – p17). This section allows the reader to understand during a short-circuit the VSG polymorphic functioning in operations.

6.3.1 Example of the polymorphic VSG behaviour

Figure 6.2 represents the configuration of the example detailed in this section. For this example, the inverter considered is similar to the inverter used in Chapter 4 (4.3 – p84), a Schneider Electric Conext CL 25 of a 25 kVA inverter and the simulated load is a 12.5 kVA. A VSG inverter, traditional or polymorphic, is supplying the load as a phase-neutral short-circuit is created at the inverter output at time $t = 0.5167$ s during 0.5 s. From Figure 6.3 to Figure 6.6 show the polymorphic VSG behaviour during a short-circuit compared to a traditional VSG.

*Figure 6.2: Test configuration for the polymorphic validation concept.*

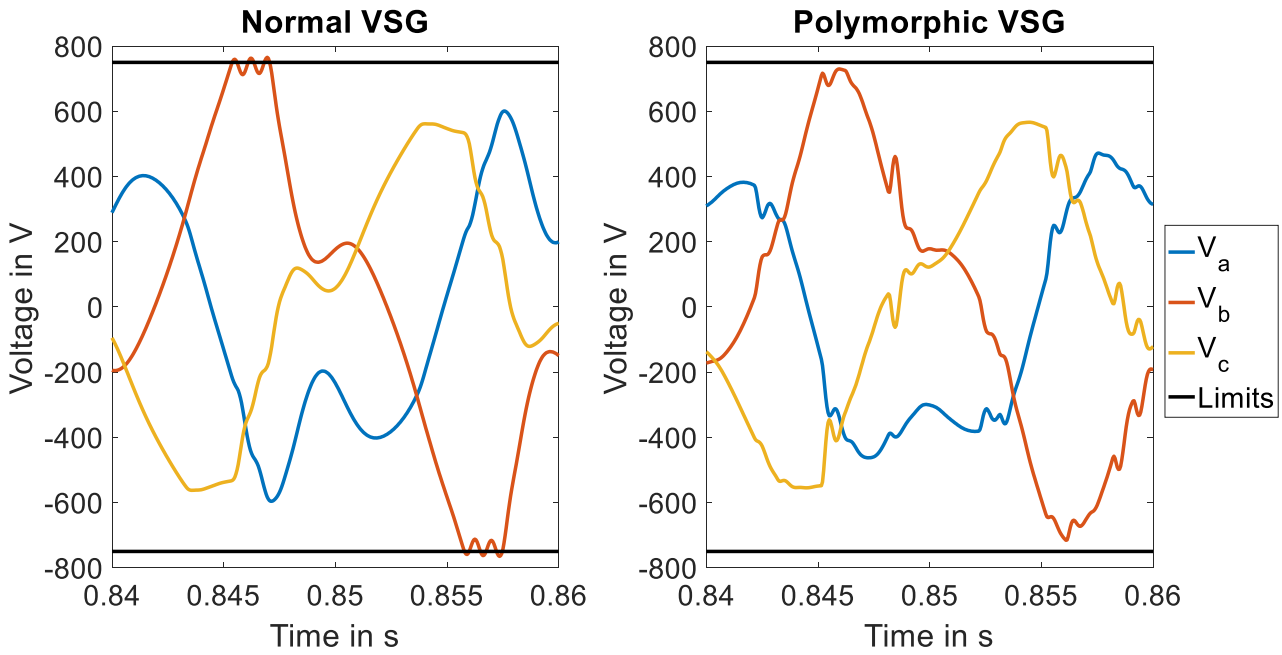


Figure 6.3: Voltages period for both normal and polymorphic VSG during the short-circuit.

Figure 6.3 shows the output three-phase voltages during the short-circuit for both traditional and polymorphic VSG inverters. It can be noted that thanks to the polymorphic control, the output voltage limit is not reached by the advanced VSG. In Figure 6.3, the voltage oscillations that are visible for the polymorphic VSG are due to the parameters modifications, as highlighted in Figure 6.4. In Figure 6.4, the SM parameters, L_d , L'_d and L_q are modified to avoid the inverter output voltages to reach its limit. The two other parameters that the polymorphic control can adapt, the resistor R_s and the transient time response, are not visible in Figure 6.4 as they are equal to their reference value during the mono-phasic short-circuit.

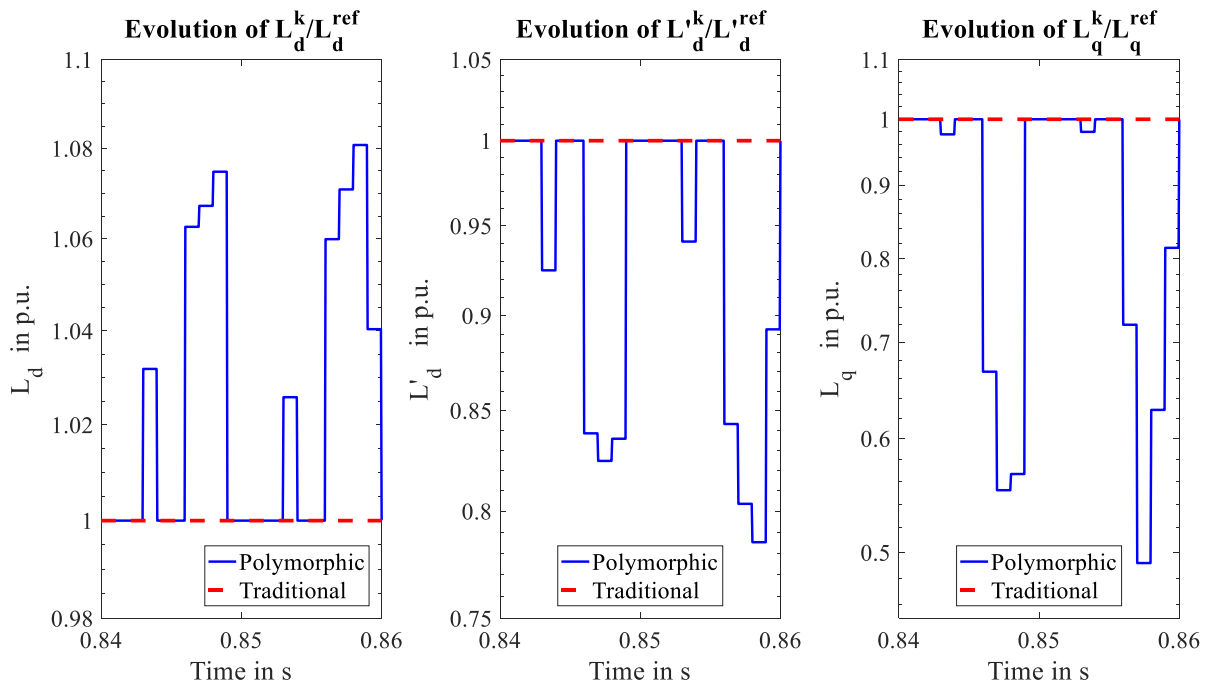


Figure 6.4: Parameters evolution during a period for both normal and polymorphic VSG during short-circuit.

The voltage oscillations in Figure 6.3 around the voltage limit concerning the traditional VSG are linked to the inverter saturation. Hence, the inverter saturation means that there is a risk that the VSG control does not return in stable states and stays in stable states. Thanks to the polymorphic VSG, this risk caused by the inverter saturation is minimized.

Figure 6.5 represents the output three-phase positive currents during the short-circuit. Thanks to the polymorphic VSG, the current limit is not reached by the inverter contrary to the traditional VSG where the current limit is reached. The fact that the inverter reaches its limits means that its internal components, like the switches, rapidly deteriorate, minimizing the inverter lifetime. The inverter can reach the current limit, but it degrades the system on long term.

An element that will have to be taken into account for the development of the polymorphic VSG in microgrid is the detection of short circuits by the protections. Indeed, as the set of SM parameters changes depending on the events, the currents will not have the same behaviours during short-circuits, making it difficult to design the short-circuit protection. This case highlights the necessity to study in detail the impact of the polymorphic VSG-based inverter integration in microgrid or traditional grid considering traditional short-circuit protection based only on the measured currents.

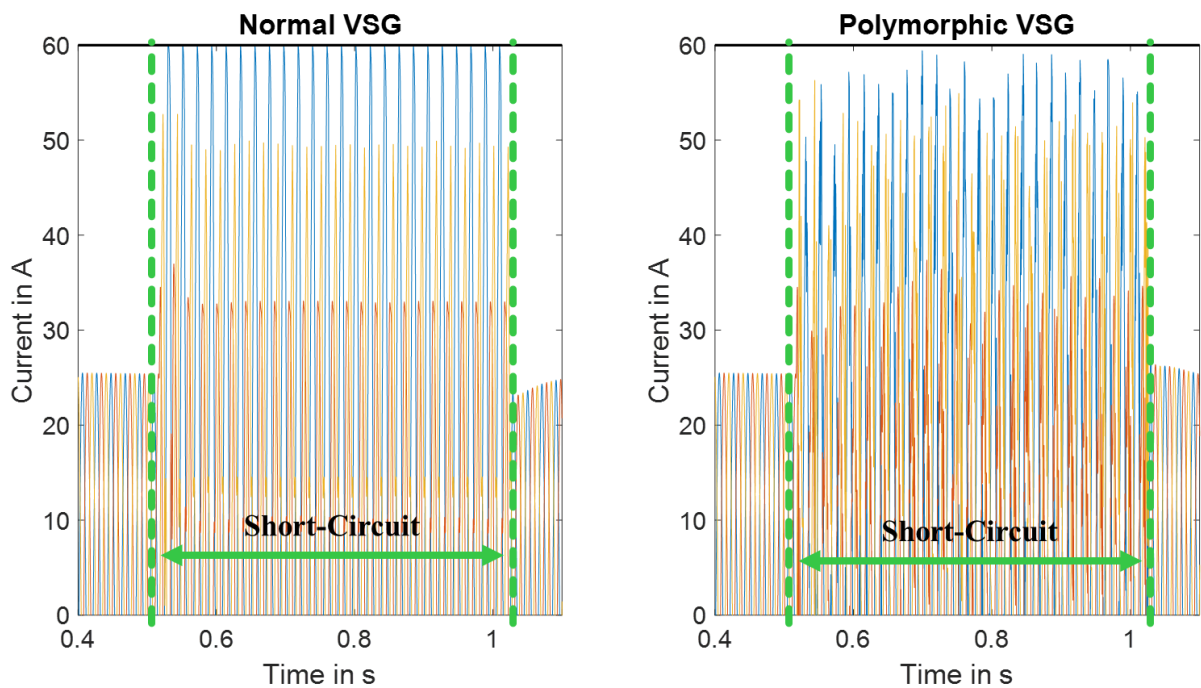


Figure 6.5: Evolution of the currents during short-circuit for both normal and polymorphic VSG.

Figure 6.6 shows the parameters evolution during the short-circuit. It can be noted that only three parameters, L_d , L'_d and L_q are presented. Indeed, the two parameters R_s and T'_{do} are constant during the entire simulation and equal to their reference values.

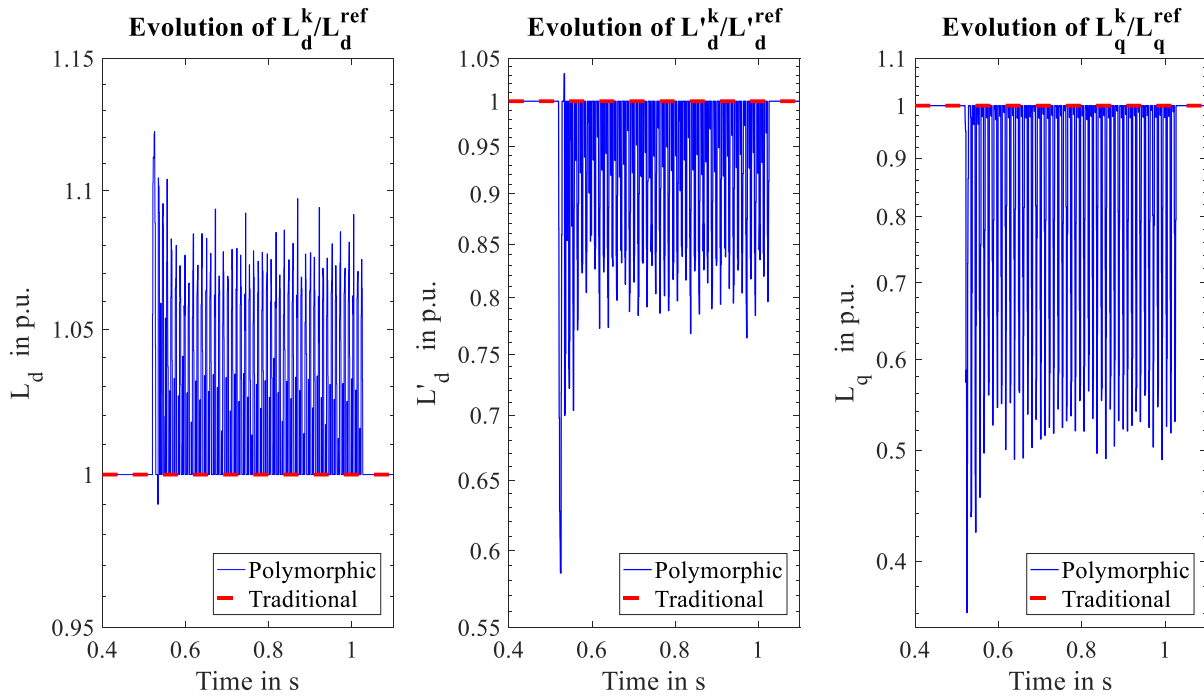


Figure 6.6: Evolution of the optimal parameters during a short-circuit.

Figure 6.6 also highlights the fact that the polymorphic control does not modify the set of SM parameters when it's not necessary as before and after the short-circuit, each parameter is equal to its reference values. Figure 6.6 also highlights the fact that the optimisation of the parameters L_d and L_q are quite opposite: the parameter L_d is generally increased as the parameter L_q is generally decreases. Hence, the non-salient hypothesis should not be respected for the resolution of the optimisation problem.

The fact that the parameters L_d , L'_d , L_q show a lot of variations could explain the voltages and currents oscillations that are visible in the polymorphic VSG compared to the traditional VSG in Figure 6.3 and Figure 6.5.

As the behaviour of the polymorphic VSG has been showed with this example with a short-circuit, the next section will present the global results of the polymorphic control during different scenarios.

6.3.2 Scenarios definition

The objective is to identify if the polymorphic VSG is capable to avoid or minimize the inverter deterioration, due to overvoltage, overcurrent or saturation, during harsh events that could occurs in a microgrid. Hence, the harsh events considered are the following:

- **Short-circuit:** phase-neutral, phase-phase, three phases short-circuit with different durations, preferably short-time as they are more impacting. In this case, the VSG is the sole power source on the microgrid as a short-circuit is applied directly at the output of the inverter.

- **Grid connexion to a microgrid and harsh load variations:** a generator is supplying loads and a polymorphic VSG is connected to this microgrid. Then different loads impacts and loads sheddings are rapidly introduced to destabilise the microgrid and harm the VSG-based inverter.

For both events, different combinations of loads characteristics, active and reactive power consumptions, are tested. As different solutions will be investigated and tested in order to make possible a future implementation of the polymorphic control in a real industrial inverter, two sets of scenarios are necessary, one for the learning process and one for the validation process. Hence, two scenarios are described below for both sort-circuit and parallelism tests.

- **For the scenario 1**

- Active power possibilities: $P = + [0.5 \% ; 15 \% ; 30 \% ; 45 \% ; 60 \%]$ of the system maximal active power.
- Reactive power possibilities: $Q = \pm [0.5 \% ; 15 \% ; 30 \% ; 45 \% ; 60 \%]$ of the system maximal reactive power.

The exhaustive set of combinations of active and reactive power are tested for phase-neutral, phase-phase, triphasic short-circuits and harsh loads impacts for each VSG inverter, traditional and polymorphic, when supplying the microgrid.

- **For the scenario 2**

- Active power possibilities: $P = + [0.5 \% ; 15 \% ; 30 \% ; 45 \% ; 60 \%]$ of the system maximal active power.
- Reactive power possibilities: $Q = \pm [0.5 \% ; 15 \% ; 30 \% ; 45 \% ; 60 \%]$ of the system maximal reactive power.

Similarly, the entire combinations of active and reactive power are tested for phase-neutral, phase-phase, triphasic short-circuits and harsh loads impacts for each VSG inverter, traditional and polymorphic, when supplying the microgrid.

6.3.3 Global results on the polymorphic control

Table 6.3 presents the results of the polymorphic control integrated in the VSG control compared to the traditional VSG for both scenario 1 and scenario 2 set of combinations. In Table 6.3, the evolution represents the variation in the number of violations compared to the traditional VSG. Hence, a negative symbol means that the number of reaches has reduced compared to the traditional VSG, a positive symbol implies that the number of reaches has increased compared to the traditional VSG.

In Table 6.3, it can be noted the polymorphic control totally remove the inverter overvoltage risk which is an advantage for both the inverter and the load connected to the microgrid. The fact that the inverter risk of saturation is reduced by more than seventy percent is a major advantage as there is a risk that the inverter stays in unstable states after saturating. Concerning the risk to reach the maximal

current, the effect of the polymorphic VSG is less performant than for the overvoltage or the duty ratio. Indeed, the output inverter currents are more linked to the load characteristics than the inverter control. Hence, as mainly short-circuit have been tested, it is logical that the maximal current is reached even by the polymorphic VSG.

Table 6.3: Limits reaches number and evolution for both normal and polymorphic VSG.

Characteristics	Traditional VSG		Polymorphic VSG	
	Number	Evolution in %	Number	Evolution in %
Current	424 978	-	357 519	-15.9 %
Voltage	43 671	-	0	-100.0 %
Duty Ratio	158 519	-	43 603	-72.5 %

In Table 6.4 is noted the simulation time for both scenarios. Hence, considering the bloc unit time necessary for the polymorphic VSG and it is not possible to implement this solution in a real inverter. In addition, in Table 6.4, the block unit time is the time needed to solve a single optimisation problem. The block unit time is measured based on the different simulations that have been done on a computer with the following configuration: Intel® Core™ i7-6820HQ, CPU @2.7 GHz, RAM 16 Go.

Table 6.4: Time simulation for both normal and polymorphic VSG.

	Traditional VSG	Polymorphic VSG
Simulation time	7 minutes	4 hours and 3 minutes
Block unit time	-	1880 μ s
Additional CPU load	-	189 %

Once the time necessary to solve a single optimisation problem is determined, based on the sampling frequency of the polymorphic control, 1 kHz, it is possible to calculate the possible addition time on the CPU in comparison of the maximal period. Hence the additional CPU load on the control card is based on the following equation, considering the maximal period of the polymorphic control is 1000 μ s:

$$\frac{\text{Block unit time}}{\text{Maximal period of the polymorphic control}} \quad \text{eq 6.8}$$

As highlighted in Table 6.4, the polymorphic control necessities a lot of time due to different elements:

- Application of the polymorph control each 1kHz.
- Resolution of the optimisation problem.
- No optimisation of the code to minimize the time simulation (such as pre-compiled control).

As the polymorphic VSG advantage compared to the traditional VSG have been proved with the different tests, the next step of the study is to investigate different solutions that may permit to develop a real online polymorphic VSG. Indeed, the duration of the different simulations highlight the fact that

the optimisation problem resolution may not be possible in operation. As the different investigated solutions are based on the evolution of the set of SM parameters, the next part of this section will study the parameters evolution for the entire simulation set. In the following section, the evolution of the different parameters is studied in order to develop future solutions that may be implementable in the industrial inverter.

In Table 6.5 can be found the number of times the polymorphic VSG parameters have changed a parameter value and the number of different values that the polymorphic VSG parameters have taken. It can be noted that the parameters L_d^k has more variations than the other two parameters L_d^k and L_q^k . In addition, the parameters R_s^k and T'_{do^k} are never modified by the polymorphic control. Hence, the future polymorphic control can be optimised by removing the control on R_s^k and T'_{do^k} parameters.

Table 6.5: Parameters variations during the different scenarios.

Parameter	Total number of values	Number of different values
L_d^k	9 696	7 701
$L_d'^k$	31 667	23 610
L_q^k	17 596	11 290
R_s^k	0	0
T'_{do^k}	0	0

Now that the concept of the polymorphic has been integrated in the VSG control and tested for multiple scenarios, the objective of the following section is to investigate different solutions to make possible an implementation of the polymorphic VSG in an industrial inverter.

6.4 Investigated solutions for the polymorphic integration

In this section is detailed different solutions that have been investigated, the comparison of the different proposed solutions is presented in another section, 6.5 (p147).

The first solution doesn't consider the notion of portability and implementable in an inverter that is the main subject of the other investigated solutions but is considered a way to the increase of the prediction horizon, avoid long time simulation in order to study its impact on the polymorphic VSG performance. Indeed, the prediction horizon that has been selected in the polymorphic VSG, 1 ms, is limited compared to the electrical period, 20ms.

The other investigated solutions are more orientated about enabling the polymorphic VSG integration in an industrial inverter. The problem mainly lies in the computation time and the memory burden that need to be contained at the price of a small drop in the performance and the corresponding gain.

6.4.1 Parabolic Prediction Solution

A solution is proposed to avoid long time simulation due to high prediction horizon length while increasing this horizon. The objective of this solution is to study a solution that increase the prediction horizon and its impact on the VSG performances.

The investigated solution is based on a prediction using a parabola approximation instead of the entire state-space model in eq 6.1. This solution will enable the polymorphic control to detect events more rapidly without increasing the time simulation thanks to the parabolic approximations of the output currents, i_L^d and i_L^q , the output voltages e^d and e^q , and the duty ratio, α^d and α^q .

Below is detailed the methodology in order to determine the parabolic equation that will be used to approximate the output currents, i_L^d and i_L^q , the output voltages e^d and e^q , and the duty ratio, α^d and α^q for the prediction horizon. For each variable of interest, i_L^d , i_L^q , e^d , e^q , α^d and α^q , a parabolic equation needs to be determined.

The definition of the parabola equation is reminded below in eq 6.9:

$$\mathcal{P}: a \cdot x^2 + b \cdot x + c = y \quad \text{eq 6.9}$$

Where a, b and c are the parabola coefficients, y is a variable of interest in study and x is the decision instant.

In order to determine the different parameters a, b and c of the parabola equation, three measures are necessary for each of the six variables of interest. Hence, the three measures that are considered for the parameters a, b and c determination are:

- Saved measures at previous decision time: y_{-1} .
- Measures at decision time: y_0 .
- Predicted profiles at time +1: y_{+1}

To avoid the non-detection of the voltage and current overshoots or saturation with only the parabola approximation, a prediction based on the state-space model in eq 6.1 is still done at each decision step. Hence, the predicted profiles are available to determine the parabola approximation parameters a, b and c . The two measures and the prediction profiles enable to determine the different parabola parameters as:

$$\begin{bmatrix} y_{-1} \\ y_0 \\ y_{+1} \end{bmatrix} = \begin{bmatrix} 1 & -1 & 1 \\ 0 & 0 & 1 \\ 1 & 1 & 1 \end{bmatrix} \cdot \begin{bmatrix} a \\ b \\ c \end{bmatrix} = M \cdot \begin{bmatrix} a \\ b \\ c \end{bmatrix} \quad \text{eq 6.10}$$

hence,
$$\begin{bmatrix} a \\ b \\ c \end{bmatrix} = M^{-1} \cdot \begin{bmatrix} y_{-1} \\ y_0 \\ y_{+1} \end{bmatrix} = \begin{bmatrix} 1/2 & -1 & 1/2 \\ -1/2 & 0 & 1/2 \\ 0 & 1 & 0 \end{bmatrix} \cdot \begin{bmatrix} y_{-1} \\ y_0 \\ y_{+1} \end{bmatrix} \quad \text{eq 6.11}$$

with the determination of the parameters a, b, c and the parabola equations, it is possible to determine a predicted element of the variable of interest y , at time $+i$, with:

$$y_{+i} = [i^2 \quad i \quad 1] \cdot M^{-1} \cdot \begin{bmatrix} a \\ b \\ c \end{bmatrix} \quad \text{eq 6.12}$$

Combining eq 6.11 and eq 6.12, for each of the six variables of interest, the output currents, i_L^d and i_L^q , the output voltage e^d and e^q , and the duty ratio, α^d and α^q , it is possible to build an approximation parabola in order to detect deterioration risks more rapidly based on:

$$y_{+i} = [i^2 \quad i \quad 1] \cdot \begin{bmatrix} 1/2 & -1 & 1/2 \\ -1/2 & 0 & 1/2 \\ 0 & 1 & 0 \end{bmatrix} \cdot \begin{bmatrix} y_{-1} \\ y_0 \\ y_{+1} \end{bmatrix} \quad \text{eq 6.13}$$

Hence, if a saturation, a voltage or a current overshoot is detected with the approximation, a prediction is then launched with the state-space model defined in eq 6.1 but considering the extended prediction horizon. Thanks to the parabolic approximation and an extended prediction for i time, the new prediction horizon is considered as $[0, i \times N]$.

So, the optimisation problem decision vector of this new optimisation problem with an increase prediction horizon $[0 ; i \times N]$, at decision instant k , are the set of SM parameters $p^k, p^k \in \mathbb{M}_{5,1}$, the vector $\varepsilon_E^k, \varepsilon_E^k \in \mathbb{M}_{i \times N, 1}$ for the relaxation on the voltage, the vector $\varepsilon_{i_L}^k, \varepsilon_{i_L}^k \in \mathbb{M}_{i \times N, 1}$ for the relaxation on the current, the vector $\varepsilon_\alpha^k, \varepsilon_\alpha^k \in \mathbb{M}_{i \times N, 1}$ for the relaxation on the saturation. The different elements of the decision vector, $p^k, \varepsilon_E^k, \varepsilon_{i_L}^k$ and ε_α^k are still constant over the prediction horizon. To simplify the notation in the optimisation problem, the variable $\bar{\varepsilon}$ is defined as:

$$\bar{\varepsilon} = \begin{bmatrix} \varepsilon_E^k \\ \varepsilon_{i_L}^k \\ \varepsilon_\alpha^k \end{bmatrix}, \varepsilon \in \mathbb{M}_{3 \times i \times N, 1}$$

so, the solution of the optimisation problem is defined as:

$$S^k = \begin{bmatrix} p^k \\ \bar{\varepsilon} \end{bmatrix}, S^k \in \mathbb{M}_{3 \times i \times N + 5, 1}$$

Hence, the optimisation problem that is implemented in the polymorphic control is defined as:

$$\min_{p^k \in \mathbb{J}, \bar{\varepsilon} \geq \mathbb{O}_{3 \times i \times N, 1}} \sum_{i=1}^5 \left| \frac{p^{ref}(i) - p^k(i)}{p^{ref}(i)} \right|^2 + \beta \cdot \sum_{i=1}^5 \left| \frac{p^{k-1}(i) - p^k(i)}{p^{ref}(i)} \right|^2 + \mu \cdot \sum_{i=1}^{3 \times i \times N} \bar{\varepsilon}^2(i) \quad \text{eq 6.14}$$

under: $\begin{bmatrix} V_E^{[0; i \times N]}(\hat{X}_\Delta^0, p^k) \\ V_{i_L}^{[0; i \times N]}(\hat{X}_\Delta^0, p^k) \\ V_\alpha^{[0; i \times N]}(\hat{X}_\Delta^0, p^k) \end{bmatrix} - \bar{\varepsilon} \leq \mathbb{O}_{3 \times i \times N, 1}$

where p^{ref} is the reference set of SM parameters, p^k the candidate values of the SM parameter at the decision instant k constant for the prediction horizon $[0; i \times N]$, p^{k-1} is the previous applied set of parameters at the decision instant $k - 1$, the domain \mathbb{J} is defined in eq 6.6, the parameters $\varepsilon_E^k, \varepsilon_{i_L}^k$ and

ε_α^k are the slack decision variables and the elements β , V_{lim} and μ are adjusting coefficients for the cost function.

The above optimisation problem eq 6.14 is solved with the same NLP solver CasADi with the function “*nlpsol*” [76].

Figure 6.7 is the representation of the inputs and outputs of the polymorphic control with an enhanced prediction. The inputs of this control are the state-space vectors inputs, \hat{X}_Δ^0 , the previous state-space vectors inputs, \hat{X}_Δ^{-1} and the previous instant applied solution of the optimisation problem S^{k-1} . The outputs of this control are the solution of the optimisation problem S^k .

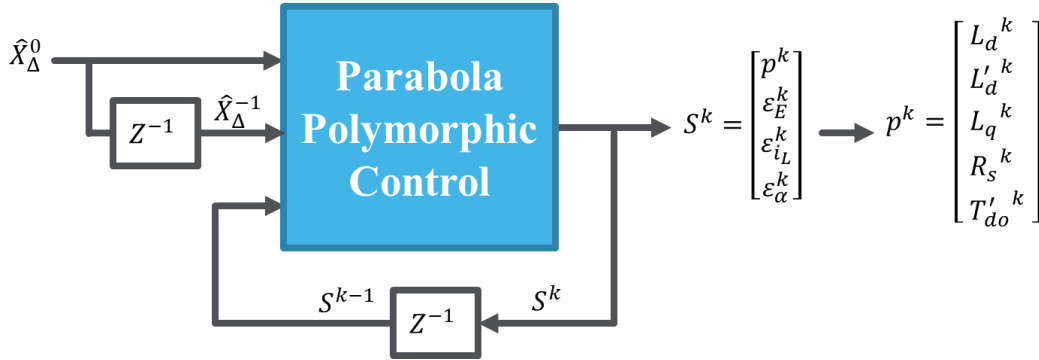


Figure 6.7: Scheme of the polymorphic control with a parabolic approximation.

The methodology of this proposed solution to increase the prediction horizon is detailed below. For the comparison with the other investigated solutions, it has been decided to increase the prediction time by 5, so $i = 5$.

• Methodology of parabola polymorphic control

- ➔ Real model prediction for a prediction horizon of $[0, N]$.
- ➔ Determination of the parameters a, b and c based on y_{-1}, y_0 and y_{+1} for each of the six variables of interest, current, voltage and duty ratio in axe d and axe q.
- ➔ Parabolic approximation for 4 more time steps ($i = 5$) thanks to the model described in eq 6.13
 - No reach of the violation: reference parameters.
 - A violation is reached:
 - Real prediction for $[0 ; i \times N]$ with eq 6.1:
 - No violation: reference parameters.
 - Violation: optimisation resolution of eq 6.14 ($i = 5$)

Table 6.6 presents the time simulation for scenario 1 of the presented solution, the polymorphic VSG with a parabolic approximation and the polymorphic VSG, both with a prediction horizon of $[0; 5.N]$ (extended for the polymorphic VSG).

Table 6.6: Time simulation for parabola polymorphic VSG and polymorphic VSG for scenario 1.

	Parabola approximation with a prediction horizon [0; 5. N]	Polymorphic VSG with a prediction horizon [0; 5. N]
Time	3 hours and 42 minutes	28 hours and 12 minutes

Table 6.7 details the number and evolution of both solutions, in comparison with a traditional VSG with fixed parameters during scenario 1. It can be noted that the proposed solution, with a parabolic approximation, has similar results to the polymorphic VSG with a fixed and extended prediction horizon of [0; 5. N] for 10 % of the polymorphic VSG simulation time with the extended prediction horizon.

Hence, the investigated solution to increase the prediction horizon based on a parabolic approximation enables the system to produce similar results in curtailing the time simulation by a coefficient 10 compared to a polymorphic VSG with the same prediction horizon.

Table 6.7: Limits reaches number and evolution for parabola polymorphic VSG and polymorphic VSG during scenario 1.

	Traditional VSG	Parabola approximation with a prediction horizon [0; 5. N]		Polymorphic VSG with a prediction horizon [0; 5. N]	
Characteristics	Number	Number	Evolution in %	Number	Evolution in %
Current	216 890	194315	-10.41	193079	-10.98 %
Voltage	31 865	4951	-84.46	3521	-88.95 %
Duty Ratio	120 733	46008	-61.89	35226	-70.82 %

Now that the solution to increase the prediction horizon is detailed, the next solutions investigate have as main objective the integration of the polymorphic concept in an industrial inverter.

6.4.2 Regression models of the polymorphic VSG behaviour

The objectives of the regression models are: avoid the resolution of the optimisation problem and minimize the uncertainties. The regression models are only based on the optimised parameters the reference parameters are removed from the studied data. As it was identified only the parameters L_d^k , $L_d'^k$ and L_q^k have been considered for the regression since the parameters R_s^k, T_{do}^k are always constant. It should be noted that each of the three parameters have a dedicated regression model. Indeed, as the only the modified parameters are kept for the regression, in removing the reference value for each parameter, the three different regression models have different and dedicated inputs and outputs vectors.

So, for each simulation and each decision time, the relevant inputs of the polymorphic control, have been recovered and accumulated in the same vector: the vector \hat{X}_Δ^0 and the previous decision time set of parameters p^{k-1} , a total of 21 inputs. The slack variables $\varepsilon_E^k, \varepsilon_{i_L}^k, \varepsilon_\alpha^k$ are not considered of the regression. These input vectors constitute the data that will be used for the determination of the regression model.

Each parameter has its own dedicated inputs vector noted $X^{L_d^k}$, $X^{L_d'^k}$ and $X^{L_q^k}$ and output $Y^{L_d^k}$, $Y^{L_d'^k}$ and $Y^{L_q^k}$. The output vector of the regression model, $Y^{L_d^k}$, $Y^{L_d'^k}$ and $Y^{L_q^k}$, are constituted of the concatenation of the parameters L_d^k , $L_d'^k$ and L_q^k that are different of their reference values.

Hence, for a decision instant i and j an element of the vectors $X^{L_d^k}$ and $Y^{L_d^k}$, the vector $X^{L_d^k}$ and $Y^{L_d^k}$ are filled following the relationship below:

$$\begin{cases} X^{L_d^k}(j) = [\hat{X}_\Delta^0(i) & p^{i-1}] \\ Y^{L_d^k}(j) = L_d^i \end{cases} \text{ if } L_d^i \neq L_d^{ref} \quad \text{eq 6.15}$$

Similarly, for a decision instant g and h an element of the vectors $X^{L_d'^k}$ and $Y^{L_d'^k}$, the vector $X^{L_d'^k}$ and $Y^{L_d'^k}$ is defined by:

$$\begin{cases} X^{L_d'^k}(g) = [\hat{X}'_\Delta^0(i) & p^{g-1}] \\ Y^{L_d'^k}(g) = L_d'^h \end{cases} \text{ if } L_d'^h \neq L_d'^{ref} \quad \text{eq 6.16}$$

Finally, for a decision instant e and f an element of the vectors $X^{L_q^k}$ and $Y^{L_q^k}$, the vector $X^{L_q^k}$ and $Y^{L_q^k}$ is determined by:

$$\begin{cases} X^{L_q^k}(f) = [\hat{X}_\Delta^0(i) & p^{e-1}] \\ Y^{L_q^k}(f) = L_q^e \end{cases} \text{ if } L_q^e \neq L_q^{ref} \quad \text{eq 6.17}$$

To determine the regression model, different methods of regressors have been studied:

- Kernel Ridge;
- Tree;
- Neighbour;
- Classification;
- Support Vector Classification.

In addition, for each regressor model, two different configurations have been studied:

- Regression on raw data.
- Regression after a standardisation (ST) and a principal component analysis (PCA).

Below are detailed the ST and the PCA methodologies that have been used for the determination of the different regression models. Then, these methodologies are applied to determine the regression models.

- **Standardisation (ST)**

With the ST, for the three input vectors $X^{L_d^k}$, $X^{L_d'^k}$ and $X^{L_q^k}$, each element of the vector is converted into a vector having a zero mean and variance equal to 1. Each 21 elements of the inputs vector have a dedicate centering mean value μ and a dedicate centering variance σ that enable the conversion. When an input has submitted a ST, the notation X_{SC} , is applied. Once the parameter μ and σ are calculated, the conversion is done with the equation below:

$$X_{SC} = \frac{X - \mu}{\sigma} \quad \text{eq 6.18}$$

With X the element of an input vector, X_{SC} the standardised of this input vector element, μ and σ the dedicate mean and variance of this input vector.

In total, there is 3×21 different centering means μ and variances σ that have to been saved for the input conversion. Hence, considering $\mathcal{M}_\sigma, \mathcal{M}_\sigma \in \mathbb{M}_{21,3}$ and $\mathcal{M}_\mu, \mathcal{M}_\mu \in \mathbb{M}_{21,3}$, the matrixes that contained the different centering variances and means for the three different parameters regression model.

- **Principal Component Analysis (PCA)**

The objective is to minimize the regression model inputs number in order to decrease the size of the regression models and keep the fundamental signal. So, the passage from standardised inputs to PCA is a matrix multiplication depending of the size of the selected PCA.

In order to select the number of inputs for the PCA, it has been decided that the inputs selected number should represent more than 96 % of the entire signal. Figure 6.8 represents the signal percentage characteristics depending of the number of inputs take into account for the PCA. Hence, with Figure 6.8, it is possible to say that each parameter L_d, L_d' and L_q needs 6 inputs, combinations of the 21 inputs, to represent more than 96 % of the entire signal instead of 21.

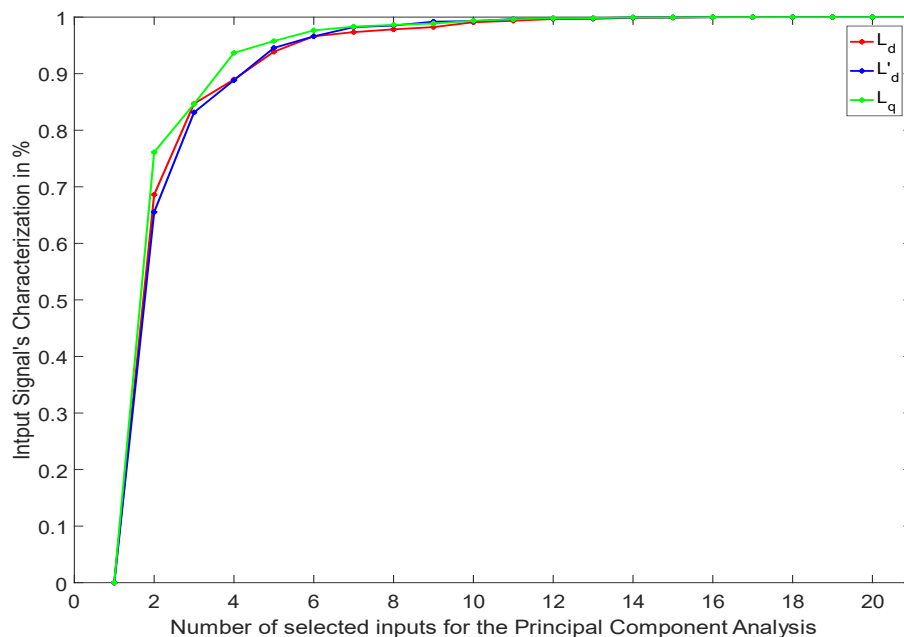


Figure 6.8: Signal's percentage depending of the inputs number for the PCA.

The PCA is calculated based on the vector after ST. So, the equation to adapt the standardised data to consider the PCA is:

$$X_{SC}^{PCA} = \mathcal{M}_{PCA} \cdot X_{SC} \quad \text{eq 6.19}$$

With X_{SC} the standardised of an input vector element, X_{SC}^{PCA} the principal component vector of this standardised element, $\mathcal{M}_{PCA}, \mathcal{M}_{PCA} \in \mathbb{M}_{6,21}$ the conversion matrix from standardised input element to standardised and PCA element. Hence, three different matrixes, each one a $\mathbb{M}_{6,21}$ matrix, have to be saved for the future conversion for each of the three regression models, noted $\mathcal{M}_{PCA}^{L_d^k}$, $\mathcal{M}_{PCA}^{L'_d^k}$ and $\mathcal{M}_{PCA}^{L_q^k}$.

Now, that the ST and PCA methodologies have been detailed, the next step is to determine the regression model. The same methodology is applied for each of the three parameters L_d^k , L'_d^k and L_q^k to determine its dedicated regression model and also for each tested regressor model. It can be noted that ones the standardised centering means and variances as well as the matrix M_{PCA} are calculated for each of the 21 inputs based on the recovered data, their values is constant.

The methodology that has been followed is described below.

- **Determination of the regression models**

1. Recuperation of $Y^{L_d^k}$, $Y^{L'_d^k}$ and $Y^{L_q^k}$ from scenario 1.
2. Permutation and mix of each parameter data vector to remove any temporal relationship.
3. Separation of this scenario 1 data vector:
 - a. 50 % of the data vector used for the regression
 - 1) Regression model with raw data

or

 - 2) Regression model with standardised and PCA data
 - i. Determination of the ST coefficients: centering means and variances.
 - ii. Determination of the PCA matrixes.
 - iii. Determination of the regression model based on the standardised and PCA inputs

Then, the regression model is validated:

- b. 50 % of the data vector used for the regression model's validation.
 - 3) Validation of the regression with raw data.
 - 4) Validation of the regression based on the standardised and PCA input data

Figure 6.9 and Figure 6.10 represent the inputs and outputs of the both polymorphic controls based on regression model with raw data or with ST and PCA data.

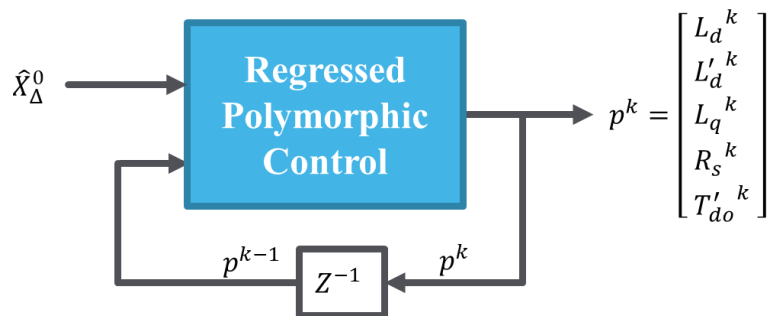


Figure 6.9: Scheme of the polymorphic control based on raw data regression model.

It can be noted that the both models have the same inputs, the state-space vectors inputs, \hat{X}_Δ^0 and the previous instant applied set of parameters p^{k-1} , and the same outputs, the set of parameters p^k . It can be noted that the parameters R_s^k and T'_{do^k} are constant and equal to their respective reference value R_s^{ref} and $T'_{do}{}^{ref}$. Concerning the regression model with ST and PCA, the different matrixes, \mathcal{M}_σ , \mathcal{M}_μ , $\mathcal{M}_{PCA}^{L_d^k}$, $\mathcal{M}_{PCA}^{L'_d^k}$ and $\mathcal{M}_{PCA}^{L_q^k}$ need to be accessible for the data conversion before sending the data to the regression model.

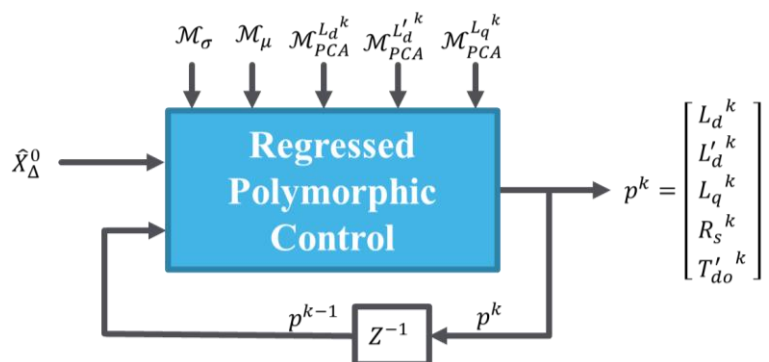


Figure 6.10: Scheme of the polymorphic control based on ST and PCA regression model.

Now that the regression model, depending of the regressor used and configuration, raw data or standardised with a PCA data, the methodology of the polymorphic control based on the regression model is detailed below.

- Methodology of regression model control

➔ Real model prediction based on eq 6.1.

- No reach of the violation: reference parameters application
- A violation is reached, so determination of the new parameters L_d^k , L'_d^k and L_q^k values:
 - Regression model based on the inputs vector.
 - Application of the regressed parameters L_d^k , L'_d^k and L_q^k

or

- Application of the ST coefficient on the inputs vectors.
- PCA matrixes multiplication on the standardised inputs vector.

- Regression models based on standardised and PCA inputs.
- Application of the regressed parameters $L_d^k, L_d'^k$ and L_q^k

In addition of the different regressor that have been investigated in the above section, the last proposed solution in order to implement the polymorphic concept in a real inverter is determination of the best parameters combinations tin operation that avoid the realisation of the overvoltage, overcurrent or saturation. The comparison of the different solutions will be presented after the next detailed section.

6.4.3 Determination of the best parameters combination

In studying the parameter evolutions, the hypothesis is that the exact value of the parameters has less importance than the fact to modify the parameters: increasing or decreasing its value. Hence, in this section, the investigated solution proposes that at each decision time, only a limited and discrete set of combination of parameters is used in the prediction and the best is taken to be the optimal solution.. The solution that is applied is the set of SM parameters that minimises the risk of deterioration and the parameters variations.

To validate this hypothesis, only three values have been selected for the possible combinations: the reference, an upper value and a lower value. Similarly to the regression models, only the parameters $L_d^k, L_d'^k$ and L_q^k have been considered for possible combination set since the parameters R_s^k, T_{do}^k are constant. In Table 6.8, the upper and lower values are determined based on the weighted average for each parameter respectively above or below the reference value that have been deployed by the polymorphic control during the simulations. Since three values are kept for each parameter, 27 sets of combinations are possible and calculated in operation by the controller.

so, the domain of possible value of the admissible parameters p^k becomes \mathbb{K} :

$$\mathbb{K} := \{L_d^{min}; L_d^{ref}; L_d^{max}\} \times \{L_d'^{min}; L_d'^{ref}; L_d'^{max}\} \times \{L_q^{min}; L_q^{ref}; L_q^{max}\} \times R_s^{ref} \times T_{do}^{ref} \quad eq\ 6.20$$

hence, the problem could be defined as:

$$\min_{p^k \in \mathbb{K}} \sum_{i=1}^5 \left| \frac{p^{ref}(i) - p^k(i)}{p^{ref}(i)} \right|^2 + \beta \cdot \sum_{i=1}^5 \left| \frac{p^{k-1}(i) - p^k(i)}{p^{ref}(i)} \right|^2$$

$$\text{under: } \begin{bmatrix} V_E^{[0;N]}(\hat{X}_\Delta^0, p^k) \\ V_{i_L}^{[0;N]}(\hat{X}_\Delta^0, p^k) \\ V_\alpha^{[0;N]}(\hat{X}_\Delta^0, p^k) \end{bmatrix} \leq \mathbb{O}_{3,N,1} \quad eq\ 6.21$$

where p^{ref} is the reference set of SM parameters, p^k the candidate values of the SM parameter at the decision instant k constant for the prediction horizon $[0; N]$, p^{k-1} is the previous applied set of parameters at the decision instant $k - 1$, the domain \mathbb{K} is defined in eq 6.20.

This problem is not solved with a dedicated solver as this problem is not defined as an optimisation problem. For each of the 27 combinations are calculated the different vectors $V_E^{[0;N]}(\hat{X}_\Delta^0, p^k)$,

$V_{i_L}^{[0;N]}(\hat{X}_\Delta^0, p^k)$ and $V_\alpha^{[0;N]}(\hat{X}_\Delta^0, p^k)$ in addition of the cost function. The combination that will be applied is the solution that minimizes both the cost function and the different vectors.

In Table 6.8 can be found the three values considered for the different parameters after analysis of the parameters set that the polymorphic control has deployed during the scenarios.

Table 6.8: Parameters values determination

Parameters	L_d^k	$L_d'^k$	L_q^k	R_s^k	T_{do}^k
Lower value	$0.67 \times L_d^{ref}$	$0.51 \times L_d'^{ref}$	$0.69 \times L_q^{ref}$	–	–
Reference value	L_d^{ref}	$L_d'^{ref}$	L_q^{ref}	R_s^{ref}	T_{do}^{ref}
Upper value	$1.22 \times L_d^{ref}$	$1.29 \times L_d'^{ref}$	$1.46 \times L_q^{ref}$	–	–

Figure 6.11 represents the inputs and the outputs of the polymorphic control with the control based on the determination of the best combination. The inputs of this model are \hat{X}_Δ^0 and the previous instant applied set of parameters p^{k-1} , and the outputs, applied set of parameters p^k . For this model, the upper and lower parameter values that have been determined need to be accessible for the determination of the different possible combinations, visible in Table 6.8.

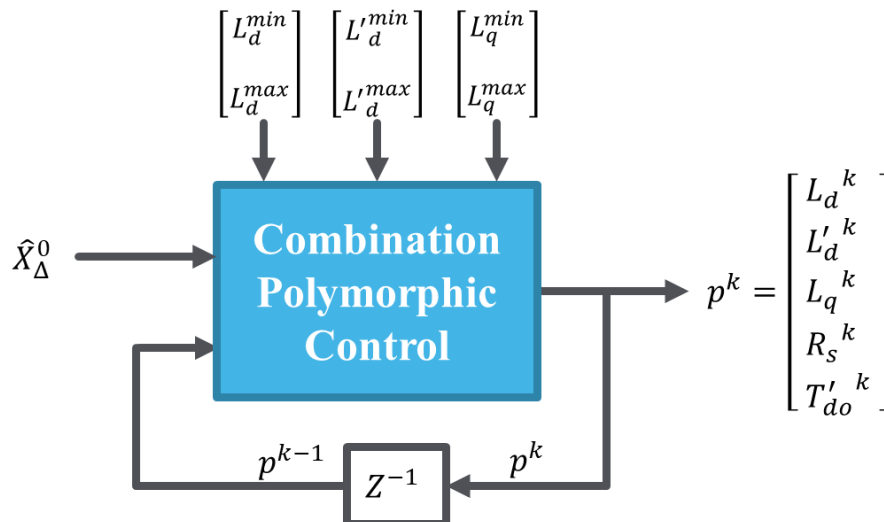


Figure 6.11: Scheme of the polymorphic control based on the determination of the best combination.

Now that the concept based on the determination of the best combination of parameters is described, the next step is to detail the methodology of application of this solution.

- **Methodology for the best parameters combination control**

→ Real model prediction based on eq 6.1.

- No reach of the violation: reference parameters.
- A violation is reached:

- Model prediction for the 27 combinations of parameters based on eq 6.1.
- Determination of the predicted deterioration risk for the 27 parameters combinations based on eq 6.21.
- Determination of the cost function for the 27 parameters combinations based on eq 6.21.
- Selection of the combination that minimize the risk value and minimises the cost function.

The determination of the best combination set concludes the different investigated solutions that have been tested in order to integrate the polymorphic control in an industrial inverter.

6.5 Comparison between the different advanced solutions

Now that the different investigated solutions have been explained and their respective methodology described, the solutions are implemented in the VSG control. Table 6.9 to Table 6.11 present the different results of the investigated solutions. Concerning the regression models, the regressor used is Kernel Ridge but the different tested regressors have similar results.

Table 6.9 shows the time simulation of the different investigated solutions, the block unit time and the additional CPU load on the control card. It can be noted that the resolution of the optimisation problem needs a lot of time. The regressions models, with raw data or with ST and PCA, are the faster solutions with 8 minutes, it is only one minute more than the traditional VSG. Concerning the combination of parameters, the simulation time represents around ten minutes, more similar in time with the regression models than the dynamic optimisation models. Hence, the only models that can be implemented in a real inverter are the regression models and the best combinations polymorphic VSG.

Table 6.9: Time simulation depending of the selected solution.

Models	Traditional VSG	Dynamic Optimisation		Regression Model		Combinations
		One step Prediction	Parabola Prediction	Regression	Regression - ST-PCA	
All simulations	7 minutes	4 hours and 3 minutes	7 hours and 24 minutes	8 minutes	8 minutes	12 minutes
Block unit time	-	1880 μs	3496 μs	8 μs	8 μs	40 μs
Additional CPU load	-	189 %	350 %	1 %	1 %	4 %

However, regarding Table 6.10 and Table 6.11, it is possible to say that the regression models are not efficient and not adapted to the polymorphic control. Indeed, the regression models increase the number of incidents meaning that these solutions increase the deterioration of the inverter. The low efficiency of both regression models shows that the regression are not optimal for the adaptation of the polymorphic control. This phenomenon may come from the extrapolation problem which seems to give too many errors. Another problem that is not visible here is the fact that a regression model takes more than 3.2 Mo which is not possible to integrate in an industrial control card.

Table 6.10: Limits reaches number depending of the selected solution.

Numbers	Traditional VSG	Dynamic Optimisation		Regression Model		Combinations
		Traditional	Prediction with Parabola	Regression	Regression - ST-PCA	
Current	424 978	357 519	381 142	383889	413607	285497
Voltage	43 671	0	9 548	45260	77984	22
Duty Ratio	158 519	43 603	97 596	227275	278908	75810

Concerning the model using the parabola approximation prediction, the results in Table 6.10 and Table 6.11 prove that one step of prediction horizon, 1 ms, is enough to have a good result concerning the polymorphic control. Indeed, the inverter is subjected to rapid and high variations due to the electrical network characteristics which reduce the prediction efficiency, making this polymorphic VSG changing parameters when it is not necessary. As expected, the time simulation is important as the prediction horizon is increased.

The best trade-off for the integration of the polymorphic control, regarding Table 6.10 and Table 6.11, seems to be the parameters set combination. Indeed, the block unit time is dramatically reduced compared to the dynamic optimisation of the first polymorphic control, for results that are similar regarding the currents and duty ratio limits, and a little below concerning the voltage limit. A possibility to improve the performances of this control is to add the maximal and minimal values to the possible values that the parameters can take.

Table 6.11: Evolution of limits reaches number depending of the selected solution.

Evolutions	Traditional VSG	Dynamic Optimisation		Regression Model		Combinations
		Traditional	Prediction with Parabola	Regression	Regression - ST-PCA	
Current	—	−21.1 %	−9.8 %	−1 %	−2.7 %	−31.7 %
Voltage	—	−100.0 %	−72.7 %	+3.6 %	+78.6 %	−64.4 %
Duty Ratio	—	−78.9 %	−55.1 %	+43.4 %	+75.9 %	−47.9 %

To conclude on the investigated solutions for the integration of the polymorphic VSG in an industrial inverter is that the best trade-off is the determination of the best combination. Indeed, this solution is constituted of equations that are simple and repetitive for each combination. The best solution is still the resolution of the optimisation problem, but the implementation in an industrial control card may not be adapted due to the CPU load limitation and the capacity limitation. In addition, the regression model solutions are not adapted for this kind of control for multiple reasons such as the number of inputs and the high time variability of the events.

6.6 Conclusion

In this chapter, the concept of polymorphic VSG is presented. The objective is not to increase the microgrid stability, in minimizing frequency or voltage oscillations, but to reduce the risk of inverter deterioration created by harsh event on the microgrid such as short-circuits. After the analytic description of the polymorphic concept, the polymorphic VSG is compared to a traditional VSG integrated in a microgrid submitting harsh events, different short-circuits in standalone or in parallel with another source in different configurations. However, the polymorphic control can't be implemented in a real inverter as its block unit time is too important for the inverter control card.

After the validation of the polymorphic control in simulations, different solutions have been investigated to make possible the realisation of a real polymorphic VSG. A first solution proposed to increase the prediction horizon length is a parabola method in order to develop on the impact of the prediction efficiency. Then, the other investigated solutions have been selected to make possible a future implementation in an industrial inverter. The different regressors solutions that have been tested are not efficient for this kind of control. The last investigated solution is the in operation determination of the best parameters combination. This solution seems the best comprise as it is implementable in the inverter and the fact that the efficiency is similar to what can be found with the resolution of the optimisation problem.

6.7 Perspectives

First, the next step is to work on the implementation of the best combination polymorphic in the real inverter. Then, a perspective of work is to improve the investigated solution based on the best combination determination. A first improvement could be the integration of the maximal and minimum values to the possibility for each parameter and develop on its impact on the block unit time. Finally, a more complete study to select the exact number of parameters could be done in order to determine the best compromise between performances with a high number of different values and rapidity of execution for its future implementation in an inverter control card.

Even if the different investigated solutions based on regressor don't have a good efficiency, a perspective could be to implement more advanced solution as neural networks. In addition, if the polymorphic control is implemented in a real inverter, more data will be disponsible to precise a possible model based on regression.

Finally, in order to ensure the development of the polymorphic VSG, its integration in a microgrid or a classical grid needs to be researched and studied. Indeed, as the VSG can adapted its parameters during harsh events, the polymorphic behaviour is not easily predictable making the notion of stability and protection a major difficult to determine.

Chapter 7. General Conclusions and Perspectives

7.1 General Conclusion

This thesis is dedicated to the VSG-based inverters and their integration in microgrids with a high level of variable renewable energy penetration. This PhD have been carried out thanks to the cooperation between two laboratories, G2Elab and Gipsa-Lab, in collaboration with Schneider Electric and its R & D team, Power Conversion.

In a first part, three SM models for the VSG implementation control in an inverter were detailed, characterised, and compared with respect to various test cases. The three SM models were a “complete” one, constituted of the all dynamic electrical equations, a “reduced” one constituted of a virtual impedance, and a “static” one based on the SM’s steady state. With the help of those models, this thesis proposed and illustrated the relevance of tests for a standardisation of inverter-based generators (notably with VSG-based controller), based on the SM standards and characteristics. The standardisation proposal tests are constituted of active and reactive power load impacts, short-circuit in standalone or parallel configurations and total harmonics distortions. The tests are designed to ensure that any VSG grid-forming inverter can be integrated in a microgrid, once respecting the proposed standards. The set of tests proposed for the standardisation of grid-friendly VSG is a first step that would necessitate to more precisely define thresholds as well as requirements for additional modification of power sources considering the parallelism of the power sources.

In a second part, three controllers, adapted to an implementation in an industrial inverter (with limited computational power), have been detailed: a PI controller, a PI controller with an observer and finally, our proposed controller, a LQR with integrator controller and observer. The performance of the observer has been validated with the study on the controller. Indeed, contrary to the PI controller alone,

PI controller and observer is stable during harsh events. However, even if the instabilities are suppressed by the used of the observer, in some configurations such as short-circuit or off-loading, the results need to be improved to ensure a better performance of the VSG regarding standardisation criteria.

The LQR controller (with integrator and observer) was analytically detailed and tested after being implemented in the VSG control. With in mind the objective to have a performant enough controller, implementable in an industrial inverter, the LQR controller proved to be the best compromise between performance and simplicity. Various experimental results were presented, based on use cases constructed in the microgrids laboratory in the Schneider Electric R & D facility in Grenoble, France. Thanks to the proposed controller, the VSG was stable and capable of supplying highly non-linear or unbalanced loads such as drives or single-phase motors as well as survive short-circuits, which are mandatory to guarantee the well-functioning and plug-and-play operation of VSG in microgrids.

Following the validation of the proposed controller, a methodology to adapt the SM model implemented in the VSG controller of any inverter, depending on its characteristics, was described. The methodology to determine adapted SM parameters and the proposed controller have been tested with various scales of platforms and inverter's PWM switching frequencies. In order to validate both the detailed methodology and the proposed controller replicability, experimental results were conducted. A laboratory-scale prototype system has been used to test the VSG control, deployed in the testbench of the G2Elab. In order to validate both the methodology and the portability of the proposed controller, the VSG-based inverter was tested in both standalone and parallel operations, integrated in a basic microgrid.

Finally, the concept of polymorphic VSG, an advanced VSG control, was presented. The objective was not to increase the microgrid stability, in minimizing frequency or voltages oscillations but to reduce the risk of deterioration created by harsh event on the microgrid such as short-circuits. After the analytic description of the polymorphic concept, the polymorphic VSG is compared to a traditional VSG integrated in a microgrid subject to harsh events, like short-circuits in standalone configuration or in parallel with other sources. After the validation of the polymorphic concept and control in simulations, different solutions have been investigated. A first solution was proposed to increase the prediction horizon in the form of a parabola method in order to increase the prediction efficiency of the polymorphic control. Then, the other solutions that have been investigated have been selected with the constraint to make possible a future implementation in an industrial inverter with limited computational capabilities.

To conclude, the VSG inverter is one of the most promising solution for the integration of renewable energy in the context of microgrid. The VSG control enables the renewable energies to be an active element of the electrical network in in giving them the possibility to stabilize the voltage or the frequency of microgrid which is not the case for most of the renewable energy connected to the electrical grid.

7.2 Perspective of work

A perspective of development for further researches could be the integration of the homopolar axis of the reference $dq0$. It has been neglected in this study, for the different models and its consideration for the VSG controller may improve the VSG performances when supplying unbalanced loads. It could be interesting to compare the proposed controller with and without homopolar axis especially during unbalanced loads impact.

Then concerning the polymorphic VSG, its integration in a microgrid or a classical grid needs to be extensively tested and studied. The next step is to work on the implementation of the best combination of SM parameters polymorphic in the real inverter to study the impact of the polymorphic VSG in a real microgrid. Indeed, as the VSG can adapt to external signals during harsh events, the polymorphic behaviour is not easily predictable making the notion of stability and protection a major aspect to analyse. Hence, a complete study is necessary to investigate the impact of the polymorphic VSG on microgrid stability and operation.

Reference

- [1] C. Marnay, F. J. Robio, and a. S. Siddiqui, "Shape of the microgrid," *2001 IEEE Power Eng. Soc. Winter Meet. Conf. Proc. (Cat. No.01CH37194)*, vol. 1, no. C, pp. 150–153, 2001, doi: 10.1109/PESW.2001.917022.
 - [2] M. Farrokhhabadi *et al.*, "Microgrid Stability Definitions, Analysis, and Examples," *IEEE Trans. Power Syst.*, vol. 8950, no. APRIL, pp. 1–1, 2019, doi: 10.1109/TPWRS.2019.2925703.
 - [3] N. W. A. Lidula and A. D. Rajapakse, "Microgrids research: A review of experimental microgrids and test systems," *Renew. Sustain. Energy Rev.*, vol. 15, no. 1, pp. 186–202, 2011, doi: 10.1016/j.rser.2010.09.041.
 - [4] E. Hossain, E. Kabalci, R. Bayindir, and R. Perez, "Microgrid testbeds around the world: State of art," *Energy Convers. Manag.*, vol. 86, pp. 132–153, 2014, doi: 10.1016/j.enconman.2014.05.012.
 - [5] R. Lasseter *et al.*, "The CERTS MicroGrid Concept," *Transm. Reliab. Progr.*, no. April, pp. 1–29, 2002.
 - [6] A. Hoke, R. Butler, J. Hambrick, and B. Kroposki, "Maximum Photovoltaic Penetration Levels on Typical Distribution Feeders," *IEEE Trans. Sustain. Energy*, no. July, 2012.
 - [7] S. V. Dhople, B. B. Johnson, and A. O. Hamadeh, "Virtual oscillator control for voltage source inverters," *Proc. 51st Annu. Allert. Conf.*, pp. 1359–1363, 2013.
 - [8] B. B. Johnson, M. Sinha, N. G. Ainsworth, F. Dorfler, and S. V. Dhople, "Synthesizing Virtual Oscillators to Control Islanded Inverters," *IEEE Trans. Power Electron.*, vol. 31, no. 8, pp. 6002–6015, 2016, doi: 10.1109/TPEL.2015.2497217.
 - [9] B. B. Johnson, S. V. Dhople, A. O. Hamadeh, and P. T. Krein, "Synchronization of parallel single-phase inverters with virtual oscillator control," *IEEE Trans. Power Electron.*, vol. 29, no. 11, pp. 6124–6138, 2014, doi: 10.1109/TPEL.2013.2296292.
 - [10] B. B. Johnson, S. V. Dhople, J. L. Cale, A. O. Hamadeh, and P. T. Krein, "Oscillator-based inverter control for islanded three-phase microgrids," *IEEE J. Photovoltaics*, vol. 4, no. 1, pp. 387–395, 2014, doi: 10.1109/JPHOTOV.2013.2280953.
 - [11] K. De Brabandere, B. Bolsens, J. Van den Keybus, A. Woyte, J. Driesen, and R. Belmans, "A Voltage and Frequency Droop Control Method for Parallel Inverters," *IEEE Trans. Power Electron.*, vol. 22, no. 4, pp. 1107–1115, 2007, doi: 10.1109/TPEL.2007.900456.
 - [12] J. M. Guerrero, J. C. Vasquez, J. Matas, M. Castilla, and L. Garcia de Vicuna, "Control Strategy for Flexible Microgrid Based on Parallel Line-Interactive UPS Systems," *IEEE Trans. Ind. Electron.*, vol. 56, no. 3, pp. 726–736, 2009, doi: 10.1109/TIE.2008.2009274.
 - [13] H.-P. Beck and R. Hesse, "Virtual Synchronous Machine," in *Proceedings of the 9th International Conference on Electrical Power Quality and Utilisation*, 2007, no. 3, pp. 1–6.
 - [14] X. Meng, Z. Liu, J. Liu, S. Wang, B. Liu, and R. An, "Comparison between inverters based on virtual synchronous generator and droop control," 2017, pp. 4077–4084, doi: 10.1109/ECCE.2017.8096710.
 - [15] S. D'Arco and J. A. Suul, "Virtual synchronous machines - Classification of implementations and analysis of equivalence to droop controllers for microgrids," *2013 IEEE Grenoble Conf. PowerTech, POWERTECH 2013*, 2013, doi: 10.1109/PTC.2013.6652456.
 - [16] Q. Zhong and G. Weiss, "Synchronverters: Grid-Friendly Inverters That Mimic Synchronous Generators," in *Control of Power Inverters in Renewable Energy and Smart Grid Integration*,
-

- vol. 58, no. 4, Chichester, West Sussex, United Kingdom: John Wiley & Sons, Ltd., 2012, pp. 277–296.
- [17] K. Visscher and S. W. . De Haan, “Virtual synchronous machines (VSG’S) for frequency stabilisation in future grids with a significant share of decentralized generation,” in *CIREC Seminar 2008: SmartGrids for Distribution*, 2008, no. 0118, pp. 82–82, doi: 10.1049/ic:20080487.
- [18] R. Hesse, D. Turschner, and H.-P. Beck, “Micro grid stabilization using the Virtual Synchronous Machine (VISMA),” *2009 Int. Conf. Renew. Energies Power Qual.*, 2009.
- [19] K. Sakimoto, Y. Miura, and T. Ise, “Stabilization of a power system with a distributed generator by a Virtual Synchronous Generator function,” in *8th International Conference on Power Electronics - ECCE Asia*, 2011, no. 2, pp. 1498–1505, doi: 10.1109/ICPE.2011.5944492.
- [20] Q.-C. Zhong and G. Weiss, “Synchronverters: Inverters That Mimic Synchronous Generators,” *IEEE Trans. Ind. Electron.*, vol. 58, no. 4, pp. 1259–1267, Apr. 2011, doi: 10.1109/TIE.2010.2048839.
- [21] H. Bevrani, T. Ise, and Y. Miura, “Virtual synchronous generators: A survey and new perspectives,” *Int. J. Electr. Power Energy Syst.*, vol. 54, pp. 244–254, Jan. 2014, doi: 10.1016/j.ijepes.2013.07.009.
- [22] V. Van Thong *et al.*, “Virtual synchronous generator: Laboratory scale results and field demonstration,” in *2009 IEEE Bucharest PowerTech*, 2009, pp. 2–7, doi: 10.1109/PTC.2009.5281790.
- [23] M. A. Rahmani, Y. Herriot, S. L. Sanjuan, and L. Dorbais, “Virtual synchronous generators for microgrid stabilization : Modeling, implementation and experimental validation on a microgrid laboratory,” in *2017 Asian Conference on Energy, Power and Transportation Electrification (ACEPT)*, 2017, vol. 2017-Decem, pp. 1–8, doi: 10.1109/ACEPT.2017.8168552.
- [24] S. D’Arco, J. A. Suul, and O. B. Fosso, “A Virtual Synchronous Machine implementation for distributed control of power converters in SmartGrids,” *Electr. Power Syst. Res.*, vol. 122, pp. 180–197, May 2015, doi: 10.1016/j.epsr.2015.01.001.
- [25] Y. Hirase, K. Abe, K. Sugimoto, and Y. Shindo, “A grid-connected inverter with virtual synchronous generator model of algebraic type,” *Electr. Eng. Japan*, vol. 184, no. 4, pp. 10–21, Sep. 2013, doi: 10.1002/ej.22428.
- [26] J. Driesen and K. Visscher, “Virtual synchronous generators,” in *2008 IEEE Power and Energy Society General Meeting - Conversion and Delivery of Electrical Energy in the 21st Century*, 2008, no. August 2008, pp. 1–3, doi: 10.1109/PES.2008.4596800.
- [27] Y. Chen, R. Hesse, D. Turschner, and H.-P. Beck, “Investigation of the Virtual Synchronous Machine in the island mode,” in *2012 3rd IEEE PES Innovative Smart Grid Technologies Europe (ISGT Europe)*, 2012, pp. 1–6, doi: 10.1109/ISGTEurope.2012.6465648.
- [28] H. Alatrash, A. Mensah, E. Mark, R. Amarín, and J. H. R. Enslin, “Generator emulation controls for photovoltaic inverters,” in *8th International Conference on Power Electronics - ECCE Asia*, 2011, vol. 3, no. 2, pp. 2043–2050, doi: 10.1109/ICPE.2011.5944502.
- [29] C. Li, R. Burgos, I. Cvetkovic, D. Boroyevich, L. Mili, and P. Rodriguez, “Analysis and design of virtual synchronous machine based STATCOM controller,” *2014 IEEE 15th Work. Control Model. Power Electron.*, pp. 1–6, 2014, doi: 10.1109/COMPEL.2014.6877134.
- [30] Y. Chen, R. Hesse, D. Turschner, and H.-P. Beck, “Comparison Of Methods For Implementing Virtual Synchronous Machine On Inverters,” *2012 Int. Conf. Renew. Energies Power Qual.*, vol. 1, no. 10, pp. 734–739, 2012.
- [31] Y. Ma, W. Cao, L. Yang, F. F. Wang, and L. M. Tolbert, “Virtual Synchronous Generator Control of Full Converter Wind Turbines with Short-Term Energy Storage,” *IEEE Trans. Ind. Electron.*, vol. 64, no. 11, pp. 8821–8831, 2017, doi: 10.1109/TIE.2017.2694347.
- [32] K. Sakimoto, K. Sugimoto, and Y. Shindo, “Low voltage ride through capability of a grid connected inverter based on the virtual synchronous generator,” in *2013 IEEE 10th International*
-

- Conference on Power Electronics and Drive Systems (PEDS)*, 2013, pp. 1066–1071, doi: 10.1109/PEDS.2013.6527178.
- [33] Y. Hirase *et al.*, “Autonomous power management in microgrids using virtual synchronous generators,” *Microgrids Des. Appl. Control*, vol. 228, no. July, pp. 2437–2447, 2018, doi: 10.1016/j.apenergy.2018.07.103.
- [34] O. Mo, S. D’Arco, and J. A. Suul, “Evaluation of Virtual Synchronous Machines With Dynamic or Quasi-Stationary Machine Models,” *IEEE Trans. Ind. Electron.*, vol. 64, no. 7, pp. 5952–5962, Jul. 2017, doi: 10.1109/TIE.2016.2638810.
- [35] J. Liu, Y. Miura, and T. Ise, “Comparison of Dynamic Characteristics Between Virtual Synchronous Generator and Droop Control in Inverter-Based Distributed Generators,” *IEEE Trans. Power Electron.*, vol. 31, no. 5, pp. 3600–3611, May 2016, doi: 10.1109/TPEL.2015.2465852.
- [36] Jia Liu, Y. Miura, and T. Ise, “Dynamic characteristics and stability comparisons between virtual synchronous generator and droop control in inverter-based distributed generators,” in *2014 International Power Electronics Conference (IPEC-Hiroshima 2014 - ECCE ASIA)*, 2014, no. 3, pp. 1536–1543, doi: 10.1109/IPEC.2014.6869789.
- [37] Mingxuan Li *et al.*, “A power decoupling control strategy for droop controlled inverters and virtual synchronous generators,” in *2016 IEEE 8th International Power Electronics and Motion Control Conference (IPEMC-ECCE Asia)*, 2016, pp. 1713–1719, doi: 10.1109/IPEMC.2016.7512552.
- [38] Q.-C. Zhong, G. C. Konstantopoulos, B. Ren, and M. Krstic, “Improved Synchronverters with Bounded Frequency and Voltage for Smart Grid Integration,” *IEEE Trans. Smart Grid*, vol. 3053, no. c, pp. 1–1, 2016, doi: 10.1109/TSG.2016.2565663.
- [39] M. A. Torres L., L. A. C. Lopes, L. A. Moran T., and J. R. Espinoza C., “Self-Tuning Virtual Synchronous Machine: A Control Strategy for Energy Storage Systems to Support Dynamic Frequency Control,” *IEEE Trans. Energy Convers.*, vol. 29, no. 4, pp. 833–840, Dec. 2014, doi: 10.1109/TEC.2014.2362577.
- [40] J. Liu, Y. Miura, H. Bevrani, and T. Ise, “Enhanced Virtual Synchronous Generator Control for Parallel Inverters in Microgrids,” *IEEE Trans. Smart Grid*, vol. PP, no. 99, pp. 1–10, 2016, doi: 10.1109/TSG.2016.2521405.
- [41] International Electrotechnical Commission, “IEC 60034-1 section 9.11.3,” 2004.
- [42] I. Standard, “INTERNATIONAL STANDARD,” vol. 2005, 2005.
- [43] Institute of Electrical and Electronics Engineers and IEEE-SA Standards Board, *IEEE guide for test procedures for synchronous machines. Part I, Acceptance and performance testing*. New York: Institute of Electrical and Electronics Engineers, 2010.
- [44] International Organization for Standardization, “ISO 8528-5:2013 - Reciprocating internal combustion engine driven alternating current generating sets — Part 5: Generating sets,” Switzerland, 2013.
- [45] P. Kundur, *Power System Stability and Control*. New York: McGraw-Hill, 1994.
- [46] D. Arricibita, P. Sanchis, and L. Marroyo, “Virtual synchronous generators classification and common trends,” in *IECON 2016 - 42nd Annual Conference of the IEEE Industrial Electronics Society*, 2016, pp. 2433–2438, doi: 10.1109/IECON.2016.7793025.
- [47] Y. Hirase, K. Sugimoto, K. Sakimoto, and T. Ise, “Analysis of Resonance in Microgrids and Effects of System Frequency Stabilization Using a Virtual Synchronous Generator,” *IEEE J. Emerg. Sel. Top. Power Electron.*, vol. 4, no. 4, pp. 1287–1298, Dec. 2016, doi: 10.1109/JESTPE.2016.2581818.
- [48] M. P. Boucherot, “Experiences and new considerations on parallel alternators coupling (in French),” *La Houille Blanche*, no. 8, pp. 276–283, Aug. 1904, doi: 10.1051/lhb/1904053.
- [49] A. Moulichon, L. Garbuio, V. Debusschere, M. A. Rahamani, and N. Hadjsaid, “A Simplified

- Synchronous Machine Model for Virtual Synchronous Generator Implementation,” *2019 IEEE Power Energy Soc. Gen. Meet.*, pp. 1–5, 2019.
- [50] Y. Hirase, K. Abe, K. Sugimoto, K. Sakimoto, H. Bevrani, and T. Ise, “A novel control approach for virtual synchronous generators to suppress frequency and voltage fluctuations in microgrids,” *Appl. Energy*, vol. 210, pp. 699–710, 2018, doi: 10.1016/j.apenergy.2017.06.058.
- [51] H. Zhao, H. Zeng, and Q. Yang, “Virtual synchronous generator based multi-loop control of renewable DGs in island microgrids,” in *2016 Chinese Control and Decision Conference (CCDC)*, 2016, pp. 423–428, doi: 10.1109/CCDC.2016.7531022.
- [52] D. J. Hogan, F. Gonzalez-Espin, J. G. Hayes, G. Lightbody, L. Albiol-Tendillo, and R. Foley, “Virtual Synchronous-Machine Control of Voltage-Source Converters in a Low-Voltage Microgrid,” in *2016 18th European Conference on Power Electronics and Applications (EPE'16 ECCE Europe)*, 2016, pp. 1–10, doi: 10.1109/EPE.2016.7695503.
- [53] C. F. dos Santos, F. B. Grigoletto, and M. Stefanello, “Power quality improvement in a grid connected voltage source inverter using the concept of virtual synchronous machine,” in *2015 IEEE 13th Brazilian Power Electronics Conference and 1st Southern Power Electronics Conference (COBEP/SPEC)*, 2015, pp. 1–5, doi: 10.1109/COBEP.2015.7420075.
- [54] M. Chen and X. Xiao, “Hierarchical frequency control strategy of hybrid droop/VSG-based islanded microgrids,” *Electr. Power Syst. Res.*, vol. 155, pp. 131–143, 2018, doi: 10.1016/j.epsr.2017.10.011.
- [55] C. Andalib-Bin-Karim, X. Liang, and H. Zhang, “Fuzzy-Secondary-Controller-Based Virtual Synchronous Generator Control Scheme for Interfacing Inverters of Renewable Distributed Generation in Microgrids,” *IEEE Trans. Ind. Appl.*, vol. 54, no. 2, pp. 1047–1061, Mar. 2018, doi: 10.1109/TIA.2017.2773432.
- [56] D. Jovcic, L. A. Lamont, and L. Xu, “VSC transmission model for analytical studies,” in *2003 IEEE Power Engineering Society General Meeting (IEEE Cat. No.03CH37491)*, 2004, pp. 1737–1742, doi: 10.1109/PES.2003.1267418.
- [57] L. Harnefors, M. Bongiorno, and S. Lundberg, “Input-admittance calculation and shaping for controlled voltage-source converters,” *IEEE Trans. Ind. Electron.*, vol. 54, no. 6, pp. 3323–3334, 2007, doi: 10.1109/TIE.2007.904022.
- [58] A. Pearson, “Linear optimal control systems,” *IEEE Trans. Automat. Contr.*, vol. 19, no. 5, pp. 631–632, Oct. 1974, doi: 10.1109/TAC.1974.1100628.
- [59] J. A. Suul, S. D’Arco, and G. Guidi, “Virtual Synchronous Machine-Based Control of a Single-Phase Bi-Directional Battery Charger for Providing Vehicle-to-Grid Services,” *IEEE Trans. Ind. Appl.*, vol. 52, no. 4, pp. 3234–3244, Jul. 2016, doi: 10.1109/TIA.2016.2550588.
- [60] T. Chen, L. Chen, T. Zheng, X. Chen, and S. Mei, “General control strategy to limit peak currents of Virtual Synchronous Generator under voltage sags,” in *2016 IEEE Power and Energy Society General Meeting (PESGM)*, 2016, pp. 1–5, doi: 10.1109/PESGM.2016.7741458.
- [61] Y. Hirase, O. Noro, K. Sugimoto, K. Sakimoto, Y. Shindo, and T. I. Osaka, “Effects and analysis of suppressing frequency fluctuations in microgrids using virtual synchronous generator control,” in *IECON 2015 - 41st Annual Conference of the IEEE Industrial Electronics Society*, 2015, pp. 000043–000049, doi: 10.1109/IECON.2015.7392074.
- [62] E. W. Kimbark, *Power System Stability*, vol. III Syncho. IEEE Press Power Systems Engineering Series, 1994.
- [63] L. L. Grigsby, *Power System Control and Stability*, CRC Press. 2007.
- [64] L. Bun, B. Raison, G. Rostaing, S. Bacha, A. Rumeau, and A. Labonne, “Development of a real time photovoltaic simulator in normal and abnormal operations,” in *IECON 2011 - 37th Annual Conference of the IEEE Industrial Electronics Society*, 2011, pp. 867–872, doi: 10.1109/IECON.2011.6119424.
- [65] A. Mercier, C. Benoit, Y. Besanger, A. Rumeau, and C. Boudinet, “Comparative study of solar panel decentralized controls in low voltage network with real time simulation,” *IEEE Power*
-

- Energy Soc. Gen. Meet.*, vol. 2015-Sept, 2015, doi: 10.1109/PESGM.2015.7286205.
- [66] A. Ovalle, G. Ramos, S. Bacha, A. Hably, and A. Rumeau, “Decentralized control of voltage source converters in microgrids based on the application of instantaneous power theory,” *IEEE Trans. Ind. Electron.*, vol. 62, no. 2, pp. 1152–1162, 2015, doi: 10.1109/TIE.2014.2336638.
- [67] A. Djoudi, S. Bacha, H. Chekireb, H. Iman-Eini, and C. Boudinet, “Adaptive Sensorless SM-DPC of DFIG-Based WECS under Disturbed Grid: Study and Experimental Results,” *IEEE Trans. Sustain. Energy*, vol. 9, no. 2, pp. 570–581, 2018, doi: 10.1109/TSTE.2017.2748966.
- [68] B. Guo, S. Bacha, M. Alamir, A. Mohamed, and C. Boudinet, “LADRC applied to variable speed micro-hydro plants: Experimental validation,” *Control Eng. Pract.*, vol. 85, no. February, pp. 290–298, Apr. 2019, doi: 10.1016/j.conengprac.2019.02.008.
- [69] Quang Linh Lam, “Advanced control of microgrids for frequency and voltage stability : robust control co-design and real-time validation,” Université Grenoble Alpes, 2018.
- [70] E. de Jong *et al.*, “European White Book on Real-Time Power Hardware-in-the-loop testing,” 2012.
- [71] Y. Hu, W. Wei, Y. Peng, and J. Lei, “Fuzzy virtual inertia control for virtual synchronous generator,” in *2016 35th Chinese Control Conference (CCC)*, 2016, vol. 2016-Augus, pp. 8523–8527, doi: 10.1109/ChiCC.2016.7554718.
- [72] J. Alipoor, Y. Miura, and T. Ise, “Power System Stabilization Using Virtual Synchronous Generator With Alternating Moment of Inertia,” *IEEE J. Emerg. Sel. Top. Power Electron.*, vol. 3, no. 2, pp. 451–458, Jun. 2015, doi: 10.1109/JESTPE.2014.2362530.
- [73] M. Yu *et al.*, “Use of an inertia-less Virtual Synchronous Machine within future power networks with high penetrations of converters,” in *2016 Power Systems Computation Conference (PSCC)*, 2016, pp. 1–7, doi: 10.1109/PSCC.2016.7540926.
- [74] D. Li, Q. Zhu, S. Lin, and X. Y. Bian, “A Self-Adaptive Inertia and Damping Combination Control of VSG to Support Frequency Stability,” *IEEE Trans. Energy Convers.*, vol. 32, no. 1, pp. 397–398, 2017, doi: 10.1109/TEC.2016.2623982.
- [75] Y. Chen, R. Hesse, D. Turschner, and H.-P. Beck, “Improving the grid power quality using virtual synchronous machines,” *2011 Int. Conf. Power Eng. Energy Electr. Drives*, no. May, pp. 1–6, 2011, doi: 10.1109/PowerEng.2011.6036498.
- [76] J. A. E. Andersson, J. Gillis, G. Horn, J. B. Rawlings, and M. Diehl, “CasADi: a software framework for nonlinear optimization and optimal control,” *Math. Program. Comput.*, vol. 11, no. 1, pp. 1–36, Mar. 2019, doi: 10.1007/s12532-018-0139-4.
-

Appendixes

Appendix 1. Reference model for the state-space validation

The synchronous machine, in p.u., is the implementation of the SM equations in continuous. The connexion between the inverter model and the SM is the voltage V_c in single line, e^d and e^q in dq-axis. The SM model is not represented here, but the SM model used is the complete one that has been detailed in the Chapter 2 (2.3.1 – p12).

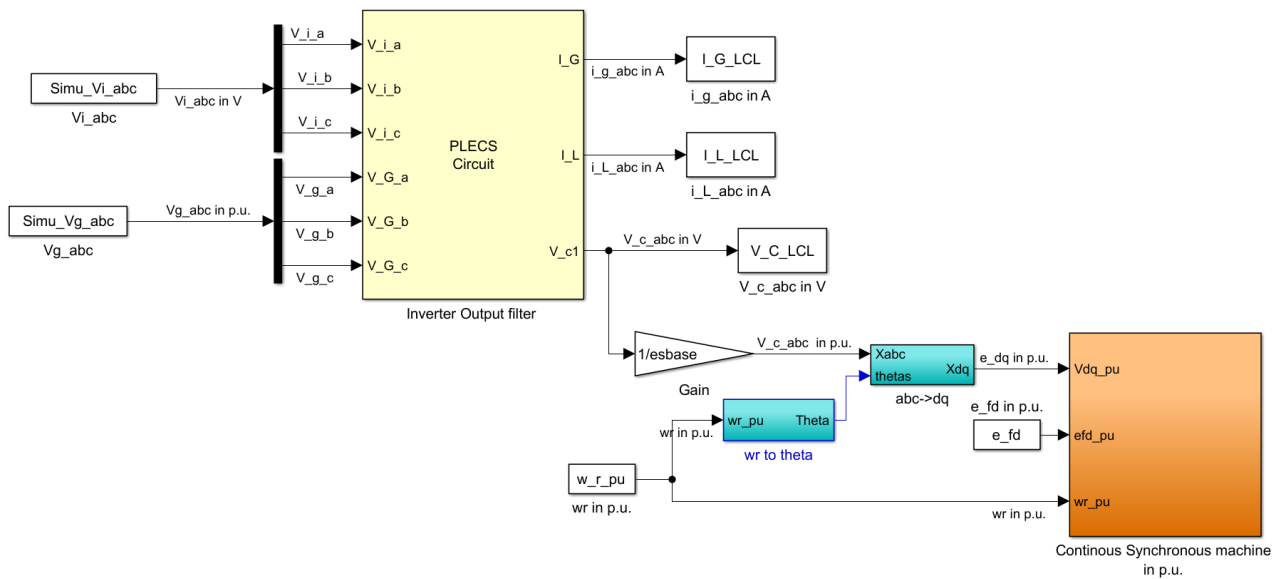


Figure 1: Global Comparison model, connexion of the SM to the inverter output filter.

The inverter output filter is modelled with PLECS® and has as input the inverter voltage V_i , the grid voltage V_g in abc-axis, and the rotor electrical angular velocity ω_r to convert the abc-axis variables in dq for the SM model. The outputs for the validation of the filter will be both inverter and grid currents i_L and i_g as well as the voltage V_c . The other inputs of the inverter and the SM model in Simulink® are the voltage e_{fd} necessary to control and validated the SM model as it can be seen in Figure 1.

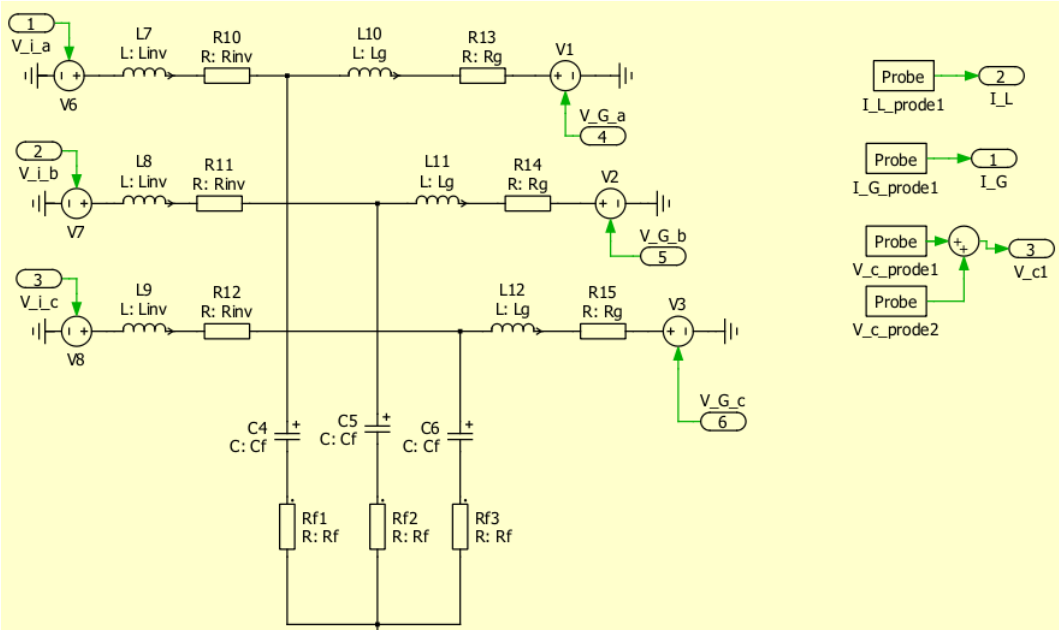


Figure 2: Inverter output filter.

Appendix 2. Inputs for the models for validation

Below, the different inputs of the complete model for the state-space validation.

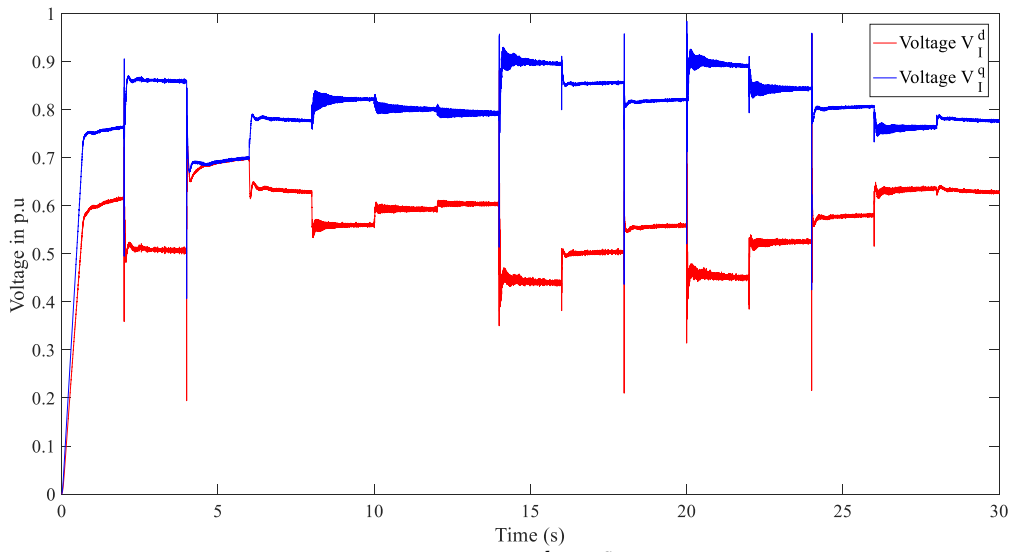


Figure 3: Voltage V_i^d et V_i^q profile.

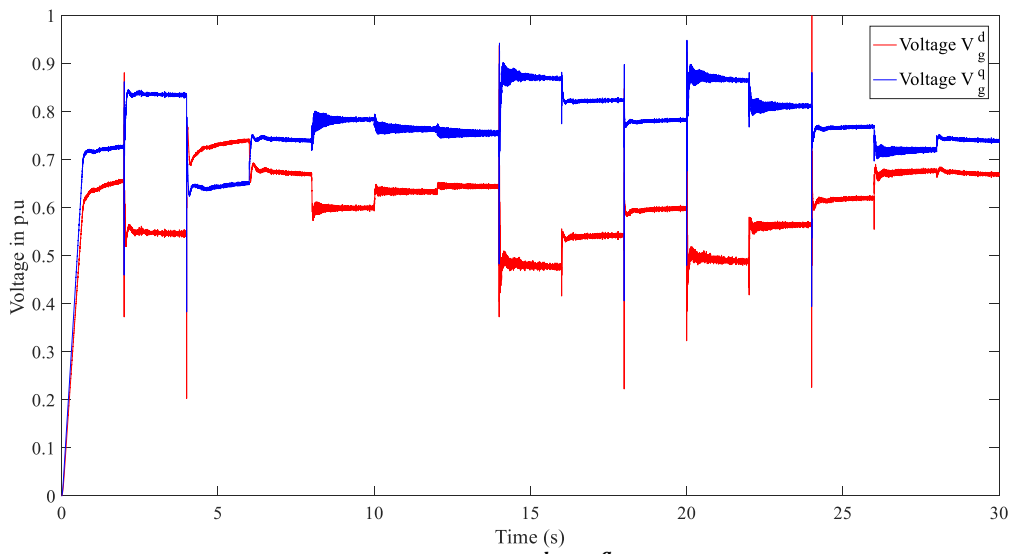


Figure 4: Voltage V_g^d et V_g^q profile.

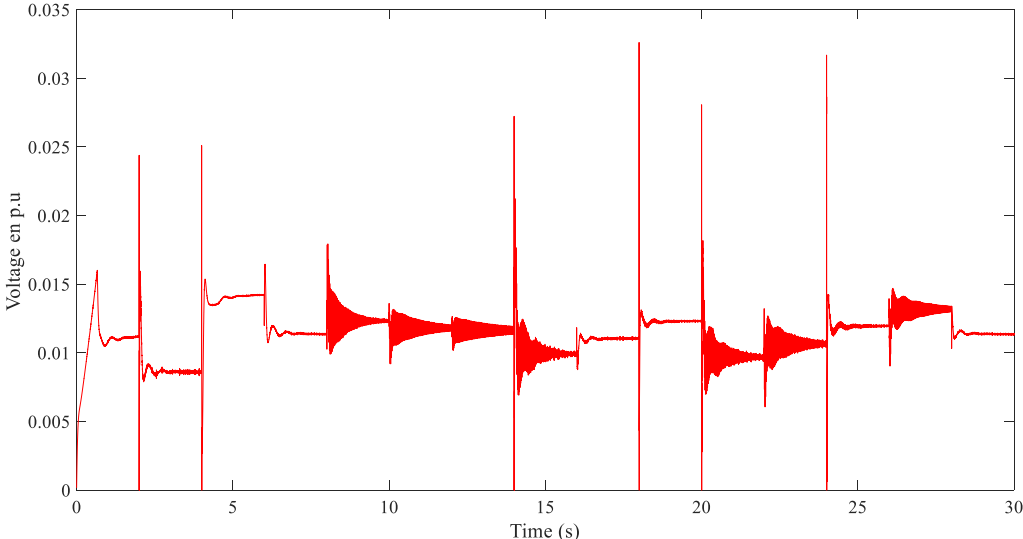


Figure 5: Voltage e_{fd} profile.

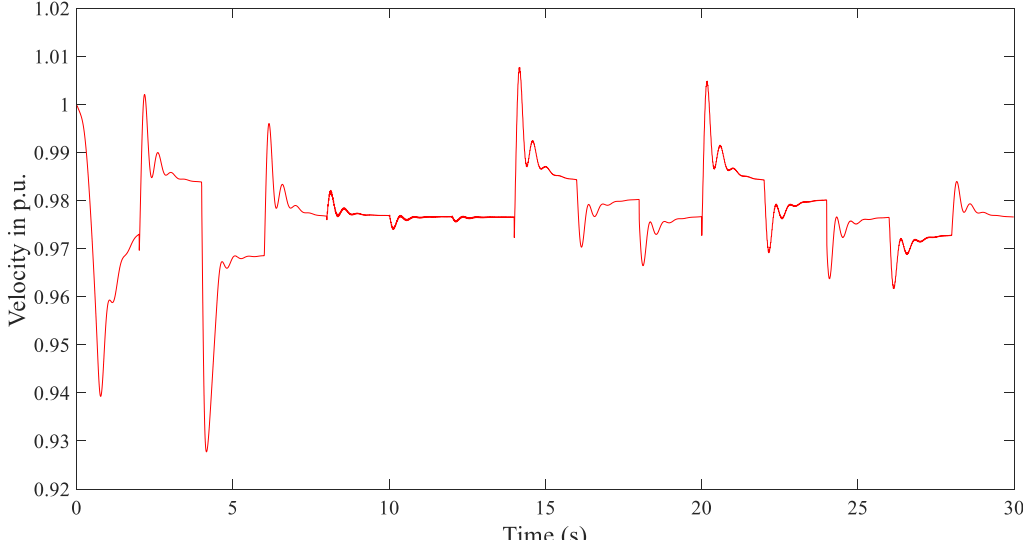


Figure 6: Rotor electrical angular velocity ω_r profile.

Appendix 3. Complete State-space model validation

In the different figures below, Figure 7 to Figure 17, state-space variables compared to the reference model variable.

The difference between the both models, the offset visible in the different figures below, are certainly due to the hypothesis ω_r . Indeed, the parameter ω_r is used to convert both voltages e^d and e^q , from abc-axis to dq-axis, in addition ω_r is also used in the SM model.

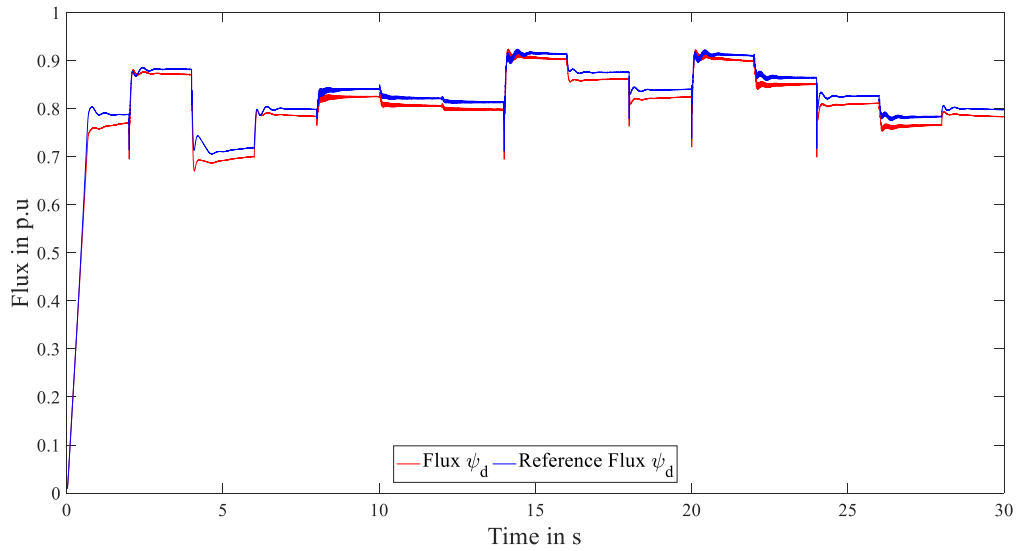


Figure 7: Flux ψ_d from state-space and reference models.

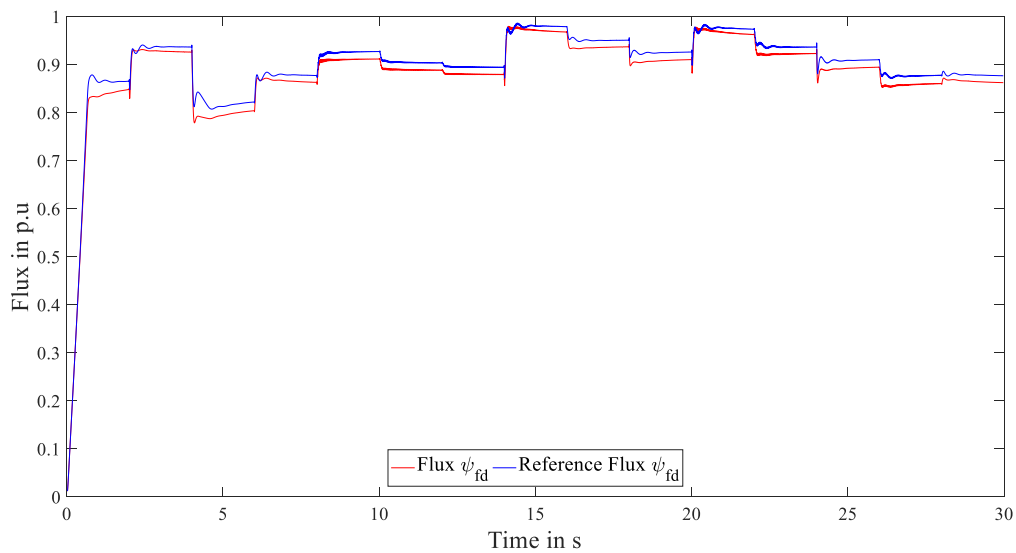


Figure 8: Flux ψ_q from state-space and reference models.

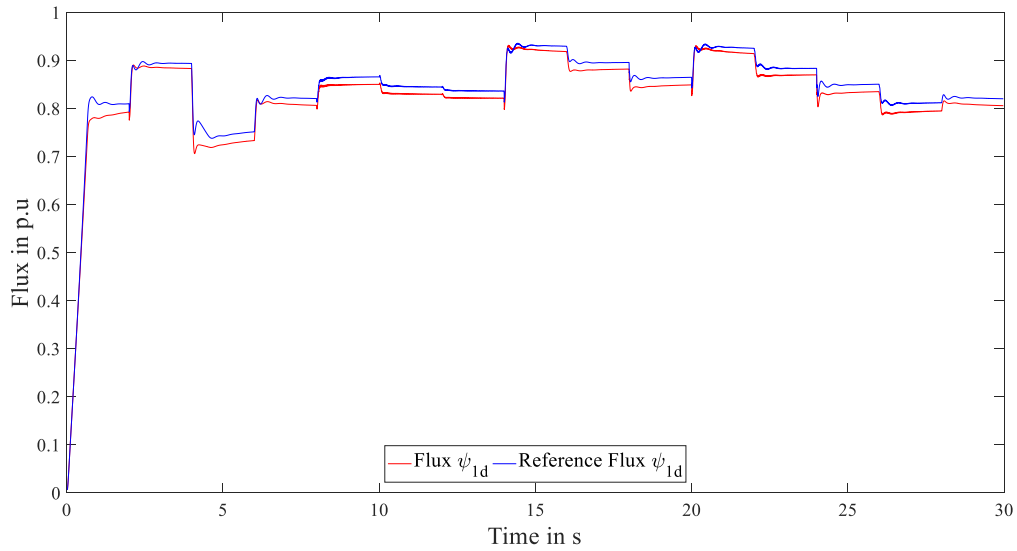


Figure 9: Flux ψ_{fd} from state-space and reference models.

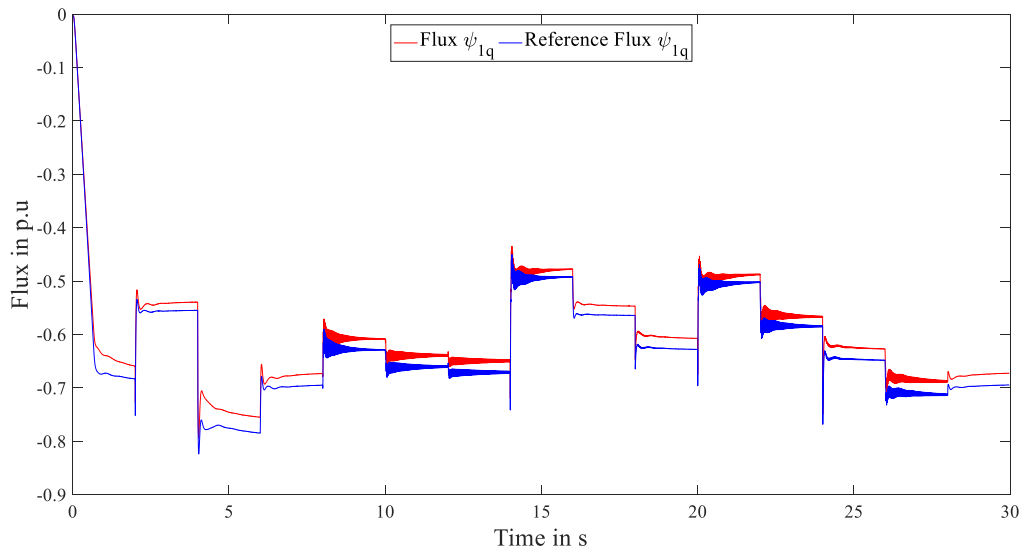


Figure 10: Flux ψ_{1d} from state-space and reference models.

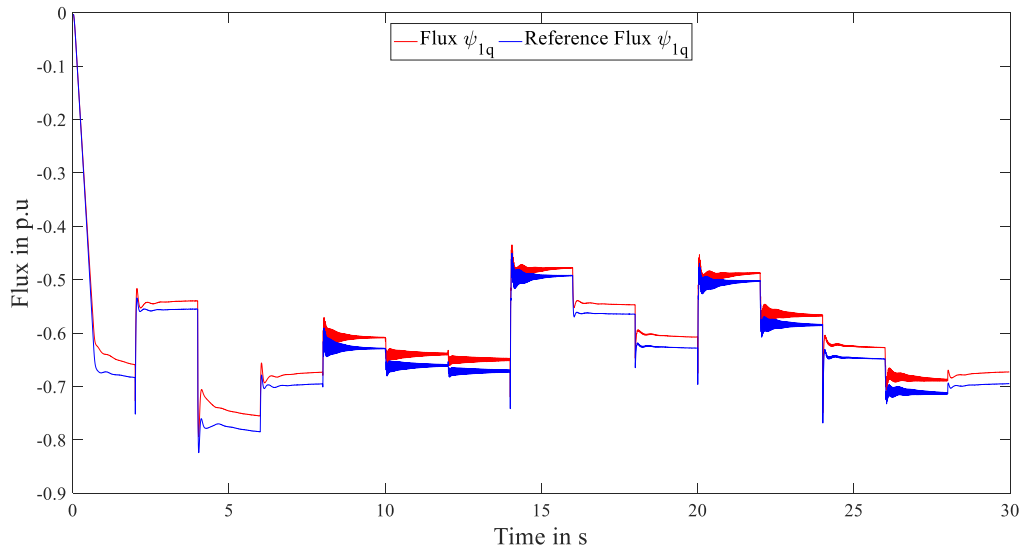


Figure 11: Flux ψ_{1q} from state-space and reference models.

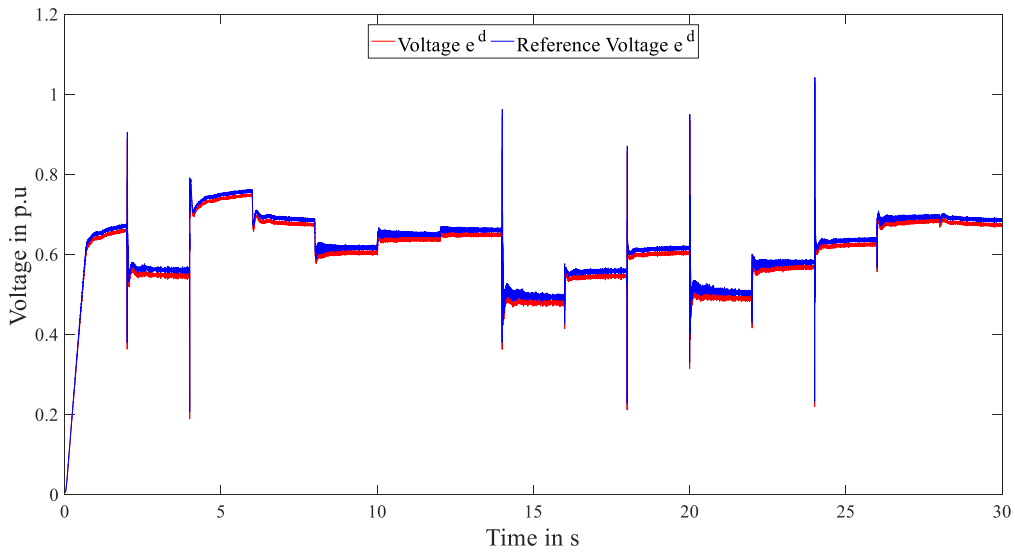


Figure 12: Voltage e^d from state-space and reference models.

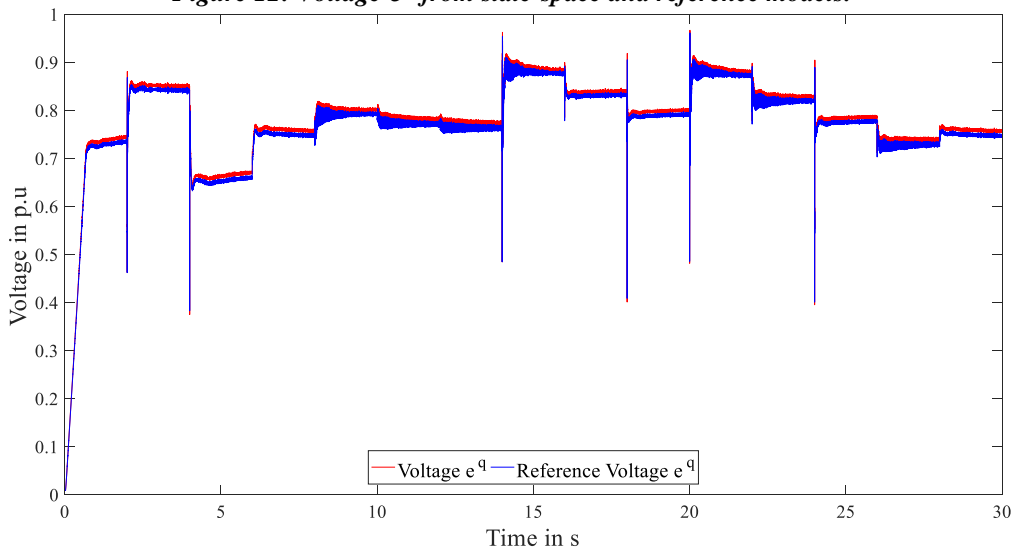


Figure 13: Voltage e^q from state-space and reference models.

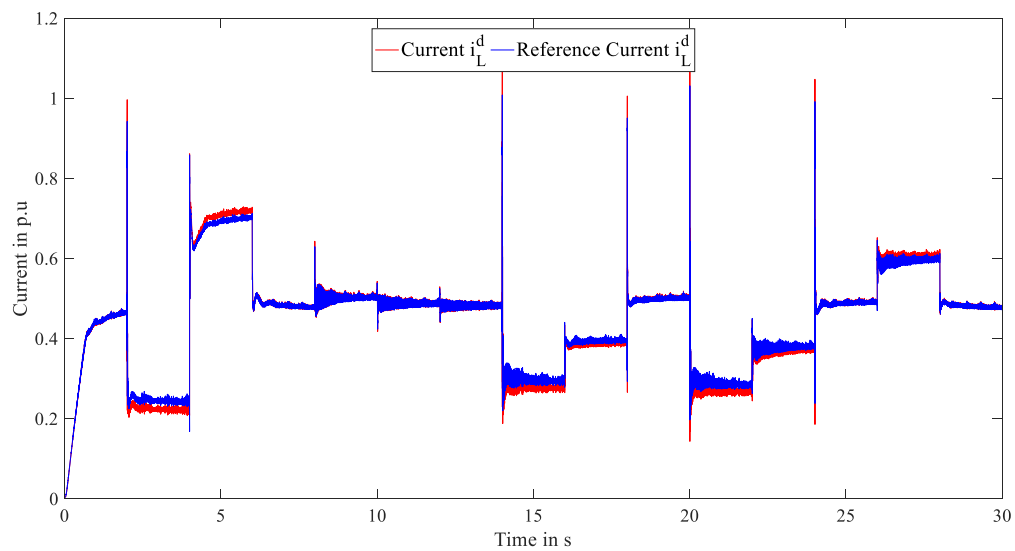


Figure 14: Current i_L^d from state-space and reference models.

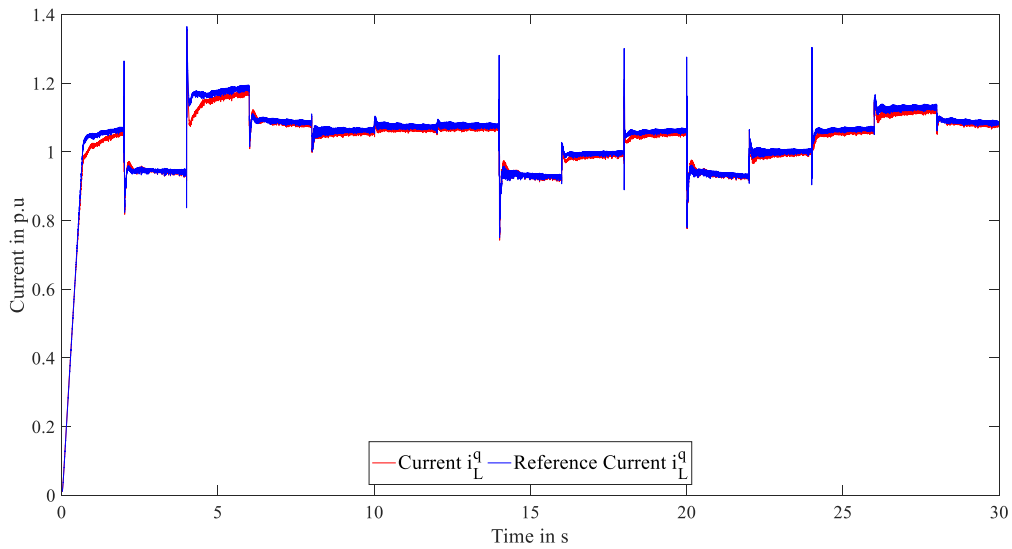


Figure 15: Current i_L^q from state-space and reference models.

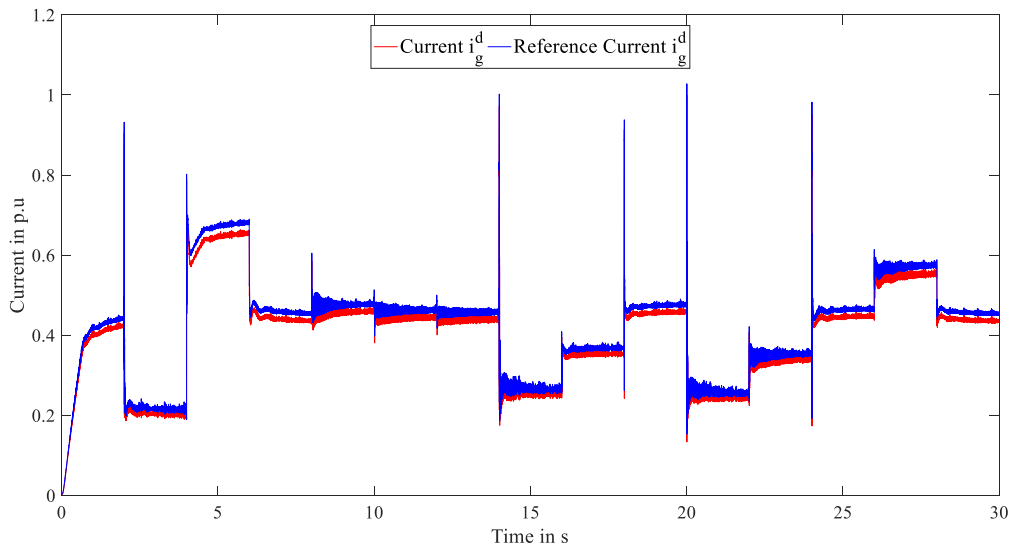


Figure 16: Current i_g^d from state-space and reference models.

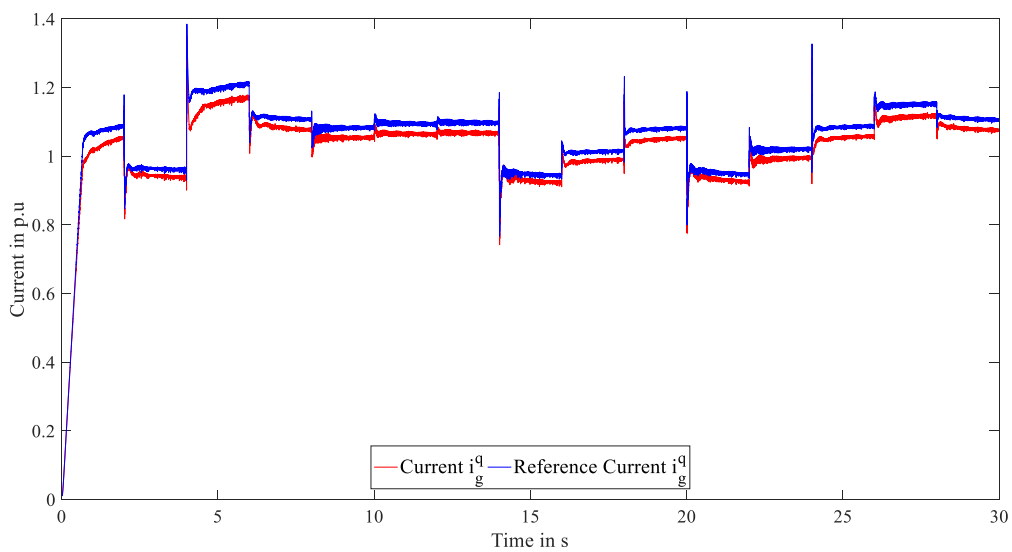


Figure 17: Current i_g^q from state-space and reference models.

Appendix 4. Observer and PI controller

Figure 18 to Figure 20 represent the different observed states of the PI and observer controller: the voltages e_{fd} , V_g^d and V_g^q . In comparison with Figure 3.11 to Figure 3.13, it's possible to say that the results are similar as the error is relatively the same for the observer alone and the observer integrated in the PI controller. In comparing Figure 3.14 (p56) and Figure 3.15 (p57) with Figure 21 and Figure 22, the reader can see that the observer has similar dynamic.

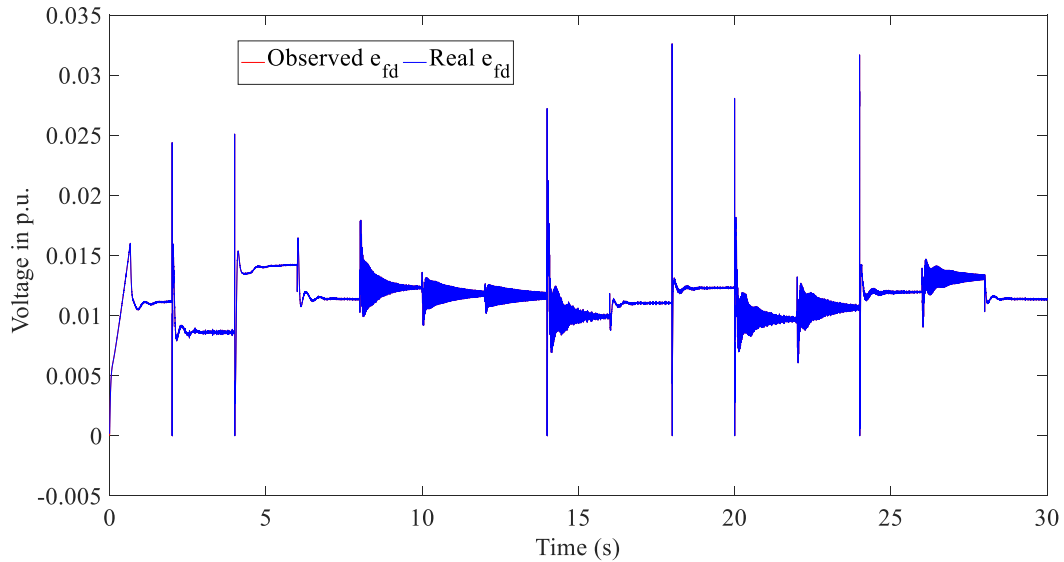


Figure 18: Voltage \widehat{e}_{fd} compared to e_{fd} for PI controller and observer.

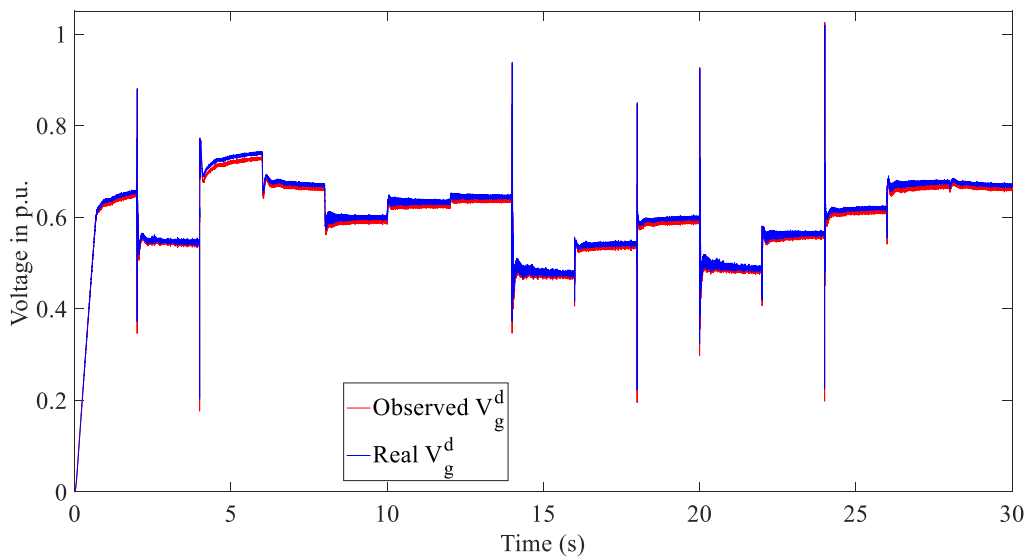


Figure 19: Voltage \widehat{V}_g^d compared to V_g^d for PI controller and observer.

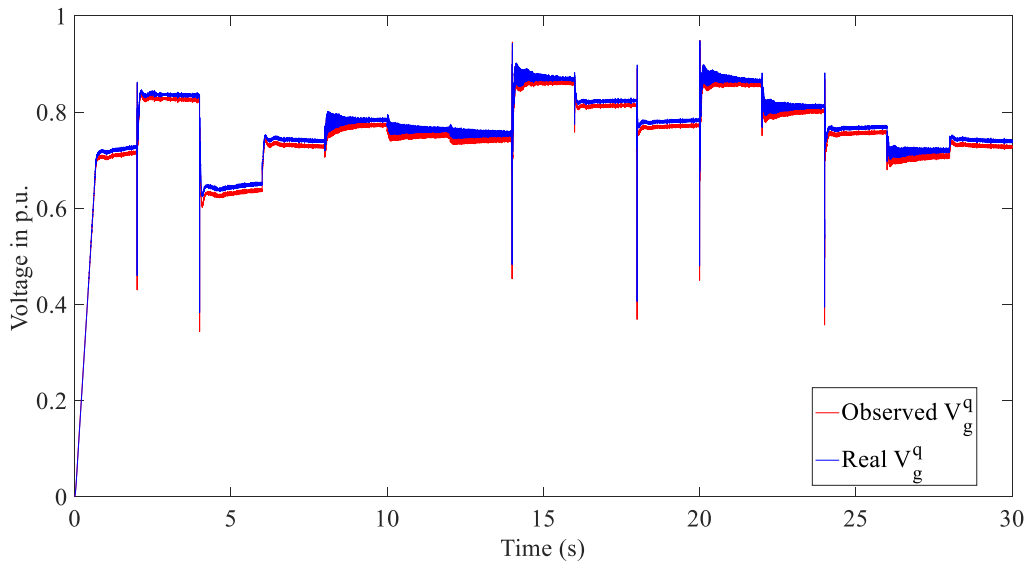


Figure 20: Voltage \widehat{V}_g^q compared to V_g^q for PI controller and observer.

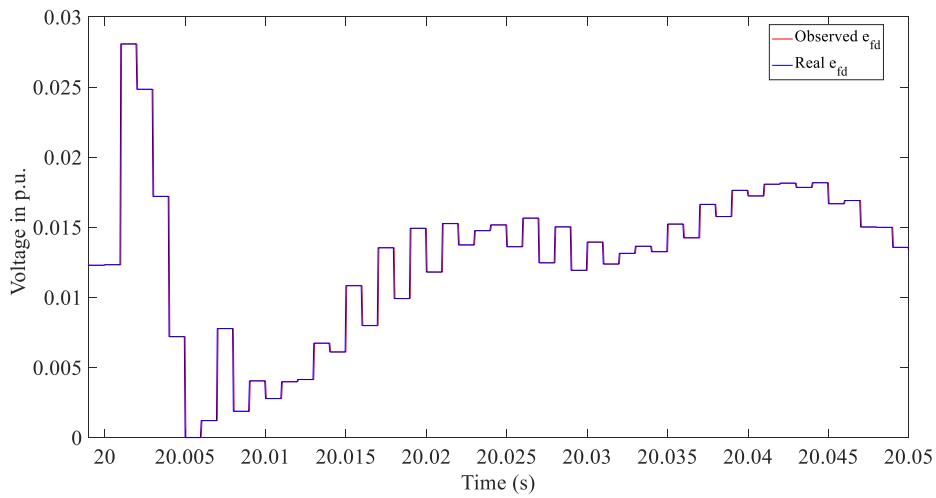


Figure 21: Zoom on voltage \widehat{e}_{fd} compared to e_{fd} for PI controller and observer.

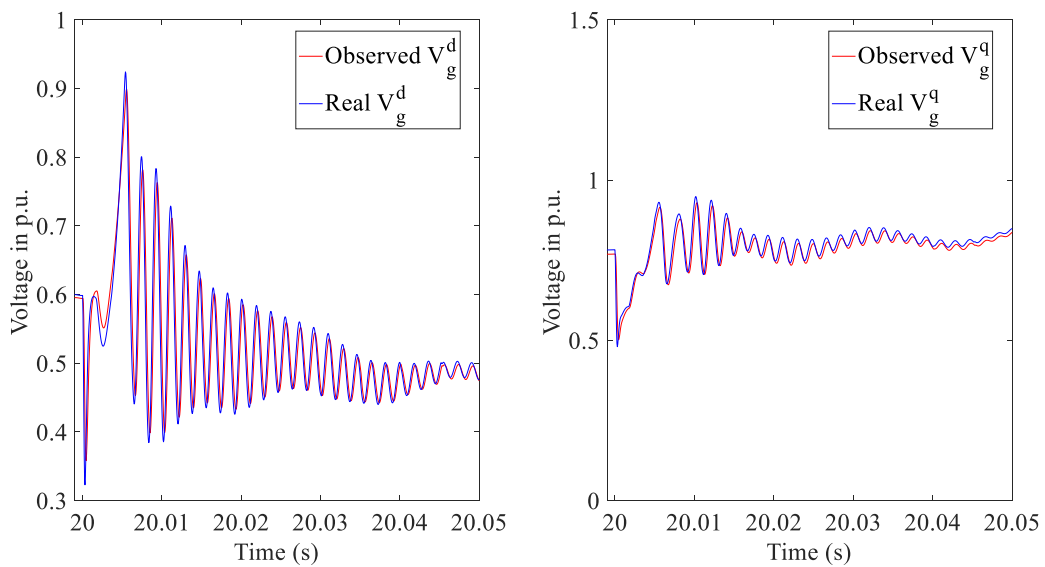


Figure 22: Zoom on voltages \widehat{V}_g^d and \widehat{V}_g^q compared to V_g^d and V_g^q for observer and PI controller.

Appendix 5. Proposed controller observer simulations

The three figures below, result from the simulation with the perturbation described in Appendix 2 (p163). Figure 23 to Figure 25 represent the different observed states of the observed proposed controller. In comparison with Figure 3.11 to Figure 3.13 (p55 – p56), and Figure 23 to Figure 25, it's possible to say that the results are similar, the observer integrated in the PI controller, even during the high variability and the observer integrated in our proposed controller.

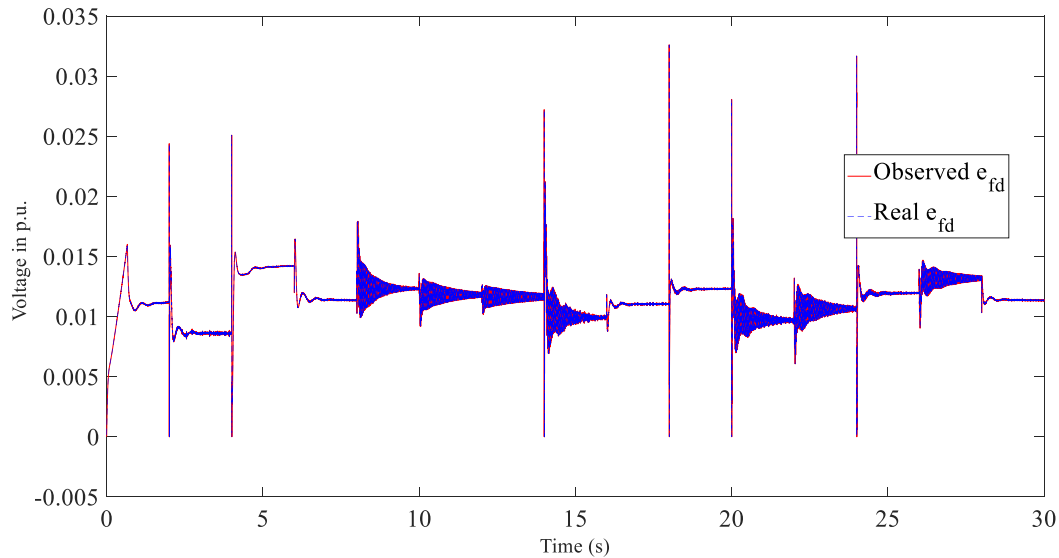


Figure 23: Voltage \widehat{e}_{fd} compared to e_{fd} for the proposed controller.

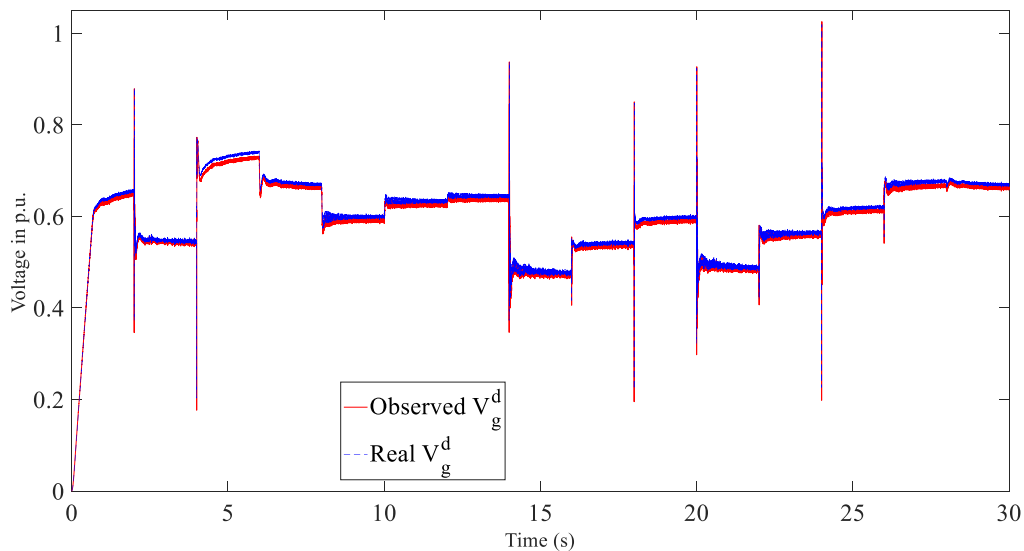


Figure 24: Voltage \widehat{V}_g^d compared to V_g^d for the proposed controller.

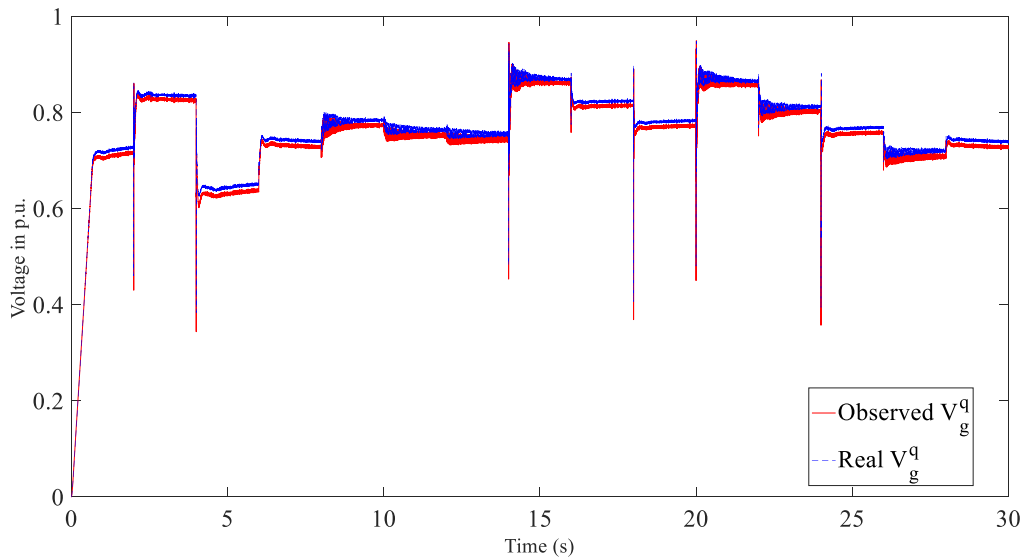


Figure 25: Voltage \widehat{V}_g^a compared to V_g^d for the proposed controller.

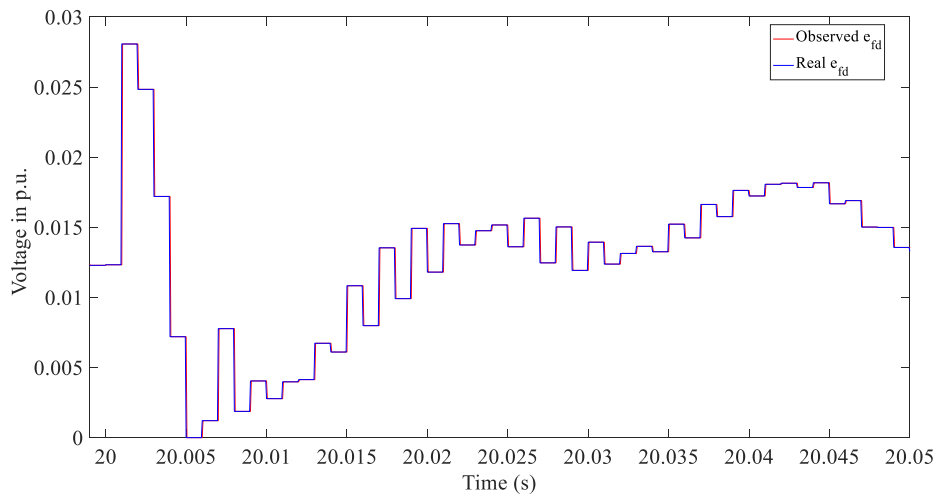


Figure 26: Zoom on Voltage \widehat{e}_{fd} compared to e_{fd} for the proposed controller.

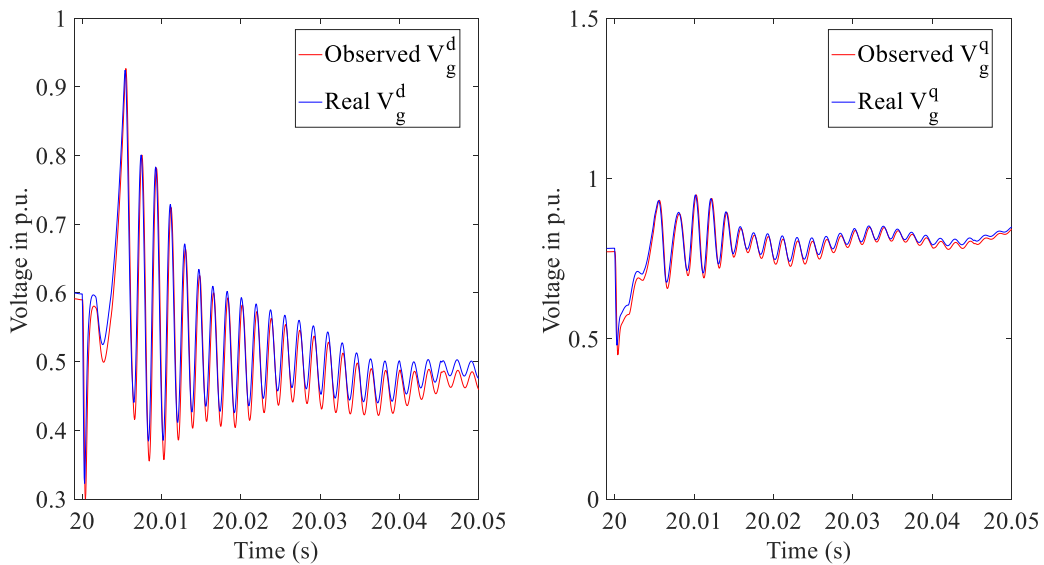


Figure 27: Zoom on voltages \widehat{V}_g^a and \widehat{V}_g^q compared to V_g^d and V_g^q for the proposed controller.

Appendix 6. Determination of the proposed controller parameters

In order to identify the impact of the different parameters of the proposed controller, a significative variations grid voltage, V_g^d and V_g^q is applied at the output of the controlled system with the proposed controller. Figure 28 shows in blue the grid voltages used before and in red, the voltage that is used in this study.

In this study, the mean square tracking error $\Delta\varepsilon$, the difference between the synchronous machine currents, i^d and i^q and the outputs inverter currents, i_L^d and i_L^q , and the mean square variation of the duty ratio $\Delta\alpha$ between the reference, α^{d*} and α^{q*} , and the real applied value α^d and α^q are both considered for the parameters determination.

In addition, the different values for the both parameters $Q_{X_{SYS}}$ and $Q_{U_{SYS}}$ will be applied and teste, form 1 to 10^{10} .

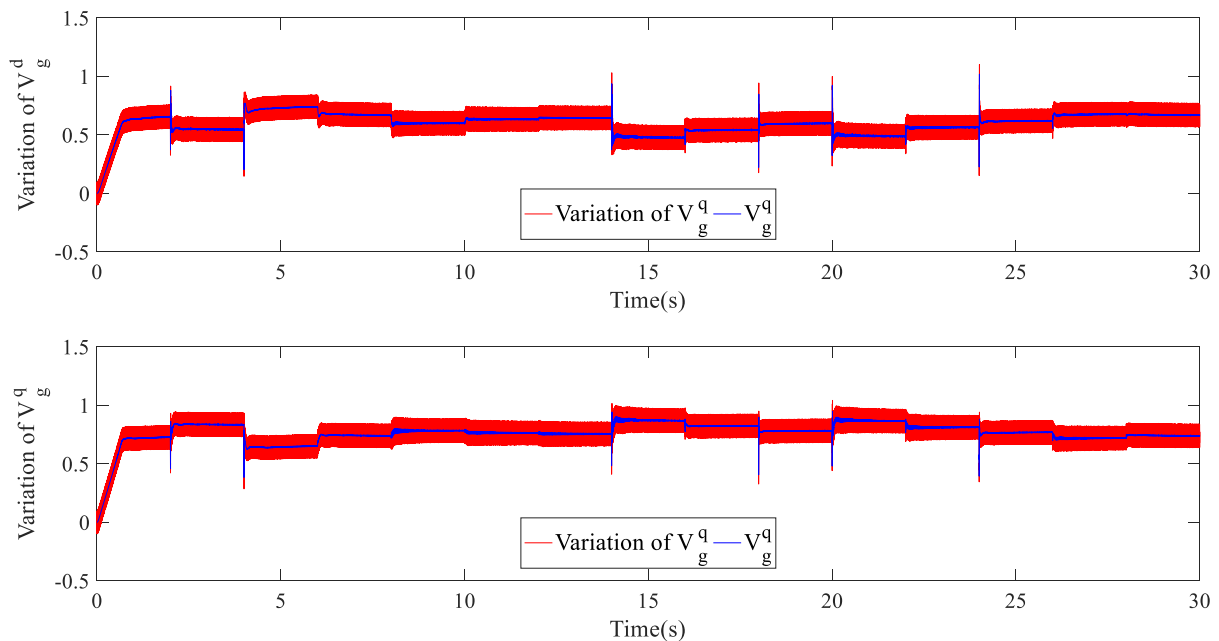


Figure 28: Grid voltages V_g^d and V_g^q with the addition of a random noise of 10%.

Figure 29 shows that the mean square deviation of $\Delta\varepsilon$, curve in red, is not influenced by the variations of the penalty $Q_{X_{SYS}}$. Indeed, $\Delta\varepsilon$'s mean square deviation is included between $[0,4 \cdot 10^{-5}; 1,5 \cdot 10^{-5}]$, an augmentation of only 10^{-5} for an important penalty R_{corr} 's variation, $[1; 10^{10}]$.

The $\Delta\alpha$'s mean square deviation, curve in blue, are highly linked to the value to penalty R_{corr} as the values vary in the interval of $[8,7 \cdot 10^{-6}; 4,7 \cdot 10^{-2}]$. Figure 29 highlights that the duty ratios $\Delta\alpha$ mean square deviation stays near the value of 10^{-5} for penalty $Q_{X_{SYS}}$ inferiors or equals to 10^5 , for higher value of $Q_{X_{SYS}}$, the duty ratios α_d and α_q 's mean square deviation increases rapidly.

To avoid the inverter's duty ratio saturation, the penalty value $Q_{X_{SYS}}$ should be increased to reduce the impact on the $\Delta\varepsilon$ and $\Delta\alpha$. Figure 29 permits to identify $Q_{X_{SYS}} = 100 \cdot \mathbb{I}_{11}$ as it seems to be a compromise between the three objectives.

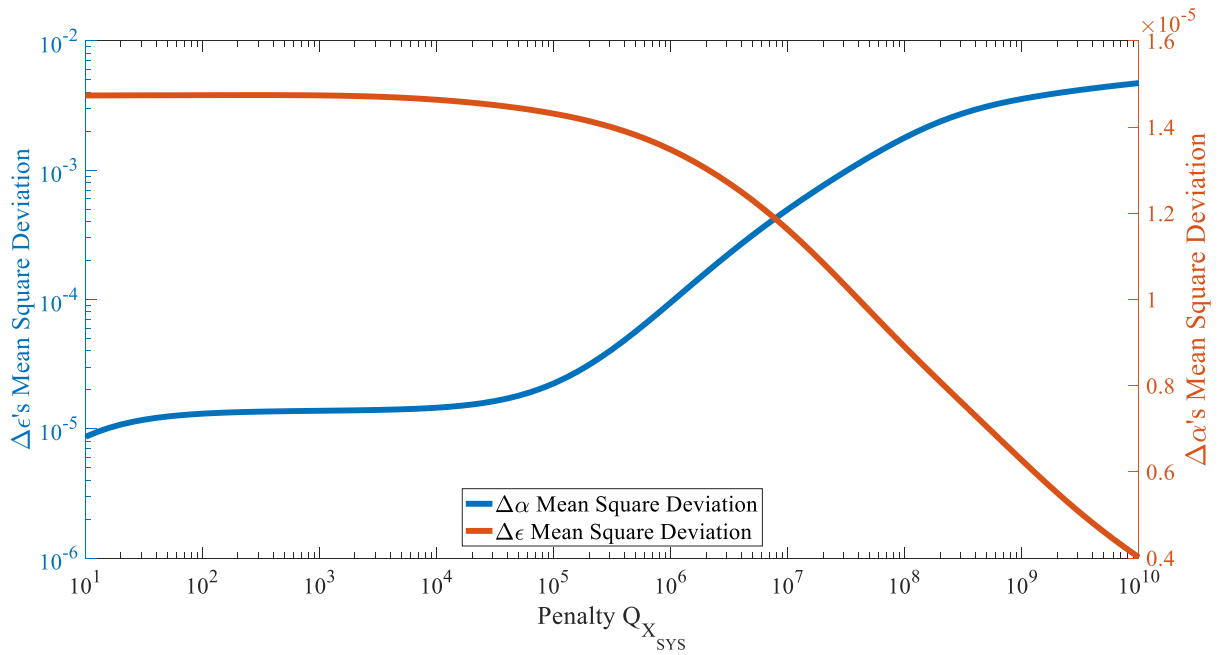


Figure 29: Impact of Penalty $Q_{X_{SYS}}$ evolution on evolution on $\Delta\epsilon$ and $\Delta\alpha$.

Figure 30 shows that the mean square deviation of $\Delta\epsilon$, curve in red, is not influenced by the variation of the penalty $Q_{U_{SYS}}$. Indeed, $\Delta\epsilon$ mean square deviation is included between $[7,5 \cdot 10^{-5}; 2 \cdot 10^{-3}]$ compare to $\Delta\alpha$ mean square deviation.

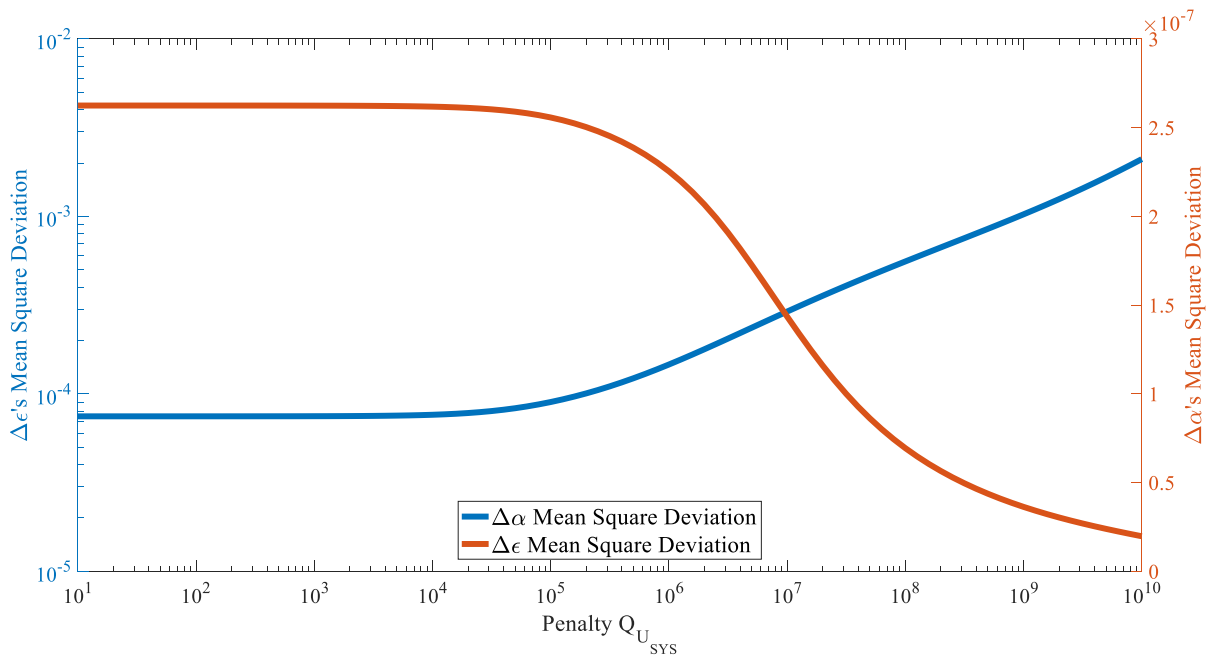


Figure 30: Impact of Penalty $Q_{U_{SYS}}$ evolution on $\Delta\epsilon$ and $\Delta\alpha$.

The $\Delta\alpha$ mean square deviation, curve in blue, are highly linked to the value to penalty $Q_{U_{SYS}}$ as the values vary in the interval of $[1 \cdot 10^{-3}; 0,4 \cdot 10^{-3}]$. Figure 30 highlights that the duty ratios $\Delta\alpha$ mean square deviation stays near the value of 10^5 for penalty $Q_{U_{SYS}}$ inferiors or equals to 10^5 , for higher values of $Q_{U_{SYS}}$, the duty ratios $\Delta\alpha$ mean square deviation increases rapidly.

As a rapid comparison with the Figure 29, the variation of the mean square deviation of ε and α 's mean square deviation has better results and that the variations are less important with the controller on the derivative term of U.

To avoid the inverter's duty ratio saturation, the penalty value $Q_{U_{SYS}}$ is increased to minimize the impact on the $\Delta\varepsilon$ mean square variation and $\Delta\alpha$ mean square deviation. The Figure 30 identifies a possible solution of $Q_{X_{SYS}} = 100 \cdot \mathbb{I}_2$ as seems to be a compromise between the different objectives of the proposed controller.

Appendix 7. Robustness study

A study of the robustness is performed to consider the uncertainties on the grid electrical parameters that are included in the proposed controller: L_L and R_L , L_g and R_g , C_f and R_f . As the synchronous machine is virtual, implemented in the VSG control, the robustness study of the synchronous machine parameters has no justification.

To identify the impact of the uncertainties in proposed controller, the study considers a variation for 1 % to 500 % of each parameter values to determine the deviance on the observed grid voltages \widehat{V}_g^d and \widehat{V}_g^q , and the observed grid currents \widehat{i}_g^d and \widehat{i}_g^q , due to the uncertainties.

As the field e_{fd} voltage is determined by the VSG control, the voltage e_{fd} is always available. In addition, the e_{fd} voltage is not impacted by the different parameters L_L and R_L , L_g and R_g , C_f and R_f .

As visible in Figure 31, the uncertainties on the inverter's parameters, L_L and R_L , has no an impact on observed voltages \widehat{V}_g^d and \widehat{V}_g^q .

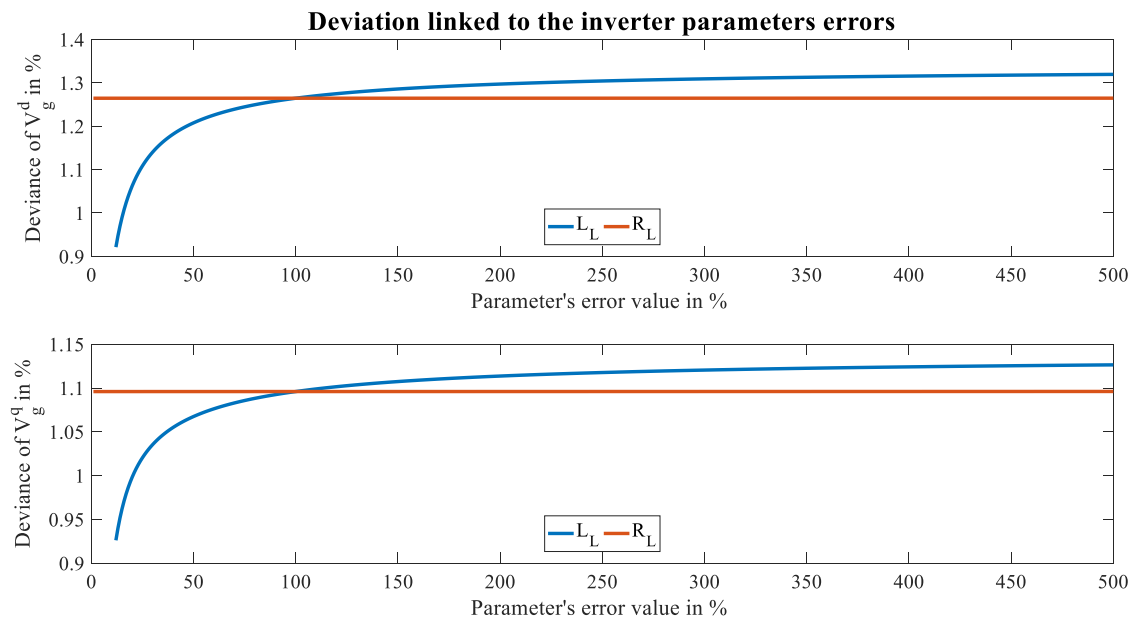


Figure 31: Deviance of \widehat{V}_g^d and \widehat{V}_g^q due to the errors on the inverter parameters value, L_L and R_L .

Similarly, Figure 32 highlights that the values of the capacitor filter, C_f and R_f has no impact on the determination of the observed voltages \widehat{V}_g^d and \widehat{V}_g^q as the deviance is inferior to 1.5% even for values 5 times greater than real parameters.

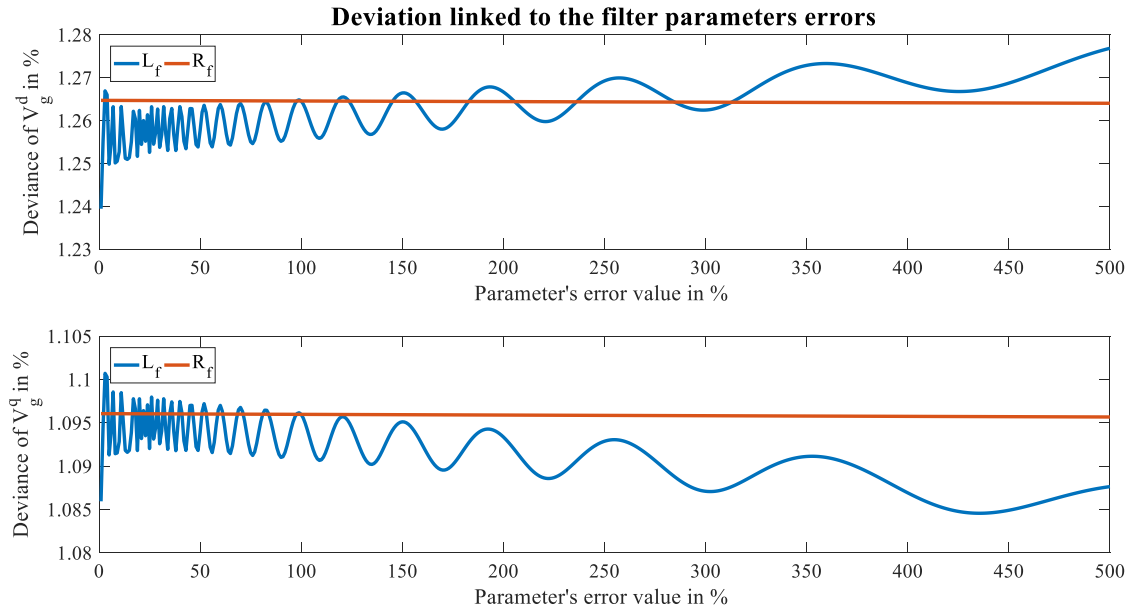


Figure 32: Deviance of \widehat{V}_g^d and \widehat{V}_g^q due to the errors on the filter parameters value, C_f and R_f

Concerning the grid parameters, L_g and R_g , only the value of the resistance R_g has impacted on the value of the observed voltages \widehat{V}_g^d and \widehat{V}_g^q , but for 500 % of incertitude on the value, the deviance is inferior to 10% as shows in Figure 33.

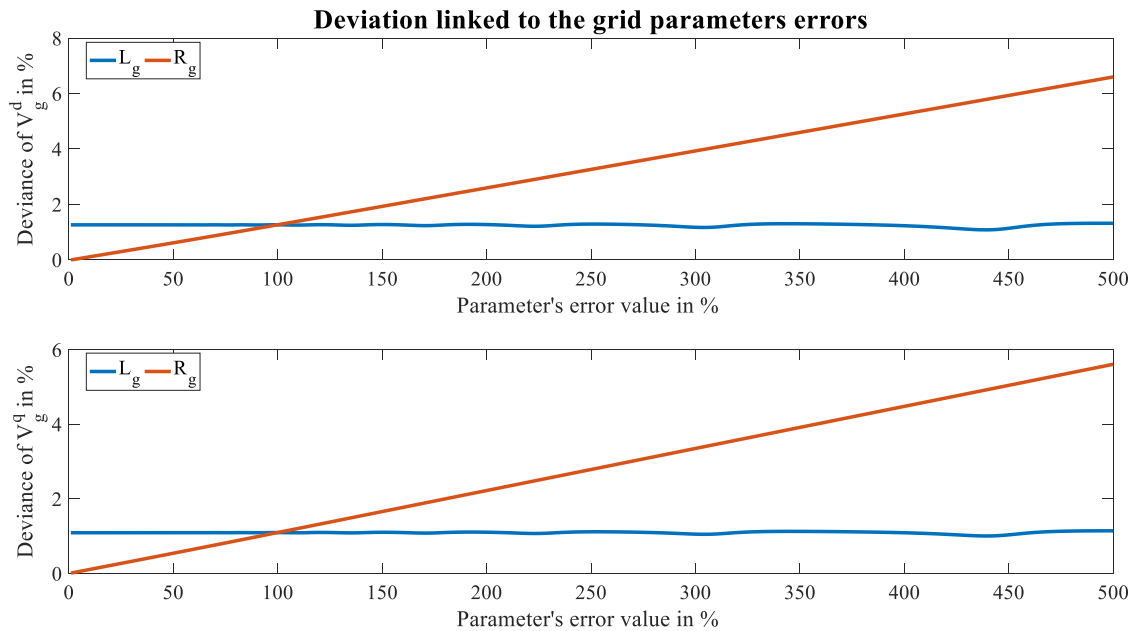


Figure 33: Deviance of \widehat{V}_g^d and \widehat{V}_g^q due to the errors on the grid parameters value, L_g and R_g

Figure 34 to Figure 36 show that the observed grid currents are \widehat{i}_g^d and \widehat{i}_g^q not impacted by the uncertainties on the different parameters, L_L and R_L , L_g and R_g , C_f and R_f , the different deviances stayed below the value of 5 %.

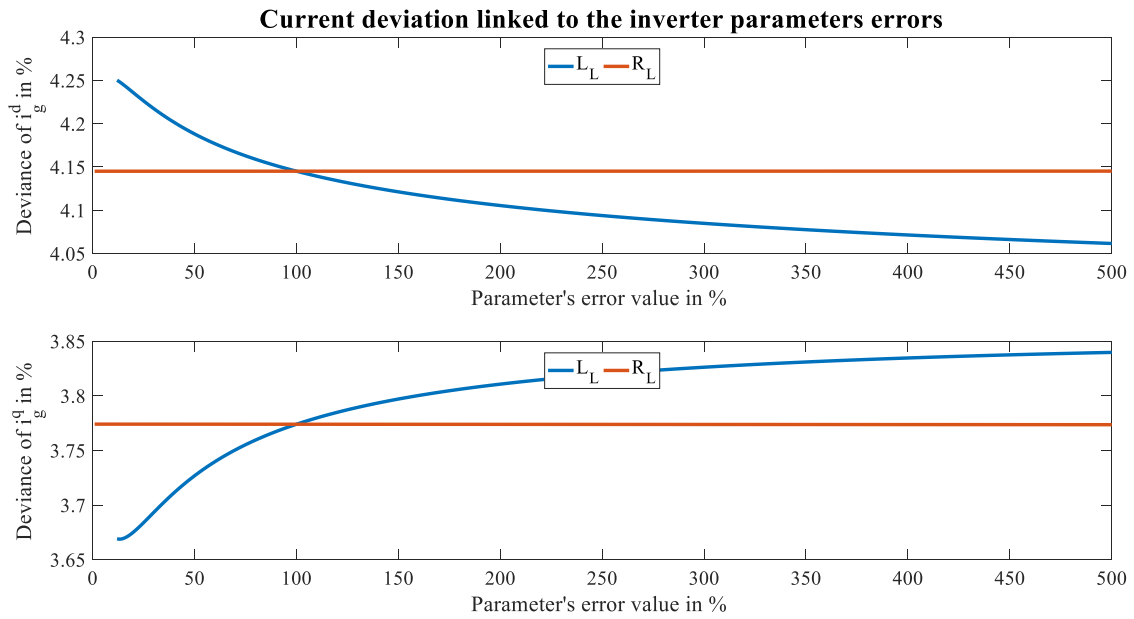


Figure 34: Deviance of \hat{i}_g^d and \hat{i}_g^q due to the errors on the inverter parameters value, L_L and R_L .

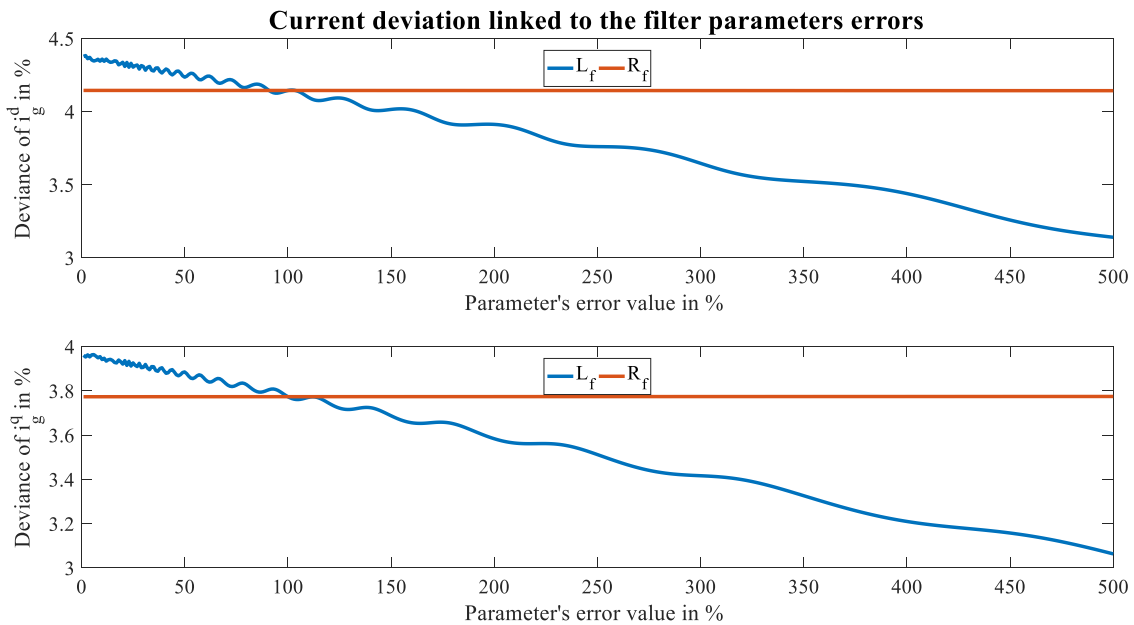


Figure 35: Deviance of \hat{i}_g^d and \hat{i}_g^q due to the errors on the filter parameters value, C_f and R_f

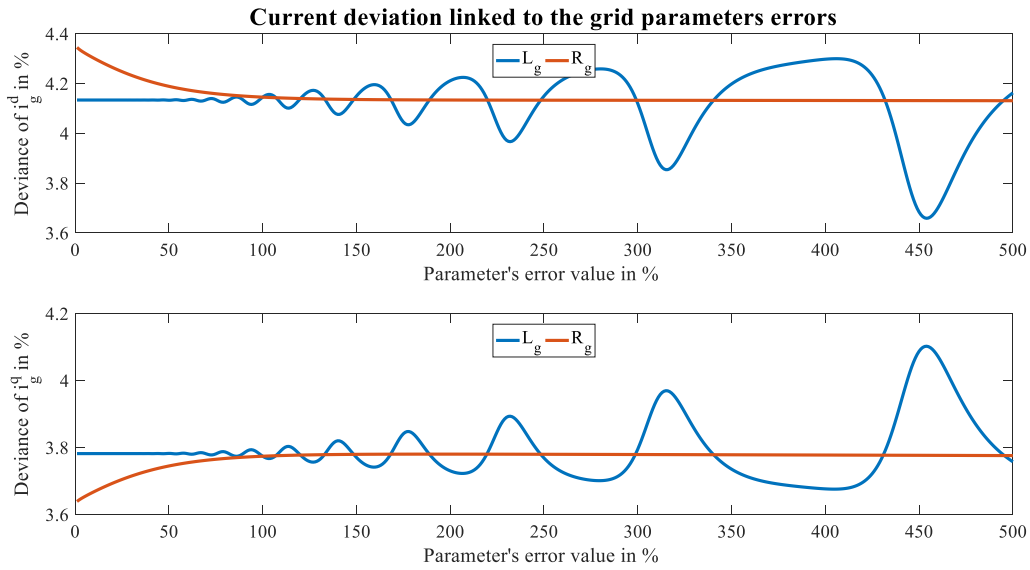


Figure 36: Deviance of \hat{i}_g^d and \hat{i}_g^q due to the errors on the grid parameters value, L_g and R_g

Hence, with Figure 28 to Figure 36, the robustness study shows that the deviation is small-scale, even for high uncertainties in the different parameters' values. These good results are possible thanks to the insertion of an integrator in the proposed controller that reduces the impact of the uncertainties on electrical parameters.

Appendix 8. Analytic Study of the different current controllers for VSG-based inverters application

In this appendix, the different current controllers that are presented in this thesis, the PI controller (p47), the PI controller integrated a state observer (p57), and the proposed controller (p66) are analytically compared to the previous solution deployed in the VSG inverter at the Schneider Electric laboratory, a PI controller integrated stabilizing virtual impedances, that is presented in [23].

Even if the current controller is highly detailed in [23], the equations are reminded below and the state-space model presented in this appendix for comparison with the other studied current controllers. In this controller, stabilizing virtual impedances are added between the synchronous machine model and the inverter model as detailed in [28] and represented in the diagram below:

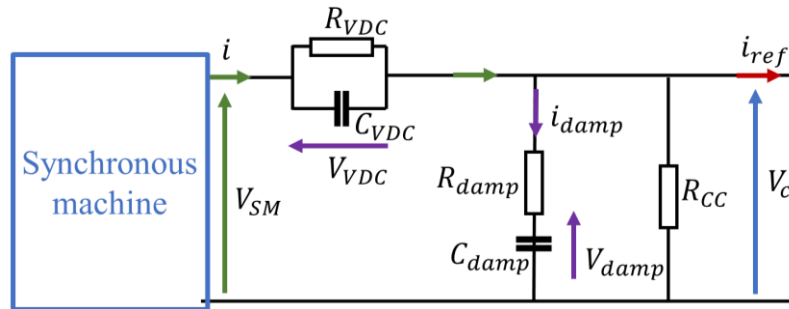


Figure 37: Single line diagram of the integrated virtual impedances filters at the output of the synchronous machine model

with:

- V_{SM} represents the voltage applied to the synchronous machine model.
- i represents the output synchronous machine currents.
- V_{VDC} represents the voltage thought the RC parallel filter, considering R_{VDC} and C_{VDC} respectively the resistor and the capacitor of the filter.
- V_{damp} and i_{damp} represent respectively the voltage and the current thought the RC series filter, considering R_{damp} and C_{damp} respectively the resistor and the capacitor of the filter.
- i_{ref} is the new reference currents of the system instead of i .
- V_c is the input voltage that is applied to the inverter model and that permits the connexion between the synchronous machine model and the inverter model.

Hence, the additional equations to the system, composed of the synchronous machine model and the grid connected inverter model, are resumed below, in p.u.:

$$\frac{dV_{damp}}{dt} = \frac{(V_c - V_{damp})}{R_{damp} \cdot C_{damp}} \quad (1)$$

$$\frac{dV_{VDC}}{dt} = \frac{1}{C_{VDC}} \cdot i - \frac{V_{VDC}}{R_{VDC}} \quad (2)$$

$$V_{SM} = V_c + V_{VDC} \quad (3)$$

$$i_{ref} = i - \frac{(V_c - V_{damp})}{R_{damp}} - \frac{V_c}{R_{CC}} \quad (4)$$

so, the equivalent state-space equations for the different parameters in p.u. and in dq-axis that need to be added to model the PI controller with virtual impedances, considering the dq-axis derivation described in 2.2.2 (p10), and considering that $\begin{bmatrix} i^d \\ i^q \end{bmatrix} = C_{SYS} \cdot X_{SYS}$, are:

$$\begin{bmatrix} \dot{V}_{damp}^d \\ \dot{V}_{damp}^q \end{bmatrix} = \omega_{base} \left(\frac{1}{R_{damp} \cdot C_{damp}} \begin{bmatrix} e^d \\ e^q \end{bmatrix} + \begin{bmatrix} -\frac{1}{R_{damp} \cdot C_{damp}} & \omega_r \\ -\omega_r & -\frac{1}{R_{damp} \cdot C_{damp}} \end{bmatrix} \cdot \begin{bmatrix} V_{damp}^d \\ V_{damp}^q \end{bmatrix} \right) \quad (5)$$

$$\begin{bmatrix} \dot{V}_{VDC}^d \\ \dot{V}_{VDC}^q \end{bmatrix} = \omega_{base} \left(\frac{1}{C_{VDC}} \cdot C_{SYS} \cdot X_{SYS} + \begin{bmatrix} -\frac{1}{R_{VDC}} & \omega_r \\ -\omega_r & -\frac{1}{R_{VDC}} \end{bmatrix} \cdot \begin{bmatrix} V_{VDC}^d \\ V_{VDC}^q \end{bmatrix} \right) \quad (6)$$

$$\begin{bmatrix} V_{SM}^d \\ V_{SM}^q \end{bmatrix} = \begin{bmatrix} e^d \\ e^q \end{bmatrix} + \begin{bmatrix} V_{VDC}^d \\ V_{VDC}^q \end{bmatrix} \quad (7)$$

$$i_{ref} = \frac{1}{C_{VDC}} \cdot C_{SYS} \cdot X_{SYS} - \begin{bmatrix} \frac{1}{R_{damp}} + \frac{1}{R_{CC}} & 0 \\ 0 & \frac{1}{R_{damp}} + \frac{1}{R_{CC}} \end{bmatrix} \cdot \begin{bmatrix} e^d \\ e^q \end{bmatrix} \quad (8)$$

with the additional equations, (5) to (8), the state-space model with the additional impedances is, in dq and p.u.:

$$\begin{bmatrix} \dot{X}_{SYS} \\ \dot{X}_{Filter} \end{bmatrix} = \begin{bmatrix} A_{SYS} & A_{F1} \\ A_{F2} & A_{F3} \end{bmatrix} X_{SYS} + \begin{bmatrix} B_{SYS} \\ \mathbb{O}_{4,2} \end{bmatrix} \cdot U_{SYS} + \begin{bmatrix} G_{SYS} \\ \mathbb{O}_{4,3} \end{bmatrix} \cdot W_{SYS}$$

$$Y_{SYS} = \begin{bmatrix} C_{SYS} - \left(\frac{1}{R_{damp}} + \frac{1}{R_{CC}} \right) \cdot [\mathbb{O}_{2,7} \quad \mathbb{I}_2 \quad \mathbb{O}_{2,2}] \quad \mathbb{O}_{2,4} \end{bmatrix} \cdot \begin{bmatrix} X_{SYS} \\ X_{Filter} \end{bmatrix}$$

where X_{SYS} is the regulated system's states, X_{Filter} is the regulated states coming from the two additional and virtual filters, U_{SYS} is the regulated system's command, W_{SYS} is the system's exogenous inputs and finally Y_{SYS} is the regulated system's outputs.

$$X_{SYS} = [\psi_d \quad \psi_q \quad \psi_{fd} \quad \psi_{1d} \quad \psi_{1q} \quad i_L^d \quad i_L^q \quad e^d \quad e^q \quad i_g^d \quad i_g^q]^t, X_{SYS} \in \mathbb{M}_{11,1}$$

$$X_{Filter} = [V_{damp}^d \quad V_{damp}^q \quad V_{VDC}^d \quad V_{VDC}^q]^t, X_{Filter} \in \mathbb{M}_{4,1}$$

$$U_{SYS} = \begin{bmatrix} V_i^d \\ V_i^q \end{bmatrix}, U_{SYS} \in \mathbb{M}_{2,1}; W_{SYS} = \begin{bmatrix} e_{fd} \\ V_g^d \\ V_g^q \end{bmatrix}, W_{SYS} \in \mathbb{M}_{3,1} \text{ and } Y_{SYS} = \begin{bmatrix} i^d \\ i^q \end{bmatrix}, Y_{SYS} \in \mathbb{M}_{2,1},$$

the matrixes A_{SYS} , B_{SYS} , G_{SYS} and C_{SYS} , $A_{SYS} \in \mathbb{M}_{11,11}$; $B_{SYS} \in \mathbb{M}_{11,2}$; $G_{SYS} \in \mathbb{M}_{11,3}$ and $C_{SYS} \in \mathbb{M}_{2,11}$, are given in part 3.2.2 (p43) and were the matrices, A_{F1} , A_{F2} and A_{F3} , are defined as :

$$A_{F1} = \omega_{base} \begin{bmatrix} \mathbb{I}_2 & \mathbb{O}_{2,2} \\ \mathbb{O}_{9,2} & \mathbb{O}_{9,2} \end{bmatrix}, A_{F2} = \omega_{base} \begin{bmatrix} \mathbb{O}_{2,5} & \mathbb{O}_{2,2} & \frac{1}{R_{damp} \cdot C_{damp}} & \mathbb{O}_{2,2} \\ \frac{1}{C_{VDC}} \cdot C_{SYS} & \mathbb{O}_{2,2} & \mathbb{O}_{2,2} & \mathbb{O}_{2,2} \end{bmatrix}$$

$$A_{F_3} = \omega_{base} \cdot \begin{bmatrix} -\frac{1}{R_{damp} \cdot C_{damp}} & \omega_r & & & \\ & -\omega_r & -\frac{1}{R_{damp} \cdot C_{damp}} & & \\ & & & \mathbb{O}_{2,2} & \\ & & & & -\frac{1}{R_{VDC}} & \omega_r \\ & & \mathbb{O}_{2,2} & & -\omega_r & -\frac{1}{R_{VDC}} \end{bmatrix}$$

Hence, following the same methodology that is described in 3.3.1 (p47), the PI controller forces the inverter output currents to follow the reference currents, i_{ref}^d and i_{ref}^q . The new variable ε output is defined as the difference between the inverter's currents, i_L^d and i_L^q , compared to the synchronous machine's currents i_{ref}^d and i_{ref}^q :

$$\varepsilon = \begin{bmatrix} i_{ref}^d - i_L^d \\ i_{ref}^q - i_L^q \end{bmatrix} = \left(C_{SYS} - \begin{bmatrix} \mathbb{O}_{2,5} & \mathbb{I}_2 \end{bmatrix} \cdot \left(\frac{1}{R_{damp}} + \frac{1}{R_{CC}} \right) \mathbb{I}_2 \quad \mathbb{O}_{2,2} \right) \quad \mathbb{O}_{2,4} \cdot \begin{bmatrix} X_{SYS} \\ X_{Filter} \end{bmatrix}$$

hence,

With $C_\varepsilon^{filter} = \left(C_{SYS} - \begin{bmatrix} \mathbb{O}_{2,5} & \mathbb{I}_2 \end{bmatrix} \cdot \left(\frac{1}{R_{damp}} + \frac{1}{R_{CC}} \right) \mathbb{I}_2 \quad \mathbb{O}_{2,2} \right) \quad \mathbb{O}_{2,4}$, $C_\varepsilon^{filter} \in \mathbb{M}_{2,13}$, the model is now defined by:

$$\begin{bmatrix} \dot{X}_{SYS} \\ \dot{X}_{Filter} \end{bmatrix} = \begin{bmatrix} A_{SYS} & A_{F_1} \\ A_{F_2} & A_{F_3} \end{bmatrix} X_{SYS} + \begin{bmatrix} B_{SYS} \\ \mathbb{O}_{4,2} \end{bmatrix} \cdot U_{SYS} + \begin{bmatrix} G_{SYS} \\ \mathbb{O}_{4,3} \end{bmatrix} \cdot W_{SYS}$$

$$\varepsilon = C_\varepsilon^{filter} \cdot \begin{bmatrix} X_{SYS} \\ X_{Filter} \end{bmatrix}$$

Similarly to 3.3.1 (p47), the equations of the PI-controlled system integrated the filters are, in p.u. and dq-axis:

$$\begin{bmatrix} \dot{X}_{SYS} \\ \dot{X}_{Filter} \\ \dot{\varepsilon}_{PI} \end{bmatrix} = \begin{bmatrix} \begin{bmatrix} A_{SYS} & A_{F_1} \\ A_{F_2} & A_{F_3} \end{bmatrix} + \begin{bmatrix} B_{SYS} \\ \mathbb{O}_{4,2} \end{bmatrix} \cdot K_p \cdot C_\varepsilon^{filter} & \begin{bmatrix} B_{SYS} \\ \mathbb{O}_{4,2} \end{bmatrix} \cdot K_i \\ K_p \cdot C_\varepsilon^{filter} & \mathbb{O}_{2,2} \end{bmatrix} \cdot \begin{bmatrix} X_{SYS} \\ X_{Filter} \\ \varepsilon_{PI} \end{bmatrix} + \begin{bmatrix} G_{SYS} \\ \mathbb{O}_{4,3} \\ \mathbb{O}_{2,3} \end{bmatrix} \cdot W_{SYS}$$

with the model outputs:

$$\begin{bmatrix} V_i^d \\ V_i^q \end{bmatrix} = \left(\left(\begin{bmatrix} \mathbb{O}_{2,7} & \mathbb{I}_2 & \mathbb{O}_{2,2} \end{bmatrix} + K_p \cdot C_\varepsilon^{filter} \right) \quad K_i \right) \cdot \begin{bmatrix} X_{SYS} \\ \varepsilon_{PI} \end{bmatrix}$$

$$\varepsilon = \left[K_p \cdot C_\varepsilon^{filter} \quad \mathbb{O}_{2,2} \right]$$

Now that the PI controller integrated the virtual impedances is described in state-space model, it's possible to analytically compare the different current controllers detailed in this thesis. In Table 1 below can be found the different parameter values that have been considered for the comparison between the current controllers.

Table 1: Parameters definition for the different current controllers.

Parameters	Values	Unit	
K_p	3500	—	
K_i	300	—	
RC parallel filter	R_{VDC}	6	Ω
	C_{VDC}	60e-6	F
RC series filter	R_{damp}	6	Ω
	C_{damp}	1e-3	F
R_{CC}	6	Ω	

In the following figures, Figure 38 and Figure 39, the different currents controllers, the classical PI controller, the PI controller with virtual impedances, the PI controller integrated and the proposed solution are analytically represented in bode diagram, magnitude and phase, based on the input voltages e_{fd} , V_g^d and V_g^q and the output controlled duty ratio, α^d and α^q .

Figure 38, magnitude characteristic, shows that the current controllers PI and PI + filter have similar magnitude, with a high resonance peak at high frequencies. This resonance, for the PI + filter, is reduced thanks to the insertion of the resistance R_{CC} but nevertheless remains relatively important. The disadvantage of the high frequencies resonance peak is that it has a real impact on the stability of the system, especially during short circuits, which is a major disadvantage for these two controls.

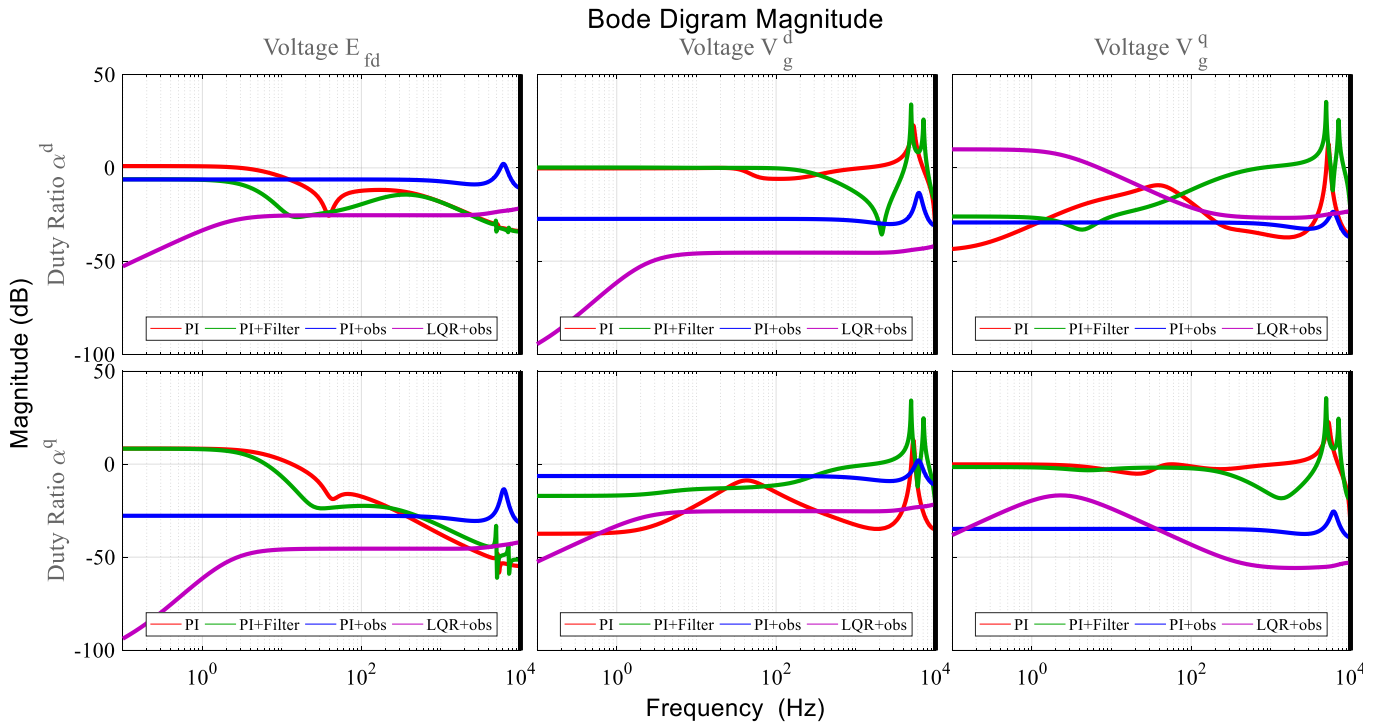


Figure 38: Bode magnitude diagram of the four different currents controllers considering the inputs voltages e_{fd} , V_g^d , V_g^q and outputs duty ratio α^d and α^q .

It can be noted that thanks to the integration of the observer, the both systems, PI + observer and the proposed controller, the resonance peak is reduced for the PI + observer or totally removed in the case of the proposed controller. Hence, the observer helps stabilizing the current controllers.

However, the PI + observer possesses a magnitude characteristic that is constant and could represent a problem for the lower frequencies, especially when the system is off-loading as it is visible in Figure 3.22 (p61), with high stable oscillations. One of the major advantages of the proposed controller is that it rejects the low frequencies and also that it is not as impacted by the high frequencies as the three other current controllers as it can be seen with its magnitude characteristic in Figure 38.

Figure 39 represents the phase characteristics of the four current controllers. It can be noted that the phase shift for the PI and the PI + filters is important and can reach 720 degrees. Indeed, with the insertion of RC filters, in addition of consuming some power and decreasing the total efficiency, the phase shift between the inputs and the outputs can reach important values and the global phase shift can be analytically calculated based on the methodology below:

$$S_{damp} = 3 \cdot \frac{E_n}{\sqrt{\left(\frac{\omega_{base}}{C_{damp}} \times Z_{base}\right)^2 + (R_{damp} \times Z_{base})^2}} ; P_{damp} = 3 \cdot \frac{E_n^2}{R_{damp}}$$

$$S_{VDC} = 3 \cdot \frac{E_n}{\sqrt{\left(\frac{\omega_{base}}{C_{VDC}} \times Z_{base}\right)^2 + (R_{VDC} \times Z_{base})^2}} ; P_{VDC} = 3 \cdot \frac{E_n^2}{R_{VDC}}$$

$$\cos(\phi) = \frac{P_{VDC} + P_{damp}}{S_{VDC} + S_{damp}}$$

considering the values used for the filters, the phase shift is $\cos(\phi) = 0.41$ which represent a high phase shift between the voltage inputs and the controlled duty ratios.

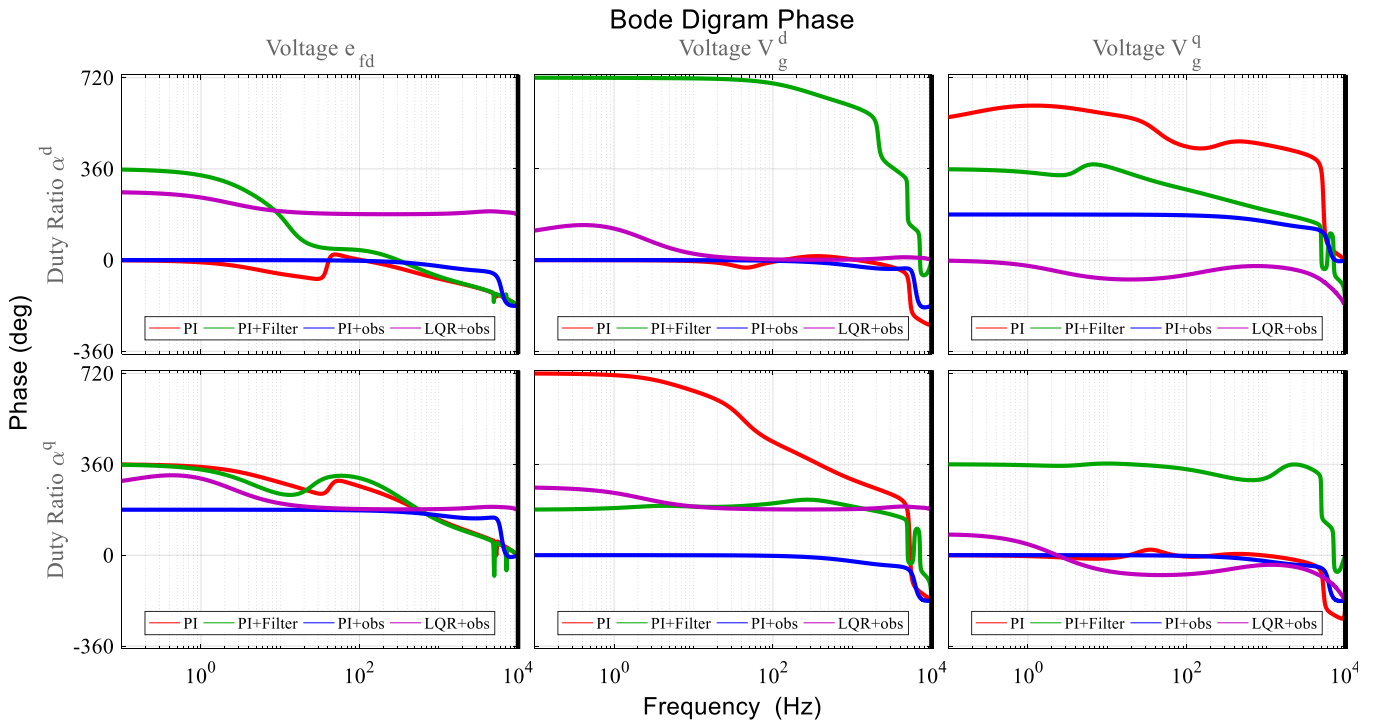


Figure 39: Bode magnitude phase of the four different currents controllers considering the inputs voltages e_{fd} , V_g^d , V_g^q and outputs duty ratio α^d and α^q .

Hence, an important advantage of the observer, for the PI + observer and the proposed controller is that the phase shift is mainly constant and near zero between the inputs and the controlled outputs. So, an important advantage of the integration of a state observer in the current controller is that it permits to mainly keep the phase shift between the voltages inputs and the controlled duty ratios constant, even equals to zeros in the case of the PI controller with the observer.

To conclude on the impact of integration of a state observer in the current controller is that it greatly helps stabilize the system, especially during high frequencies phenomena as short-circuits, in addition to reduce the phase shift between the voltages inputs e_{fd} , V_g^d and V_g^q , and the controlled duty ratio α^d and α^q .

Regarding both figures, Figure 38 and Figure 39, even if the state observer solve different problem as the phase shift and the high frequencies resonance in the case of a PI controller, the best current controller is the proposed controller as it's also reject the lower frequencies phenomena in order to ensure the stability system especially off-loading.

Appendix 9. Schneider Electric Single Line Microgrid

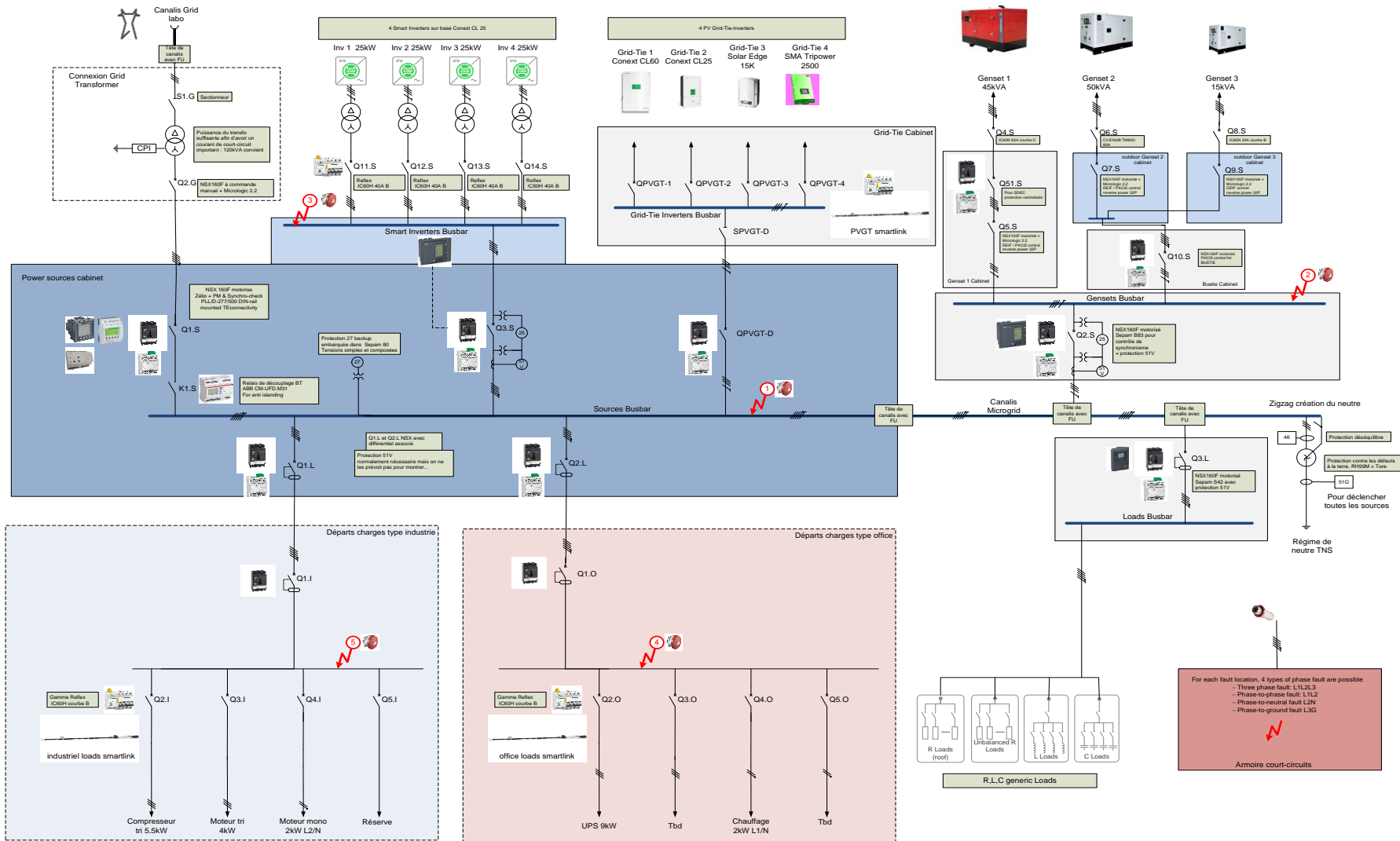


Figure 40: Single Line Diagram of the Schneider Electric Microgrid Laboratory.

Appendix 10. Adaption of the proposed controller for the reduced model

This state-space reduced SM model in dq-axis and p.u. is:

$$\begin{aligned}\dot{X}_{SYS} &= A_{SYS} \cdot X_{SYS} + B_{SYS} \cdot U_{SYS} + G_{SYS} \cdot W_{SYS} \\ Y_{SYS} &= C_{SYS} \cdot X_{SYS}\end{aligned}$$

where X_{SYS} is the regulated system's states, U_{SYS} is the regulated system's command, W_{SYS} is the system's exogenous inputs and finally Y_{SYS} is the regulated system's outputs.

$$\begin{aligned}X_{SYS} &= [\psi_d \quad \psi_q \quad \psi_{fd} \quad i_L^d \quad i_L^q \quad e^d \quad e^q \quad i_g^d \quad i_g^q]^t, X_{SYS} \in \mathbb{M}_{9,1} \\ U_{SYS} &= \begin{bmatrix} \alpha_d \\ \alpha_q \end{bmatrix}, U_{SYS} \in \mathbb{M}_{2,1}; W_{SYS} = \begin{bmatrix} e_{fd} \\ V_g^d \\ V_g^q \end{bmatrix}, W_{SYS} \in \mathbb{M}_{3,1} \text{ and } Y_{SYS} = \begin{bmatrix} i^d \\ i^q \end{bmatrix}, Y_{SYS} \in \mathbb{M}_{2,1} \\ Y_{meas} &= [i^d \quad i^q \quad \psi_d \quad \psi_q \quad \psi_{fd} \quad i_L^d \quad i_L^q \quad e^d \quad e^q \quad e_{fd}]^t, Y_{meas} \in \mathbb{M}_{10,1}\end{aligned}$$

It can be noted that the fluxes ψ_{1d} and ψ_{1q} have been removed from the regulated system's states X_{SYS} as the dampers are not included in the reduced model.

The matrix A_{SYS} , B_{SYS} , G_{SYS} and C_{SYS} , $A_{SYS} \in \mathbb{M}_{9,9}$; $B_{SYS} \in \mathbb{M}_{9,2}$; $G_{SYS} \in \mathbb{M}_{9,3}$ and $C_{SYS} \in \mathbb{M}_{2,9}$, are given below:

$$\begin{aligned}A_{SYS} &= \omega_{base} \cdot \begin{bmatrix} A_{MS} & A_E \\ \mathbb{0}_{6,3} & A_{LCL} \end{bmatrix} \text{ with } A_{MS} = \begin{bmatrix} -a_1 & \omega_r & 0 \\ -\omega_r & -a_3 & 0 \\ a_4 & 0 & -a_4 \end{bmatrix}, A_E = \omega_r \cdot \begin{bmatrix} \mathbb{0}_{2,2} & \mathbb{I}_2 & \mathbb{0}_{2,2} \\ \mathbb{0}_{1,2} & \mathbb{0}_{1,2} & \mathbb{0}_{1,2} \end{bmatrix}, \\ A_{LCL} &= \begin{bmatrix} -\frac{R_L}{L_L} & \omega_r & -\frac{1}{L_L} & 0 & 0 & 0 \\ -\omega_r & -\frac{R_L}{L_L} & 0 & -\frac{1}{L_L} & 0 & 0 \\ \left(\frac{1}{C_f} - \frac{R_f \cdot R_L}{L_L}\right) & 0 & -R_f \cdot \left(\frac{1}{L_L} + \frac{1}{L_g}\right) & \omega_r & -\left(\frac{1}{C_f} - \frac{R_f \cdot R_g}{L_g}\right) & 0 \\ 0 & \left(\frac{1}{C_f} - \frac{R_f \cdot R_L}{L_L}\right) & -\omega_r & -R_f \cdot \left(\frac{1}{L_L} + \frac{1}{L_g}\right) & 0 & -\left(\frac{1}{C_f} - \frac{R_f \cdot R_g}{L_g}\right) \\ 0 & 0 & \frac{1}{L_g} & 0 & -\frac{R_g}{L_g} & \omega_r \\ 0 & 0 & 0 & \frac{1}{L_g} & -\omega_r & -\frac{R_g}{L_g} \end{bmatrix}\end{aligned}$$

$$B_{SYS} = \omega_{base} \cdot \begin{bmatrix} 0 & 0 \\ 0 & 0 \\ 0 & 0 \\ \frac{V_{DC}}{2 \cdot L_L} & 0 \\ 0 & \frac{V_{DC}}{2 \cdot L_L} \\ \frac{R_f \cdot V_{DC}}{2 \cdot L_L} & 0 \\ 0 & \frac{R_f \cdot V_{DC}}{2 \cdot L_L} \\ 0 & 0 \\ 0 & 0 \end{bmatrix}; G_{SYS} = \omega_{base} \cdot \begin{bmatrix} 0 & 0 & 0 \\ 0 & 0 & 0 \\ 1 & 0 & 0 \\ 0 & 0 & 0 \\ 0 & 0 & 0 \\ 0 & \frac{R_f}{L_g} & 0 \\ 0 & 0 & \frac{R_f}{L_g} \\ 0 & -\frac{1}{L_g} & 0 \\ 0 & 0 & -\frac{1}{L_g} \end{bmatrix};$$

$$C_{SYS} = \begin{bmatrix} -c_1 & 0 & c_2 & 0 & 0 & 0 & 0 & 0 & 0 & 0 & 0 & 0 \\ 0 & -c_3 & 0 & 0 & 0 & 0 & 0 & 0 & 0 & 0 & 0 & 0 \end{bmatrix}.$$

Then, considering the integrator addition, the new matrixes are defined as:

$$\bar{A}_{SYS} = \begin{bmatrix} A_{SYS}^s & \mathbb{O}_{9,2} \\ C_\varepsilon^s & \mathbb{I}_2 \end{bmatrix}, \bar{B}_{SYS} = \begin{bmatrix} B_{SYS}^s \\ \mathbb{O}_{2,2} \end{bmatrix}, \bar{C}_{SYS} = \begin{bmatrix} G_{SYS}^s \\ \mathbb{O}_{2,2} \end{bmatrix} \text{ and } \bar{C}_\varepsilon^s = [C_\varepsilon^s \quad \mathbb{O}_{2,2}].$$

Hence, when integrating U_{SYS} in regulated system's states X_{SYS} in system, the matrixes become:

$$\underline{A}^s = \begin{bmatrix} \bar{A}_{SYS}^s & \bar{B}_{SYS}^s \\ \mathbb{O}_{2,9} & \mathbb{I}_2 \end{bmatrix} - \begin{bmatrix} \mathbb{O}_{9,2} \\ \mathbb{I}_2 \end{bmatrix}. K^s, \underline{A}^s \in \mathbb{M}_{13,13}; \underline{C}^s = [\bar{C}_\varepsilon^s \quad \mathbb{O}_{2,2}], \underline{C}^s \in \mathbb{M}_{2,13}.$$

To conclude, the proposed controller with the reduced model is defined by:

$$\hat{X}_\Delta^+ = A_\Delta^s \cdot \hat{X}_\Delta + B_\Delta^s \cdot \begin{bmatrix} Y_{meas} \\ \varepsilon^* \end{bmatrix}$$

$$Y_\Delta = C_\Delta^s \cdot \hat{X}_\Delta + D_\Delta^s \cdot \begin{bmatrix} Y_{meas} \\ \varepsilon^* \end{bmatrix}$$

$$\text{With } X_\Delta = \begin{bmatrix} \bar{X}_{SYS} \\ U_{SYS} \\ W_{SYS} \end{bmatrix}, X_\Delta \in \mathbb{M}_{16,1}; Y_\Delta = \begin{bmatrix} Y_{meas} \\ \varepsilon \\ \Delta U \end{bmatrix}, Y_\Delta \in \mathbb{M}_{11,1}, \text{ and where the different matrixes are}$$

defined as:

$$L_{obs\Delta} = \begin{bmatrix} L_X^X & \mathbb{O}_{9,4} & L_W^X \\ \mathbb{O}_{4,9} & \mathbb{O}_{4,4} & \mathbb{O}_{4,3} \\ L_X^W & \mathbb{O}_{3,4} & L_W^W \end{bmatrix} \text{ with the different parameters of } L_{obs\Delta}$$

$$A_\Delta^s = \begin{bmatrix} \underline{A}^s & (\underline{A}^s - \mathbb{I}_{13}) \cdot \begin{bmatrix} K_W^X \\ K_W^U \end{bmatrix} \\ \mathbb{O}_{3,13} & \mathbb{I}_3 \end{bmatrix} - L_{obs\Delta} \cdot [C_{meas} \quad \mathbb{O}_{10,4} \quad H_{meas}], A_\Delta^s \in \mathbb{M}_{16,16};$$

$$B_{\Delta}^s = \left[L_{obs_{\Delta}} \quad (\mathbb{I}_{13} - \underline{A}^s) \cdot \begin{bmatrix} K_{\varepsilon}^X \\ K_{\varepsilon}^U \end{bmatrix} \right], B_{\Delta}^s \in \mathbb{M}_{16,14};$$

$$C_{\Delta}^s = \begin{bmatrix} [C_{\varepsilon}^s \quad \mathbb{O}_{4,2}] & H_{meas}^s \\ \underline{C}^s & -\underline{C}^s \cdot \begin{bmatrix} K_W^X \\ K_W^U \end{bmatrix} \\ -K^s & -K^s \cdot \begin{bmatrix} K_W^X \\ K_W^U \end{bmatrix} \end{bmatrix}, C_{\Delta}^s \in \mathbb{M}_{14,16} \text{ and}$$

$$D_{\Delta}^s = \begin{bmatrix} \mathbb{O}_{10,10} & \mathbb{O}_{10,2} \\ \mathbb{O}_{2,10} & \mathbb{I}_2 - \underline{C}^s \cdot \begin{bmatrix} K_{\varepsilon}^X \\ K_{\varepsilon}^U \end{bmatrix} \\ \mathbb{O}_{2,10} & -K^s \cdot \begin{bmatrix} K_{\varepsilon}^X \\ K_{\varepsilon}^U \end{bmatrix} \end{bmatrix}, D_{\Delta}^s \in \mathbb{M}_{14,14}.$$

Résumé français étendu

Le mémoire, « Conception d'un système adaptatif dynamique de générateur synchrone virtuel pour la stabilisation des micro-réseaux électriques à fort taux de pénétration d'énergie renouvelable », est organisé en 7 Chapitres avec une conclusion générale, des perspectives, la liste des références bibliographiques et les appendices associés. Cet ensemble est précédé par un résumé, un sommaire, la liste des illustrations et des tables, des acronymes, et par une introduction générale qui permet de rappeler le contexte, la problématique, l'organisation et les contributions générales de la thèse.

Le Chapitre 1 introduit dans un premier temps le contexte général de la thèse en définissant un micro-réseau, sa capacité à fonctionner en modes îloté et connecté au réseau principal et son importance comme solution d'intégration des sources à énergie renouvelable (DER). Cependant, l'intermittence des sources DER a été soulignée particulièrement dans le contexte d'un micro-réseau, ce qui peut conduire à des problèmes de stabilité voir à un blackout du système si mal contrôlé. Ce constat conduit à faire un état de l'art sur les différentes stratégies de contrôle des onduleurs interfaçant ces ressources d'énergies distribuées qui sont connectées sur le micro-réseau. Une solution basée sur le principe du **VSG** (Virtual Synchronous Générateur) a été retenue et trouve tout son intérêt par rapport à une utilisation dans un contexte industriel en collaboration avec l'entreprise Schneider Electric.

De plus, dans le Chapitre 1 peut être trouvé l'organisation de la thèse, en 5 Chapitres et une conclusion ainsi que les contributions de la thèse. Il n'y a pas de Chapitre dédié à l'état de l'art, le choix ayant été fait d'un état de l'art au fil de l'eau pour chaque Chapitre. Le Chapitre 2 traite de la modélisation de la machine synchrone qui peut être embarqué dans le contrôle du VSG. Le Chapitre 3 aborde les différentes stratégies de commande de la solution VSG. Ensuite les Chapitres 4 et 5 sont dédiés à la validation expérimentale et à la répliquabilité du contrôle VSG sur d'autres type d'onduleur. Le Chapitre 6 revient sur la commande du VSG au travers de l'auto-réglage des paramètres en fonctionnement pendant des cas critiques tels que les courts-circuits ou les défaillances sur le micro-réseau.

Le Chapitre 2 présente différents modèles de machine synchrone retenus pour la comparaison et leur implémentation possible comme référence pour le contrôle du VSG. Le schéma général de la boucle de contrôle de l'onduleur pour émuler une machine synchrone est donné au Chapitre 1. On y voit les régulations de tension et fréquence de la machine synchrone puis la régulation en courant de l'onduleur. La modélisation de la machine synchrone reprend l'approche de Park avec deux enroulements amortisseurs (un sur chacun des axes d et q). Le premier modèle est le modèle complet de la machine (avec les amortisseurs), les équations sont rappelées, ce qui conduit à une équation d'état à 5 variables (5 flux considérés). Dans un second temps, les amortisseurs sont négligés (donc les flux associés) ce qui réduit le modèle à 3 variables. Le dernier modèle est le modèle statique, se basant sur les équations de Behn Eschenburg. Pour chaque modèle, les hypothèses considérées sont bien rappelées.

Dans un second temps, les trois modèles retenus sont comparés. D'abord sur leur réponse fréquentielle, puis en termes de stabilité (pour un VSG en mode îloté sur une charge), en termes de respect des limites harmoniques, et enfin pour la stabilité lors d'une marche en parallèle de différentes sources (générateur et VSG). Pour la stabilité, une séquence de fonctionnement est définie avec plusieurs niveaux de charge du VSG (en actif et réactif) et des phases à vide, puis un court-circuit triphasé. La comparaison est réalisée pour les courants stator du modèle avec des différences qui concernent les phases transitoires et subtransitoire. La stabilité en fréquence est aussi regardée. Lors d'un court-circuit le courant subtransitoire et transitoire peut être très élevé pour une machine synchrone réelle. Toutefois, il n'y a pas intérêt à ce que l'onduleur suive ce comportement pour éviter les pics de courant nuisibles à la fiabilité des transistors. Ensuite, la comparaison sur charge non linéaire est réalisée avec un redresseur à diodes sur charge résistive. Enfin, pour la stabilité lors de la marche en parallèle de deux VSG, l'absence d'amortisseurs sur deux des modèles oblige à un réglage spécifique du régulateur de vitesse. Pour un fonctionnement en parallèle avec un générateur synchrone, seul le modèle statique doit être corrigé au niveau de ses régulateurs de tension et vitesse. Le dernier point de comparaison effectué porte sur l'implémentation dans un ordinateur et la capacité de calcul utilisé par le modèle (celui-ci ne doit pas consommer plus de 70-75% de la capacité).

En conclusion de ce Chapitre, le modèle réduit paraît comme le plus prometteur dans le cas de son utilisation pour le contrôle basé sur le VSG pour des applications industrielles.

Dans le Chapitre 3, trois stratégies de contrôleurs, **PI** (Proportionnel Intégral), **PI** et observateur, **LQR** (Linear Quadratic Regulator) et observateur, adaptées à une possible implémentation dans un onduleur industriel, ont été développées.

L'objectif est d'étudier la stabilité de ces contrôleurs lors de leur intégration dans le contrôle du VSG en boucle fermée. En utilisant un onduleur (25 kVA, 400V, 36 A) et par le biais de tests en simulation, ce Chapitre montre bien les limitations du contrôleur **PI** a assuré la stabilité du système en boucle fermée en présence de différentes perturbations (charge

fortement inductive ou capacitive, sans charge et puissance active du VSG $\leq 70\%$ ou puissance réactive du VSG $\geq 30\%$). Le Chapitre souligne également la non possibilité du contrôleur à assurer un fonctionnement de l'onduleur sans saturation lorsque des courts-circuits surviennent sur le micro-réseau électrique.

Pour contourner ces instabilités du contrôleur PI, vérifiées en simulation, il est proposé d'utiliser un observateur d'état pour d'estimer les variations de la charge à la sortie de l'onduleur (tensions et courant coté réseau). Cette solution, qui est basée sur la dynamique de l'observateur, a pour avantage d'améliorer les performances du VSG en évitant les saturations de l'onduleur durant les courts-circuits de courte durée par exemple.

Les performances de l'observateur et du contrôleur PI en boucle fermée ont été testées et validées en simulation et les résultats obtenus montrent que les courants de l'onduleur suivent bien ceux du modèle virtuel de la machine synchrone. Le contrôleur PI avec observateur est ensuite intégré dans le contrôle du VSG et testé en simulation. Les résultats obtenus montrent clairement que le système en boucle fermée est stable (tensions, courants et rapports cycliques triphasés de l'onduleur) lors d'un test de délestage contrairement au cas où l'observateur n'est pas utilisé.

Dans la dernière partie du Chapitre, il est mentionné que le contrôleur PI peut ne pas être le contrôleur le plus optimisé pour le VSG en boucle fermée. Ce constat, vérifié en simulation par la présence d'oscillations sur les courants triphasés de l'onduleur lorsque la charge est désactivée, conduit à proposer un contrôleur LQR en plus de l'observateur. Par rapport aux solutions traditionnelles existantes dans la littérature (contrôleur proportionnel et résonnant) et pour éviter le rajout des impédances ou à des solutions complexes (contrôleurs H_∞ , flou, ...), le choix du contrôleur LQR semble être une des solutions la plus adaptée dans le contexte de l'implémentation de ces contrôleurs dans un onduleur industriel réel. Le contrôleur LQR est développé avec un intégrateur et associé à l'observateur. L'ajout d'une action intégrale et la présence de la dynamique de l'observateur est pertinente car elle permet certainement d'éviter les saturations de la commande, comme il a été montré en simulation. Le contrôleur proposé a été testé et validé en simulation. Le contrôleur LQR proposé aide à minimiser le risque de saturation de l'onduleur en présence des perturbations.

De même que les contrôleurs PI, PI+observateur, l'intégration du contrôleur LQR avec observateur dans le contrôle du VSG en boucle fermée a été testé avec le même onduleur utilisé pour tester le contrôleur PI. Les résultats de simulation obtenus ont confirmé les bonnes performances du contrôleur (stabilité, non-saturation de l'onduleur) en présence des perturbations considérées.

Pour clore ce Chapitre, il est proposé quelques perspectives et extensions intéressantes, notamment la prise en compte du fonctionnement en mode déséquilibré du système de puissance considéré et l'étude de commandabilité et d'observabilité.

Le Chapitre 4 comprend deux parties qui sont dédiées respectivement à l'implémentation du contrôle du VSG sur la carte du banc d'essai de l'onduleur industriel de l'entreprise Schneider Electric et à la validation du VSG par des tests expérimentaux. Dans la première partie, afin de respecter les limites de surcharge du CPU (Central Process Unit) du banc d'essai expérimental, le système de contrôle du VSG, est échantillonné avec trois fréquences différentes : 20 kHz, 6.6kHz, 1kHz (au lieu d'une seule fréquence élevée, soit 20kHz). Cette séparation fréquentielle trouve tout à fait son intérêt, les calculs de la charge CPU en pourcentage pour l'ensemble du contrôle du VSG implémenté sur la carte existante de l'onduleur montrent bien que les limites de surcharge du CPU sont respectées.

Dans la deuxième partie du Chapitre, les performances du contrôle du VSG sont évaluées de manière expérimentale en mode îloté et connecté au réseau. Une étape préliminaire dans un environnement **HIL** (Hardware-in-the-loop) a été menée pour s'assurer de la fiabilité et ainsi éviter une détérioration de matériel. Les tests ont été menés dans une configuration source isolée en considérant différentes configurations de la charge : démarrage avec la charge maximale, l'impact de connexion et de déconnexion de la charge maximale, charge fortement inductive, charges non linéaire ou déséquilibrées, des courts-circuits, des démarrages de moteur asynchrone. Ce dernier cas est intéressant car sur un réseau fort le moteur absorbe un courant élevé au démarrage (5 à 6 le courant nominal). Dans le cas présent, le contrôle réduit la tension pour limiter la surintensité, d'où un démarrage plus long. Dans le modèle connecté au réseau, le contrôle du VSG est évalué en fonctionnement parallèle avec un générateur et avec un autre VSG.

Les résultats expérimentaux obtenus, tant en mode îloté qu'en mode connecté au réseau principal, confirment l'efficacité des performances du contrôle du VSG proposé.

Dans la première partie du Chapitre 5, deux problèmes liés à l'adaptation du contrôle du VSG avec d'autres onduleurs industriels sont mentionnés. Le premier problème est lié à l'adaptation des paramètres de la machine synchrone aux nouvelles caractéristiques d'un nouvel onduleur (courant nominal et maximum, tension nominal et fréquence de commutation) pour le contrôle du VSG. Le deuxième problème concerne les contrôleurs de courant à définir pour le nouvel onduleur. Ainsi, un calcul analytique des paramètres basé sur le modèle complet de la machine synchrone est présenté en prenant en compte les limites du nouvel onduleur pour résoudre le premier problème.

Ensuite, en tenant compte des caractéristiques du banc d'essai développé au sein du laboratoire G2Elab et des calculs analytiques des paramètres de la machine synchrone en fonction des limites de l'onduleur, le système de contrôle du VSG est adapté en fonction de ces nouveaux paramètres. Afin de montrer l'efficacité du contrôle du VSG dans le banc d'essai, des tests similaires à ceux du Chapitre précédent en modes îloté et connecté au réseau ont été évalués. L'implémentation est faite au sein de la plateforme du G2Elab sur un onduleur de

4kVA Un réseau émulé est connecté à cet onduleur physique via un amplificateur de puissance. Le couplage entre la partie physique et virtuelle se fait via un ensemble couplé de sources de tension réelles et de sources de courant émulée.

Les résultats obtenus confirment la répliquabilité et la portabilité du contrôle du VSG proposé avec la méthodologie détaillée et le contrôle proposé en Chapitre 3.

Dans le Chapitre 6, le concept du VSG polymorphique est présenté. Il consiste à optimiser l'ensemble des paramètres de la machine synchrone embarquée dans le VSG pour éviter la détérioration de l'onduleur pendant des surtensions, des surintensités et des saturations. En ce qui concerne le modèle réduit de la machine synchrone proposée pour le VSG, 5 paramètres, L_d , L_q , L_d' , R_s et T_d0' , sont choisis pour définir le problème d'optimisation afin d'éviter de dépasser les limites maximales admissibles par l'onduleur en termes de courants, tensions et rapports cycliques, ce qui permet d'éviter ou de minimiser les dommages de l'onduleur. Le problème d'optimisation est basé sur une fonction objective exprimée sous la forme de la différence entre les modules des variables désirées (courant, tension et saturation) et leurs limites respectives. La solution du problème d'optimisation du contrôle polymorphique est d'obtenir un ensemble de paramètres de la machine de façon à ce que cette différence soit égale à zéro. Ensuite, afin de minimiser le temps de calcul (charge CPU) de l'implémentation du contrôle polymorphique sur les onduleurs industriels, trois solutions telles que la prédiction parabolique, les modèles de régression (Standardisation et Principal Component Analysis) et la détermination de la meilleure combinaison de paramètres sont examinées pour le contrôle polymorphique.

Il est montré, après comparaison, que la meilleure solution d'un point de vue du temps de calcul est celle de "la meilleure combinaison de paramètres". Cette comparaison valide bien l'intérêt de la procédure adoptée en simulation.

La conclusion fait l'objet du Chapitre 7. Elle rappelle l'objectif du mémoire, le contexte de la thèse et les divers points traités. Cette partie reprend de manière synthétique les contributions de ce travail de thèse, à savoir l'utilisation de l'onduleur VSG et son contrôle pour l'intégration des énergies renouvelables dans le contexte d'un micro-réseau. Dans la conclusion est listé un certain nombre de perspectives lié aux travaux effectués pendant la thèse. Par exemple, la prise en compte de la composante homopolaire dans les différents modèles du VSG permettrait certainement d'améliorer les performances du VSG dans le cas de charges déséquilibrées.

Résumé

Les sources classiques d'énergie distribuée (DER) fournissant de l'énergie aux microgrids (généralement des groupes électrogènes diesel) sont progressivement remplacées par des onduleurs basés sur des sources d'énergie renouvelables (RES). Cependant, l'intermittence des sources d'énergie renouvelables pose des problèmes de stabilité majeurs, en particulier dans le contexte des microgrids, notamment parce que ces sources diminuent l'inertie disponible du réseau électrique. Par conséquent, les stratégies de contrôle traditionnelles pour les onduleurs, qui interfacent les différents DER connectés aux micro-réseaux électriques, doivent être adaptées.

Le générateur virtuel synchrone (VSG) est l'une des solutions les plus populaires pouvant participer à l'augmentation de l'inertie des microgrids et pouvant être intégré dans les études de stabilité traditionnelles car il présente des similitudes avec une machine synchrone. Le VSG étant encore un concept récent, principalement pris en compte pour l'intégration de la DER dans un réseau, diverses problématiques demeurent non résolues (certaines d'entre elles sont abordées dans ce manuscrit). De plus, les différentes solutions trouvées dans la littérature ne prennent pas en compte les aspects industriels et pratiques de son développement (également pris en compte dans cette thèse industrielle).

Cette thèse est dédiée aux onduleurs basés sur le VSG et à leur intégration dans des microgrids à forte pénétration d'énergie renouvelable variable. Cette thèse a été réalisée grâce à la coopération de deux laboratoires, G2Elab et Gipsa-Lab, en collaboration avec Schneider Electric et son équipe de R & D, Power Conversion.

Abstract

The classical distributed energy resources (DER) supplying energy to microgrids (usually diesel generator-sets) are progressively supplanted by supplier based on renewable energy sources (RES). However, the intermittency of RES leads to major stability issues, especially in the context of microgrids, notably because these sources usually decrease the available inertia of the grid. Hence, the traditional control strategies for inverters, interfacing the various DERs connected to the microgrid, needs adapting.

The virtual synchronous generator (VSG) is one of the most popular solution that can participate in increasing the microgrids inertia and that could be integrated into traditional stability studies because it presents similarities with a synchronous machine. As the VSG is still a recent concept, mostly considered for the DER integration in microgrid, various problematics remain unresolved (some of which are addressed in this manuscript). In addition, the different solutions that can be found in the literature do not consider the industrial and practical aspect of its development (also considered in this industrial thesis).

This thesis is dedicated to the VSG-based inverters and their integration in microgrids with a high level of variable renewable energy penetration. This PhD have been carried out thanks to the cooperation between two laboratories, G2Elab and Gipsa-Lab, in collaboration with Schneider Electric and its R & D team, Power Conversion.
